Role of dendritic equiaxed grains in macrosegregation formation : numerical modeling of laboratory benchmarks and industrial ingot solidification

Tao Wang

To cite this version:

Tao Wang. Role of dendritic equiaxed grains in macrosegregation formation : numerical modeling of laboratory benchmarks and industrial ingot solidification. Chemical and Process Engineering. Université Grenoble Alpes [2020-..]; Northeastern University (Shenyang), 2021. English. NNT : 2021GRALI054 . tel-03326505

HAL Id: tel-03326505
https://theses.hal.science/tel-03326505v1

Submitted on 13 Dec 2021

THÈSE

Pour obtenir le grade de

DOCTEUR DE L'UNIVERSITE GRENOBLE ALPES

préparée dans le cadre d'une cotutelle *entre la Communauté Université Grenoble Alpes* et *l'université du Nord-Est de Chine*

Spécialité : **Matériaux, Mécanique, Génie civil, Electrochimie**
Arrêté ministériel : 25 mai 2016

Présentée par

Tao Wang

Thèse dirigée par **Pr. Yves Delannoy** et **Pr. Engang Wang**
codirigée par **Dr. Olga Budenkova**

préparée au sein des **Laboratoires SIMaP/EPM** et **EPM (Université du Nord-Est de Chine)**
dans **L'école Doctorale I-MEP^2** et **L'école Supérieure de Métallurgie (Université du Nord-Est de Chine)**

Rôle des grains équiaxes dendritiques dans la formation de macroségrégation: modélisation numérique des benchmarks laboratoires et solidification de lingot industrielle

Thèse soutenue publiquement le **1 June 2021**,
devant le jury composé de :

M. Valéry BOTTON
Professeur à l'INSA Lyon, Président
M. Hervé COMBEAU
Professeur à l'Université de Lorraine, Rapporteur
Mme. Nathalie MANGELINCK-NOEL
Directrice CNRS Section 15, Rapporteuse
M. Ilya PESHKOV
MCF (Associate Professor) at University of Trento, Examinateur
M. Frederic AYELA
Professeur à l'UGA, Examinateur
M. Yves DELANNOY
Professeur à l'UGA, Grenoble INP, Directeur de Thèse
M. Engang WANG
Université du Nord-Est de Chine, Directeur de Thèse
Mme. Olga BUDENKOVA
Chercheuse CNRS, Invitée, Co-encadrante
M. Yves FAUTRELLE
Professeur Emerite à l'UGA, Grenoble INP, Invité

Role of dendritic equiaxed grains in macrosegregation formation: numerical modeling of laboratory benchmarks and industrial ingot solidification

by
Tao Wang

Supervised by
Prof. Yves Delannoy, Prof. Engang Wang, Dr. Olga Budenkova

A dissertation submitted in partial fulfillment
of the requirements for the degree of Doctor of Philosophy
in the subject of I-MEP2
in the Communauté Université Grenoble Alpes
and
in the subject of Ferrous Metallurgy
in the Northeastern University

China
2021

Acknowledgements

None of the works presented in this thesis would have become a reality without the support and encouragement from my supervisors, my family, my friends and many people who once offered me help.

At first, I would like to express my high respect and sincere thanks to Prof. Yves Delannoy. As the supervisor of this thesis, he is knowledgeable in the field of magnetic hydrodynamics, and is easy-going in daily life. He gave me many times lectures on mathematical modeling and is always ready to help me. With his generous help, I was well fitted into the new team and devoted myself to research work.

I would like to express my deep gratitude to Prof. Engang Wang. He has been directing me since I was a master student, and under his guidance I entered the academic field. He also devoted a lot of effort to this PhD project and gave me many insightful comments.

I feel considerably grateful to Dr. Olga Budenkova, who is very responsible and responsive during the time she guiding me. She made great contribution to this work including formulating the research plan, debugging the developed code, and proofreading the thesis. It was with her encouragement and tireless help that I was able to make continuous progress.

My sincere thanks also go to Prof. Yves Fautrelle for introducing me to study in SIMAP/EPM laboratory and for his many useful suggestions on my research.

I would like to thank to my friends, Dazhao Gou, Hongfei Wang, Bin Yang, Jin Xu, et al. and especially to Tingyu, for your warm help and companionship. I am also grateful to my colleagues, Sergey Semenov, Qingwei Bai, Lingling Xuan, Xinming Xing, Ahmed Nouri, Gourav Sen, Florin Baltaretu, Abdelmounaim Ahmine, et al. It is really a fruitful and pleasant experience working with you.

Most importantly, I would like to give my deepest appreciation and best wishes to my parents. Thank you for bringing me up under the hardship of living and for your consistent support during my time pursuing the PhD.

Resumé

Cette thèse concerne la solidification d'alliages et plus particulièrement la modélisation de la macroségrégation des lingots métallurgiques sous l'effet de la croissance de grains équiaxes en mouvement au sein de la phase liquide. Le développement d'un modèle numérique basé sur des moyennes de volume y est présenté, suivi par des tests sur des expériences modèles et par une application à la coulée d'un lingot industriel.

Un modèle modernisé de solidification équiaxe à trois phases a été développé, avec une nouvelle expression de la longueur de diffusion requise dans l'équation de croissance des grains. L'effet drastique du modèle de longueur de diffusion a été démontré par des simulations de solidification d’alliage Sn-5_{pds}% Pb dans une cavité parallélépipédique, similaire à l'expérience de Hebditch-Hunt. La fiabilité de ce nouveau modèle de solidification équiaxe a été testée à l'aide d'une simulation numérique du benchmark AFRODITE de solidification de l'alliage Sn-10_{pds}% Pb avec brassage électromagnétique. Les distributions calculées de température au cours de la solidification et de la macro-ségrégation finale sont en bon accord avec les résultats expérimentaux. L'effet de l'intensité de la force de Lorentz utilisée pour le brassage sur la macro-ségrégation finale a été analysé numériquement. Enfin, le modèle de solidification équiaxe développé dans cette thèse a été utilisé pour étudier la formation de la macro-ségrégation dans un lingot d'acier de 2,45 tonnes. Le mécanisme de formation de la macro-ségrégation dans le lingot a été analysé et l'effet de l'intensité du refroidissement a été étudié. De plus, l'effet du brassage électromagnétique sur le processus de solidification et sur la formation de macro-ségrégation dans le lingot a été étudié par une série de simulations numériques.

Mots clés: solidification des alliages; simulation numérique; mouvement des grains équiaxes; macro-ségrégation; brassage électromagnétique; coulée continue d’acier

Abstract

This thesis concerns the solidification of alloys and more particularly the modeling of macrosegregation in metallurgical ingots due to the growth of equiaxed grains in motion within the liquid phase. The development of a numerical model based on volume average method is presented, followed by tests on benchmark experiments and by an application to the casting of an industrial ingot.

First, a modernized three-phase multiscale equiaxed solidification model has been developed, in which a new expression of the diffusion length required in the equation of grain growth has been introduced. The drastic effect of the diffusion length model has been demonstrated through simulations for solidification of Sn-5 wt% Pb alloy in a brick-shaped cavity that mimics the Hebditch-Hunt experiment. Then, the reliability of that new equiaxed solidification model has been tested using a numerical simulation of the AFRODITE benchmark experiment on solidification of Sn-10 wt% Pb alloy with electromagnetic stirring. The predicted distributions of temperature during the solidification and of the final macro-segregation agreed well with experimental results. The effect the intensity of the Lorentz force used for stirring on final macrosegregation pattern has been analyzed numerically. Finally, the equiaxed solidification model developed in this work has been used to study the formation of macrosegregation in a 2.45 ton industrial steel ingot. The formation mechanism of macrosegregation in the ingot has been analyzed and the effect of cooling intensity has been studied. In addition, the effect of electromagnetic stirring on solidification process and macrosegregation formation in the ingot has been investigated through a series of simulations.

Key words: alloy solidification; numerical simulation; equiaxed grain movement; macrosegregation; electromagnetic stirring; steel casting

Table of contents

List of figures in French summary

List of figures

List of tables in French summary

List of tables

Nomenclature

A_{emf}	amplitude of electromagnetic force ($\mathrm{N\ m^{-3}}$)
A_E	amplitude of the potential vector ($\mathrm{T\ m}$)
B	magnetic induction intensity (T)
c_i	solute concentration in *i*- phase (wt%)
c_{mix}	solute concentration of the mixture of solid and liquid (wt%)
c_{eut}	eutectic concentration (wt%)
c_l^*, c_s^*	equilibrium concentration at *f*-*s* or *d*-*s* interface (wt%)
c_{env}	concentration at *l*-*d* interface (wt%)
c_p^i	specific heat for *i*-phase ($\mathrm{J\ kg^{-1}K^{-1}}$)
c_0	initial concentration (wt%)
C_E	adjustable coefficient (1)
d_e, d_s	grain diameter (m)
d_k	characteristic length (m)
D_l	diffusion coefficient in liquid ($\mathrm{m^2s^{-1}}$)
ε	dissipation of turbulent energy ($\mathrm{m^2s^{-2}}$)
f	AC current frequency (Hz)
f_i	volume fraction of *i*- phase (1)
f_p^e, f_p^s	packing limit fraction (1)
f_s^e	solid fraction within grains (1)
$\vec{F}_{Bi}$	buoyancy force of *i*-phase ($\mathrm{kg\ m^{-2}s^{-2}}$)
$\vec{F}_{Ei}$	electromagnetic force acting on *i*-phase ($\mathrm{kg\ m^{-2}s^{-2}}$)
h_i	enthalpy of of *i*- phase ($\mathrm{J\ kg^{-1}}$)
H^*	interfacial heat transfer coefficient ($\mathrm{W\ m^{-3}K^{-1}}$)
J_{ij}	species transfer rate from *i*- phase to *j*- phase ($\mathrm{m\ s^{-1}}$)
J_Φ	species transfer rate from nucleation ($\mathrm{kg\ m^{-3}s^{-1}}$)

k	solute partition coefficient (1)
$k_E\ k_E^*\ k_{emf}$	wave vector (m^{-1})
k_ε	turbulent kinetic energy ($\mathrm{m}^2\mathrm{s}^{-2}$)
K_{ij}	liquid-equiaxed drag coefficient ($\mathrm{kg\ m}^{-3}\mathrm{s}^{-1}$)
l_i	diffusion length of *i*- phase (m)
L	latent heat ($\mathrm{J\ kg}^{-1}$)
m	slope of liquidus in phase diagram (K)
M_Φ	mass transfer rate from nucleation ($\mathrm{kg\ m}^{-3}\mathrm{s}^{-1}$)
M_{ij}	mass transfer rate from *i*- phase to *j*- phase ($\mathrm{kg\ m}^{-3}\mathrm{s}^{-1}$)
n_{max}	maximum equiaxed grain density (m^{-3})
n	grain number density (m^{-3})
N_Φ	nuclei production rate ($\mathrm{m}^{-3}\mathrm{s}^{-1}$)
Re	Reynolds number (1)
Sh	Sherwood number (1)
S_e^M	surface concentration of the equivalent sphere (m^{-1})
S_e^J	diffusion surface concentration of the grain phase (m^{-1})
t	time (s)
T_i	temperature (K)
T_f	melting temperature (K)
T_{nucl}	nucleation temperature
T_{eut}	eutectic temperature (K)
T_q	temperature at the solid-liquid interface (K)
T_0	initial temperature (K)
ΔT	constitutional undercooling (K)
ΔT_{nucl}	nucleation undercooling (K)
$\vec{u}_i$	velocity vector of *i*- phase ($\mathrm{m\ s}^{-1}$)
$\vec{U}_{ij}^D$	momentum transfer rate from *i*- phase to *j*- phase ($\mathrm{kg\ m}^{-2}\mathrm{s}^{-2}$)
v_{env}	envelope growth velocity ($\mathrm{m\ s}^{-1}$)

v_{ds}	*d-s* interface growth velocity ($\mathrm{m\ s^{-1}}$)

Greek Symbols

β_T	thermal expansion coefficient ($\mathrm{K^{-1}}$)
β_c	solutal expansion coefficient (1)
Γ	Gibbs-Thomson coefficient (m K)
κ_i	thermal conductivity for *i*-phase ($\mathrm{W\ m^{-1}K^{-1}}$)
λ_2	secondary arm spacing (m)
μ	magnetic permeability ($\mathrm{V\ s\ A^{-1}\ m^{-1}}$)
μ_i	viscosity of *i*- phase ($\mathrm{kg\ m^{-1}s^{-1}}$)
ρ_i	density of *i*- phase ($\mathrm{kg\ m^{-3}}$)
ρ_{ref}	reference density ($\mathrm{kg\ m^{-3}}$)
ρ_s^b	density of solid phase for buoyancy
σ	electrical conductivity ($\mathrm{Ohm^{-1}cm^{-1}}$)
τ	pole pitch in electromagnetic linear motor (m)
Ψ_i	a intensive medium property (-)
ϕ_{M}	shape factor of dendritic envelope growth (1)
ϕ_{J}	sphericity of dendritic envelope (1)

Subscripts

d	interdendritic liquid phase
$e : d + s$	equiaxed grain phase
$f : l + d$	liquid phase
l	extradendritic liquid phase
s	interdendritic solid phase

French Summary

Introduction

Des matériaux résistant aux hautes températures et à la corrosion, ou ayant une plasticité élevée, sont nécessaires pour la construction des turbines, des appareils à pression, des tôles de navire, etc. Le mélange de plusieurs métaux, c'est-à-dire la fabrication d'alliages, tels que l'acier, les superalliages, les alliages d'aluminium ou autre, permet d'obtenir des combinaisons de propriétés physiques requises pour des applications particulières. La principale méthode d'élaboration des alliages est la coulée continue, qui constitue 98,3 % de la production d'acier. D'autres techniques de coulée, telles que la coulée en lingots, la refusion sous laitier et la coulée centrifuge sont également utilisées en fonction de la demande pratique de produits. Un phénomène fondamental au cours du processus de coulée est la solidification, c'est-à-dire le passage du matériau de l'état liquide à l'état solide. Pendant la solidification, une ségrégation des composants se produit à l'interface solide-liquide, car le réseau cristallin du matériau solide émergent ne peut pas accepter tous les atomes du soluté, et les rejette ainsi dans le liquide. On sait que les conditions locales affectent la microstructure, et que la microstructure définit les propriétés du produit final. Par conséquent, les produits formés à partir de mêmes composants peuvent avoir des structures finales et des performances fonctionnelles distinctes si la solidification s'est produite dans des conditions différentes. Des conditions de solidification incorrectes entraînent des défauts graves dans le produit final comme la porosité, la fissuration et une forte ségrégation.

On pourrait s'attendre à ce qu'une meilleure compréhension des phénomènes complexes qui se superposent pendant la solidification puisse contribuer à une amélioration de la qualité de la coulée. Cependant, l'analyse post-mortem d'échantillons issus d'une coulée ne fournit des informations que sur l'état final de la solidification, et peut être assez surprenante car l'évolution des différents phénomènes dans le temps reste obscure. Quant aux expériences in-situ, elles portent souvent sur des échantillons de petite taille et sur un écoulement convectif plutôt faible. Donc, les résultats de l'observation in-situ ne pourraient pas être facilement transposés à des processus de solidification à grande échelle. Par conséquent, une modélisation numérique est nécessaire pour comprendre comment l'émergence d'une structure de solidification colonnaire ou équiaxe affecte la convection et le transport du soluté pendant le processus de solidification. Une bonne modélisation de la solidification des alliages fait intervenir de multiples champs physiques et des phénomènes à plusieurs échelles. Les premières descriptions théoriques du processus de solidification étaient principalement basées sur un seul ou un nombre limité de phénomènes tels que l'analyse thermique, l'analyse des écoulements, la théorie de la nucléation et la morphologie de la solidification. Plus tard, grâce à la combinaison et à la vérification de descriptions théoriques et de pratiques de production, la prédiction et le contrôle qualitatifs des structures et des défauts typiques des pièces coulées ont été atteints. Cependant, la compréhension quantitative globale fait défaut et le contrôle du système complexe de la solidification n'est toujours pas réalisé. Nous pensons que le modèle moyenné en volume proposé il y a quelque temps pourrait être une solution pour obtenir une description et une prédiction multidomaine/multiéchelle du processus de solidification des alliages multicomposants, même pour des champs de température et d'écoulement complexes. Grâce aux progrès réalisés au cours des dernières décennies, le modèle moyenné en volume peut être appliqué aujourd'hui pour prédire et optimiser le procédé de coulée industriel.

Dans la coulée de produits industriels, on s'attend souvent à obtenir une grande région de grains équiaxes car ce type de structure est supposé plus homogène que la structure constituée de grains colonnaires. D’un autre côté, on sait que la sédimentation des grains équiaxes lors de la solidification peut provoquer une ségrégation négative au fond des gros lingots. La simulation numérique de la solidification avec des grains équiaxes est plus compliquée qu'avec des grains colonnaires, car il faut tenir compte de phénomènes tels que la nucléation, la traînée des grains par rapport à la phase liquide et leur blocage dû à l'interaction avec les parois et les autres grains. Actuellement, la méthode des moyennes volumiques permet de simuler la solidification équiaxe sous convection forcée à l'échelle macroscopique. Cependant, malgré la diversité des modèles de solidification équiaxe existants, la fiabilité des résultats qu'ils produisent reste incertaine, principalement pour les trois raisons suivantes. Tout d'abord, ces modèles reposent sur diverses hypothèses physiques utilisées pour fermer le système d'équations et contiennent de nombreux paramètres semi-empiriques auxquels les résultats numériques sont très sensibles. Ensuite, bien que de sérieux efforts expérimentaux et théoriques aient été faits pour comprendre l'effet de la convection sur les phénomènes de solidification, ils n'ont pas vraiment été étendus aux écoulements turbulents, tels que ceux des procédés industriels surtout sous brassage électromagnétique. Enfin, il y a un manque de données expérimentales qui pourraient aider à valider le modèle de solidification dans un régime purement équiaxe en présence de convection.

Les expériences de référence ("benchmark") en solidification sont indispensables, car elles fournissent des données précieuses pour la validation des modèles de solidification. Le benchmark le plus connu a été réalisé par Hebditch et Hunt il y a plusieurs décennies. Dans ce travail, la distribution de la concentration à différentes étapes de la solidification est analysée, en regard de la macrostructure solidifiée. Cette expérience a été modélisée à plusieurs reprises et aujourd'hui, sa configuration ainsi que les conditions limites spécifiées servent de référence pour certaines études numériques. Par la suite, quelques dispositifs de référence ont été développés de manière similaire. Cependant, la plupart de ces expériences (y compris celle de Hebditch et Hunt) produisent principalement une structure colonnaire et ne sont donc pas adaptées à la validation d'un modèle de solidification équiaxe. Un autre benchmark expérimental de solidification est réalisé au laboratoire SIMAP/EPM en France et est appelé ci-après AFRODITE. En plus de caractéristiques similaires à celles des autres expériences de référence, AFRODITE comporte un moteur électromagnétique linéaire placé sous la cavité, capable de brasser l'alliage pendant la solidification. Avec un brassage électromagnétique opposé à la convection naturelle (force de Lorentz opposée à la vitesse de la convection thermosolutale), la structure des échantillons obtenus expérimentalement est principalement constituée de grains équiaxes. De plus, dans AFRODITE, la distribution bidimensionnelle de la température est enregistrée en temps réel. Ces caractéristiques font d'AFRODITE une bonne référence pour tester les performances du modèle macroscopique de solidification équiaxe sous un écoulement convectif.

L'objectif de cette thèse est de développer un modèle de solidification équiaxe triphasique, qui prend en compte la croissance des grains équiaxes, leur mouvement et la formation de la macro-ségrégation. Une étude de sensibilité du modèle, dans le cas du benchmark de Hebditch et Hunt, a fait ressortir l'importance d'un des paramètres du modèle : la longueur de diffusion. Ensuite le modèle numérique développé a été utilisé pour simuler l'expérience de solidification AFRODITE afin de tester ses performances et d'étudier l'effet de la brassage électromagnétique. Enfin, une simulation numérique a été faite pour prédire le processus de solidification et la macroségrégation dans un lingot industriel, en mettant particulièrement l'accent sur l'effet de l'intensité du refroidissement de surface.

La thèse se compose de 6 chapitres.

Le **chapitre 1** présente des notions allant de la théorie de la solidification aux mécanismes de formation de la macro-ségrégation qui sont nécessaires à la compréhension du sujet. Il présente également l'état de l'art des simulations numériques pour la solidification et la macro-ségrégation.

Le **chapitre 2** présente une analyse documentaire des modèles moyennés en volume actuellement utilisés pour les simulations de solidification. Plusieurs points clés du modèle de solidification sont passés en revue, notamment la nucléation, la croissance des grains, le transfert de soluté et l'échange de quantité de mouvement.

Le **chapitre 3** présente un modèle de solidification équiaxe multi-échelle à trois phases dans lequel certaines approximations concernant le transport du soluté à l'échelle microscopique sont rassemblées d'une nouvelle manière et incorporées dans des équations de transport macroscopiques. La simulation de la solidification d'un alliage Sn-5_{pds}% Pb dans une cavité parallélépipédique – configuration similaire à l'expérience Hebditch-Hunt – a permis d'étudier l'influence sur les résultats du calcul de la longueur de diffusion, un paramétré utilisé dans le modèle.

Dans le **chapitre 4**, ce modèle de solidification équiaxe est utilisé pour la simulation de l'expérience AFRODITE. Cette expérience fournit une évolution de la distribution de la température lors de toute la solidification et une carte de ségrégation finale, ce qui facilite la validation de la simulation numérique. La prédiction des distributions de température et de la macroségrégation correspondent bien aux résultats expérimentaux, ce qui indique la fiabilité du modèle développé. La macroségrégation a été analysée à la fois sous convection naturelle et sous brassage électromagnétique: l'influence de l'intensité du brassage sur la distribution du nombre de grains et la macro-ségrégation est ainsi étudiée de manière numérique.

Dans le **chapitre 5**, notre modèle de solidification équiaxe est utilisé pour étudier la formation de la macro-ségrégation dans un lingot d'acier industriel de 2,45 tonnes. La simulation révèle le rôle crucial du mouvement des grains équiaxes dans la formation de la ségrégation à grande échelle dans le lingot. L'effet de l'intensité du refroidissement de surface sur la solidification des lingots est étudié par la variation du coefficient de transfert thermique. L'effet du brassage électromagnétique est étudié à l'aide d'une série de simulations permettant de discuter de l'effet du sens de brassage, de son intensité et de la position du brasseur. Ces résultats fournissent une base pour améliorer les conditions de coulée et la conception des moules.

Enfin, le **chapitre 6** présente des conclusions et des recommandations pour les recherches futures.

Chapitre 1 Solidification et ségrégation

Le processus de solidification peut être décomposé en deux étapes: **la nucléation** et **le croissance** du grain. La nucléation crée une interface solide-liquide initiale pour la croissance ultérieure du grain qui s'accompagne d'une ségrégation. Du point de vue de la thermodynamique, l'événement de nucléation nécessite un certain degré de **surfusion** pour garantir que l'énergie libre de la phase solide soit inférieure à celle de la phase liquide. Sous cette condition remplie, en raison de la fluctuation aléatoire et de la collision des atomes de métal, une phase transitoire composée d'embryons ou de clusters se formera dans la masse fondue. Parmi les embryons, ceux dont la taille est supérieure au rayon critique de nucléation peuvent rester stables sous forme de nucléi (germes) ou continuer à se développer sous forme de grains. Ce processus est appelé **"nucléation spontanée"** [1]. La nucléation spontanée nécessite une surfusion assez élevée pour produire une quantité significative de germes, ce qui est contraire aux observations courantes dans la solidification des alliages. La solidification industrielle repose davantage sur une **nucléation hétérogène**, ce qui signifie que les germes apparaissent sur des interfaces existantes, telles que la surface d'inclusions ou de fragments dendritiques de solide, telles que la surface interne des moules, etc. Une fois que la nucléation a eu lieu, les germes grossissent progressivement avec l'ajout d'atomes attachés à la surface du solide.

Laissant de coté la question de la nucléation, on rappelle que la solidification ou la refusion des alliages se produit dans une gamme de températures, à savoir entre **liquidus** T_l et **solidus** T_s, toutes deux dépendantes de la composition de l'alliage, i.e. de la concentration du soluté (Fig. RF.1.1(a)). Pour un diagramme de phase linéarisé, la température du liquidus peut être exprimée sous la forme

$$T_l\left(c_l\right)=T_m+mc_l=T_l\left(c_0\right)+m\left(c_l-c_0\right)$$

où $m<0$ est **la pente du liquidus**, c_0 est la concentration initiale (nominale) du soluté et c_l est la concentration locale du soluté dans le liquide. De plus, l'équilibre entre la composition de la phase solide et de la phase liquide à l'interface est décrit par un **coefficient de partition** $k = c_0/c_l$. Ce dernier signifie que pendant la solidification, l'élément soluté a tendance à passer d'une phase à l'autre, ce qui se produit en raison de la différence de potentiel chimique entre les phases solide et liquide. Le cas général pour la construction du diagramme de phase est $\mathrm{m}(k-1)>0$, c'est-à-dire $k<1$. Cette dernière condition suppose que le soluté est **rejeté** par la phase solide pendant la solidification, ce qui crée une couche limite de concentration du soluté en amont de l'interface solide-liquide. Cela signifie que la température du liquidus varie et qu'il existe une région où elle est supérieure à la température thermodynamique du liquide, c'est-à-dire qu'il existe ce qu'on appelle une **surfusion chimique** (ou **surfusion constitutionnelle** ou **surfusion solutale**) (Fig. RF.1.1).

On suppose que le surfusion chimique est à l'origine de l'**instabilité de l'interface** car une petite perturbation du front de la solidification lors de son avancement peut provoquer une redistribution rapide du soluté et affecter la température du liquidus, c'est-à-dire affecter les conditions de solidification. Un effet positif de feed-back pourrait se produire occasionnellement et les perturbations de la forme du front pourraient augmenter. Les expériences de solidification ont montré que l'interface solide-liquide a tendance à passer d'une forme plane à une forme “perturbée” (ondulée, cellulaire), puis à une croissance dendritique (Fig. RF.1.2), ce que l'on appelle le phénomène d'**instabilité de l'interface**.

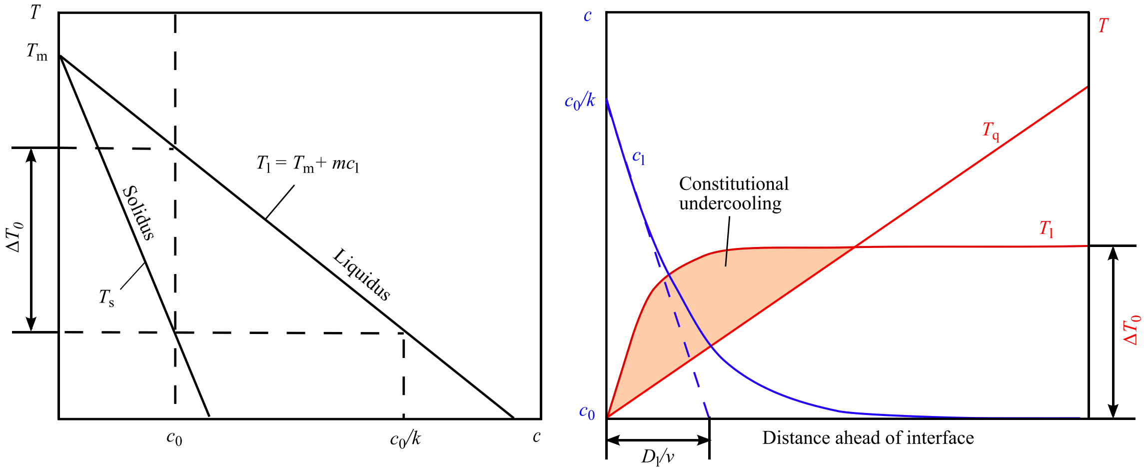

(a) (b)

Fig. RF.1.1 Diagramme de phase linéarisé pour un alliage eutectique binaire (a) et schéma montrant la surfusion chimique (surfusion constitutionnelle) là où la température de liquidus est supérieure à la température thermodynamique du liquide (b)

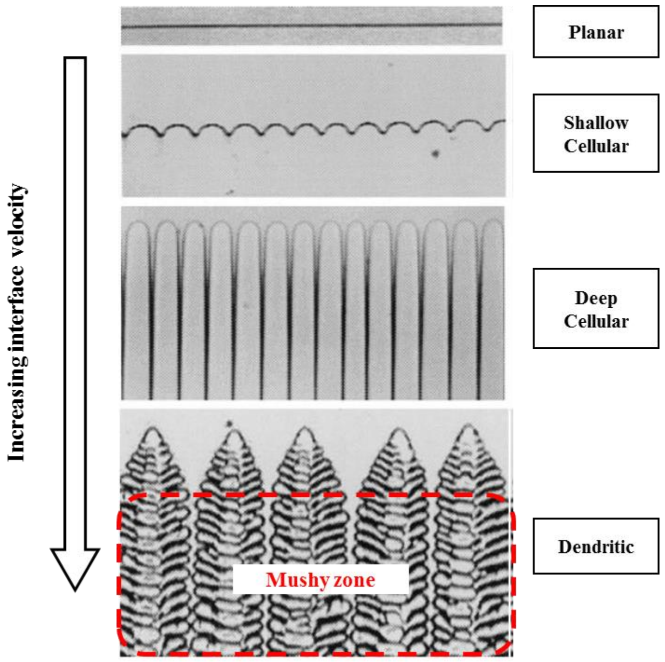

Fig. RF.1.2 Transition de l'interface planaire solide-liquide vers celle ayant une microstructure cellulaire et dendritique pendant la solidification directionnelle d'un alliage binaire dont la vitesse de croissance augmente (de haut en bas) [5]

En ce qui concerne la **ségrégation**, il est usuel de distinguer la **microségrégation** et la **macroségrégation**. La **microségrégation** fait référence à l'inhomogénéité de la composition chimique à petite échelle (µm) au sein des dendrites. La **macroségrégation** est l'inhomogénéité de la composition à l'échelle du lingot et est censée être plus préjudiciable que la microségrégation, car elle ne peut pas être éliminée par un traitement thermique ou un laminage ultérieur. Trois mécanismes de base sont à l'origine de la macroségrégation: (i) **l'écoulement convectif naturel ou forcé** de la phase liquide, (ii) **le mouvement des grains équiaxes** et (iii) l'écoulement liquide provoqué par le **retrait et la déformation**.

(i) **L'écoulement convectif** de la phase liquide est un agent important de la macroségrégation, car il transporte les molécules plus efficacement que la diffusion. La convection provoquée par la gravité, dite naturelle, existe dans presque tous les processus de solidification en conditions terrestres en raison de l'inhomogénéité de la température et de la concentration dans la masse fondue. La formation de macroségrégation est associée à un écoulement dynamique à travers la région partiellement solide – **zone pâteuse** – d'une pièce coulée. Dans la plupart des cas, un afflux du liquide plus pauvre en soluté remplace le liquide enrichi dans la zone pâteuse, ce qui entraîne une diminution de la concentration entre les dendrites, et le flux sortant de la zone pâteuse enrichit le liquide en volume. On suppose que l'application de forces externes, telles que le **brassage électromagnétique** (EMS), est capable de réduire la ségrégation à la fois à l'échelle micro et macro [30-33]. Cependant, il faut savoir que l'utilisation de l'EMS peut rendre la ségrégation plus prononcée (Fig. RF.3(b)) ou même créer de nouveaux défauts, par exemple ce qu'on appelle la "bande blanche" dans les billettes de coulée continue [9].

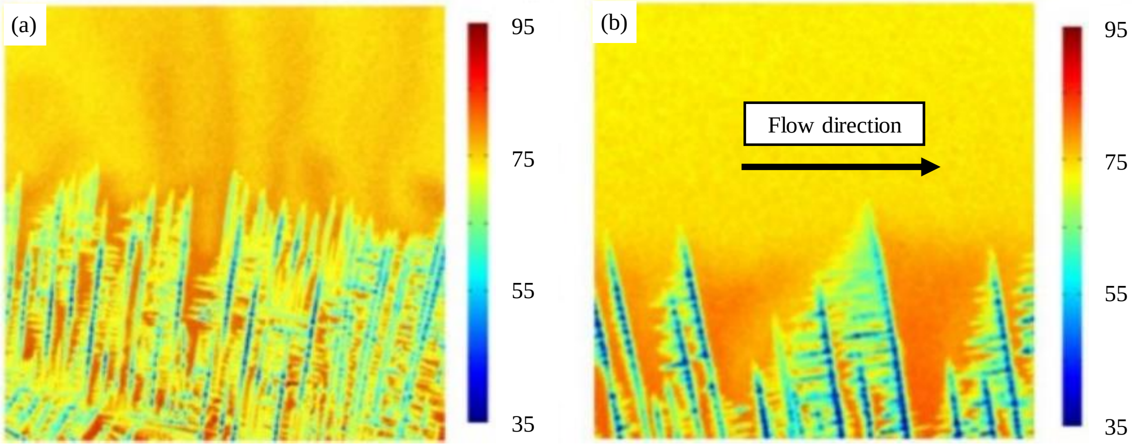

Fig. RF.1.3 Images instantanés de la structure dendritique et du champ de composition issues de la radiographie in-situ de l'alliage In-Ga en cours de solidification, à gauche : convection naturelle, à droite : convection dans la direction horizontale forcée par agitation électromagnétique [29]

(ii) Même dans un liquide restent repos, les **grains équiaxes peuvent flotter ou sédimenter** si leur masse volumique est différente de celle du liquide environnant. Le mouvement des grains devient plus complexe avec la convection dans le liquide et peut être encore plus déroutant sous convection forcée. Dans le cas d'un alliage à coefficient de partition $k < 1$, les grains sont pauvres en soluté tandis que le liquide enrichi est emporté par l'écoulement alentour. Une fois que les grains équiaxes se rapprochent les uns des autres, une région à ségrégation négative se forme. En particulier, parmi les différentes hypothèses [26, 37-40] proposées pour expliquer la formation de cône de ségrégation négative dans un lingot d'acier de 65 t (fig. RF.1.4), la sédimentation des cristaux équiaxes est largement considérée comme la raison cruciale.

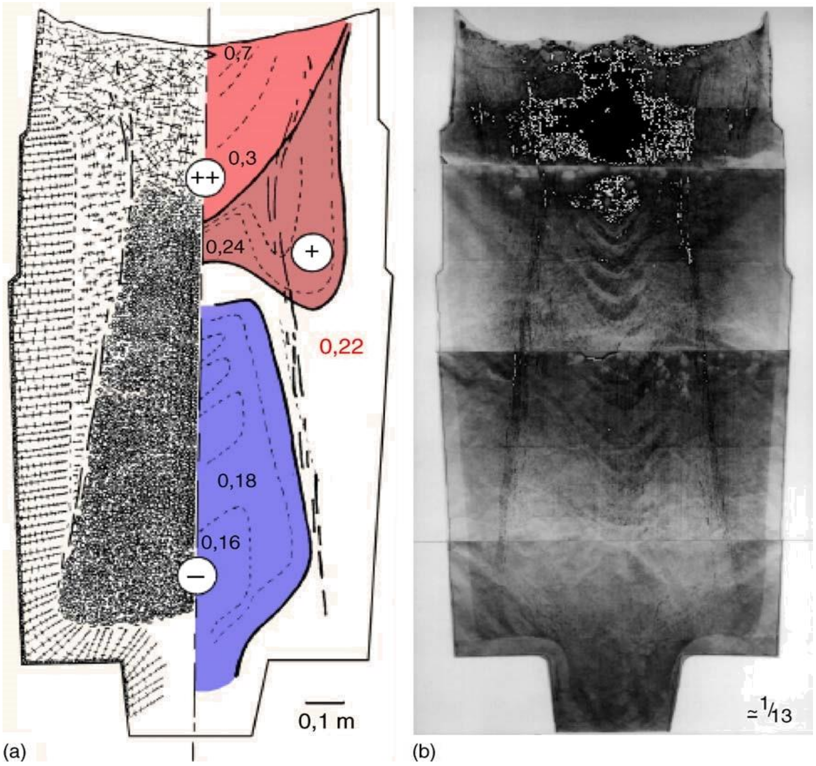

Fig. RF.1.4 Coupe longitudinale d'un lingot d'acier de 65 tonnes; (a) macrostructure et macro-ségrégation du carbone, (b) soufre empreinte [12]

(iii) Le **retrait à la solidification** est le résultat du passage de la phase liquide à la phase solide lorsque la masse volumique varie entre les phases. L'apport du liquide enrichi pour compenser le retrait de solidification entraîne une augmentation locale de la concentration de soluté. Cela donne lieu à ce que l'on appelle la "ségrégation inverse de surface" et à la ségrégation négative au cœur de la coulée. Ce phénomène s'avère important pour la prévision de la macro-ségrégation dans la coulée continue du cuivre [43] et des alliages à base d'aluminium [42,44].

Enfin, la **déformation de la zone pâteuse** peut se produire au cours du processus industriel et entraîner une compression (locale) ou un élargissement de cette dernière. Cela implique l'écoulement d'un liquide hautement enrichi vers l'extérieur ou l'intérieur de la zone **pâteuse** qui conduit à la ségrégation [45-48].

Simulations numériques de la solidification et macroségrégation : état de l'art

Le processus de solidification combine des phénomènes trans-échelle : de la nucléation à l'échelle atomique (Å) [49], à la croissance des dendrites et au transport du soluté à l'échelle micro (µm) et jusqu'à la conduction thermique et à l'écoulement multiphasique à l'échelle macro (m). (Fig. RF.1.5). Il est encore inconcevable de prendre en compte toutes ces échelles dans une procédure de modélisation unique. La difficulté est donc liée à la sélection des processus à modéliser qui seraient liés aux caractéristiques principales de l'échantillon solidifié, par exemple, la carte de concentration, la taille et la structure des grains, l'espacement des bras de dendrite primaire et secondaire. Depuis le siècle dernier, les développements des modèles de solidification à l'échelle macro (échelle de l'échantillon) et à l'échelle micro (échelle de quelques dendrites) se faisaient en parallèle et leur complétude était étroitement liée aux progrès des techniques et des ressources informatiques.

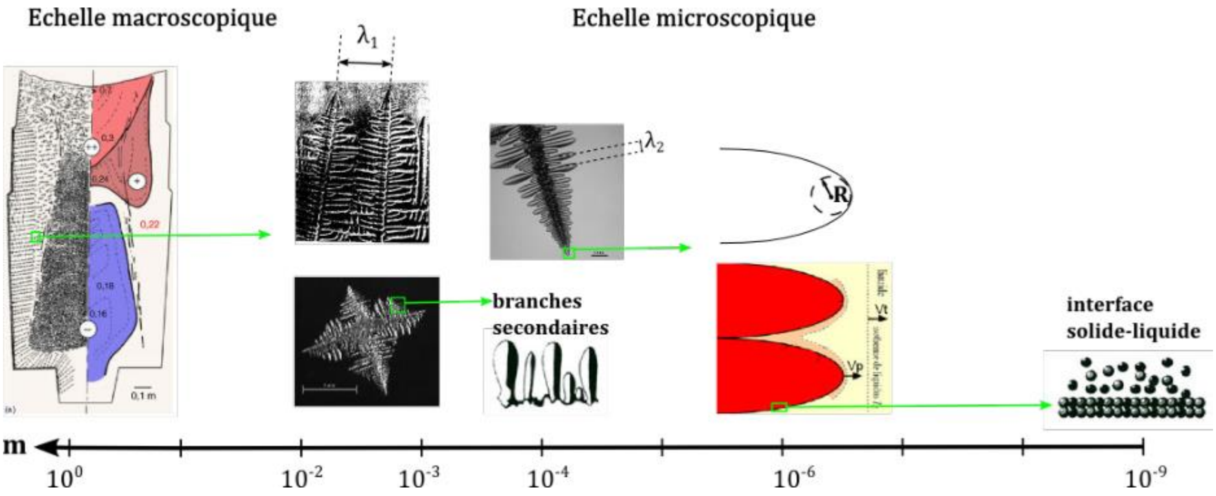

Fig. RF.1.5 Échelles caractéristiques de la solidification des alliages de taille décroissante de gauche à droite [25]

Actuellement, le **modèle de champ de phase** est souvent utilisé pour faire des recherches approfondies sur la théorie de la solidification et pour expliquer l'évolution de la microstructure observée dans les expériences [59]. L'inconvénient du modèle de champ de phase est qu'il consomme une quantité énorme de ressources informatiques. Par conséquent, il est encore loin de pouvoir l'appliquer à la modélisation industrielle. Selon la loi de Moore, une simple simulation numérique bidimensionnelle du processus de solidification des pièces coulées utilisant le modèle de champ de phase ne pourrait pas être possible avant l'année 2055 [49, 60].

En ce qui concerne la simulation de la solidification à l'échelle macro, **les méthodes moyennées en volume** sont aujourd'hui les plus avancées pour la simulation numérique des procédés de coulée. Les modèles équiaxes développés et appliqués au cours de cette thèse, présentés plus loin dans le mémoire, sont basés sur des moyennes volumiques.

Il convient toutefois de noter que depuis quelques années, de nouveaux modèles sont apparus et ont commencé à se développer rapidement pour mieux décrire divers phénomènes à méso-échelle, tels que les modèles d'enveloppe [66] et du réseau d'aiguilles dendritiques [67].

En ce qui concerne le développement du modèle numérique, une question très importante se pose concernant sa validation et sa vérification. Cela peut être fait en utilisant des expériences dites **benchmark**, c'est-à-dire des **expériences de référence**. Dans la thèse, les simulations de deux benchmarks de solidification à l'échelle laboratoire ont été réalisées: l'expérience Hebditch-Hunt [27] et AFRODITE [87]. Pour leurs descriptions le lecteur est invité à se reporter aux **chapitres 3 et 4**. Un **benchmark numérique** a été proposé par ailleurs [81] pour comparer des modèles de solidification colonnaire utilisant un système simplifié d'équations. Les distributions finales de ségrégation différaient fortement selon la méthode numérique (volume finis, éléments finis, méthode « sans maillage ») et les schémas utilisés [82] (premier où deuxième ordre, différence centrale ou upwind). Cela indique que le problème simulé est non-linéaire avec des phénomènes fortement couplés. La simulation des benchmarks à l'échelle laboratoire [72-80] est présentée dans la section 1.3.2 du mémoire. En ce qui concerne l'échelle industrielle, le cas de la **solidification de lingot** [40, 99-101 et références internes] peut être considéré comme un benchmark. Sa description détaillée est donnée la section 1.3.3 de la thèse et sa simulation numérique est présentée au **chapitre 5**.

Conclusion

Bien que de nombreux travaux de modélisation pour la solidification aient été publiées ailleurs, le mécanisme de formation de la macroségrégation dans de nombreuses études expérimentales reste obscur et la prédiction quantitative de la macroségrégation est toujours difficile. En se basant sur l'examen de nombreux travaux expérimentaux et de simulation, on peut conclure que la macroségrégation est souvent affectée par la croissance et le mouvement de grains équiaxes dont l'origine peut être différente. Lorsque l'on considère le mouvement des grains équiaxes, de nombreux paramètres numériques, tels que la fraction limite de blocage, la forme des grains, la densité numérique de grains, etc., sont capables d'affecter le processus de solidification et la carte finale de macroségrégation. C'est pourquoi cette thèse est consacrée à la modélisation de la solidification en régime équiaxe, en examinant en détail l'effet des différents paramètres utilisés dans le modèle. Avant d'appliquer le modèle de solidification équiaxe aux études du processus de solidification et de formation de macroségrégation dans le lingot d'acier, des simulations sont effectuées pour deux benchmarks.

Chapitre 2 Modèles de solidification moyennés en volume: état de l’art

La méthode moyennée (en volume et/ou statistique) est un instrument permettant de calculer la structure de solidification et la ségrégation des solutés à l'échelle de l'échantillon, en tenant compte de la cinétique de croissance des dendrites et des processus de ségrégation à l'interface solide-liquide, mais pour ces derniers de manière considérablement simplifiée.

La méthode moyennée en volume est en cours de développement depuis plusieurs décennies. En 1987, Rappaz et Thevoz [111] ont formulé un modèle de solidification moyenné en volume pour la croissance d'un grain dendritique d’alliage binaire tenant compte de la vitesse de croissance contrôlée par la diffusion du soluté à micro-échelle et de l'évolution du champ du soluté autour du grain. En utilisant cette méthode, Ganesan et Poirier [112] ont dérivé des équations de transport de la masse et de quantité de mouvement dans la zone pâteuse. Ni et Beckermann [113,114] ont appliqué un **modèle équiaxe globulaire à deux phases** à la solidification de l'alliage Al-4％Cu en tenant compte l’écoulement convectif à l'échelle macro. Par la suite, Wang et Beckermann [115,116] ont étendu le modèle à deux phases au **modèle à trois phases** (solide, liquides inter- et extradendritique), et ont proposé un modèle empirique pour calculer la résistance à l'écoulement dans chaque phase liquide. Ensuite, Nielsen et al. [119] ont proposé de prendre en compte la forme des grains dendritiques en utilisant des **facteurs de forme** dans le calcul de la concentration de surface. En suivant cette idée, Wu et Ludwig ont construit plusieurs modèles pour la solidification équiaxe, y compris le modèle globulaire à deux phases [120] et le modèle dendritique à trois phases [121]. Ils ont également développé un modèle de **solidification mixte colonnaire-équiaxe**, comprenant un modèle à trois phases (colonnaire, équiaxe et liquide) [122] et **un modèle à cinq phases** (liquide, liquide interdendritique dans le grain équiaxe, solide dans le grain équiaxe, liquide interdendritique dans le grain colonnaire, et solide dans le grain colonnaire) [123]. Les principes de base de ces modèles et certaines problématiques sont abordés ci-dessous.

La solidification suppose une transition de l'état liquide à l'état solide accompagnée de phénomènes de transport à micro-échelle dans chaque phase. La modélisation à l'échelle macro devrait traiter les processus de transport pour chaque quantité physique Ψ_i qui se produit dans chaque phase et tenir compte des sources supplémentaires de cette quantité en raison de la transition de phase. Ici Ψ_i représente une quantité conservative, notamment la masse, la quantité de mouvement, l'énergie, la concentration du soluté ou **la densité numérique de grains**. Cette dernière correspond au nombre de grains par unité de volume, ou à la « concentration » des grains. La présence de la phase *i*, n'importe où dans l'espace et à tout moment, est définie à l'échelle micro avec une fonction caractéristique de phase :

$$X_i\left(\vec{x},t\right)=\begin{cases}1 & f\left(\vec{x},t\right) \text{ within phase } i\\ 0 & \text{elsewhere}\end{cases}$$

Il est à noter que la signification d'une "phase" dans un modèle numérique peut être différente d'une définition traditionnellement acceptée en thermodynamique. Par exemple, les trois phases qui sont souvent représentées dans les modèles modernes de solidification équiaxe sont : la phase solide, la phase liquide interdendritique et la phase liquide extradendritique.

Pour passer de la description microscopique à la description macroscopique, il faut d'abord choisir un volume macroscopique élémentaire représentatif V_0 et y inclure toutes les phases possibles. Ensuite, on moyenne l'équation de transport microscopique d'une quantité physique Ψ_i sur V_0 pour chaque phase. Cette procédure définit:

– la fraction volumique de la phase *i*:

$$f_i=\frac{V_i}{V_0}=\frac{1}{V_0}\int_{V_0}X_i\mathrm{d}V=\frac{V_i}{V_0}$$

– la moyenne de Ψ_i sur le volume:

$$\langle\Psi_i\rangle=\frac{1}{V_0}\int_{V_0}\Psi X_i\mathrm{d}V$$

– et la moyenne de Ψ_i pondérée sur le volume de la phase *i* (moyenne intrinsèque):

$$\langle\Psi_i\rangle^i=\frac{1}{V_i}\int_{V_0}\Psi X_i\mathrm{d}V=\frac{1}{f_i}\langle\Psi_i\rangle$$

Finalement, l'équation moyennée de transport de Ψ_i à l'échelle **macroscopique** s'écrit:

$$\frac{\partial f_i\langle\Psi_i\rangle^i}{\partial t}+\nabla\left(f_i\langle\Psi_i\rangle^i\langle\vec{u}_i\rangle^i\right)=\langle\Psi_i\rangle^i_{diff}+\langle\Psi_i\rangle^i_{source} \qquad \text{(RF.2.1)}$$

où le second terme du membre de gauche représente l'advection, alors qu'au membre de droite on trouve le terme de transport diffusif et le terme source pour la quantité physique Ψ_i. L'expression de chacun de ces termes dépend de la variable physique considérée Ψ_i, comme le résume le tableau RF.1.1. Une notation simplifiée est utilisée pour les valeurs moyennées sur les volumes: $\langle\rho_i\rangle^i$ est écrite ci-dessous comme ρ_i, $\langle u_i\rangle^i$comme u_i, etc.

Table RF.2.1 Définition des termes dans l'Eq. (RF.2.1)

Quantité conservative	Ψ	$\langle \Psi_i \rangle^i_{diff}$	$\langle \Psi_i \rangle^i_{source}$		
			Changement de phase	Échange entre phases	Source additionnelle
Densité numérique de grains	n	0	0	0	Taux de nucleationN_Φ
Masse	$f_i\rho_i$	0	$M_{ij} = S^{\text{int}}_{ij} v^*_{ij} \rho_i$	0	Taux de transfert de masse
Quantité de mouvement	$f_i\rho_i\vec{u}_i$	$\nabla\left[f_i\mu_i\left(\nabla\vec{u}_i + \left(\nabla\vec{u}_i\right)^{\mathrm{T}}\right)\right]$	$\vec{U}^M_{ij} = M_{ij}\vec{u}^*$	$\vec{U}^D_{ij} = K_{ij}\left(\vec{u}_j - \vec{u}_i\right)$	Poids et autres forces de volume
Énergie	$f_i\rho_i h_i$	$\nabla\left(f_i\kappa_i\nabla T\right)$	$Q^M_{ij} = M_{ij}h^*$	$Q^D_{ij} = H^*\left(T_j - T_i\right)$	Chaleur Joule
Concentration de soluté	$f_i\rho_i c_i$	$\nabla\left(f_i D_i \rho_i \nabla c_i\right)$	$J^M_{ij} = M_i c^*_{ij}$	$J^D_{ij} = \rho_i D_i / l_i\left(c^* - c_i\right)$	0

L'étape suivante consiste à définir les termes sources relatifs au changement de phase (transformation d'une phase en une autre) et les termes d'échange de quantités physiques à travers l'interface entre les phases.

Le taux de nucléation N_ϕ dans l'équation pour la densité numérique des grains

La nucléation est une étape essentielle dans la formation de la microstructure, car la densité numérique de grains détermine la taille instantanée et finale des grains. Comme indiqué ci-dessus, les germes proviennent principalement de la nucléation non spontanée qui peut être traitée comme une nucléation instantanée ou homogène. Le modèle instantané suppose que tous les germes apparaissent dans une plage de température étroite [135]. Le modèle de nucléation hétérogène définit la relation entre le taux de nucléation et la valeur de la surfusion, ce qui imite l'activation continue des inoculants (embryons) pendant le processus de refroidissement. Les expressions mathématiques utilisées pour décrire ces processus avec une explication détaillée se trouvent dans le texte principal de la thèse (eq. (2.3) et (2.4) dans la section 2.3 de la Thèse).

En outre, pour affiner la structure des grains et améliorer la qualité de la coulée, un procédé pratique consiste à augmenter la densité numérique de grains. Parmi les différentes méthodes appliquées dans l'industrie, on peut citer (1) l'application d'une force externe, telle que l'agitation électromagnétique ou mécanique pour favoriser la fragmentation des dendrites; (2) l'ajout d'un agent de nucléation approprié. Des exemples de description mathématique du taux de nucléation avec ces deux mécanismes sont donnés dans la thèse (eqs. (2.5) et (2.6) dans la section 2.3 de la thèse).

Modèle de changement de phase: taux de transfert de masse M_i

Puisque l'hypothèse de l'équilibre thermique à l'échelle d'un grain est largement acceptée, la croissance de la dendrite est principalement contrôlée par la diffusion du soluté. Le modèle de croissance des grains qui définit la quantité de masse transférée M_i vers la phase i en raison du changement de phase est crucial pour la simulation de la solidification: toutes les équations conservatrices données ci-dessus dans le tableau RF.2.1 (sauf celle pour la densité numérique de grains) contiennent un terme lié à M_i. Dans le modèle moyenné en volume, le changement de phase est lié au déplacement d'une interface (entre phases) à laquelle une surface peut être attribuée. En général, la source de masse dans une phase $i$peut être écrite comme "flux de densité" à travers une interface, c'est-à-dire comme $M_i = S_i^{int} v_i^* \rho_i$ où S_i^{int} est la surface spécifique de l'interface et v_i^* est la vitesse de déplacement de la surface. Le calcul de ces variables peut être effectué de différentes manières en fonction de l'hypothèse sur la forme des grains et des lois cinétiques. Par exemple, les grains des phases solides peuvent être considérés comme globulaires/cylindriques ou dendritiques, colonnaires ou équiaxes (Fig. RF.2.1).

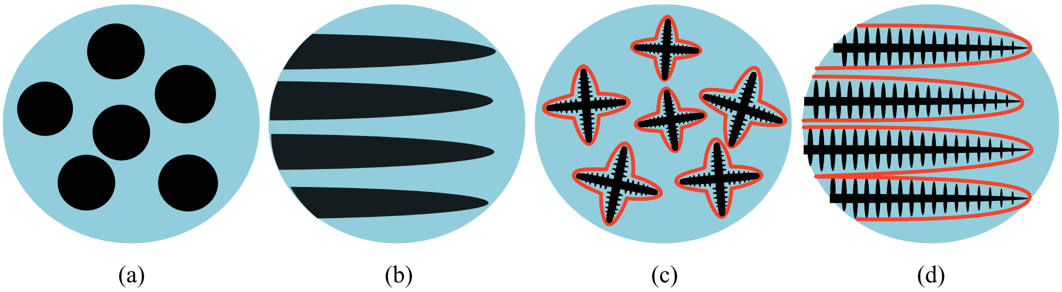
(a) (b) (c) (d)

Fig. RF.2.1 Morphologie schématique des grains: (a) grain globulaire équiaxe, (b) grain cylindrique colonnaire, (c) grain dendritique équiaxe, et (d) grain dendritique colonnaire; dans (c) et (d) la surface de l'enveloppe est montrée avec la ligne rouge

Dans le cas des grains **globulaires/cylindriques,** deux phases sont considérées dans la modélisation: solide et liquide. Par conséquent, la surface à travers laquelle la masse est transportée correspond à la surface du solide et peut être calculée soit à partir de la densité numérique de grains n (pour les grains globulaires), soit en utilisant la distance entre les grains (pour les grains cylindriques colonnaires), appelée **espacement des dendrites primaires**. Les grains dendritiques sont généralement décrits avec l'utilisation de trois phases, ce qui permet de séparer d'une part le liquide entre les bras de dendrite secondaires (et d'ordre supérieur), et d'autre part le liquide autour du grain. Cela signifie que le changement de phase se produit entre la phase solide et le liquide dit **interdendritique** et entre le liquide **interdendritique** et **extradendritique**. Une surface imaginaire, appelée **enveloppe**, qui englobe le squelette solide et le liquide interdendritique, est traditionnellement utilisée pour faciliter la description du processus de solidification. Ainsi, le transfert de masse entre le liquide interdendritique et extradendritique M_{le} se produit à travers l'enveloppe ayant une surface spécifique S_{env} dont la représentation mathématique est similaire à celle de la surface des grains globulaires/cylindriques. Cependant, le transfert de masse entre le liquide interdendritique et le solide M_{ds} se produit à travers l'interface solide-liquide dont la surface spécifique S_{sd} est généralement définie par l'espacement entre les bras secondaires de dendrite λ_2.

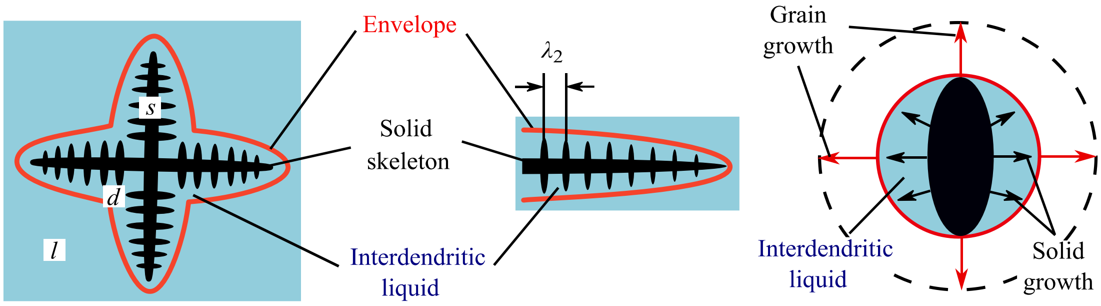

Fig. RF.2.2 Présentation schématique de la structure dendritique et de croissance du grain : le squelette solide se développe au détriment du liquide interdendritique, mais l'extrémité de la dendrite se propage dans le liquide extradendritique

Enfin, pour obtenir les termes source liés à chaque type de changement de phase, on a besoin de la vitesse de déplacement de l'interface correspondante. Bien que les modèles d'équilibre basés sur la règle du levier ou de Scheil soient toujours utilisés, la plupart des modèles supposent que la vitesse de diffusion du soluté dans le liquide n’est pas instantanée. Par conséquent, des modèles basés sur la surfusion constitutionnelle sont utilisés. Parmi eux, le modèle KGT (d'après Kurz, Giovanola et Trivedi) [144] pour le grain colonnaire et le modèle LGK (d'après Lipton, Kurz et Glicksman) [145] pour le grain équiaxe sont utilisés pour décrire la vitesse de la pointe de la dendrite. Cependant, la vitesse moyenne de l'expansion de l'enveloppe est différente de celle obtenue pour la pointe de la dendrite. Cette différence est corrigée par divers **facteurs de forme** présentés dans le tableau RF.2.2 pour différentes formes de grains dendritiques.

Flux diffusif du soluté J_i^D

La redistribution du soluté entre la phase solidifiée et le liquide, avec son transport ultérieur par diffusion et convection dans ce dernier, est un phénomène important dans la formation de la macro-ségrégation. Cependant, il faut noter que la croissance des grains, leurs flottement/sédimentation et même le phénomène de blocage sont également affectés par le taux d'échange du soluté, de manière indirecte, en particulier dans le cas d'un écoulement convectif. Selon la description du phénomène de solidification (chapitre 1), les processus à prendre en compte sont (1) le rejet du soluté par le solide vers liquide, (2) l'incorporation de soluté par le déplacement de l'interface solide-liquide, (3) le transport du soluté rejeté dans le liquide par diffusion et, éventuellement, par convection.

Table RF.2.2 Facteurs de forme des dendrites [123]

Grain équiaxe		Grain colonnaire	
Sphère $\phi_e^{env} = \phi_e^{sph} = 1$	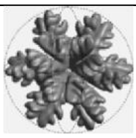	cylindre $\phi_c^{env} = \phi_c^{sph} = 1$	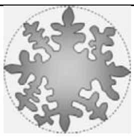
Octaèdre $\phi_e^{env} = 1/\sqrt[3]{\pi}$ $\phi_e^{sph} = \sqrt[3]{\pi}/\sqrt{3}$		Square $\phi_c^{env} = \sqrt{2}/\sqrt{\pi}$ $\phi_c^{sph} = \sqrt{\pi}/2$	
OSP6+ $\phi_e^{env} = \sqrt[3]{11/32\pi}$ $\phi_e^{sph} = \sqrt[3]{484\pi}/(12+\sqrt{3})$		OSW4++ $\phi_c^{env} = 1/\sqrt{\pi}$ $\phi_c^{sph} = \sqrt{\pi/10}$	

\+ 6 pyramides droites à base carrée (OSP6) avec angle au sommet 18.43º;

++ 4 prismes à base carrée (OSW4) avec angles au sommet 60º.

Comme présenté dans le tableau RF.2.1, le terme J_i^M est lié à l'échange du soluté entre deux phases par changement de phase liquide-solide et le terme J_i^D est la flux entre eux par diffusion. Cependant, en raison de la forme complexe du grain solide, l'estimation de l'épaisseur de la couche de diffusion autour de celui-ci n'est pas évidente, et donne lieu à une large variété d'expressions lorsque l'on considère le flux convectif autour du grain. Un schéma de distribution du soluté dans un modèle triphasé est donné dans la figure RF.2.3.

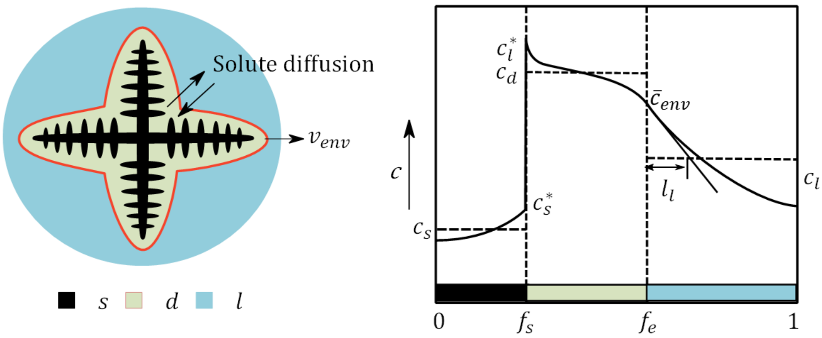

Fig. RF.2.3 Schéma d'un grain dendritique et distribution du soluté dans le modèle à trois phases: diffusion négligeable du soluté dans le liquide interdendritique, flux diffusif du soluté vers le liquide extradendritique fonction de la longueur de diffusion l_l

Alors que la diffusion dans le liquide interdendritique est généralement négligée [24,63,117,118], il peut arriver que l'enrichissement du liquide extradendritique dépende largement de l'intensité de la diffusion du soluté du liquide interdendritique vers le liquide extradendritique. Le tableau RF.2.3 donne quelques exemples d'estimation de la longueur de diffusion effective proposée dans les modèles à deux et trois phases.

Table RF.2.3 Longueur de diffusion devant la pointe de la dendrite dans les modèles de solidification équiaxe

Référence	Phases type de grain	Longueur de diffusion l_l or l_f
Rappaz et Thévoz [150]	l, d, s dendritique	$l_l = D_l / v_{tip}$ (Sans écoulement)
Ni et Beckermann [114]	f, s globulaire	$l_f = \frac{d_s}{2}\left(\frac{1}{1-\left(1-f_f\right)^{1/3}} + \frac{Sc^{1/3}Re^a}{3f_f}\right)^{-1}$
Wang et Beckermann [115]	l, d, s dendritique	$l_l = \frac{d_e}{2+0.865\left(\frac{C_\varepsilon}{f_l}\right)^{1/3}\left(\frac{f_l\lvert\vec{u}_l-\vec{u}_e\rvert}{D_l}\right)^{1/3}}$ avec $C_\varepsilon = C_\varepsilon\left(f_l\right)$
Appolaire et Combeau [152]	l, d, s dendritique (cristal isolé en milieu infini)	$l_l = \min\left(d_e / Sh, D_l / v_{tip}\right)$ où $Sh = 2 + 0.6Sc^{1/3}Re^{1/2}$
Wu et Ludwig [148]	l, d, s dendritique	$l_l = \begin{cases} d_e / 2 & \text{croissance globulaire} \\ D_l / v_{\text{env}} & \text{croissance dendritique} \end{cases}$

Mouvement du liquide et dendrites: phases “hydrodynamiques” et la force de traînée

L'expression de l'échange de quantité de mouvement (ou force de traînée) entre les phases i et j, désignée par $\overrightarrow{U}_{ij}^{D}$ (tableau RF.2.1), dépend du choix des phases qui représentent le mouvement macroscopique dans le système. La phase j relative au grain dendritique peut être présentée uniquement comme le squelette solide dans le liquide (Fig. RF.2.4(a)), ou comme une union du squelette solide et du liquide interdendritique (ce qui donne un grain) dans le liquide extradendritique (Fig. RF.2.4(b)). Dans ce dernier cas, cependant, une différence de vitesse macroscopique entre la phase solide, le liquide interdendritique et le liquide extradendritique peut être prise en compte (Fig. RF.2.4(c)). Il est courant de traiter l'échange de quantité de mouvement en termes de phase liquide i passant par un milieu j en utilisant un coefficient d'échange généralisé K_{ij} et la différence des vitesses des phases, c'est-à-dire comme $\overrightarrow{U}_{ij}^{D} = -\overrightarrow{U}_{ij}^{D} = K_{ij}(\vec{u}_j - \vec{u}_i)$. En outre, le coefficient d'échange peut être exprimé avec la perméabilité K d'un milieu poreux ou par le coefficient de traînée C_D et le facteur de configuration F_{CD} en fonction de la "configuration" du milieu j soumis à l'écoulement du fluide i.

$$K_{le} = F_K\left(f_e, d_e\right)\frac{\mu_l}{K} = F_{CD}\left(f_e, d_e\right)C_D\rho_l\left|\vec{u}_l - \vec{u}_e\right| \qquad \text{(RF.2.2)}$$

Une des possibilités est de traiter chaque grain équiaxe comme une particule flottant dans une grande quantité de liquide, et d'obtenir la force de traînée totale comme une somme pondérée des forces sur toutes les particules (Fig. RF.2.5(a)). Une autre option consiste à considérer un groupe de grains comme une unité compacte (Fig. RF.2.5(b)). Le tableau RF.2.4 présente quelques modèles utilisés pour calculer le coefficient d'échange de quantité de mouvement.

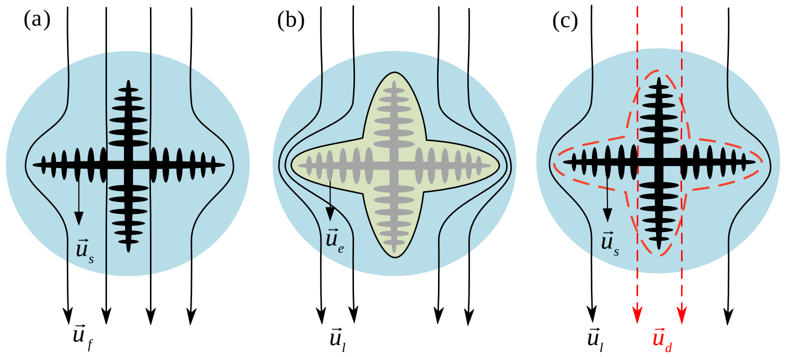

Fig. RF.2.4 Présentation de différentes unions de phases: (a) dendrite solide (*s*-phase) et phase liquide (*f*-phase), (b) grain équiaxe (*e*-phase) et liquide extradendritique (*l*-phase); (c) dendrite solide (*s*-phase) liquide interdendritique (*d*-phase) et liquide extradendritique (*l*-phase)

Table RF.2.4 Coefficient d'échange de quantité de mouvement

Référence	Phases ou unions, type de grain	Coefficient pour Eq. (RF.2.2)
Wu et Ludwig [148]	$l, e{=}(d \cup s)$ dendritique	$K_{le} = F_k\left(f_l, d_e\right)\frac{\mu_l}{K} = \begin{cases} \frac{180\mu_l f_e^2}{f_l d_e^2} & f_e < f_{sc} \\ \frac{\mu_l f_l^2}{K} & f_e > f_{sc} \end{cases}$
Ni et Beckermann [114]	f, s globulaire	$K_{fs} = F_{CD}\left(f_s, d_s\right) C_D \rho_l \left\lvert \vec{u}_f - \vec{u}_s \right\rvert$ $F_{CD} = \frac{3}{4}\frac{f_s}{d_s},\ C_D = \frac{48 C_{ke}\left(1 - f_f\right)}{Re} + C_{ie}$ $Re = \frac{\rho f_f d_s}{\mu_f}\left\lvert \vec{u}_f - \vec{u}_s \right\rvert$ $C_{ke} = 0.5, C_{ie} = 7/3$ pour $f_f \le 0.5$ $C_{ke}\left(f_f, Re\right),\ C_{ie}\left(f_f, Re\right)$ pour $f_f > 0.5$
Apollaire et Combeau [152]	l, d, s dendritique (cristal isolé en milieu infini)	$F_{CD} = \frac{\rho_f \pi d_e^2}{8},\ C_D = \frac{C_D^{'}}{1.2376\log\left(\Phi / 0.1556\right)}$ où $C_D^{'}\left(Re\right)$, $\left(d_e / \sqrt{K}\right)$, Φ est sphéricité
Leriche et Combeau [24]	$f{=}(l \cup d), s$ dendritique	Région du lisier: $F_{CD} = \frac{3\rho}{4}\frac{f_e}{d_e},\ C_D = \frac{48 C_{ke}\left(1 - f_l\right)}{Re} + C_{ie}$ $C_{ke} = 0.5,\ C_{ie} = 7/3$ pour $f_e > 0.5$ $C_{ke}\left(f_l, Re\right)$, $C_{ie}\left(f_l, Re\right)$ pour $f_e \le 0.5$ Région bloquée: $K = \frac{\lambda_2^2}{20\pi^2}\frac{f_f^3}{\left(1 - f_f\right)^2}$

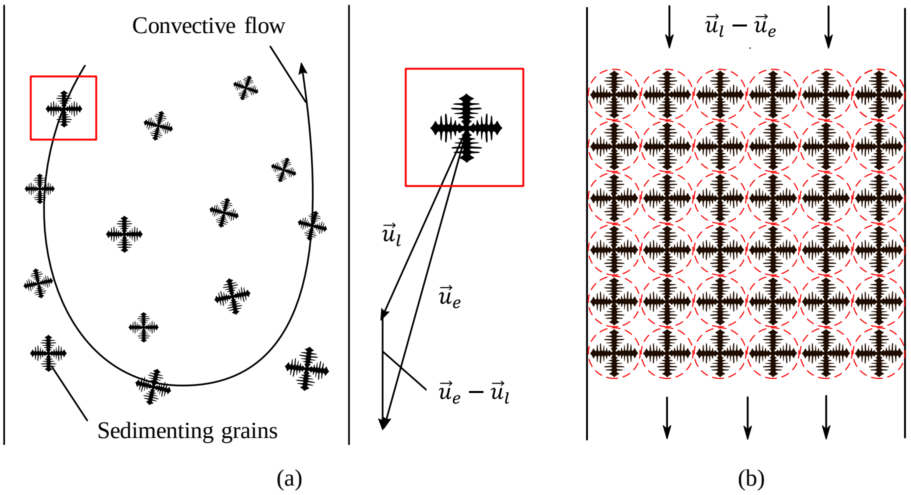

Fig. RF.2.5 Illustration de la définition de la force de traînée dans le cas de mouvement libre des grains équiaxes dans le liquide (a) et si le liquide traverse le “réseau” des grains équiaxes (b)

Blocage des grains équiaxes

Le blocage des grains équiaxes est un phénomène qui se produit lorsque les grains équiaxes s'attachent aux parois du creuset ou aux autres grains qui étaient déjà attachés aux parois. Avant d'être bloqués, les grains se déplacent librement dans le liquide, tandis qu'après avoir été bloqués, ils sont fixés et forment une structure rigide semblable à celle des grains colonnaires. Dans les modèles numériques, cette transition est traitée avec une fraction limite de blocage, qui peut être associée soit à la fraction volumique de la phase de grains f_p^e, soit à la fraction volumique de la phase solide f_p^s, selon les phases hydrodynamiques utilisées dans le modèle (Fig. RF.2.6).

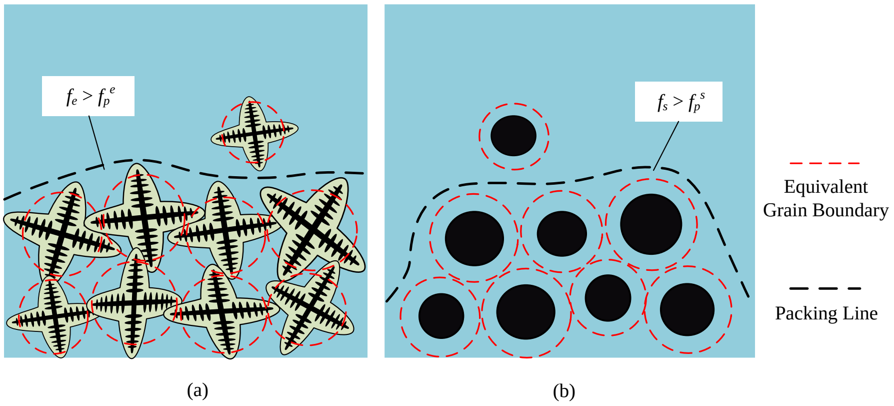

Fig. RF.2.6 Schéma de blocage des grains dans le modèle à trois phases (a) et le modèle à deux phases (b)

Ainsi, on suppose que pour un grain équiaxe en mouvement libre dont la fraction volumique augmente jusqu'à la fraction limite de blocage, sa vitesse devrait tomber à zéro, ce qui peut être réalisé numériquement de différentes manières. Les valeurs adoptées pour la limite de blocage ont un effet important sur les résultats des calculs, car le mouvement du grain équiaxe s'arrête brusquement [83]. Un algorithme de blocage des grains adapté à l'écoulement convectif a été proposé dans la thèse (cf. chapitre 3).

Conclusion

L'histoire et la théorie du modèle moyenné en volume ont été introduites. On peut en conclure que cette méthode présente d'importants avantages pour décrire les phénomènes multiéchelles, d'autant plus qu'on peut aisément l'étendre à de nouveaux phénomènes. Des problématiques importantes liées à l'utilisation de moyennes de volume en solidification ont fait l'objet d'un examen approfondi, notamment les taux de nucléation, de changement de phase, de transfert de soluté (liés à une longueur de diffusion), l'échange de quantité du moment entre phases et le blocage des grains. On remarque que la plupart de ces questions sont étroitement liées à la modélisation de la solidification en régime équiaxe. Chacun de ces paramètres peut avoir un effet significatif sur le résultat de la modélisation. Les différents choix possibles donnent une grande incertitude pour le calcul. Ainsi, l'étude du rôle de chaque hypothèse et de chaque paramètre numérique est une étape critique dans le développement d'un modèle numérique approprié. Le prochain chapitre sera consacré à cette activité.

Chapitre 3 Solidification équiaxe: traitement des questions clé et application du modèle aux expériences de références

Dans ce chapitre, en abordant les questions de choix des paramètres évoquées au chapitre 2, nous présentons un modèle de solidification à trois phases adapté à la convection naturelle dans le liquide. Après une brève description du modèle à trois phases, nous présentons le traitement du coefficient d'échange de la quantité du moment et un nouvel algorithme pour le blocage des grains. Ensuite, nous étudions l'effet de la longueur de diffusion dans le liquide extradendritique, avec écoulement convectif, sur le processus de solidification d'un grain dendritique unique et sur la solidification d'un lingot dans un benchmark. Enfin, l'algorithme est révisé et un système d'équations recommandé est présenté.

Modèle équiaxe à trois phases

Pour le modèle, nous avons choisi une présentation basée sur l'utilisation du concept d'enveloppe comme une surface imaginaire qui enferme un squelette dendritique solide (*s*-phase) avec une certaine quantité de liquide entre ses bras, appelé liquide interdendritique (*d*-phase). L'intérieur de l'enveloppe, (solide et le liquide interdendritique), est un grain équiaxe (*e*-phase) et l'extérieur de l'enveloppe est le liquide extradendritique (l-phase). Selon l'approche moyennée en volume, chaque phase est représentée par sa fraction volumique : f_s pour la phase solide, f_d, f_l pour le liquide inter- et extradendritique. La fraction des grains est $f_e = f_s + f_d$, et la contrainte $f_e + f_l = 1$ est respectée. Le liquide interdendritique et le squelette solide se déplacent ensemble donc partagent le même champ de vitesse $\vec{u}_e$, différent de la vitesse du liquide extradendritique $\vec{u}_l$. À l'échelle macro, on écrit des équations de conservation de quantité de mouvement seulement pour les grains et pour le liquide extradenritique (équations de Navier-Stokes dans le cas de l'écoulement laminaire). Ces équations prennent en compte la force de flottabilité selon l'approximation de Boussinesq et d'autres force externes (notamment, la force électromagnétique dans le chapitre 4).

Le système d'équations contient également les équations de transport de concentration intrinsèque moyenne des phases, notamment c_l (concentration dans la phase extra-dendrittique), c_e et c_s (pour la phase des grains et la phase solide). En outre, une concentration moyenne associée avec la surface de l'enveloppe c_{env}, est introduite, ainsi que les concentrations c_l^* et c_s^* pour l'interface entre le liquide et le solide. Le processus de solidification est décrit par l'expansion de l'enveloppe qui représente la croissance du grain, et l'expansion du squelette solide. La vitesse pour le premier est définie à l'aide du modèle LGK [145] et un facteur de forme (cf. Tableau RF.2.4 chapitre 2), la vitesse de second est établie à partir de la conservation de concentration illustrée dans la Fig. RF.3.2.

Le système des équations est expliqué en détail dans la section 2.1 du mémoire, seules les nouveautés de notre modèle sont présentées ci-dessous.

Modèle d'échange de quantité de mouvement

Il était intéressant de comparer différentes expressions pour un échange de quantité de mouvement entre phases dans un problème de sédimentation de grains équiaxes en liquide stationnaire. Le bilan de force dans le problème est donné par l'équation RF.3.1 (Fig. RF.3.1a) et donne directement la vitesse d'équilibre de l'équation RF.3.2 :

$$\vec{U}_{le}^{D} = K_{le}\left(\vec{u}_e - \vec{0}\right)V_0 = f_e\left(\rho_s - \rho_l\right)V_0\vec{g} \tag{RF.3.1}$$

$$u_{sed} = f_e\left(\rho_s - \rho_l\right)g / K_{le} \tag{RF.3.2}$$

Nous avons choisi de comparer les force de traînée calculées par la loi de Stokes, par les modèles de Kozeny-Carman [153], de Ni et Beckermann [114] et de Happel [154], dont les expressions mathématiques sont données dans le texte principal du mémoire (section 2.1.1), avec les autres paramètres numériques de ces calculs.

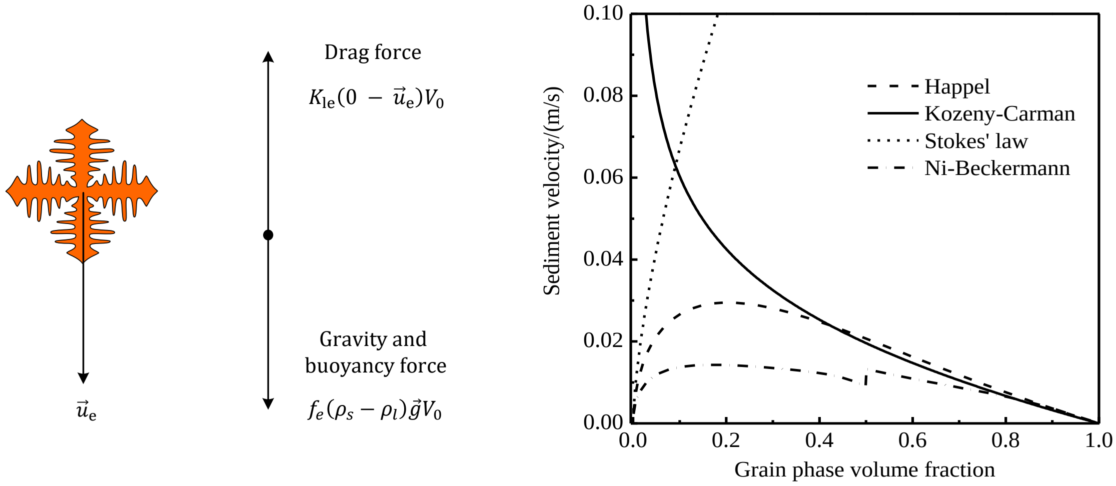

Fig. RF.3.1. Schéma des forces sur un grain equiaxe dans un liquide au repos et vitesse d'équilibrede sédimentation calculée par l'équation RF.3.2

Cette comparaison a montré que le modèle Carman-Kozeny ne parvient pas à prédire une vitesse nulle pour les grains dont la fraction est faible (c'est-à-dire les très petits grains au début de la solidification) qui pourraient être considérés comme étant en suspension dans le liquide. La loi de Stokes sous-estime la surface des grains dendritiques dont la fraction s'approche de l'unité, ce qui conduit à une vitesse de sédimentation trop élevée. Le modèle de Happel et la loi proposée par Ni et Beckermann donnent des résultats similaires pour les grains dont la fraction est proche de zéro ou, au contraire, supérieure à 0.8. Nous avons choisi le modèle de Happel en raison de son comportement lisse dans toute la gamme de la fraction des grains.

Modèle de longueur de diffusion

Différentes méthodes de calcul de la longueur de diffusion l_l dans le liquide extradendritique ont été discutées dans l'introduction et sont rappelées dans le Tableau RF.3.3 et la Figure RF.3.2. Toutes ces méthodes mettent l'accent sur la vitesse à la pointe de la dendrite, le diamètre actuel et final du grain (ou d'enveloppe), et la vitesse relative entre le grain et la phase liquide.

L'effet de la longueur de diffusion – ou, en fait, du modèle choisi pour son calcul – lors de la croissance d'un grain dans un volume fermé, avec un taux de refroidissement imposé, est étudié dans le mémoire (section 2.2.1). Nous montrons que l'équation (RF.3.3) surestime significativement l_l au début de la solidification, où son comportement est non monotone. Cependant, les équations (RF.3.5) et (RF.3.6) peuvent donner à nouveau une évolution non monotone de l_l lors de la croissance ultérieure du grain, contrairement aux équations (RF.3.3-RF.3.4). Comme l'indique la discussion approfondie de la section 3.3.1 du mémoire, la phase solide n'est pas affectée alors que vitesse de croissance de l'enveloppe (donc du grain) dépend fortement de l'écoulement convectif autour des grains qui contrôle l'enrichissement du liquide extradendritique.

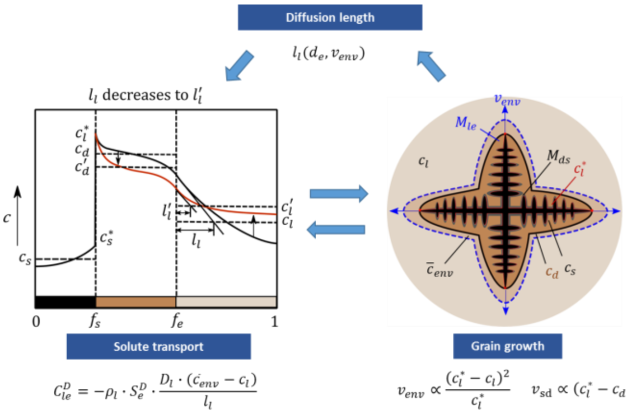

Fig. RF.3.2 Relation entre la longueur de diffusion l_l, le transport du soluté et la croissance du grain

Table RF.3.1 Équations pour le calcul de l_l

$$l_l = \frac{D_l}{v_{\mathrm{env}}} \tag{RF.3.3}$$

$$l_l = \min\left[\frac{d_e}{2}, \frac{D_l}{v_{\mathrm{env}}}\right] \tag{RF.3.4}$$

$$l_l = \min\left[\frac{d_e}{2}\left(\frac{1}{1-(1-f_l)^{\frac{1}{3}}}\right)^{-1}, \frac{D_l}{v_{\mathrm{env}}}\right] \tag{RF.3.5}$$

$$l_l = \min\left[\frac{d_e}{2}\left(\frac{1}{1-(1-f_l)^{\frac{1}{3}}} + \frac{Sc^{\frac{1}{3}} Re^a}{3 f_l}\right)^{-1}, \frac{D_l}{v_{env}}\right] \tag{RF.3.6}$$

Benchmark de Hebditch-Hunt

Les expériences de Hebditch et Hunt il y a plusieurs décennies [27] sont considérées comme benchmark en raison des données disponibles sur les procédés. Cette expérience a d'ailleurs servi d'application à un modèle équiaxe [85], bien qu'une solidification à structure colonnaire ait été observée dans l'expérience réelle. La première validation du modèle équiaxe développé dans cette thèse utilisé également l'expérience Hebditch-Hunt, dans laquelle un alliage Sn-5%$_{\mathrm{pds}}$Pb a été solidifié dans une cavité rectangulaire dont une paroi latérale est refroidie à l'eau (Fig. RF.3.3).

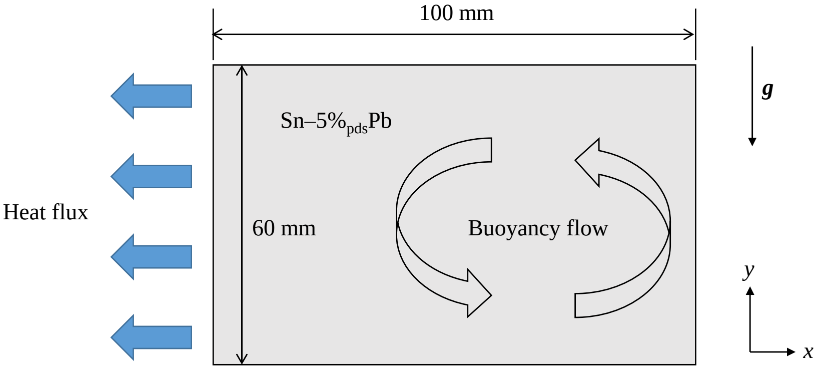

Fig. RF.3.3 Schéma du problème de la solidification de Sn-5%$_{\mathrm{pds}}$Pb correspondant à l'expérience Hebditch-Hunt

Deux simulations sont présentées dans la thèse: le cas A avec la longueur de diffusion l_l donnée par l'équation (RF.3.3) et le cas B avec l_l donnée par l'équation (RF.3.6), où l'effet de convection est pris en compte. Les autres paramètres numériques des cas A et B sont identiques. Les autres paramètres numériques pour les cas A et B sont identiques. Les propriétés de l'alliage, l'état initial et les conditions limites sont décrits dans la section 3.3 du mémoire. Au début de la solidification, le liquide proche de la paroi refroidie descend par convection thermogravitaire. La nucléation se déclenche sur la paroi refroidie lorsque la surfusion locale est supérieure à la surfusion de nucléation. Selon les propriétés des matériaux (voir le tableau 3.1 dans le texte principal de la thèse), les grains ont une masse volumique supérieure à celle du liquide. Donc, sous l'effet de la traînée et de la gravité, ils sont transportés par l'écoulement du fluide vers le bas, se sédimentent, et s'accumulent au fond de la cavité, formant une couche à faible ségrégation négative tandis qu'une couche liquide enrichie en Pb est située quelques millimètres au-dessus. Au cours de la solidification, ces phénomènes de ségrégation deviennent plus prononcés et on arrive au blocage des grains dans la partie basse de la cavité (Fig. RF.3.4).

En comparant les deux cas, on constate que la frontière de la couche bloquée est plus haute pour le cas A (Fig. RF.3.4(a.2) et RF.3.4(b.2)), c'est-à-dire si la convection n'est pas prise en compte lors du calcul de la longueur de diffusion. Cela signifie que la croissance des grains est plus rapide dans le cas A, comme dans le cas du grain unique étudié auparavant. À 75 s, puisque le liquide pur (extradendritique) occupe plus de volume dans le cas B que dans le cas A, l'écoulement engendré par la convection naturelle est plus intense dans le cas B. De plus, en raison de l'écoulement descendant plus intense à travers la couche bloquée, la ségrégation dans le cas B se révèle plus forte, avec une valeur maximale au fond de la cavité, alors que dans le cas A, le liquide le plus enrichi est poussé vers le haut par les grains. On note également une région de concentration minimale à l'intérieur de la couche bloquée qui se trouve près de la paroi refroidie dans le cas B, mais près de la paroi opposée dans le cas A.

Cette différence de distribution de la concentration observée entre le cas A et le cas B, qui semble mineure, se transforme lors de la solidification en cartes de ségrégation finale complètement différentes (Fig. RF.3.5). La formation des canaux est observée pour le cas B (Fig. RF.3.5(b)), comme pour les modèles de solidification colonnaire [70,91,166]. La concentration augmente en bas à droite dans le cas B, alors que dans le cas A une couche de ségrégation positive discontinue est présente en haut (Fig. RF.3.5(a)). D'autre part la différence entre la concentration maximale et minimale est significativement plus faible dans le cas A que dans le cas B.

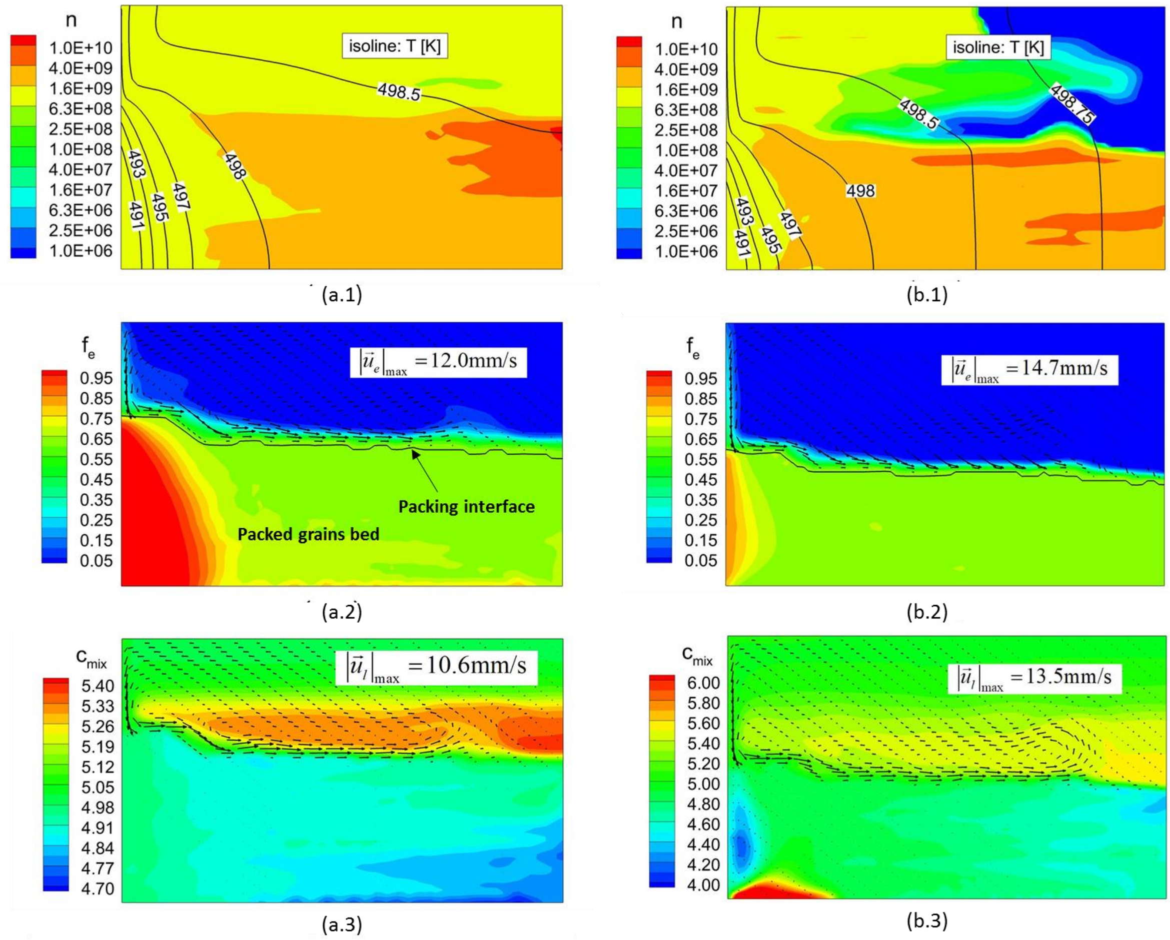

Fig. RF.3.4 État à 75 s de solidification pour les cas A (colonne de gauche) et B (colonne de droite):
(a.1 et b.1) densité numérique de grains et lignes isothermes;
(a.2 et b.2) fraction de grain f_e et vitesse des grains, au-dessous de la ligne noire les grains sont bloqués;
(a.3 et b.3) concentration du soluté dans le mélange (en $\%_{\text{pds}}$Pb) vitesse dans la phase liquide

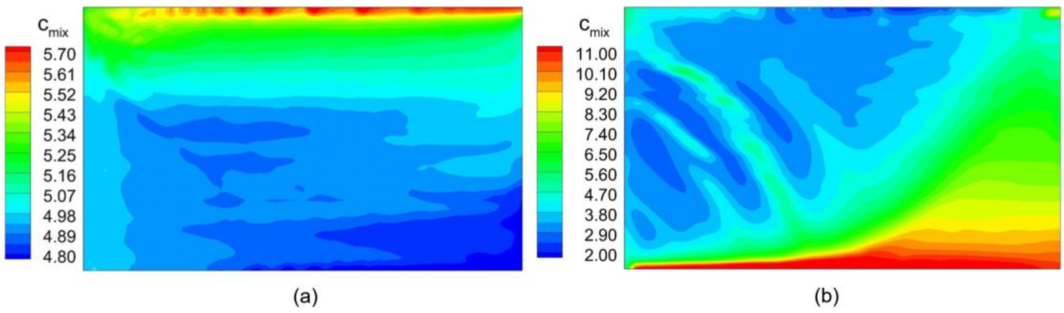

Fig. RF.3.5 Distribution finale de la concentration c_{mix}:
(a) cas A avec l_l donnée par l'équation (RF.3.3); (b) cas B avec l_l donnée par l'équation (RF.3.6)

Conclusion

Un modèle de solidification à trois phases a été modernisé et appliqué à la simulation de la solidification équiaxe du Sn-5$\%_{\text{pds}}$Pb avec le transport des grains par la convection naturelle.

Dans le modèle, l'utilisation de l'approximation de Happel pour le coefficient d'échange de quantité de mouvement entre les deux phases nous a permis de traiter l'interaction entre le liquide et les grains pour toute la gamme de fraction de grains. Un critère supplémentaire a été proposé pour le traitement du phénomène de blocage des grains, ce qui nous a permis de surmonter les difficultés liées au blocage des grains au centre de la cavité. Mais la nouveauté principale du modèle consiste à utiliser une équation pour le calcul de la longueur de diffusion, jamais utilisée auparavant dans les simulations avec des modèles à moyenne volumique. L'équation choisie combine des facteurs affectant la longueur de diffusion dans le liquide extradendritique, y compris l'écoulement autour du grain. L'effet drastique du modèle adopté est démontré par deux simulations de la solidification d'un alliage binaire Sn-5%$_{\text{pds}}$Pb dans une configuration similaire à celle de la benchmark de Hebditch et Hunt. Les résultats numériques montrent que le cas avec l'équation adoptée prédit une croissance de la couche des grains bloqués au fond de la cavité plus lente, la formation de canaux près du côté refroidissement, et une distribution finale de la ségrégation avec une couche enrichie au fond. Globalement, la distribution finale de ségrégation est similaire aux résultats obtenus avec le modèle colonnaire utilisé précédemment ainsi qu'au modèle expérimental

Chapitre 4. Modélisation du benchmark AFRODITE avec convection naturelle et brassage électromagnétique

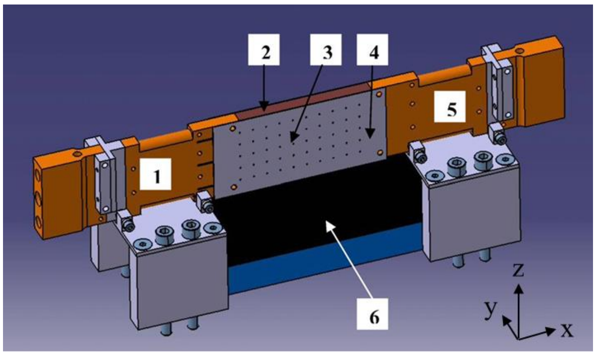

Fig. RF.4.1 Schéma du dispositif AFRODITE : 1. Échangeur de chaleur gauche, 2. Échantillon de Sn−10%$_{\text{pds}}$Pb, 3. Matrice de thermocouples, 4. Creuset en inox, 5. Échangeur de chaleur droite, 6. Moteur linéaire [87]

Le benchmark expérimental AFRODITE de solidification (Fig. RF.4.1) a été développé au laboratoire SIMAP/EPM (Grenoble, France) afin de comprendre la formation de la macroségrégation pendant la solidification et pour fournir des données quantitatives de validation des modèles numériques. La distribution de température à l'intérieur de la cavité est contrôlée par des échangeurs de chaleur en contact avec les parois latérales de la cavité. Un réseau de thermocouples sur une grande face du creuset permet de suivre l'évolution de la distribution bidimensionnelle de la température pendant la solidification. Un brasseur plan constitué de bobines électriques est placé sous la cavité pour provoquer un brassage électromagnétique (EMS) du liquide dont l'intensité et la direction peuvent être contrôlées. Récemment, Hachani et coll. [90]. ont présenté une série d'expériences avec le dispositif AFRODITE visant à étudier l'effet des différents modes d'EMS sur la solidification d'un alliage Sn−Pb. Ce travail a comparé quatre conditions de solidification : (1) convection naturelle ; (2) force électromagnétique et convection naturelle de même sens ; (3) force électromagnétique opposée à la convection naturelle ; (4) force électromagnétique alternée périodiquement. Dans le cas (3) avec la force de Lorentz opposée à l'écoulement thermogravitaire, la structure des échantillons était principalement constituée de grains équiaxes de taille légèrement inhomogène (Fig. RF.4.2). Dans cette thèse, nous avons simulé ce cas expérimental avec le modèle de solidification équiaxe décrit au chapitre 2. Des études préalables ont été nécessaires pour trois aspects du dispositif expérimental : la force électromagnétique agissant dans le liquide, le traitement de l'écoulement turbulent et la définition des conditions limites thermiques.

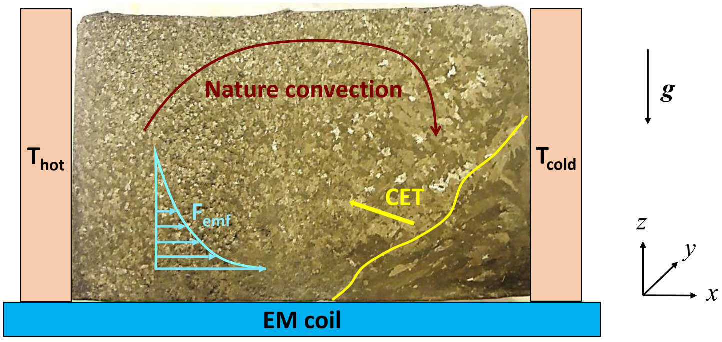

Fig.RF.4.2 Alliage Sn−10%$_{\text{pds}}$Pb solidifié dans l'expérience AFRODITE avec forces electromagnetiques opposées à la convection naturelle [90]. La force électromagnétique décroît exponentiellement vers le haut, la convection naturelle dans le liquide, initialement due à la distribution thermique, est accrue par le rejet de soluté lourd (Pb) à la solidification près de la frontière froide

Modélisation préalable de la force électromagnétique

Dans le dispositif, un ensemble de bobines plates (semblable à un moteur linéaire) a été placé sous la cavité pour créer un brassage du liquide. La solution analytique au problème électromagnétique bidimensionnel équivalent a été présentée par Wang et al. [169] et a fourni une expression de la force effective agissant le long de l'axe x avec une amplitude décroissant avec la distance à la bobine :

$$F_x = C_E \pi f \sigma k_E A_E^2 \exp\left(-2k_E z\right) \qquad \text{(RF.4.1)}$$

où C_E est un paramètre ajustable tenant compte de la taille finie de la bobine (**à déterminer**), A_E correspond à l'amplitude du potentiel vectoriel à la surface interne du fond de la cavité (**à déterminer**), $k_E = \pi/\tau$ est un nombre d'onde défini par le pas entre les pôles de la bobine τ. Wang et al. [169] ont indiqué que pour tenir compte de l'épaisseur finie de la cavité, le nombre d'onde k_E doit être remplacé par $k_E^* = \left[k_E^2 + (\pi/2a)^2\right]^{1/2}$ où a est la demi-épaisseur de la cavité. Pour le brasseur utilisé dans l'expérience, ces paramètres valent $k = 65.45$ m^{-1} et $k^* \approx 320$ m^{-1}.

En utilisant la vélocimétrie Doppler à ultrasons, Hachani et al.[90] ont mesuré la vitesse dans un alliage GaInSn à température ambiante, dans une cavité identique à celle utilisée dans l'expérience AFRODITE, soumise soumis à des forces électromagnétiques équivalentes. Les profils mesurés sur deux lignes, horizontale et verticale, de la composante de vitesse parallèle à ces lignes, ont permis dans la présente thèse de déterminer les paramètres (amplitude A_{emf} et nombre d'ondes k_{emf}) de la loi de force électromagnétique :

$$F_x = A_{emf} \exp\left(-2k_{emf} z\right) \qquad \text{(RF.4.2)}$$

Des simulations ont été effectuées pour l'alliage GaInSn dont les propriétés sont données dans le texte principal de la thèse (tableau 4.1). Le meilleur accord entre les simulations numériques et les mesures a été obtenu avec $160 \text{ N m}^{-3} < A_{emf} < 320 \text{ N m}^{-3}$ et $k_{emf} = k = 65.45$ m^{-1}. Comme la conductivité électrique, la masse volumique et la viscosité de l'alliage Ga-Sn-In étaient différentes de celles de l'alliage SnPb utilisé dans l'expérience de solidification, l'amplitude de la force a dû être recalculée [167]. Après cet réajustement, l'amplitude à prendre dans les simulations avec l'alliage Sn-Pb se trouve dans la limite: $94 \text{ N m}^{-3} < A_{emf} < 189 \text{ N m}^{-3}$.

Prise en compte les instabilités hydrodynamiques via le modèle $k_\varepsilon - \varepsilon$ réalisable

En faisant des simulations, nous avons établi que pour atteindre la convergence des équations hydrodynamiques au début de la solidification, nous avons besoin d'un modèle hydrodynamique turbulent. Cependant, l'approche théorique standard de la turbulence, basée sur la décomposition de Reynolds des équations de Navier-Stokes, implique une procédure de moyenne temporelle des équations de transport. Ainsi les équations s'appliquent aux champs moyens dans le temps (vitesse, température, concentration). D'autre part, les équations de la solidification sont obtenues avec des moyennes volumiques. L'application consécutive de ces deux procédures de moyenne − sur un volume représentatif et sur le temps − au système initial d'équations microscopiques instantanées n'est pas évidente, car les phénomènes de transport à micro-échelle ne peuvent pas être traités sans tenir compte des fluctuations rapides de la vitesse, température et concentration. Autrement dit, les deux procédures de moyenne ne pourraient en fait pas être réalisées indépendamment. D'une manière plus rigoureuse, les deux procédures pourraient être remplacées par une seule moyenne statistique d'ensemble [117, 118, 170]. Cependant, les équations finales contiendraient toujours des termes liés à des combinaisons de phénomènes à micro-échelle et de courte durée, pour lesquels des relations de fermeture seraient nécessaires [170]. La définition de ces dernières est un problème difficile dont la résolution n'était pas prévue dans le travail présent. Après avoir examiné les modèles turbulents utilisés dans la modélisation de la solidification [172-174], nous avons conclu que le modèle k_ε–ε turbulent réalisable était adapté à la simulation de la solidification de l'alliage Sn-Pb sans modification des équations de fermeture liées à la transition de phase. Pour être plus précis, cela a été possible car l'intensité de la turbulence était modérée au début du processus et diminue au cours de la solidification.

La différence entre le système d'équations à résoudre dans le cas de l'écoulement laminaire et dans le cas du modèle k_ε–ε turbulent consiste en l'utilisation de la viscosité turbulente dans les équations de quantité de mouvement, de la conductivité thermique turbulente dans l'équation de transport d'énergie et du coefficient de diffusion turbulent dans l'équation de transport de concentration. Selon ce modèle de turbulence, ces diffusivités turbulentes sont fonction de l'énergie turbulente k_ε et sa dissipation ε, deux variables calculées pour le mélange des phases avec deux équations supplémentaires. Le système d'équations pour le transport macroscopique est donné dans le texte principal de la thèse par les équations (4.11)−(4.17) avec les relations de fermeture et les paramètres fournis dans le tableau 4.3.

L'état initial, les conditions aux limites, et propriétés de l'alliage

Au cours de l'expérience, la distribution de la température avant la solidification ainsi que la vitesse de refroidissement pendant la solidification sont programmées et contrôlées via des mesures de température sur les échangeurs de chaleur. Cependant, une résistance de contact peut exister entre la paroi et le volume en solidification et dépendre de la mouillabilité des parois par la fonte, du mouvement du liquide et de la répartition de la fraction liquide dans le volume en raison du rétrécissement pendant la solidification (Fig. RF.4.3(a)) [91,166]. La différence réelle de température à travers le volume est donc plus faible que celle imposée aux échangeurs de chaleur.

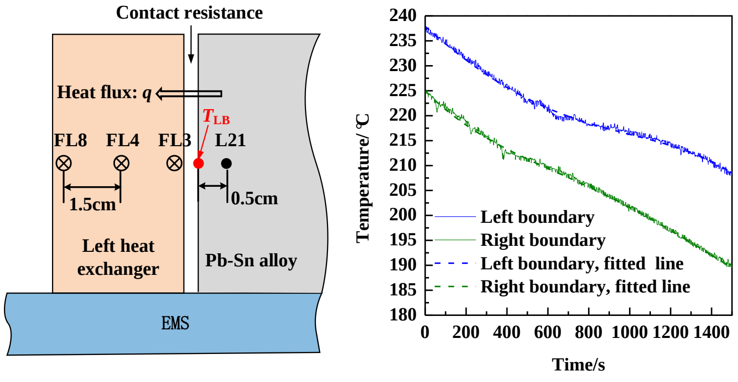

(a) (b)

Fig. RF.4.3 (a) Schéma montrant la résistance de contact entre l'échangeur de chaleur du dispositif AFRODITE et l'échantillon ; (b) Évolution de la température aux parois estimée à partir des mesures, depuis le moment initial choisi pour le calcul numérique

Interpolation polynomiale pour la paroi gauche:

$$T'_{\mathrm{LB}} = -7.051342\times10^{-12}t^4+1.066523\times10^{-8}t^3+1.0992\times10^{-5}t^2 - 0.0362674t+T_{0\mathrm{L}}\ \ \mathrm{K} \qquad \text{(RF.4.3)}$$

Interpolation polynomiale pour la paroi droite:

$$T'_{\mathrm{RB}} = 8.13619\times10^{-12}t^4 - 3.303026\times10^{-8}t^3+4.33585\times10^{-5}t^2 - 0.041834t + T_{0\mathrm{R}}\ \ \mathrm{K} \qquad \text{(RF.4.4)}$$

En outre, en transitoire la vitesse de refroidissement des frontières de l'échantillon peut s'écarter de celle programmée à cause d'un important dégagement de chaleur latente et/ou si le refroidissement liquide n'est pas suffisant (Fig. RF.4.3(b)). Pour tenir compte de tous ces effets, la température du côté intérieur des parois latérales a été préalablement recalculée à partir de la mesure de la température effectuée par les thermocouples placés sur les échangeurs de chaleur et ceux du côté frontal de la cavité. Par la suite, l'évolution de la température de la paroi gauche et droite a été approximée par les fonctions polynomiales approchées des équations RF.4.3 et RF.4.4. L'état initial des simulations est du liquide pur au repos à concentration uniforme nominale de 10%$_{\mathrm{pds}}$ de Pb, avec un gradient de température uniforme dans la cavité depuis $T_{0L} = 237.9$ K à gauche jusqu'à $T_{0R} = 225.0$ K à droite.

Les propriétés de l'alliage sont données dans le tableau 4.4 du texte principal de la thèse. Il faut noter que contrairement au cas précédent, la masse volumique des grains solides (prise en compte dans le terme de flottabilité de la phase granulaire) est inférieure à la masse volumique initiale (et de référence) de l'alliage. Par conséquent, les grains ont tendance à flotter vers le haut alors que le liquide enrichi a tendance à descendre.

Résultats des calculs

Une fois que le calcul est activé et que la convection se développe dans la cavité, il faut environ 40 secondes pour atteindre une distribution de température quasi stationnaire définie par le transfert de chaleur par convection. La majorité de la cavité est occupée par la convection forcée mais en haut dé la paroi gauche un petit vortex de convection naturelle survit. La solidification, qui se déclenche dès que la température locale devient inférieure de la température du liquidus (à ~ 240 s), est initiée en haut de la paroi la plus froide (à droite). Même si peu après la nucléation se produit sur toute la surface de cette paroi latérale, les grains équiaxes sont amenés principalement vers le coin haut par la convection engendrée par la force électromagnétique ainsi par leur propre flottation (Fig. RF.4.4a). Au cours de la solidification, puisque le rejet du Pb rend la phase liquide plus dense du côté froid, la force de flottabilité thermo-solutale devient plus importante et contrecarre l'effet de la force électromagnétique. Progressivement, le vortex de convection naturelle s'étend du coin supérieur gauche à toute la région haute de la cavité (Fig. RF.4.4b). Lorsque la valeur de la fraction volumique des grains équiaxes atteint la limite de blocage, les grains à côté de la paroi deviennent bloqués et, par conséquent, immobiles. Les autres grains sont amenés vers le haut où ils croissent.

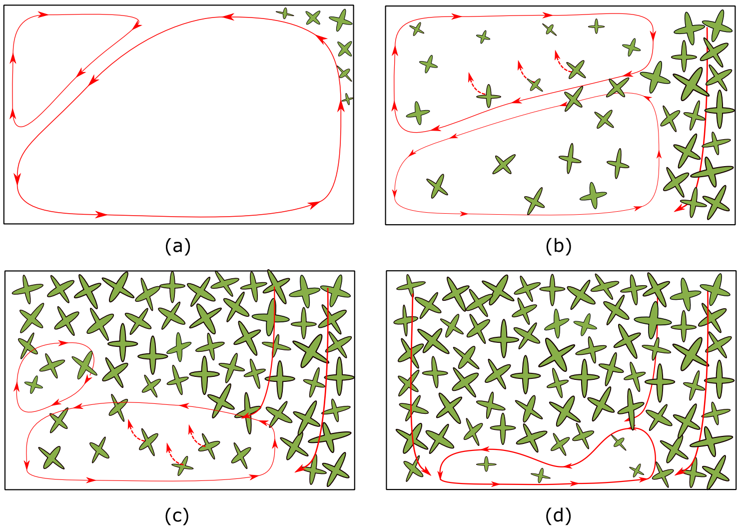

Fig. RF.4.4 Écoulement du liquide et mouvement des grains à différentes étapes de la solidification (a) ~300 s: convection forcée majoritaire, petite zone de convection naturelle thermique en haut de la paroi chaude; (b) ~540 s: Conv.forcée amortie par les grains bloqués en paroi, conv. thermo-solutale en haut, moins intense; (c) ~900 s: Grains bloqués majoritaires + descente de liquide enrichi, petits tourbillons de conv.naturelle & forcée; (d) 1440 s: très faible convection forcée, la descente du liquide résiduel continue entre les grains bloqués

Entre 540 s et 900 s de la solidification (Fig. RF.4.4b et Fig. RF.4.4c), la couche de grains bloqués s'étend des grains situent dans la partie haute de la cavité vers le bas et vers la gauche. Vers $t = 900$ s une moitié de la cavité est remplie par des grains bloqués, qui forment un "réseau rigide" (Fig. RF.4.4c). L'écoulement du liquide entre les grains bloqués est faible, mais il contribue à la macro-ségrégation finale: le liquide enrichi en Pb descend continuellement vers le bas, appauvrissant la partie haute du volume tout en enrichissant la partie en bas. Le vortex engendré par la force électromagnétique existe toujours sous la région rigide, mais il est déplacé vers la paroi latérale plus chaude et a tendance à se rétrécir vers le bas, et l'autre vortex au-dessus n'occupe qu'une petite région près de la paroi plus chaude. Vers t = 1400 s, un faible écoulement forcé existe encore prés du fond de la cavité avec une vitesse maximale de seulement 0.1 mm s^{-1} (Fig. RF.4.4d). Cette partie du liquide est très enrichie et nécessite une température plus basse pour se solidifier. Le liquide résiduel descend encore vers le fond.

Une découverte remarquable dans les simulations est que le comportement des courbes de refroidissement issues de calculs (Fig. RF.4.5) correspond aux étapes de solidification décrites ci-dessus. En particulier, les oscillations sont liées à l'amortissement instantané de la convection forcée et à l'intensification de la convection naturelle en raison de l'enrichissement en Pb rejeté dans le liquide.

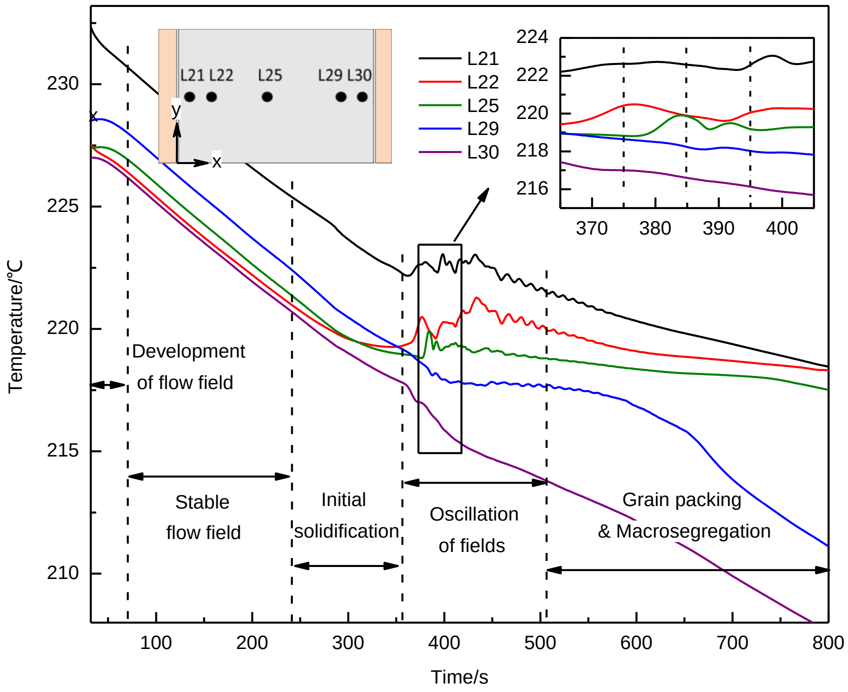

Fig. RF.4.5 Courbes de refroidissement issues de simulations à l'emplacement des thermocouples L21, L22, L25, L29 et L30 (y = 30 mm pour tous et x = 5 mm, x = 15 mm, x = 45 mm, x = 85 mm et x = 95 mm respectivement)

La distribution finale calculée de la densité numérique de grains montre une augmentation presque monotone de la paroi droite (plus froide) à la paroi gauche (plus chaude) ainsi qu'une couche en haut caractérisée par une densité numérique de grains élevée (Fig. RF.4.6(a.1)). Cela correspond au résultat expérimental avec des grains équiaxes assez fins en haut de la cavité, des grains plus gros près du côté froid et des grains plus fins près du côté chaud (Fig. RF.4.6(a.4)).

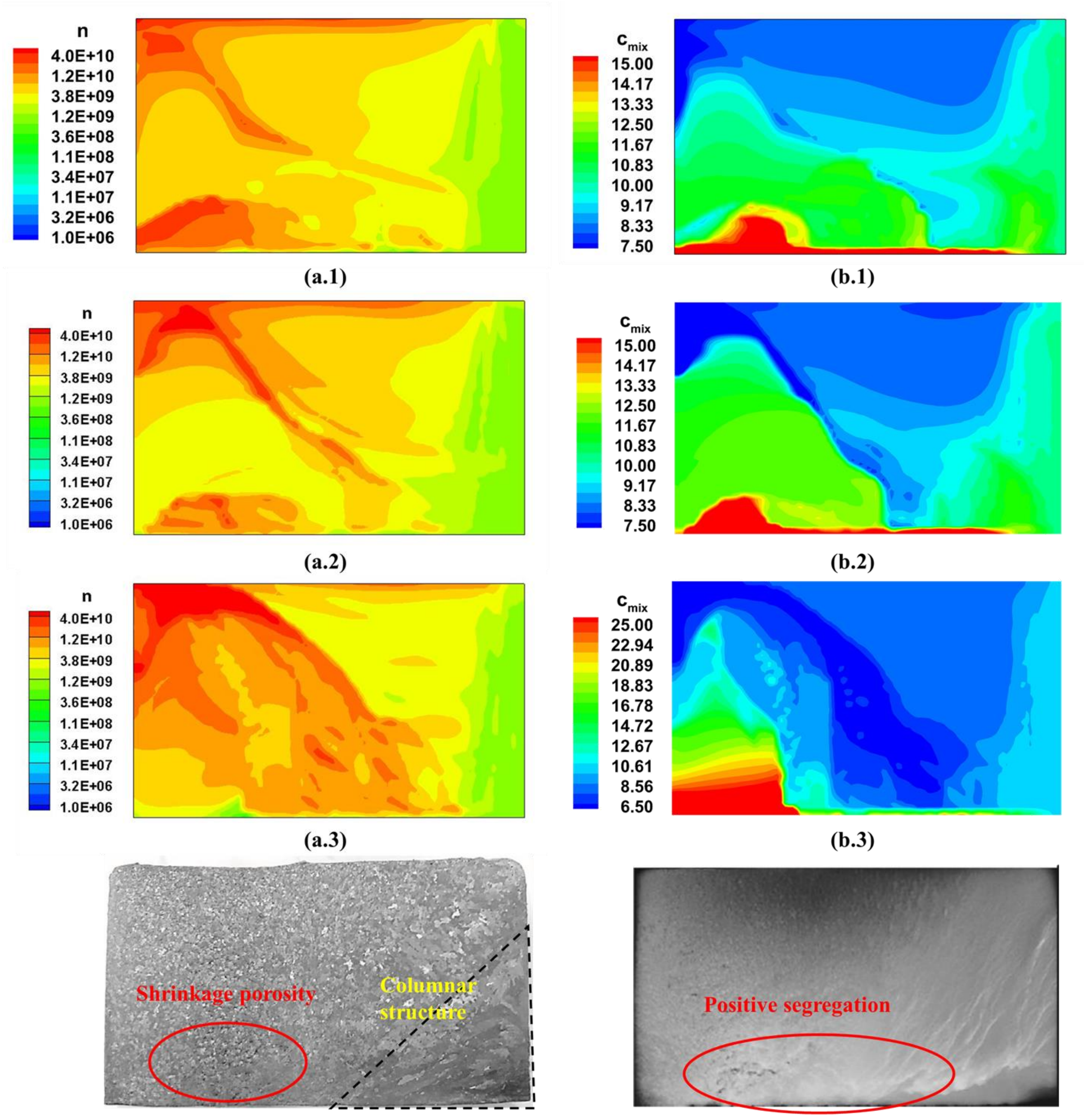

(a.1) (b.1)

(a.2) (b.2)

(a.3) (b.3)

(a.4) (b.4)

Fig. 4.6 Distribution calculée de densité numérique des grains (a.1-3) et magroségrégation calculée (b.1-3) pour trois intensités de brassage (1: A_{emf} = 180 N m^{-3}, 2: A_{emf} = 150 N m^{-3}, 3: A_{emf} = 110 N m^{-3}) comparées aux données expérimentales reproduites de la publication [30] : structure des grains (a.4) et radiographie de l'échantillon (b.4)

De plus, au fond de la cavité où se produit la dernière étape de la solidification, la simulation montre une densité numérique de grains assez importante. Dans l'expérience, cette région est occupée par des porosités à cause du rétrécissement qui indique également qu'elle a été solidifiée à la fin du processus. La distribution calculée finale de macroségrégation montre une variation de la concentration de Pb entre 7.5%$_{pds}$ à 15%$_{pds}$ avec une ségrégation positive au centre du fond de la cavité et une région de ségrégation négative située dans la partie haute

(Fig. RF.4.6(b.1)). La carte de ségrégation obtenue numériquement correspond qualitativement à la radiographie de l'échantillon solidifié (Fig. RF.4.6(b.4)). Quelques canaux de ségrégation dans le coin droit en bas ne sont pas reproduits dans les calculs, ce qui est probablement lié à la croissance des grains colonnaires, qui n'est pas prise en compte dans la simulation actuelle.

Finalement, afin de comprendre le rôle de l'EMS, nous avons effectué les calculs avec différentes intensités de la force de Lorentz. Les figures RF.4.6 (a.2, b.2, c.1 et c.2) montrent la distribution de la densité numérique des grains et la macro-ségrégation finale calculés avec les valeurs du coefficient ajustable A_{emf} = 150 N m^{-3} et A_{emf} = 110 N m^{-3}.

Conclusion

Dans ce travail un modèle de solidification équiaxe à trois phases, moyenné en volume, prenant en compte le transport des grains, est appliqué à la modélisation de l'expérience AFRODITE de solidification d'alliage Sn-10%$_{\text{pds}}$Pb avec convection forcée pilotée par une force électromagnétique. Bien que le modèle ait fourni des résultats proches de ceux de l'expérience, de nombreuses questions se posent concernant les paramètres numériques et les équations de fermeture.

L'une d'entre elles, qui concerne les paramètres liés à la croissance des grains dendritiques en cas d'écoulement turbulent, a déjà été mentionnée ci-dessus. À cette question s'ajoute le problème de traitement de la force de traînée des grains dendritiques et l'amortissement de la turbulence dans la zone pâteuse. Une autre question concerne la variation de la force électromagnétique à l'échelle macro pendant la solidification puisque la conductivité électrique du solide peut être plus élevée que celle du liquide. De plus, on suppose généralement que l'agitation électromagnétique favorise la fragmentation des dendrites et que ces fragments servent de sites de nucléation ou de grains équiaxes déjà présents. Ceci peut être introduit dans le modèle en utilisant diverses hypothèses [23,178]. Dans le présent travail, tous ces phénomènes n'ont pas été pris en compte pour diminuer le nombre de paramètres incertains, mais ils méritent tous une étude plus approfondie.

Chapitre 5 Application du modèle de solidification équiaxe pour simuler la macroségrégation d'un lingot industriel

La fabrication des lingots de grande taille est un processus fondamental dans l'industrie. La formation de macroségrégation dans le lingot est inévitable à cause de la grande durée de solidification nécessaire. Le coût extrêmement élevé du processus empêche la réalisation d'un grand nombre d'expériences, c'est pourquoi la simulation numérique est le principal outil pour révéler les mécanismes qui conduisent à l'apparition de défauts dans le but d'optimiser le processus. Le développement des modèles équiaxes présentés dans ce mémoire est principalement motivé par leur utilisation ultérieure dans la modélisation de la solidification des lingots. Ce chapitre présente la modélisation de la solidification d'un lingot de 2.45 tonnes (similaire à [40, 86, 109,179]) avec le modèle de solidification équiaxe à trois phases développé dans la thèse. Le rôle du déplacement des grains équiaxes dans la formation de la macro-ségrégation est analysé et l'effet de certains facteurs de processus est étudié.

Géométrie et conditions aux limites

On modélise la macro-ségrégation observée dans une expérience connue [93] de coulée d'un lingot d'acier de 2.45 tonnes (Fe−0.45%$_{\text{pds}}$C). Le domaine de calcul est 2D axisymétrique et réduit au lingot (Fig. RF.5.1(a)). Au début de la simulation, le métal fondu dans le moule est supposé immobile avec une température uniforme de 1769 K (1 K au-dessus de la température du liquidus). Les conditions de refroidissement sont appliquées directement à la surface du lingot et sont écrites sous forme d'échange de chaleur par convection tenant compte du transfert de chaleur à travers les différents éléments de l'installation. Comme dans la réf. [131], la température externe est fixée à 373 K et deux coefficients différents de transfert de chaleur par convection sont appliqués: $h_{sup} = 30$ W m^{-2}K^{-1}dans la zone haute et $h_{inf} = 300$ W m^{-2}K^{-1}dans la zone basse. Les propriétés de l'alliage sont indiquées dans le Tableau 5.1 du texte principal de la thèse.

Le modèle équiaxe à trois phases des Chapitres 3 et 4 est utilisé, avec une modification de l'étape de nucléation qui est rendue similaire à l'algorithme proposé dans la référence [40] :

$$N_\phi = \begin{cases} n_{max}/\mathrm{d}t & \text{si } \Delta T > \Delta T_{nucl} \text{ et } \displaystyle\int_0^t N_\phi \, \mathrm{d}t = 0 \text{ (aucune nucléation auparavant)} \\ n_{max}/\mathrm{d}t & \text{si } \Delta T > \Delta T_{nucl} \text{ et } n < 1 \text{ (n dans le liquide sous-refroidi est trop petit)} \\ 0 & \text{sinon} \end{cases} \qquad \text{(RF.5.1)}$$

Résultats de calculs

Dès que le calcul est lancé, un gradient de température positif dirigé vers l'axe du volume est établi. Puisque $h_{inf} \gg h_{sup}$, la zone la plus froide du lingot est dans le coin près du fond (Fig. RF.5.1(b)), où la nucléation commence lorsque la température locale devient inférieure à celle du liquidus. En raison de la forte vitesse de refroidissement, la température près de la surface du lingot diminue rapidement, ce qui permet aux grains nouvellement nucléés de croître rapidement. Ils sont "retenus" par la paroi (ou par les grains déjà bloqués) et deviennent inamovibles dès que leur fraction volumique arrive à la fraction limite de blocage.

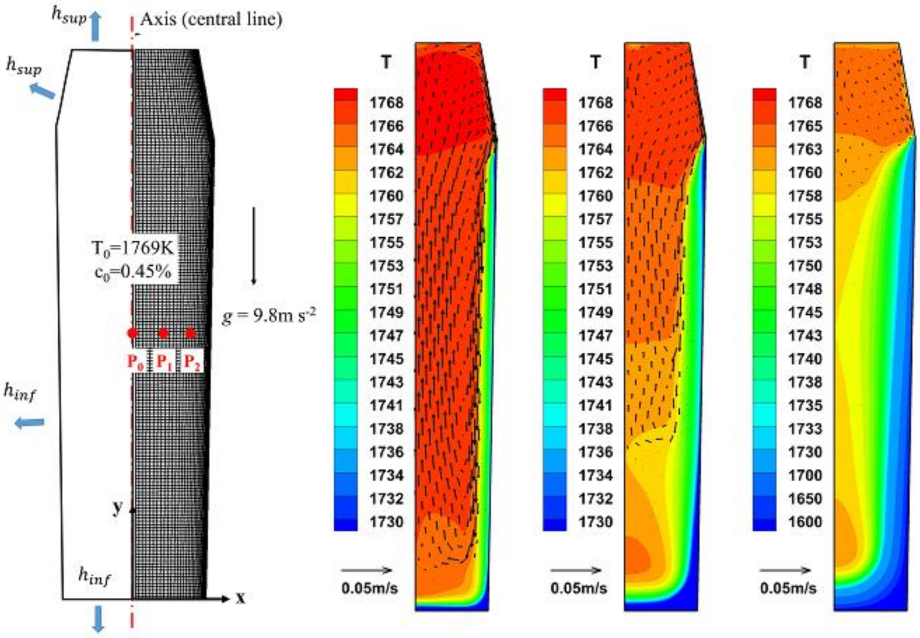

Fig. RF.5.1 Domaine de calcul, maillage et conditions de calcul du lingot de 2.45 t; distributions de température et écoulement de la phase liquide calculés à 100 s, 200 s et 400 s

À t = 20 s, une fine couche de grains bloqués est principalement située près du fond et de la paroi latérale inférieure (Fig. RF.5.2(a)). Juste en dehors de la couche bloquée, un écoulement descendant du liquide se développe sous l'action de la force de flottabilité thermique (Fig. RF.5.1(b)). Certains petits grains sont entraînés par l’écoulement descendant avant d'être bloqués et s'accumulent au fond du moule. L’écoulement du liquide change de direction près du fond du volume où il se dirige vers l’axe de symétrie, puis remonte vers la région centrale du lingot. Une grande quantité de grains, en particulier ceux de petite taille, sont entraînés par l’écoulement ascendant au centre du volume. Cependant, quelques grains plus gros redescendent de nouveau au fond et s'empilent au centre du lingot (Fig. RF.5.2(b-)c). À t = 400 s, les grains équiaxes remplissent presque entièrement le moule de fusion (Fig. RF.5.2(d)). La solidification devient ensuite assez lente, car le taux de transfert de chaleur dans la région supérieure est beaucoup plus faible. Enfin, à environ t = 1000 s, le lingot entier est entièrement rempli par des grains tassés, mais la solidification se poursuivra pendant longtemps.

La distribution finale de la ségrégation obtenue dans la simulation est qualitativement similaire aux résultats expérimentaux (Fig. RF.5.3). Des canaux ségrégés sont observés dans la simulation mais, avec un maillage plus grossier, ils étaient moins prononcés et avaient une configuration différente. La région de ségrégation positive issue du calcul diffère de la forme observée dans l'expérience, et les canaux en V près de l'axe ne sont pas reproduits. Les écarts peuvent être associés principalement à deux phénomènes non pris en compte dans le modèle: la croissance dendritique colonnaire et le retrait à la solidification. La macroségrégation prédite par notre modèle le long de l'axe a été comparée à celle d'un modèle à trois phases colonnaire-equiaxe [131] pour un lingot de même taille, et montrent une meilleure concordance du présent modèle avec les expériences.

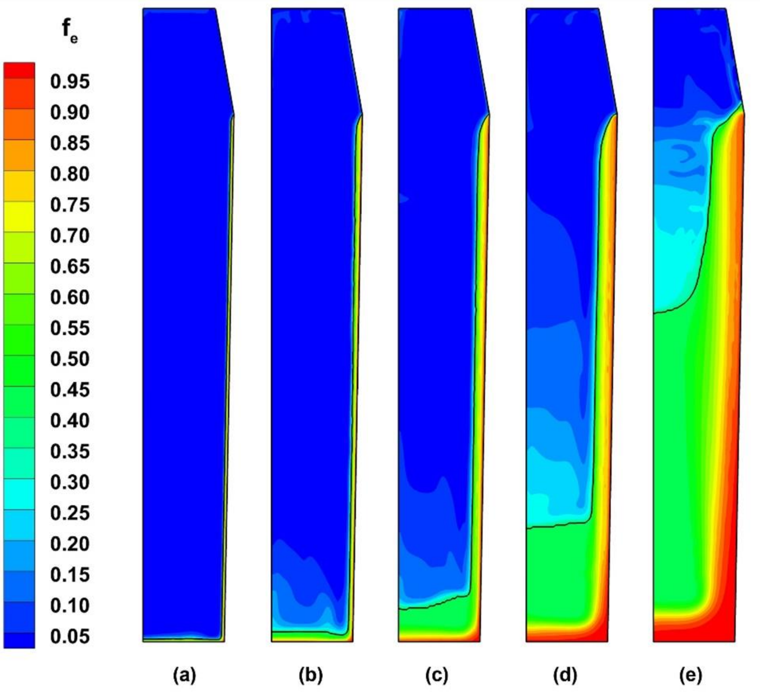

Fig. RF.5.2 Fraction de phase f_e des grains après différentes durées de solidification (a) 20 s, (b) 50 s, (c) 100 s, (d) 200 s, (e) 400 s. La ligne noire indique l'interface entre la région de grains bloqués et non-bloqués

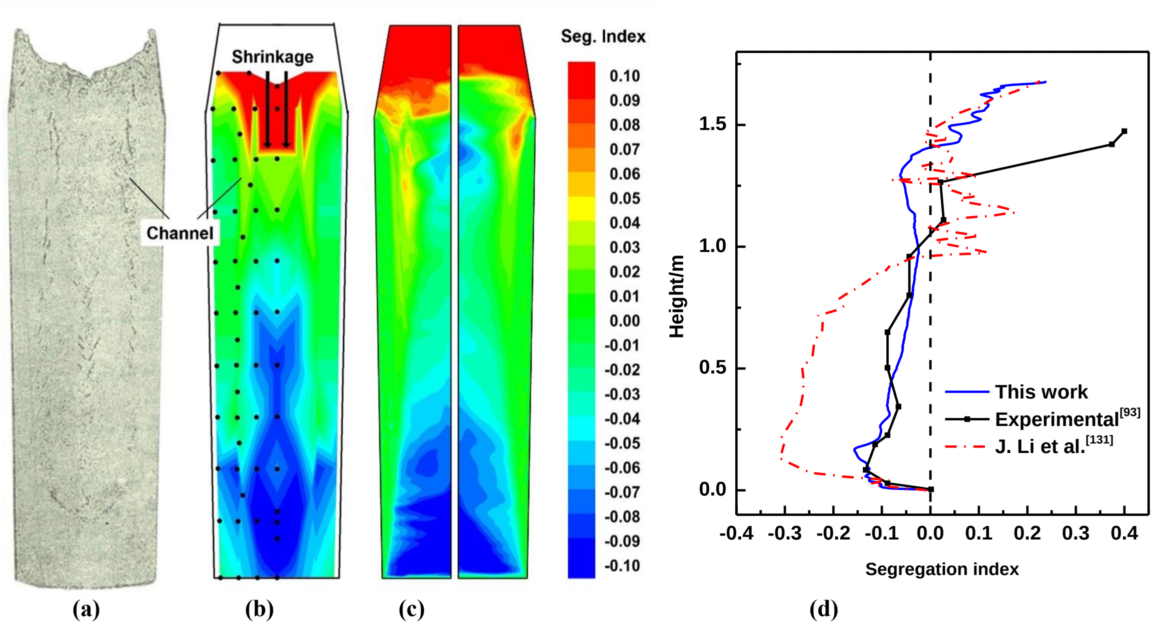

Fig. RF.5.3 Comparaison des macroségrégations expérimentales et simulées : (a) empreinte de soufre expérimentale, (b) indice de ségrégation du carbone expérimental, (c) indice de ségrégation du carbone calculé, (d) indice de segregation le long de l'axe vertical

Ensuite, dans le chapitre 5 de la thèse, l'effet de l'intensité de refroidissement du moule est examiné. Une conclusion contre-intuitive qui pourrait être tirée de ces études est qu'un refroidissement plus intense diminuerait la macroségrégation.

Enfin, l'effet du brassage électromagnétique (EMS) sur le procédé et sur la macroségrégation est étudié à l'aide d'une série de simulations. Les résultats montrent que le brassage renforce l'écoulement près de la paroi latérale, où il empêche le blocage des grains. L'EMS favorise l'accumulation des grains au fond du lingot, réduit l'échange de soluté entre les grains équiaxes et le liquide environnant, et ainsi diminue la macroségrégation dans le lingot (Fig. RF.5.4). Le brassage descendant a un effet d'homogénéisation du soluté plus visible. Quand l'intensité de l'EMS augmente, le degré de macroségrégation dans la zone centrale du lingot est réduit significativement, mais ce brassage plus intense provoque une bande à ségrégation négative dans la zone externe du lingot.

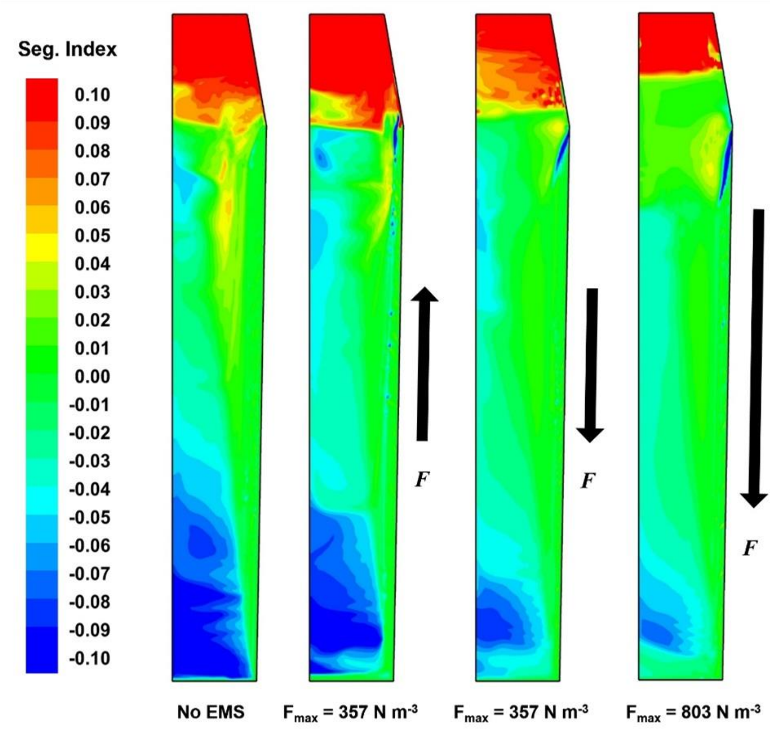

Fig. RF.5.4 Final macrosegregation maps with and without electromagnetic stirring

Conclusion

Un modèle de solidification équiaxe à trois phases a été appliqué pour étudier la formation de la macro-ségrégation dans un lingot d'acier industriel de 2.45 tonnes. Une comparaison de la macro-ségrégation calculée avec des mesures publiées [93] montre leur accord qualitatif malgré des incertitudes sur les conditions aux limites et la simplification notables des phénomènes physiques lors de leur modélisation. L'étude de l'éffet de l'intensité du refroidissement confirme qu'un refroidissement plus intense diminue la macroségrégation dans le lingot, car l'écoulement est stabilisé par le développement plus rapide de la couche bloquée. L'étude de l'effet du brassage électromagnétique montre qu'en favorisant l'accumulation des grains au fond du lingot, on réduit l'échange de soluté entre les grains équiaxes et le liquide environnant, ce qui diminue la macroségrégation du lingot.

Chapitre 6 Conclusions et recommandations

La modélisation numérique est devenue aujourd'hui un outil efficace pour révéler les phénomènes qui se produisent pendant la solidification et est potentiellement capable de prédire la macro-ségrégation dans les pièces coulées et les lingots. Le présent travail se concentre sur la modélisation numérique de la solidification en régime équiaxe avec écoulement convectif, en utilisant des moyennes volumiques pour obtenir le système d'équations à l’échelle macroscopique. La thèse présente tout d'abord une analyse bibliographique exhaustive des modèles existants, en mettant en avant plusieurs questions critiques et leur solution éventuelle. Sur la base de cette étude bibliographique, un modèle de solidification à trois phases est proposé dans lequel l'échange de quantité de mouvement entre phases et la longueur de diffusion pour le transport de soluté sont décrits avec beaucoup d'attention. Le modèle présenté est testé par des simulations de deux benchmarks avant d'être appliqué à l'étude du processus de solidification et de la formation de macroségrégations dans les lingots industriels.

Les principales conclusions tirées de l'analyse bibliographique et des nouveautés proposées dans le modèle equiaxe sont les suivantes :

(1) On constate que l'approximation de Happel pour le coefficient d'échange de quantité de mouvement entre les phases en mouvement fournit une bonne approximation à la fois pour les grains en mouvement libre et pour le régime d’un réseau dendritique immobile pour tout le spectre de la fraction de grains. En particulier, l'approximation de Happel ne conduit pas à la sédimentation (émersion) des nucléi dont la taille (fraction) est proche de zéro, présente une transition lisse vers les grains bloqués et se rapproche de la relation Carman-Kozeny traditionnellement acceptée en solidification pour une fraction volumique de grains élevée. Par conséquent, l'approximation de Happel peut être recommandée pour son utilisation dans le modèle.

(2) Le traitement du blocage des grains uniquement par une valeur critique de la fraction de grain (ou de solide) n'est pas applicable dans les procédés où le champ de température est contrôlé par la convection ou lorsque le flux convectif est intense. Dans de tels cas, la

combinaison de la distribution non-monotone de température et de l'écoulement (intense) du liquide peut conduire à une fraction élevée de grains au milieu du volume de solidification, où ils ne doivent pas être bloqués. Un critère supplémentaire de blocage est proposé, basé sur la présence d'une paroi ou de grains déjà bloqués à proximité des grains dont la fraction solide dépasse le seuil de blocage.

(3) En ce qui concerne le transport du soluté et le traitement de la longueur de diffusion dans le liquide extradendritique, il est proposé d'utiliser une équation qui combine des facteurs liés à la taille du grain et à l'écoulement convectif autour du grain.

Les principaux résultats de l'application du modèle équiaxe à la simulation de deux benchmarks et à la solidification d'un lingot industriel sont résumés ci-dessous.

(1) L'effet drastique du modèle adopté pour la longueur de diffusion dans le liquide extradendritique est démontré par la solidification d'un alliage binaire Sn-5%$_{\text{pds}}$Pb dans la configuration de l'expérience de Hebditch et Hunt. Les résultats obtenus en utilisant le modèle de la longueur de diffusion proposée dans notre travail ont été comparés aux résultats obtenus avec un modèle traditionnellement utilisé. En mettant en œuvre le nouvel modèle, on prédit une croissance plus lente de la couche des grains bloqués au fond de la cavité, la formation des canaux près du paroi refroidie, et une distribution finale de ségrégation avec une zone enrichie au fond de la cavité. Cela ressemble aux résultats expérimentaux et aux résultats de simulations avec des modèles de solidification en régime colonnaire.

(2) Pour la première fois, la modélisation de l'expérience de référence AFRODITE sur la solidification de l'alliage Sn–10pds%Pb en présence de la convection naturelle et de l'écoulement engendré par le brassage électromagnétique (EMS) a été effectué avec un modèle de solidification équiaxe. Bien que l'intensité et la distribution de la force électromagnétique dans le liquide aient été définies avec quelques incertitudes, nous pensons avoir identifié les mécanismes principaux qui définissent la ségrégation et la structure de l'échantillon dans l'expérience. Il s'avère que la convection forcée due à l'EMS domine dans le volume au début de la solidification. Avec le rejet du soluté lourd lors de la transition liquide-solide, l'écoulement forcé est amorti et la convection naturelle, bien que nettement moins intense, occupe progressivement un volume plus important dans la cavité. Les résultats de la simulation montrent que l'interaction entre l'écoulement naturel et l'écoulement due à l'EMS provoque des oscillations de la température pendant une période de la solidification. Vers la fin du procédé, lorsque les grains équiaxes sont bloqués, l'écoulement descendant de liquide fortement enrichi à travers la structure rigide entraîne une accumulation de Pb au fond de la cavité. Les résultats des calculs sont qualitativement comparables aux mesures expérimentales, y compris

l'évolution du champ de température lors du procédé, la carte finale de macroségrégation et de taille des grains. Il a été démontré que l'intensité de la force électromagnétique affecte la forme et l'emplacement de la zone de ségrégation positive.

(3) Enfin, le modèle de solidification équiaxe développé a été appliqué pour étudier la formation de la macro-ségrégation dans un lingot d'acier industriel de 2,45 tonnes. La macrostructure prédite et les résultats de la macroségrégation s'accordent qualitativement aux données expérimentales. Nous montrons que le mouvement des grains, dû à leur entraînement par le liquide puis sédimentation ultérieure par gravité, est un mécanisme responsable de la formation de la ségrégation dans ces lingots. Au départ, des grains équiaxes apparaissent et grandissent près de la paroi froide, ceux d'entre eux qui sont entraînés puis sédimentés forment un cône de ségrégation négative. Le liquide enrichi en carbone est expulsé vers la région supérieure où se produit une ségrégation positive. La circulation du liquide entre des grains bloqués est extrêmement faible et ne peut donc pas affecter la distribution de la ségrégation qui est établie bien avant la fin du processus de solidification. L'effet de l'intensité du refroidissement de surface sur la macroségrégation a été étudié à travers quatre cas de simulation avec l'utilisation de différents coefficients de transfert de chaleur de surface. Les résultats ont montré qu'un refroidissement plus intense accélère le processus de solidification, et est bénéfique pour l'homogénéité du soluté dans les lingots. Avec du brassage électromagnétique, l'accumulation des grains équiaxes en fond de lingot est favorisée, ce qui réduit l'échange entre les grains équiaxes et le liquide environnant, et donc limite la macroségrégation du lingot.

La conclusion finale est que dans cette thèse, en étudiant l'effet en régime équiaxe de quelques paramètres importants utilisés dans la plupart des modèles de solidification, nous avons pu révéler des phénomènes intéressants confirmés par l'observation expérimentale. Cependant, il faut admettre qu'il reste de nombreux problèmes de modélisation qui attendent d'être étudiés.

Introduction

Materials resistant to high temperature and corrosion or having high plasticity are necessary for construction of turbines, pressure vessel and ship plate, etc. Mixing of several metals, i.e. making of alloys, such as steel, superalloys, aluminum alloys and others, allows one to get combinations of physical properties required for particular applications. The main way of elaboration of alloys is continuous casting, which occupies 98.3% in steel making production. Other casting techniques, such as ingot casting, electroslag remelting and centrifugal casting are also used according to practical demand for products. A fundamental phenomenon during casting process is solidification, i.e. a transition of material from liquid to solid state. During solidification, segregation of the components takes place at the solid-liquid interface because crystalline cell of emerging solid material cannot accept all the atoms of the solute thus rejecting them to the liquid. It is known that local conditions affect microstructure and that microstructure defines properties of the final product. Therefore, products composed of same element components may have distinct final structures and functional performances if solidification happened with different conditions. Improper solidification condition leads to severe defects like porosity, crack and strong segregation.

Emerging solid phase can have a preferred growth direction and remain attached to the walls, forming so-called columnar phase. Otherwise, growing solid grains can be in motion inside the bulk liquid and have a more symmetrical shape, they are then called “equiaxed grains”. In industrial casting production, a large equiaxed grain region is often expected because it is supposed to provide better homogeneity than the structure consisting of columnar grains. Multiple experiments in industrial casting have indicated that movement of equiaxed grains could be an important formation mechanism of macrosegregation in the final product. Furthermore, it has been continuously supposed that electromagnetic stirring could help to avoid or at least strongly diminish the segregation. However, the macrosegregation development remains largely misunderstood when both liquid and solid phases can be in motion, because of complex interplay of multiple phenomena. Electromagnetic stirring makes this interaction even more complex.

It could be expected that better understanding of complex overlapping phenomena that occur during solidification can help to improve cast quality. Yet, post-mortem analysis of samples from casts provides information only about the final state of solidification and can be rather puzzling since evolution of various processes in time remains unclear. As for in-situ experiments, they often deal with rather weak convective flow and small sizes of samples. Therefore, results from in-situ observation could not be easily transposed to large-scale solidification processes. Consequently, numerical modeling is needed to understand how emerging of columnar or equiaxed solidification structure affects convection and solute transport during solidification process. Properly modeling alloy solidification involves multiple physical fields and multi-scale phenomena. Early theoretical descriptions of solidification process were mainly based on only one or limited number of such aspects as thermal analysis, flow analysis, nucleation theory and solidification morphology. Later, through combination and verification of theoretical description and production practice, qualitative prediction and control of typical structures and defects of castings have been achieved. However, there is a lack of global quantitative grasp of such process and controlling of complex solidification system is still not achieved. It is believed that volume average model proposed some time ago could be possible solution to realize multifield/multiscale description and prediction for the solidification process of multi-component alloys, even for complex temperature and flow fields. With advances during past decades, the volume average model can be applied nowadays to predict and optimize industrial casting process.

Numerical simulation of solidification with equiaxed grains is more challenging than with columnar ones because phenomena, such as nucleation, grains' drag by liquid phase, and their packing due to interaction with walls and other grains, have to be considered. Currently, volume average method makes simulation of equiaxed solidification under forced convection at macroscale possible. However, despite the variety of existing equiaxed solidification models, reliability of results obtained with their use remains uncertain mainly because of three reasons. First, these models rely on various physical assumptions used to close the system of equations and contain lots of empirical parameters to which numerical results are quite sensitive. Second, although serious experimental and theoretical efforts were made in order to understand effect of convection on solidification phenomena, this was not really extended for turbulent flows. Third, there is a lack of experimental data which could help to validate model of solidification in a purely equiaxed regime in presence of convection. Therefore, it is necessary to establish a more accurate mathematical model for equiaxed solidification and adapt it to multiphase flow, based on which, influence of each model parameter on calculation results has to be clarified. Besides, proper experimental data is highly needed to evaluate accuracy of equiaxed solidification model.

Benchmark solidification experiment is greatly needed because it provides useful data for validation of solidification models. The most influential benchmark experiment was performed by Hebditch and Hunt several decades ago. In that work, concentration distributions at different stages of solidification are analyzed along with presentation of solidified macrostructure. This experiment has been modeled repeatedly and nowadays its configuration along with specified boundary conditions serves as a reference for some numerical studies. After that, various benchmark installations have been developed in similar way. However, most of these experiments produce mainly columnar structure and thus are not suitable to validate equiaxed solidification model. Another benchmark solidification experimental set-up is made in SIMAP/EPM laboratory in France and is referred hereafter as AFRODITE. In addition to characteristic similar to other benchmark set-ups, in AFRODITE a linear electromagnetic motor is placed at bottom of cavity, which makes it possible to stir the alloy during solidification. In particular, it was found that for the case with the Lorentz force acting in a direction opposite to the flow caused by the gravity, the structure of the samples consisted mainly of the equiaxed grains. Also, AFRODITE can control cooling rate at lateral walls of cavity and record data of real-time temperature distribution. These features make AFRODITE a good reference for testing performance of macroscopic equiaxed solidification model under convective flow.

The objective of this thesis is to develop a three-phase equiaxed solidification model that accounts for the growth of equiaxed grains, their motion and the formation of macrosegregation. Developed numerical model is used to simulate the AFRODITE solidification experiment to test the performance of model and to study the effect of electromagnetic stirring. Finally, numerical simulations are applied to predict the macrosegregation in industrial ingot with particular emphasis on the effect of surface cooling intensity and electromagnetic stirring.

The thesis consists of six chapters.

Chapter 1 presents notions from theory of solidification to formation mechanisms of macrosegregation that are necessary for the presentation of the subject. Also, state of art of numerical simulation of solidification and macrosegregation is presented.

Chapter 2 provides a literature review for volume average models currently used for solidification simulations. Several key issues in modeling for solidification are reviewed including nucleation, grain growth, solute transfer, and momentum exchange.

Chapter 3 presents a three-phase multiscale equiaxed solidification model in which some approximations regarding solute transport at microscopic scale are put together in a new way and incorporated into macroscopic transport equations. Through simulation for solidification case of Sn-5wt% Pb alloy in a parallelepiped cavity that mimics the Hebditch–Hunt experiment, the role of diffusion length in the model on the calculation results is investigated.

In chapter 4, the proposed solidification model is validated through simulation for the

AFRODITE benchmark experiment with presence of both natural convection and electromagnetic stirring. The influence of stirring intensity on distribution of grain number density and macrosegregation is investigated.

In chapter 5, the three-phase equiaxed solidification model is applied to study the formation of macrosegregation of a 2.45 ton industrial steel ingot. The simulation indicates the crucial role of equiaxed grain movement in formation of global segregation in ingot. The effects of surface cooling intensity and electromagnetic stirring on ingot solidification are investigated. These results provide basis for improving casting craft and mold design.

Finally, in chapter 6, conclusions and recommendations for future research are made.

Chapter 1 Solidification and segregation

Despite the great progress in metallurgical technology, the lack of understanding of solidification process is still impeding the enhancement of casting technology. Solidification is a complex phenomenon which combines phase transition, multiphase flow and heat/mass transfer. During alloy solidification, macrosegregation usually appears and it is detrimental for the quality of final product and cannot be removed by subsequent treatment as the solute diffusion rate is very low in practice. Analytical prediction for solidification and macrosegregation in ingot of practical sizes is hardly possible due the complex and coupled transport phenomena. Therefore, numerical modeling is needed for prediction of macrosegregation and understanding its formation mechanism. In section 1.1, a concise introduction to solidification process and the origin of segregation is given. In section 1.2, the formation mechanism of macrosegregation during solidification are summarized. Numerical methods for prediction of solidification and macrosegregation are presented in section 1.3, where models' applications on benchmark and ingot solidification are reviewed.

1.1 Solidification phenomenon

It is convenient to consider solidification process composed of nucleation stage and grain growth stage. Nucleation provides initial solid-liquid interface for further grain growth that is accompanied with segregation. Grains will evolve to different morphologies, e.g. dendritic or non-dendritic ones, under different cooling rates, temperature gradients or solute distributions. In most solidification cases, columnar and equiaxed grain structures co-exist. The columnar-equiaxed transition (CET) phenomenon happens when equiaxed grain growth rate prevails columnar one in front of columnar dendrite tip.

1.1.1 Nucleation

From the perspective of thermodynamics, event of nucleation needs a certain degree of undercooling to ensure that the free energy of the solid phase is less than the one of the liquid phase. With this condition fulfilled, due to the random fluctuation and collision of metal atoms, some transient phase regions (embryos or clusters) will form in the melt. Among the embryos, the ones with size larger than the critical nucleation radius can exist stably as nuclei or further grow as grains. Such process is the so-called spontaneous nucleation [1]. Taking pure metal melt as an example, the critical nucleation radius R_c can be found from the variation of system free energy during nucleation process:

$$\begin{cases}\Delta G=-\frac{4}{3}\pi R^3\rho L_f\frac{\Delta T}{T_f}+4\pi R^2\gamma_{sl}\\ \frac{\mathrm{d}(\Delta G)}{\mathrm{d}R}=0\end{cases}\Rightarrow R_c=\frac{2\gamma_{sl}T_f}{\rho L_f\Delta T},\ \mathrm{n_c}=\frac{4\pi R_c^3}{3v'} \tag{1.1}$$

where γ_{sl} is surface energy; $\Delta T=T_f-T$ is the value of undercooling; T_f is melting temperature; L_f is latent heat; R is radius of embryos. Each atom occupies a volume of v', n_c is the number of atoms contained in an embryo of radius of R_c.

Spontaneous nucleation demands quite high undercooling to produce considerable amount of nuclei, which is contrary to common observations in solidification experiments. Taking example of pure Al, it is estimated that the survival of a cluster containing 1000 atoms demands an undercooling of about 100 K [2], which can hardly be achieved in practice. Indeed, solidification relies more on heterogeneous nucleation, which means that nuclei appear on existed interfaces, such as outer surface of inclusions or dendritic solid fragments, or inner surface of mold, etc. These interfaces between solid and liquid make the nucleation process easier because requirement for atoms number and activation energy is reduced. In a complete wetting case, i.e., the wetting angle is zero, nucleation can occur immediately providing that the curvature of supporting interface reaches the critical nucleation radius. In contrast, if wetting angle is as large as π, the nucleation cannot be initiated by the interface.

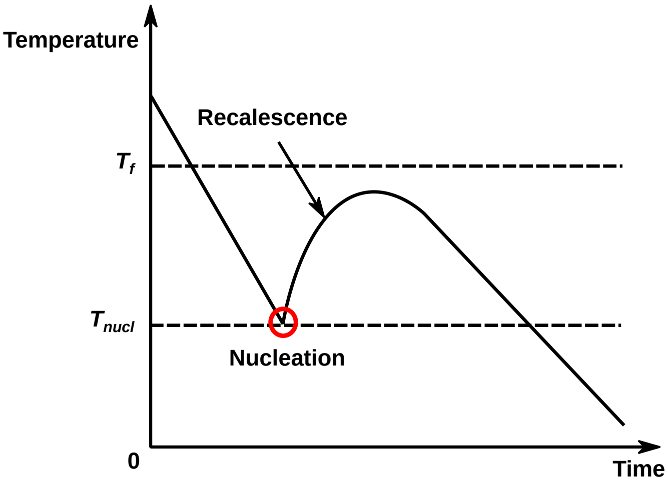

Fig. 1.1 Schematic figure of the nucleation occurrence at a certain undercooling

Considering a solidification process with cooling of melt, nucleation and solidification begin when local temperature drops below melting temperature to the required value of undercooling over one of the nucleation centers in suspension. Then local temperature rises up due to the release of latent heat, which is called recoalescence (Fig. 1.1). Once temperature begins to increase, particles nucleation over which demanding higher undercooling will never be activated.

1.1.2 Phase diagram and constitutional undercooling

After nucleation, the newly generated equiaxed grains grow up with more atoms attached to the surface of solid. Alloys' solidification or remelting happens in a range of temperature, namely, between liquidus T_l and solidus T_s, both of which depend on concentration of alloy (Fig. 1.2 (a)). Because of the difference of chemical potential between solid and liquid phases at the interface, the solute element tends to move from one phase to the other phase, which is the origin of solute segregation. If liquidus and solidus lines are assumed to be straight (linearization of the phase diagram), then liquidus temperature can be expressed as:

$$T_l\left(c_l\right)=T_l\left(c_0\right)+m\left(c_l-c_0\right) \tag{1.2}$$

where $m < 0$ is the slope of liquidus line in phase diagram (Fig. 1.2), c_0 is initial solute concentration and c_l is local solute concentration in liquid. Further, the relationship between the solid and liquid compositions at the interface in equilibrium may be described by a partition coefficient $k=c_s/c_l$.

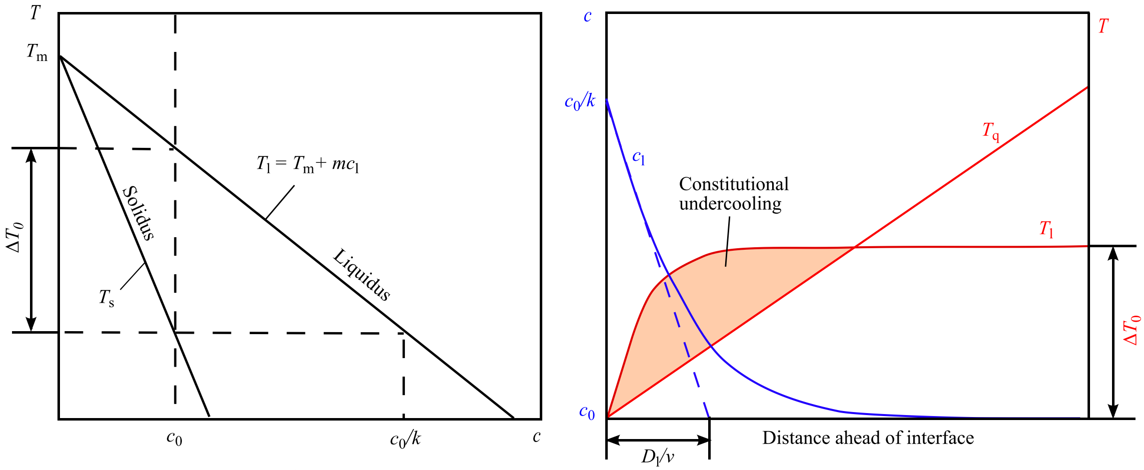

(a) (b)

Fig. 1.2 Linearized phase diagram for a binary alloy (a) and schematic of constitutional undercooling (b)

Let us consider the case of rejection of solute by the solid phase during solidification, i.e. $k<1$. Rejected solute is accumulated near the interface between solid and liquid phases. If interface movement velocity is high, the solute concentration boundary layer will be small, thus the solute concentration in liquid will decrease sharply in the direction away from interface. As seen in Fig. 1.2 (b), the local temperature T_q should be equal to $T_l(c_0/k)$ at the solid-liquid interface. Although the temperature grows towards melt, there exists a region where the liquidus temperature is larger than local temperature indicating an undercooling state, i.e. constitutional undercooling. The condition for the formation of constitutional undercooling is $G_T < mG_c$, i.e., the gradient of temperature is smaller than that of local liquidus temperature.

1.1.3 Evolution of solid-liquid interface

Experimental research found that the solid-liquid interface tends to transit from planar shape to a non-planar shape, which is referred as interface instability phenomenon. Constitutional undercooling is generally believed to be the origin of interface instability. According to Rutter and Chalmers [3] and Tiller et al. [4], at a perturbed planar interface, the solute rejected by “hills” (convex regions) is pushed to “valleys” (concave regions) and inhibited the phase transition there, because of which a small perturbation at the solid-liquid interface developed to cellular or dendritic growth. Losert et al. [5] confirmed the constitutional undercooling theory through succinonitrile alloy solidification experiment. It was found that with increase of growth speed, solid-liquid interface showed different shapes, i.e., planar, shallow cells, deep cells, or dendrites with side branches, as seen in Fig. 1.3. Mullins and Sekerka [6] pointed out that the instability occured if any Fourier component of an arbitrary perturbation grows. In other words, the planar interface would generally become unstable before the steady-state concentration profile had been established.

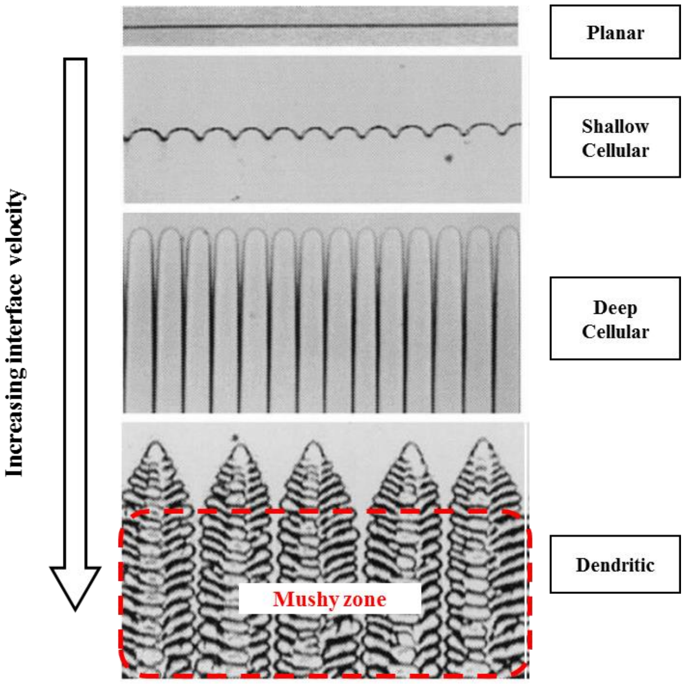

Fig. 1.3 Transition of planar solid-liquid interface into cellular and dendritic microstructure during directional solidification of a binary alloy with increasing growth speed from top to bottom [5]

1.1.4 Columnar-equiaxed transition

It is well known that there are three distinct types of solidification structure in a typical cast. Near the surface of cast, there is a region with fine equiaxed grains because large amount of grains nucleate on not ideally smooth surface and quickly grow up under strong cooling condition. With extension of solidification frontier inward the melt, the solid shell gets thicker and cooling rate decreases. Dendrites whose trunk orientation is parallel to the direction of heat flow have preference to grow [7]. In that way columnar grain structure evolves and rejected solute is accumulated ahead of the solidification front and between grains, because of which dendrite tip growth rate slows down. Zones of undercooled melt may appear in the bulk where new solid grains may nucleate and the generated grains in the undercooled melt prefer to grow radially instead of along a single direction. The growing suspended grains gradually block the tips of columnar grains, thus forming equiaxed zone [8] and the above process is the so-called columnar-equiaxed transition (CET) phenomenon.

It was found in experiment [9,10] that intensification of melt flow, e.g., electromagnetic stirring (EMS), promotes occurrence of CET. Li et al. [11] investigated the effect of stirring intensity on grain structure of silicon steel continuous casting slab. Results showed that larger current in EMS induced larger equiaxed zone (EZ) and finer grain size, as seen in Fig. 1.4, where the macrostructure figures demonstrate clearly columnar and equiaxed zones.

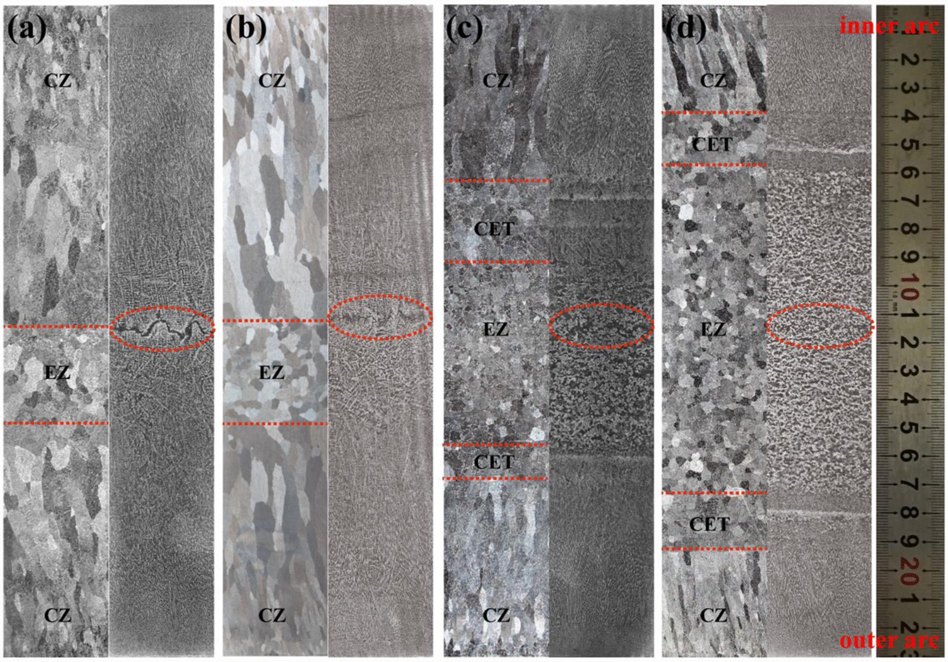

Fig. 1.4 Solidification structures of silicon steel continuous casting slabs under electromagnetic stirring with different current intensities: (a) 0 A, (b) 120 A, (c) 200 A, (d) 350 A [11]

Such effect can be explained from two aspects: (1) stirring induced forced flow "produces" dendritic fragments, which serve as nuclei of equiaxed grains. It was found that the number of dendrite fragments was proportional to the stirring intensity [12], yet, the formation mechanisms of dendrite fragments in the presence of stirring remains controversial [13–17]. (2) EMS accelerates the melt flow and heat dissipation; lower superheat and smaller temperature gradient are beneficial to the growth of equiaxed grains [18].

To predict the occurrence of CET, various mechanisms have been put up with and corresponding criteria were proposed. Hunt [7] considered that the equiaxed grains nucleate in a limited region near solidification frontier where local undercooling was larger than nucleation undercooling, thus he gave criteria for prediction of CET: (1) if the equiaxed grain volume fraction is less than $\phi_2 = 0.0049$, pure columnar grain structure appears; (2) if the fraction is larger than $\phi_2 = 0.49$, only equiaxed grains present; (3) if the fraction is located between ϕ_1 and ϕ_2, the columnar and equiaxed grains grow together as a mixture. Gäumann et al. [19,20] recommended the value $\phi_2 = 0.5$ as critical equiaxed grain fraction for CET. The improved criterion was more adaptable for a non-equilibrium state case such as rapid solidification process. Martorano et al. [8] proposed a solute interaction mechanism for CET. Gandin and Rappaz [21] proposed to use cellular-automaton technique to predict CET.

However, above methods neglected the treatment of the floating or settling of equiaxed grains as well as other phenomena that change distribution of equiaxed grains. In order to predict CET more precisely, it is indispensable to take into account the movement of equiaxed phase in a solidification model [22]. Besides, the dendrite fragments should be considered in prediction of CET. In modeling of solidification of a test casting case of Pb-Sn alloy, Zheng et al. [23] assumed the dendrite fragments as unique source of equiaxed nuclei and obtained similar CET shape as experimental observation. Yet, results could not be verified since it is not known if any fragmentation of dendrite really occurs in the experiment. Leriche et al. [24] numerically investigated the effect of number density of fragments on CET of large ingot [25].

1.2 Macrosegregation formation

It is customary to distinguish microsegregation and macrosegregation. Microsegregation refers to chemical composition inhomogeneity at small scale (μm) within dendrites, whose origin was briefly explained in section 1.1.2. Macrosegregation is the composition inhomogeneity at a scale much larger than the microstructure. It is supposed to be more detrimental than microsegregation, because it cannot be removed in subsequent heat treatment or rolling process. Macrosegregation usually decreases the hardness, plasticity and fatigue resistance. Severe macrosegregation causes defects like spots, inclusions and porosities. Below three basic mechanisms for the occurrence of macrosegregation are introduced.

1.2.1 Effect of forced convective flow

Convective flow is an important agent of macrosegregation because liquid flow moves atoms more efficiently comparing to solute diffusion [26,27]. Convective flow originated by gravity, so-called natural convection, exists almost in every solidification process on ground due to inhomogeneity of temperature and concentration in bulk liquid. Solidification promotes such inhomogeneity because of rejection of solute at the solid-liquid interface and accumulation of the latter in liquid and also because of latent heat release. Macrosegregation formation is also associated with dynamic flow through mushy zone, i.e., the partially solidified region of a casting [28]. In most cases, inflow of fresh/less segregated melt replaces enriched melt in mushy zone, leading to a decrease of solute concentration in the mush and the outflow will enrich the bulk liquid, conversely, inflow of enriched melt replacing depleted melts leads to an increase of solute concentration therein.

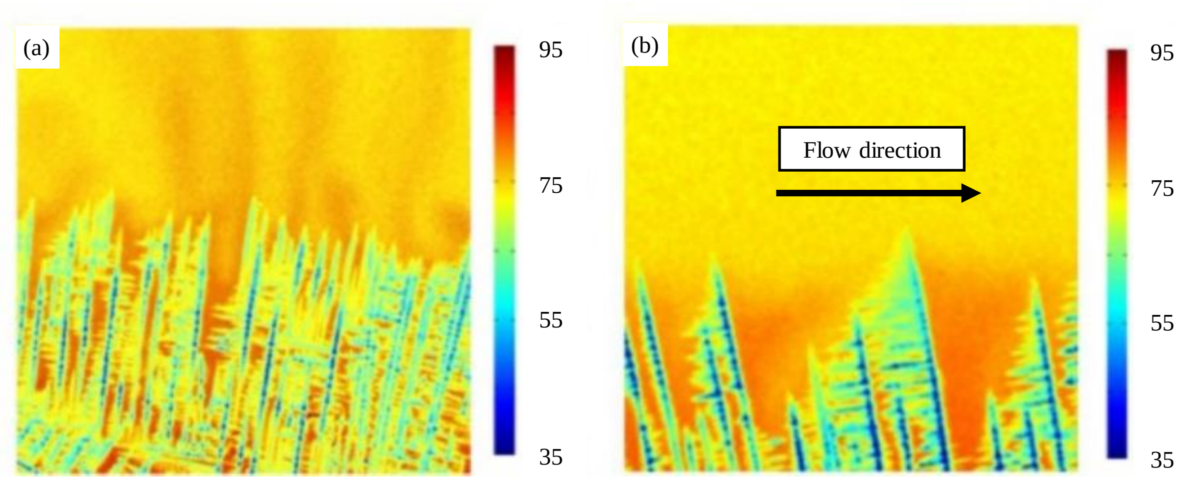

Fig. 1.5 Snapshots of dendritic structure and composition fields obtained from in-situ X-ray radiography of solidifing In-Ga alloy. Left: Natural convection. Right: Forced convection (flow is from left to right) [29]

Formation of macrosegregation defects should be avoided during solidification process and it is believed that this can be realized via the control of liquid phase motion. For example, consider In-Ga alloy solidification within a Hele-Shaw cell with natural or forced convection [29] observed with X-ray (Fig. 1.5). It was found that the development of the "chimneys" and the probability of their surviving depended sensitively on the flow field. As shown in the left figure, the flow was weak under natural convection and obvious "chimneys" developed because enriched liquid was relatively lighter and tended to move upwards. While a forced flow was generated, the dendrite arm spacing (primary and secondary) increased and the symmetry of dendrites lost. In addition, the “chimneys” disappeared because strong convection made the solute distribute more uniform ahead of dendrites.

Rather often, electromagnetic fields were used with an idea to implement such control and to affect solute distribution. For example, Wang et al. [30,31] found that the application of EMS reduced both micro- and macrosegregation of nickel-based superalloy casting. Through investigation on the effect of EMS on solidification of Pb-Sn alloy, Eckert et al. [32] concluded that periodical stirring and linear EMS inhibited the formation of channel segregation. The reason why EMS improves segregation has not been completely understood, however, two explanations may be referred: (a) EMS accelerates heat dissipation and solidification, limiting the time for segregation evolution [33]; (b) EMS increases equiaxed grain region and avoids dendritic bridging phenomenon at the end of solidification process [34]. Yet, it was also found that strengthened convective flow being structured provoked even heavier macrosegregation. In laboratory-scale experiments a so-called “fishbone” segregation pattern was observed in solidification under rotating magnetic field [35]. In industrial continuous casting, for instance, a so-called “white band” with negative segregation (Fig. 1.6) [9] usually appears due to sudden and intense liquid flow at solidification front driven by EMS. This undesired effect may be diminished by reducing velocity gradient near solidification front via two-frequency EMS [36].

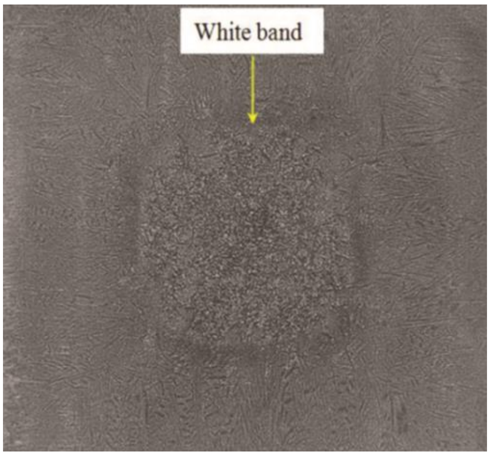

Fig. 1.6 Etched print of cross section of continuous casting billet [9]

1.2.2 Effect of equiaxed grain movement

Even in stationary liquid, equiaxed grains may float up or settle down if their density is different from that of surrounding liquid. The movement of grains becomes more complex with convection in the liquid and can be more puzzling under forced convection. For alloy with partition coefficient $k < 1$, enriched liquid will be taken away by surrounding flow while grains will be depleted of solute. Once equiaxed grains get closer to each other, negative segregated region forms. Such mechanism was used to explain the negative segregation appearing at the bottom of large ingot [12]. Fig. 1.7 presents macrostructure and macrosegregation of a 65 ton steel ingot. It is shown that equiaxed grains occupy the center of ingot and in this region a negative segregation cone is located at the bottom while an intense positive segregation appears at the top. In contrast, the columnar zone near the surface of ingot has a homogenous solute distribution.

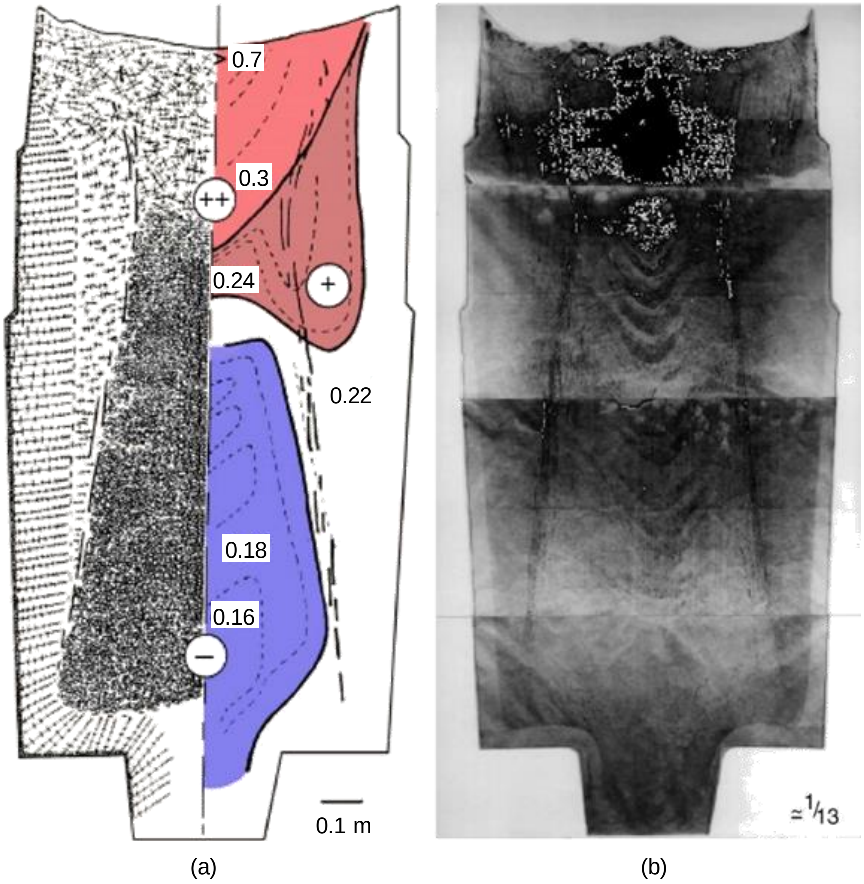

Fig. 1.7 Longitudinal section of a 65t steel ingot: (a) macrostructure and carbon macrosegregation and (b) sulphur print [12]

Among various hypotheses [26,37–40] for the formation of negative segregation cone in ingot, the settling of equiaxed grains is widely believed to be the most crucial reason. The importance of consideration of equiaxed grain movement in modeling ingot solidification will be discussed in section 1.4. In other industrial cases, such as large vertical continuous casting of steel [41] and directional continuous casting of aluminum based alloy [42], the important roles of movement of equiaxed grain in solute distribution evolution were also revealed through both experimental and numerical methods.

1.2.3 Effect of shrinkage and deformation

According to Flemings et al. [38], the movement of segregated residual liquid respect to the solid framework of the mushy zone is an important cause of macrosegregation. Without loss of generality, it is assumed that solid phase density is larger than liquid one ($\rho_s > \rho_l$) and partition coefficient k_p is smaller than 1. Below the effect of shrinkage and deformation is introduced accompanied with corresponding segregation pattern.

(1) Solidification shrinkage

Shrinkage forms during solidification because of the transition from liquid to solid states and the variation of densities between phases. Inflow of enriched melt compensating solidification shrinkage leads to an increase of solute concentration, which gives rise to a so-called "inverse surface segregation" and the negative segregation at the core of casting. This phenomenon is proved to be important for the prediction of macrosegregation in directional continuous casting of copper [43] and aluminum-based alloys [42,44].

(2) Deformation of compact mush

The compact mush represents a rigid solid skeleton of columnar dendrites or packed zone of equiaxed grains. The compression or widening of compact mush leads to outward or inward liquid flow thus causes segregation. This mechanism was used to explain the segregated peak at the centerline and the negative segregation zone aside it in continuous casting steel slab [45]. With the movement of supporting rollers, the suction and squeeze behaviors of compact mush promote macrosegregation [46]. It is suggested that macrosegregation could be reduced preferably by solid shell deformation with mechanical reduction technique. The mechanical reduction is applied near the end of casting process to reverse the liquid flow and relieve the macrosegregation [47], as illustrated in Fig. 1.8.

It should be noticed that the above mechanisms do not always be reflected in real casting results. For instance, the negative surface segregation can be expalined by volume changes during solidification, yet, another possible reason could be the melt flow through initial solidification shell, which replaces segregated melt by less segregated one. For central segregation, it is estimated that the solidification shrinkage reduces the degree of positive centerline segregation caused by bulging by about 50 percent [48]. Considering the uncertainties of above factors, the roles of solidification shrinkage and solid deformation are not considered in present thesis.

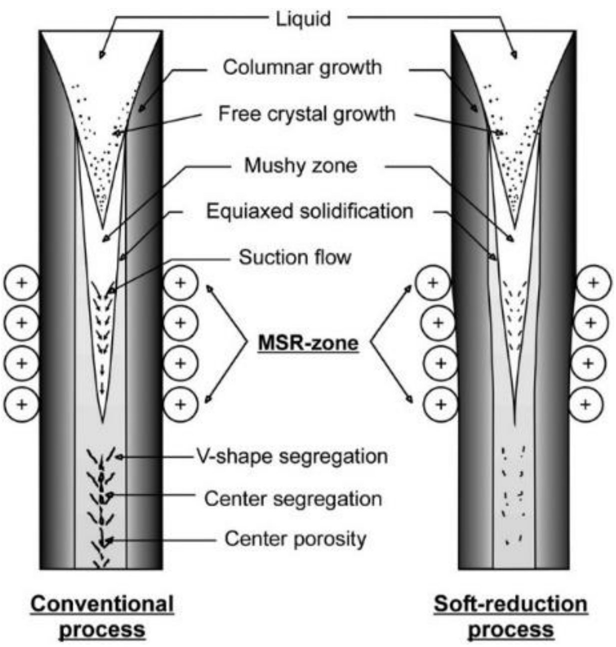

Fig. 1.8 Influence of the soft-reduction on the continuous casting process [47]

1.3 Numerical simulation of solidification: state of art

1.3.1 Review of numerical models

Solidification combines trans-scale phenomena: atom-scale nucleation (Å) [49], microscale (μm) dendrite growth and solute transport, and macroscale (m) heat conduction and multiphase flow (Fig. 1.9). It is still inconceivable to account for these scales in a unique modeling procedure, thus, the difficulty is related to the selection of processes that represent major characteristics of solidified sample, including solute concentration map, grain size, primary and secondary dendrite arm spacing, and solidification structure.

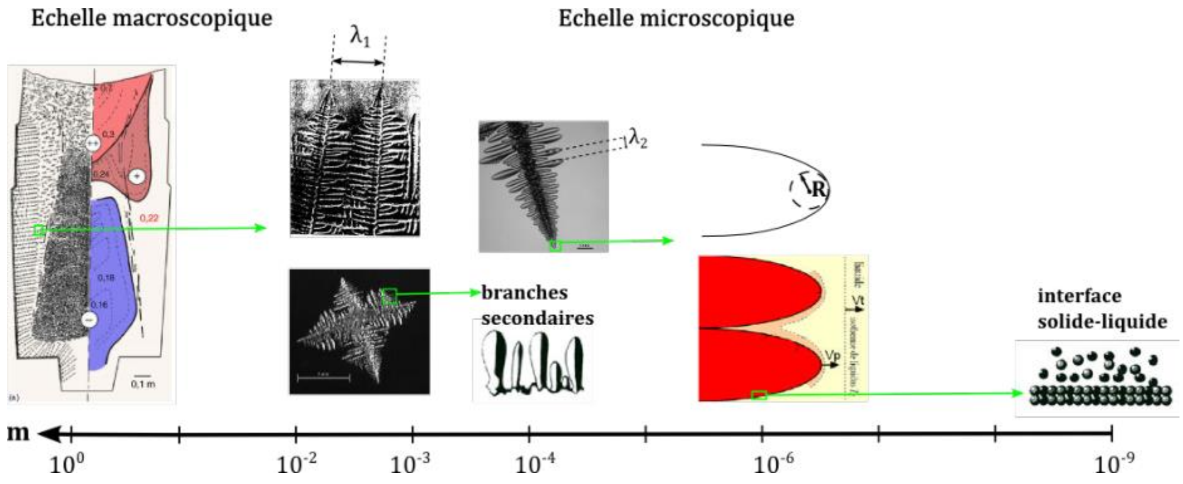

Fig. 1.9 Solidification scales with decreasing size from left to right [25]

Since last century development of solidification models at macroscale and at microscale happened in parallel and their completeness was closely related to the advances in computational technique and resource. Early macroscale models considered temperature and flow fields in simplified manners, often they did not take into account the variation of liquidus temperature due to transport of solute and growth kinetics of dendrites. Moreover, theories and models for the latter were also under development. Nevertheless, some semi-empirical models allowed prediction of nucleation rate, solid growth rate and casting solidification time [50,51]. Since then, significant progress has been made in development of models for simulation of both solidification structure evolution and macrosegregaton formation during solidification.

Regarding numerical simulation for solidification structure, one can cite Monte-Carlo [52,53], cellular automaton (CA) [54–56], and phase field (PF) methods [57,58]. CA method uses a regular arrangement of cells to map the solidification domain. The state of a cell changes according to its current state and the current states of its immediate neighbors. Compared to CA method, PF model better accounts for physical properties at solid-liquid interface such as surface tension. Therefore, PF model is often used to make in-depth investigation on solidification theory and the microstructure evolution in experiments [59]. The drawback of PF model is that it consumes huge amount of computational resource. Therefore, it is still far to apply it in an industrial process. According to Moore's law, simple two-dimensional numerical simulation of casting solidification process using PF model could not be possible before the year 2055 [49,60].

As for macroscale solidification simulation, it is important to couple multiphase flow and phase transition into numerical model. A common idea is to simplify the presentation of the solid phase in mushy zone via porous media whose phase fraction is given based upon temperature and solute concentration. With this method, Trindade et al. [61] simulated the solidification phenomenon in round bloom continuous casting process and found that the mold curvature causes the asymmetric growth of shell. CA method for grain growth is often coupled with calculations performed with finite element (FE) technique to bridge microscale and macroscale phenomena. In this way, Hou et al. [62] simulated solidification of high-carbon steel in billet continuous casting process and found that the compactness of the equiaxed zone increased obviously with electromagnetic stirring. However, the fluid flow and grains transport cannot be easily taken into account in CA-FE method. Volume average solidification model [63], which considers solidification structure evolution and solute transport, is supposed to be a better tool to simulate multi-fields/scales solidification phenomena under convection. With this method, rather good description of typical solidification phenomena can be done with limited computational resource that makes optimization of industrial processes possible. Therefore, volume average model steps nowadays ahead of other solidification models in numerical simulation for casting process. For instance, Guan et al. [64] used this method to simulate the formation of V-shaped segregation during high carbon steel billet continuous casting. Pakanati et al. [42,65] used equiaxed solidification model to simulate the direct continuous casting processes of several aluminum alloys, resulting good agreement with experimental measurements.

It should be noted however that several years ago some novel models intended for better description of various phenomena at mesoscale, such as envelope models [66] and dendritic needle network [67], appeared and started to develop. They seem to be good complements to volume average models and probably be an alternative to them.

1.3.2 Benchmark investigations

Although a number of numerical models have been developed for calculation of macroscopic heat and mass transfer during solidification, before they are used in industrial prediction, an important step is to conduct simulations for similar simplified solidification problem to test the model's performance. To verify the simulation results, corresponding solidification experiments are specially designed and are usually conducted in a rectangular cavity with rather simple boundary conditions. For convenience of operation in experiment and in-situ temperature measurement, low melting point alloy is usually used. The gathered quantitative data such as distribution of temperature and solute concentration can serve as reference for numerical simulation. This kind of experiment is called benchmark experiment. An influential benchmark experiment was performed by Hebditch and Hunt several decades ago [27]. In that experiment, specimens of Pb-Sn or Sn-Zn alloys were solidified in a thin section mold with inner dimension of 100 mm × 60 mm × 10 mm (Fig. 1.10). The solute concentration distributions at different stages of solidification were analyzed along with presentation of solidified macrostructure. The idea of Hebditch-Hunt experiment was to illustrate the important effect of natural convection on the formation of macrosegregation. The results showed that the macrosegregation arose partly because the motion of liquid led to a change in bulk liquid composition and its stratification into layers of different density. Some liquid can penetrate into the mushy zone and take away enriched liquid, resulting the enrichment and depletion in ingot. The experiment was later modeled repeatedly and nowadays its configuration along with specified boundary conditions serves as a reference for some numerical studies [37,68–70]. Most of these simulations obtained similar segregation pattern as observed from experiment and predicted the formation of segregate channels in semi-solid region. It was believed that these channels had strong effect on the overall macrosegregation pattern because enriched liquid could flow into bulk liquid through these channels.

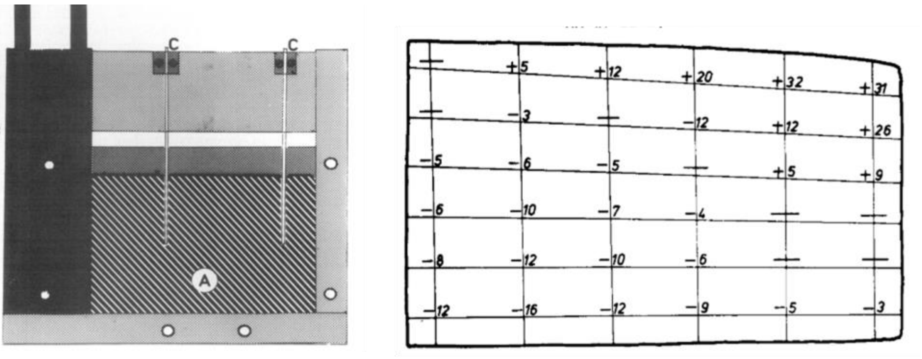

Fig. 1.10 Hebditch-Hunt solidification apparatus and macrosegregation diagram [27]

Since that, various benchmark installations have been developed in similar way. Beckermann and Viskanta [71] visualized the convection and solidification phenomena for ammonium chloride-water (NH_4Cl-H_2O) solution in an insulated test cell of a square cross section. Due to the transparent nature of ammonium chloride and its similar phase-change characteristics to those of metals and alloys, this material was then frequently used as a metal analog in experiments [72–75]. Wu and co-works [76] recently reported a simulation for a solidification experiment of NH_4Cl-70% H_2O solution with a five-phase volume average model. The work explained the experimentally observed flow phenomena. Shahani et al. [77] performed solidification of Sn-10% Pb and Pb-15% Sn alloys in graphite mold with inner dimensions of 105 mm × 105 mm × 25 mm. In that experiment set-up, a heating element was wound at one end of the cavity, while a nitrogen-cooled copper chill was placed on the other end. The power of heating and cooling intensity were controlled by a processor to maintain a constant temperature gradient. In the experiment of Prescott et al. [78], Pb-19 wt% Sn alloy was solidified in an axisymmetric annular mold of stainless steel, the recorded temperature history in ingot during solidification agreed well with simulation results by a continuum mixture model. Krane et al. [79] performed solidification experiments of different Pb-Sn alloys in a thin rectangular stainless steel mold. Water cooling heat exchangers were installed at both sides and a group of thermocouples were embedded in the mold to record temperature history. The crucial role of permeability model was discussed through comparison of fields of temperature and macrosegregation between simulation and experimental results. The authors further carried out investigation for a ternary metal alloy (Pb-5% Sb-35% Sn) [80].

In 2009, five scientific institutes in France (CEMEF, IJL, SIMAP, FAST, and TREFLE)

[81] proposed a numerical benchmark to verify the agreement of the numerical solutions obtained by different contributors. The proposed benchmark case was the solidification of Pb-18% Sn alloy in a rectangular cavity with width of 100 mm and hight of 60 mm. The geometry of domain and cooling condition are presented in Fig. 1.11(a) and some calculation results [82] from participators are compared in Fig. 1.11(b-g). The obtained results showed same segregation pattern and similar segregation degree, but the number of channels and the intensity of segregation inside the channels vary from one contribution to another. The discrepancy may be related to different uses of mesh size, stabilization scheme, etc.

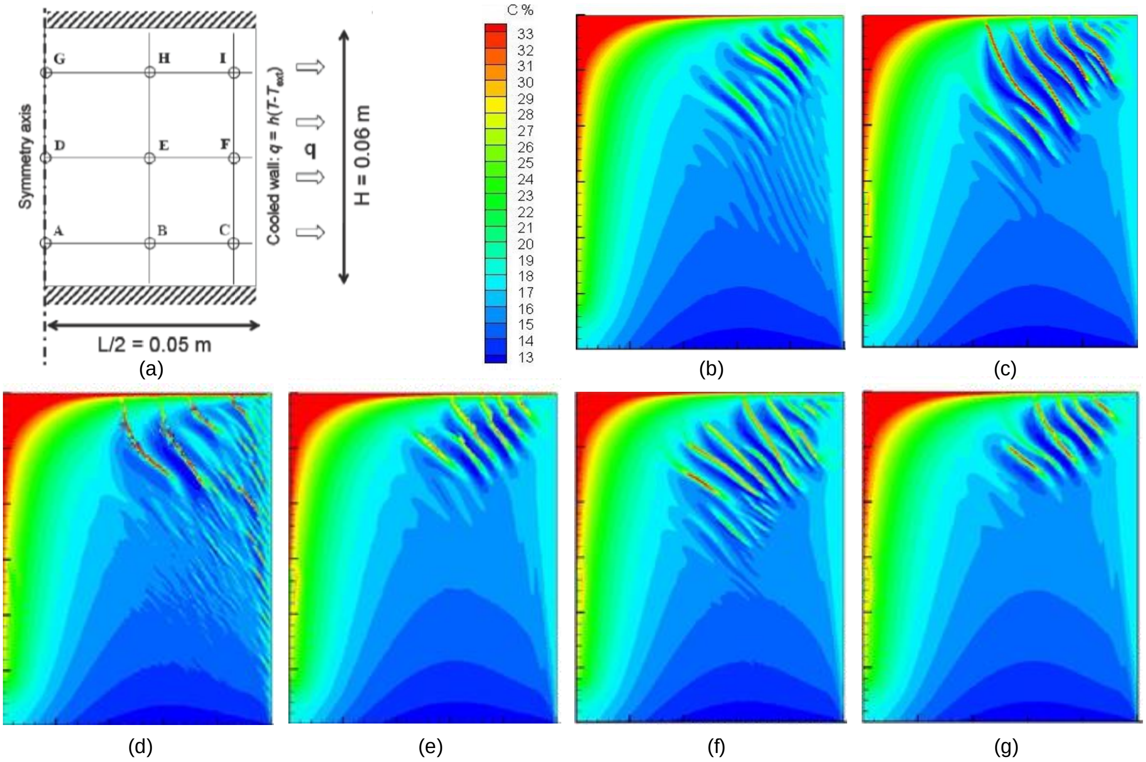

Fig. 1.11 Description of the solidification problem (a) and segregation map of average mass concentration in wt% Sn obtained by the different contributors: (b) EPM-SIMAP, (c) IJL SOLID, (d) CEMEF, (e) TREFLE, (f) IJL OpenFORM upwind, and (g) IJL OpenFORM QUICK [82]

Using the configuration of the introduced benchmarks above, equiaxed solidification models were also tested. For example, Krane et al. [83] simulated the equiaxed solidification of a ternary alloy and discussed the effect of packing limit fraction on final macrosegregation. Založnik et al. [84,85] proposed operator splitting scheme for equiaxed solidification model, and conducted a simulation in the configuration of Hebditch-Hunt benchmark. Nguyen et al. [86] put up with a finite element equiaxed solidification model and tested the model through Hebdich-Hunt benchmark before applying the model to simulation of solidification of industrial ingot. The authors also compared simulation results of Hebditch-Hunt benchmark solidification using models with fixed solid or with solid transport [69]. The simulation was made for Sn-5wt%Pb alloy and the ingot was cooled from left hand side. Results clearly showed that the sedimentation of solute-depleted grains led to a rigid solid layer and a negative segregation in the lower part, as seen in Fig. 1.12. Strictly speaking, it is not appropriate to validate the mentioned behavior of equiaxed grains through Hebditch-Hunt or mentioned other benchmark experiments because in reality these experiments produced mainly columnar solidification structure.

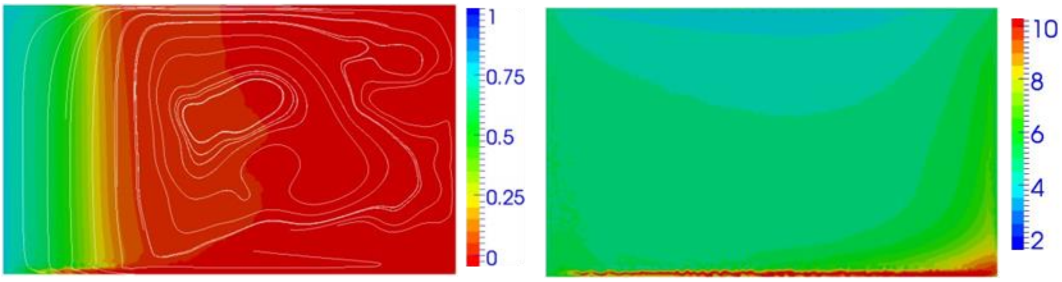

(a) Solid fraction at 100s (Fixed solid) (b) Final segregation map (Fixed solid)

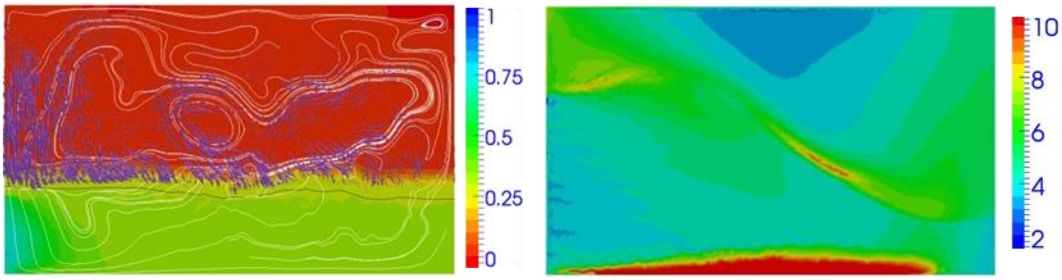

(c) Solid fraction at 100s (Solid transport) (d) Final segregation map (Solid transport)

Fig. 1.12 Comparison of simulation results without and with solid transport: (a,c) the solid velocity vectors, the liquid velocity streamlines and the solid fraction distribution at 100s and (b,d) final segregation map in wt% Pb (constructed from ref. [69])

Another benchmark solidification experimental set-up was made in SIMAP/EPM laboratory in France and is referred hereafter as AFRODITE [87]. Similar to other benchmark experiments [78,79], temperature history was recorded during solidification by a lattice of 50 thermocouples. After solidification, the post-mortem analysis of the sample was made regarding the segregation pattern (with X-ray and/or using probes), the grain structures and dendrite parameters. Distinct from other benchmark set-ups, in AFRODITE a linear electromagnetic motor was placed at the bottom of cavity, which made it possible to stir the alloy during solidification. Several experiments have been performed with AFRODITE set-up. First, Wang and Fautrelle [88] carried out solidification experiment on pure Sn with natural convection. Then, Hachani et al. [89] studied the effect of different initial concentration in solidification of a Sn-Pb alloy with natural convection. The latest results obtained with the AFRODITE set-up were related to the effect of the various modes of the electromagnetic stirring during the solidification of a Sn-Pb alloy on the macrosegregation and final structure of ingot [90]. Numerical calculations were performed for AFRODITE solidification without EMS in two-dimensional and three-dimensional configurations, using columnar solidification model [91] or mixed columnar-equiaxed solidification model [23]. Carozzani et al. [92] simulated an experiment for the solidification of Sn-3wt%Pb alloy in AFRODITE benchmark using CA-FE model. These numerical simulations well repeated solidification phenomena in AFRODITE experiments, and to some extent achieved deeper understanding of the macrosegregation formation and columnar-equiaxed transition.

In particular, it was found that for a AFRODITE experiment with the Lorentz force acting in a direction opposite to the flow caused by the gravity, the structure of the samples consisted mainly of the equiaxed grains [90]. The obtained data in this experiment actually gives valuable reference for the modeling of equiaxed solidification although it concerns more complex multiphase flow fields than other benchmark cases due to the presence of electromagnetic force. One of the purpose of current study is to simulate this particular experimental result by a developed three-phase equiaxed solidification model. This part of work as well as detailed description for AFRODITE experiment will be presented in chapter 4.

1.3.3 Numerical simulation of ingot solidification

Manufacturing of large-size ingots is a fundamental process in industrial production of heavy machinery. The first thorough study of segregation in a large number of ingots ranging from 14 cwts. (765 kg) to 172 tons was presented in the first report of a special committee of the Iron and Steel Institute of Great Britain [93]. Apart from “the very thin extreme outer skin of true chill crystals,” three zones were revealed in the ingots studied. The zone adjacent to the outer thin layer (zone 1) consisted of columnar grains directed inward, while the thickness of the zone was found to be dependent on casting conditions and steel composition. The second zone (zone 2) beyond zone 1, proceeding inward in a radial direction, was reported to be richer in segregates with an annular inner boundary “having roughly the form of a truncated cone or pyramid.” In addition, A-shape segregates were documented for this zone. Furthermore, sulfur prints and etching revealed a central zone (zone 3) in which solid grains could be considered to be equiaxed or, as said in the report, “the crystals may cease to possess the hitherto well marked columnar form” [93]. Near the central axis, V-shape segregates were usually present: The lowest part of the central zone was defined as the purest, and the top of the ingot presented strong segregation.

Various laboratory-scale experiments were developed later in order to study the effect of solidification parameters on solid structure and segregation, and patterns similar to those reported for large-size ingots were found [94–96]. These experiments served for validation of solidification models, which were further used to explain the segregation phenomenon in ingots. Thus, the gravity-induced flow of liquid through the mushy zone and the remelting of the solid phase were shown to be potentially responsible for the formation of centerline segregation, as well as of A-type and V-type segregates, depending on density variation due to liquid enrichment and on the variation and direction of the thermal gradient [97]. This analysis was then extended to multicomponent alloys [98]. State of the art regarding numerical simulations of segregation in ingots was thoroughly reviewed in 1999 [99] and 2009 [40]. Compact but detailed reviews were also provided for later periods [100,101] regarding both experimental and numerical studies aiming to reproduce segregation patterns observed in large-scale ingots.

To sum up, it was found that use of columnar solidification model does not allow one to clearly reproduce the negative segregation cone at the bottom of the ingot [102–104]. Moreover, according to references elsewhere [95], even prior to publishing the report in 1926 [93], ingots' producer already supposed that the central ingot zone was formed from free-floating equiaxed grains. One of the first attempts to numerically study the effect of the sedimentation of grains on macrosegregation was made for a 4 ton ingot [105]. Simulations were conducted for different zones with a simplified system of equations, where only the vertical component of velocity with a pre-calculated value was taken in the zone with the sedimentation cone. Yet, even when volume average models were developed [106], their use in modeling of ingot solidification was not evident because of necessity of the definition of multiple parameters for auxiliary closure equations, and this is still the case. However, the pure equiaxed solidification model was applied to the studies of macrosegregation in the 3.3 ton steel ingot [40,86,104]. It should be mentioned that soon after pure equiaxed models started being used, mixed columnar-equiaxed models [24,107] began to be exploited.

Specifically, the simulation results of ingot solidification by equiaxed models reveal following differences from the ones by columnar models (or fixed solid):

(1) Liquid flow direction

In a case with fixed solid phase, the flow is driven only by natural convection which is dominated by the concentration of carbon in most steel ingot [18].Therefore, lighter liquid ascends along the walls and heavier liquid descends in the ingot core. When solid grains move, the flow is completely modified. Solid grains, heavier than the liquid, sediment along the cooled walls and entrain the liquid, thus inducing a downward flow. This phenomenon leads to an overall flow loop descending at the solidification front and ascending in the core [86].

(2) Segregation bands

In the calculation domain with fixed solid phase, “A” shape segregation bands were often observed in simulation for ingot solidification [108]. Založnik et al. [103] found that the simulated segregation bands were triggered by the instabilities of the solidification front, that their location was determined by flow instabilities, and that their “A” or “V” orientation depended on the global direction of the flow circulation. Fig. 1.13 shows the macrosegregation map of 3.3 ton steel ingot under different buoyancy ratios N that is defined as in Eq. (1.2).

$$N = \frac{\beta_c \Delta_c}{\beta_T \Delta_T} = \frac{\beta_c}{\beta_T m} \tag{1.2}$$

where β_c and β_T are solutal and thermal expansion coefficients respectively, $m < 0$ is the slope of liquidus temperature line in phase diagram.

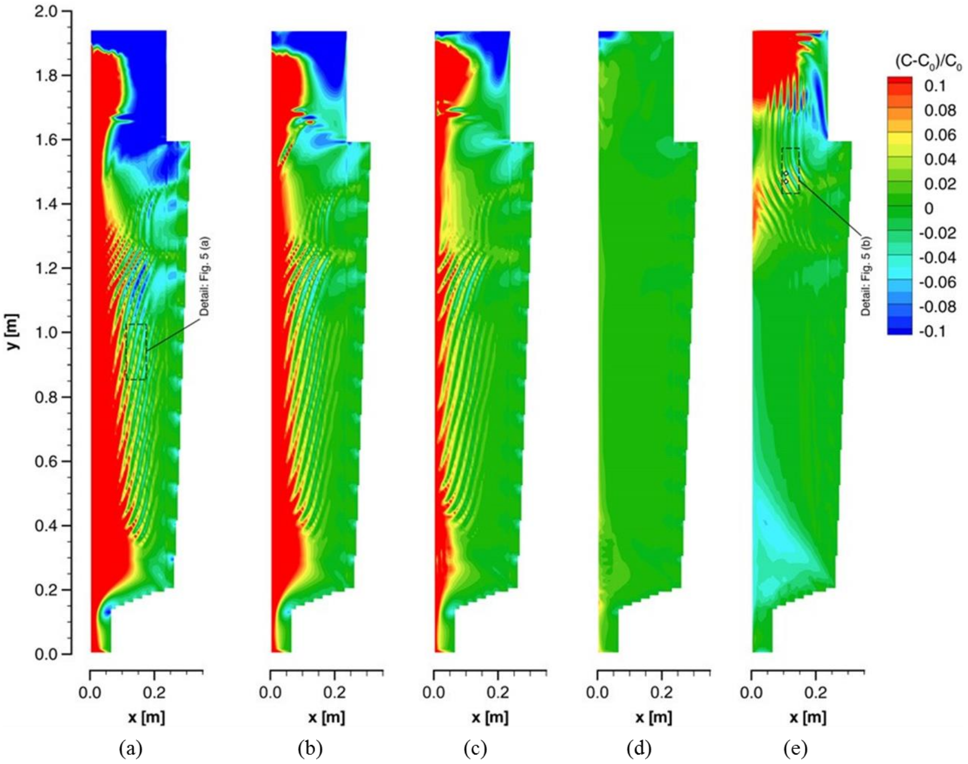

Fig. 1.13 Final macrosegregation maps of steel ingot under different buoyancy ratio: (a) N = 1.65, (b) N = 0, (c) N = –0.68, (d) N = –1, and (e) N = –1.65 [103]

Similar phenomenon was observed by Combeau et al. [40] in simulation for 3.3 ton steel ingot with dendritic equiaxed solidification model. Yet, the “A” segregation bands from equiaxed solidification model had a somewhat coarser structure and started at a higher position. Besides, the coarseness of the numerical grid prevented the direct prediction of “A” segregation. In simulation with spherical FEM equiaxed model, the “A” segregation was not declared but a positive segregated line was clearly shown near the cooling boundary [86]. In the simulation work of Liu et al. [109], another shape of "A" segregation band was reported with use of equixed solidification model, as presented in Fig. 1.14 where the effect of chosen packing limit faction on segregation bands was also shown. According to the authors, these bands were resulted from a narrow channel that forms around the position where the solidified shell in the horizontal direction met the one in the vertical direction, which served as a barrier to the fluid flow, leading to the accumulation of solute.

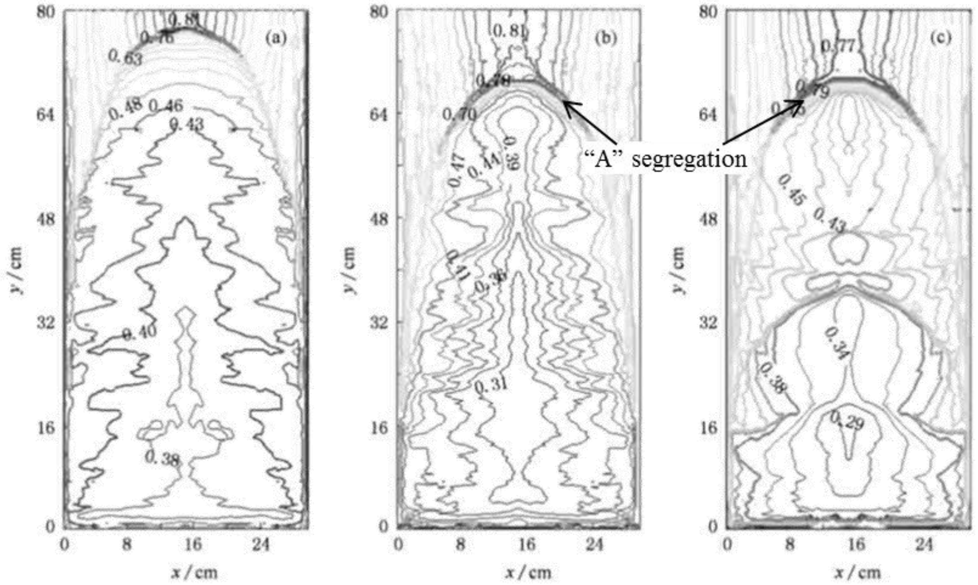

Fig. 1.14 Macrosegregation map of ingot of Fe-0.45wt%C alloy under different packing limit fraction: (a) 0.3, (b) 0.637, and (c) 0.8 [109]

(3) Negative segregation cone

In section 1.2.3, the formation of negative segregation cone at bottom was attributed to the sedimentation of equiaxed grains. However, with a model assuming fixed solid, a conic shape negative zone could also predicted in ingot, as seen in Fig. 1.13(e). It is indicated in that work [103] that the negative cone was the result of upward flow in mush driven by solute buoyancy force. The negative segregation intensity was associated to the solute expansion coefficient and also the permeability in mushy zone. Li et al. [110] presented predicted final macrosegregation maps of 3.3 ton steel ingot with fixed solid (Fig. 1.15(a)) or with moving solid (Fig. 1.15(b-c)). It was found that negative segregated cone predicted with moving solid was higher than the one calculated with fixed solid. For the case with fixed solid, most serious negative segregation was located at a small distance off the centerline [110]. In contrast, for the case with moving solid, most prominent negative segregation was located at the centerline. When the solidification shrinkage was considered, the positive segregation zone was gently shifted downwards (Fig.

1.15(c)) to the hot-top junction, yet the overall macrosegregation was not obviously changed.

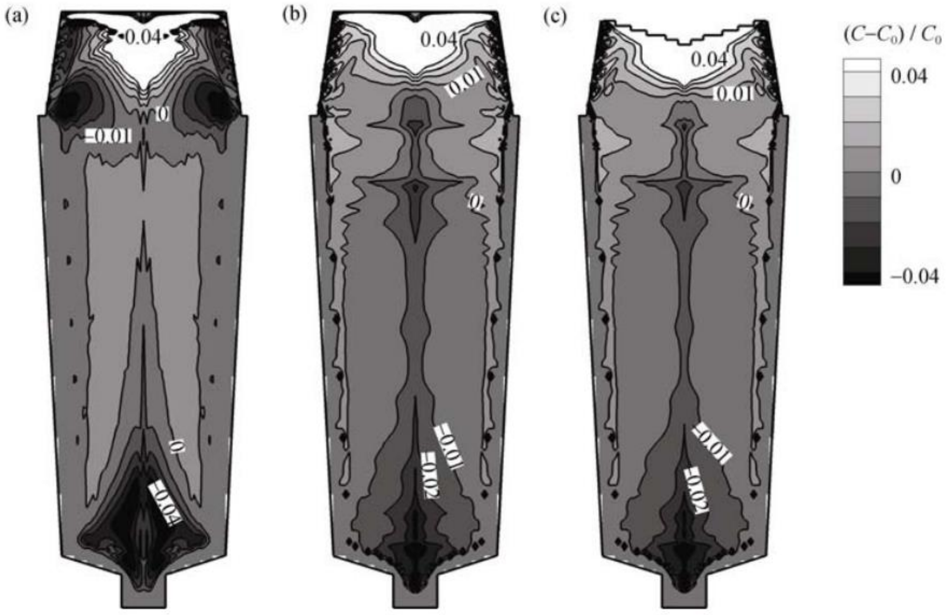

Fig. 1.15 Predicted final macrosegregation patterns in three cases: (a) fixed solid, (b) moving solid, and (c) moving solid and considering shrinkage [110]

1.4 Conclusion

The formation mechanism of macrosegregation in ingot remains unclear and quantitative prediction for macrosegregation is still difficult. Based on the review of many experimental and simulation works, it was concluded that the macrosegregation is often affected by the origin, growth and movement of equiaxed grains. Although many modeling works for solidification have been reported, current numerical simulations are still very sensitive to the choice made for closure relations and numerical parameters, besides, the application of pure equiaxed model with regard to large ingot was studied only for a very limited combination of parameters. In this thesis, special attention will be paid to the modeling of equiaxed solidification as well as the detailed review for the effect of each parameter. Before using equiaxed solidification model to investigate solidification process and macrosegregtaion formation in steel ingot, simulations are performed in advance for two mentioned benchmark solidification cases, i.e. Hebditch-Hunt benchmark and AFRODITE benchmark.

Chapter 2 Volume average solidification model: state of art

Essentially, volume average method is an way to calculate solidification structure and solute segregation at the scale of sample accounting for growth kinetics of dendrites and segregation process at the solid-liquid interface although presentation of the latter is considerably simplified. Because of the latter, the volume average model requires less computational resource (as compared to, e.g., phase field model) and is capabale of coupling phenomena which occur at various scales. In particular, it can achieve a good description of complex multiphase flow and phase transition during solidification of ingot with practical size. This chapter aims at presenting the state of art of volume average models. A brief overview of model development is given in section 2.1, which is followed by presentation of model's fundamentals in section 2.2 and further by discussion of key issues in volume average solidification models in sections 2.3 through 2.7.

2.1 Development history of volume average model

In 1987, Rappaz and Thevoz [111] put forward a volume average solidification model for growth of a unique dendritic grain of a binary alloy accounting for growth rate controlled by microscale solute diffusion and for evolution of solute field around the grain. A great advantage of this model was the ability of its embedding into macroscale models. In 1991, Ganesan and Poirier [112] derived mass and momentum transport equations for mushy zone during solidification of binary alloy using volume average method. Ni and Beckermann [113,114] applied volume average method with embedded globular (two phases) equiaxed model to simulate solidification of Al-4% Cu alloy in a side-cooling cavity accounting for macroscale convective flow. With this model, they predicted grain size distribution and segregation map in the solidified sample. After that, Wang and Beckermann [115,116] extended two-phase model to three-phase model (solid, inter- and extradendritic liquid), and proposed an empirical model to calculate flow resistance in each liquid phase. Ciobanas and Fautrelle [117,118] transposed a concept of statistical ensemble averaging method originated from gas/liquid model to solidification model. Comparing with volume averaging, statistical averaging has better description of randomness of nucleation and equiaxed grains' movement. Yet, final form of equations obtained with statistical average method resembles those obtained with volume average method in most cases. Further, Nielsen et al. [119] proposed to account for shape of dendritic grains using various shape factors in expression for surface area concentration, which is an important parameter in calculating solute transfer rate between phases. Following this idea, Wu and Ludwig built several equiaxed solidification models, including two-phase model with globular grain [120] and three-phase model with dendritic grain [121]. In the three-phase model, they emphasized important roles of shape factor, sphericity and globular-dendritic transition. The authors also developed mixed columnar-equiaxed solidification models, including three-phase model (columnar, equiaxed, and liquid) [122] and five-phase model (liquid, interdendritic liquid in equiaxed grain, solid in equiaxed grain, interdendritic liquid in columnar grain, and solid in columnar grain) [123]. Finite element based code SOLID based on volume average method and employing forward split scheme to couple macroscopic transport and grain growth was developed by Založnik and Combeau [84,85] and applied to simulation of industrial solidification case [40].

A unique advantage of volume average method is that it can be flexibly expanded to incorporate new phenomena.Therefore, more distinct functions can be developed in the future through special adjustments in model. Below some existed examples are provided:

- shrinkage, porosity, and cavity in ingot can be modeled by introducing a gas phase and differing the densities between solid and liquid phases [124];
- melt-flow induced dendrite fragment formation [125] and the addition of inoculant particles [42] can be modeled with modification of nucleation model;
- hot-tearing risk can be predicted through calculation of thermal mechanic stress [126];
- the moving behavior and distribution of inclusions can be modeled by adding Euler phases for inclusions with a proper entrapment mechanism [127,128];
- the effect of EMS on solidification and macrosegregation can be investigated by coupling electromagnetic fields [129];
- bulging effect and reduction effect on macrosegregation in continuous casting slab/bloom can be investigated by modeling the shell deformation [130].

It should be noted though that most of the current models are implemented for binary alloy systems although real alloy is composed of three or more elements. For example, in simulation of solidification kinetics of steel, a linearized Fe-C phase diagram is usually assumed [130,131], while the segregation of other elements can be estimated by Scheil equation [99]. These simplifications deviate the reality if two alloy elements have large differences in the solute partition coefficient, liquidus slope, and diffusion coefficient. However, it is almost not possible to incorporate all the thermodynamics of multicomponent alloy into volume average models.

Currently, only a few multiphase models [83,132–134] have been developed to predict ternary alloy solidification, yet, the introduction of third element greatly increases the complexity of model and uncertainty of simulation results.

2.2 Description of volume average method

Solidification supposes transition from liquid to solid accompanied with transport phenomena at microscale in each phase. Modeling at macroscale should treat transport processes for each physical quantity Ψ_i that happen within each phase and account for additional sources (or sink) of this quantity due to phase transition. Here Ψ_i represents conservative quantities including mass, momentum, energy, solute concentration, and grain number density.

Modern models propose to distinguish liquid situated between arms of dendritic grain and liquid outside of them and to consider them as different phases. For example, three phases are represented in equiaxed solidification model: solid phase, interdendritic liquid phase, and extradendritic liquid phase. Presence of phase *i*, anywhere in space at any moment of time is defined at microscale with a characteristic phase function:

$$X_i\left(\vec{x},t\right)=\begin{cases}1 & f\left(\vec{x},t\right) \text{ within phase } i\\ 0 & \text{elsewhere}\end{cases} \tag{2.1}$$

To make a transition from microscopic distribution to macroscopic one, first, a representative macroscopic volume V_0 should be chosen and includes all possible phases. Further, averaging of a microscale physical quantity Ψ_i is performed over V_0 for each phase giving rise to:

- volume fraction of a phase *i* defined as $f_i = \frac{V_i}{V_0} = \frac{1}{V_0}\int_{V_0} X_i \mathrm{d}V = \frac{V_i}{V_0}$;
- volume average values $\langle \Psi_i \rangle = \frac{1}{V_0}\int_{V_0} \Psi X_i \mathrm{d}V$;
- intrinsic volume average values $\langle \Psi_i \rangle^i = \frac{1}{V_i}\int_{V_0} \Psi X_i \mathrm{d}V = \frac{1}{f_i}\langle \Psi_i \rangle$.

Using averaging procedure, general transport equation for Ψ_i can be written as follows:

$$\frac{\partial f_i \langle \Psi_i \rangle^i}{\partial t} + \nabla\left(f_i \langle \Psi_i \rangle^i \langle \vec{u}_i \rangle^i\right) = \langle \Psi_i \rangle^i_{diff} + \langle \Psi_i \rangle^i_{source} \tag{2.2}$$

where the second term is advection term, the third one is diffusive term, the last one is source term. Expression for each of these terms depends on the physical variable under consideration as summarized in Table 2.1. Note that hereafter notation are simplified for values averaged over volumes: $\langle \rho_i \rangle^i$ is denoted as ρ_i, $\langle u_i \rangle^i$ as u_i, etc.

In Eq. (2.2), $\langle\Psi_i\rangle^i_{\text{diff}}$ for energy and solute conservation represents conductive heat transfer and molecular diffusion characterized with thermal conductivity k_i and molecular diffusion coefficient D_i, respectively, while in the momentum equation it corresponds to momentum transfer due to dynamic viscosity of fluid μ_i. The source terms $\langle\Psi_i\rangle^i_{\text{source}}$ may include several components depending on the physical field under consideration. For grain number density, it corresponds to the nucleation rate N_ϕ, while in mass transport equation, source term means the phase transition rate, i.e. solid/grain growth rate. It is related to surface area concentration, S_i^{int}, which, as discussed below, means interface area per unit volume, and to v_i^* which is average interface movement velocity. In other equations, source term is composed of a part due to phase transition, exchange between phases and "extra" sources. In Table 2.1, $\vec{u}^*$, h^* and c^* are velocity, enthalpy and solute concentration for the phase which undergoes transformation, while K_{ij} and H^* are coefficients for momentum transfer and for inner heat exchange between phases, respectively. Finally, l_i is diffusion length in phase i whose calculation will be discussed in section 2.5.

Table 2.1 Meaning of terms in Eq. (2.1)

Conservative quantities	Ψ	$\langle\Psi_i\rangle^i_{diff}$	$\langle\Psi_i\rangle^i_{source}$		
			Phase transition	Inter exchange	Extra source
Grain number density	n	0	0	0	Nucleation rate
Mass	$f_i\rho_i$	0	$M_{ij} = S_{ij}^{\text{int}} v_{ij}^* \rho_i$	0	Mass transfer rate
Momentum	$f_i\rho_i\vec{u}_i$	$\nabla\left[f_i\mu_i\left(\nabla\vec{u}_i + \left(\nabla\vec{u}_i\right)^{\mathrm{T}}\right)\right]$	$\vec{U}_{ij}^M = M_{ij}\vec{u}^*$	$\vec{U}_{ij}^D = K_{ij}\left(\vec{u}_j - \vec{u}_i\right)$	Gravity and external force
Energy	$f_i\rho_i h_i$	$\nabla\left(f_i\kappa_i\nabla T\right)$	$Q_{ij}^M = M_{ij}h^*$	$Q_{ij}^D = H^*\left(T_j - T_i\right)$	Joule heat
Solute concentration	$f_i\rho_i c_i$	$\nabla\left(f_i D_i \rho_i \nabla c_i\right)$	$J_{ij}^M = M_i c_{ij}^*$	$J_{ij}^D = \rho_i D_i / l_i\left(c^* - c_i\right)$	0

2.3 Nucleation rate in equation for grain number density

As origin of equiaxed grains, nucleation is a key step in the formation of the microstructure, meantime, grain number density determines current and final grain size. As mentioned above, nuclei in solidification mainly come from non-spontaneous nucleation, which can be affected by various unpredictable factors. Theoretical models for non-spontaneous nucleation can be classified into two types, named instantaneous model and homogeneous model. Instantaneous model assumes that all nuclei appear within a very narrow temperature range [135]. In other words, once the $T < T_{\text{nucl}}$ is satisfied, nucleation occurs and grain number density instantly reaches its maximal value: $\mathrm{d}n/\mathrm{d}T = n_{\max}\delta(T - T_{\mathrm{nucl}})$, where δ is Dirac delta function. A representative instantaneous model was put up with by Hunt [7] in 1984:

$$N_{\phi} = k_1\left(n_{\max} - n\right)\exp\left[-\frac{k_2}{\left(\Delta T\right)^2}\right] \tag{2.3}$$

where $k_1 = 10^{18} \sim 10^{22}\ \mathrm{s}^{-1}$; $k_2 = -(\Delta T_{\mathrm{nucl}})^2 \ln(N_0 \cdot k_1)$; n is the local grain number density; ΔT is the local undercooling as defined in Fig. 1.2. Instantaneous model is convenient to implement, however, it does not explain stochasticity of nuclei's size and position. Heterogeneous nucleation model defines relation of nucleation rate to the value of undercooling, that mimics continuous activation of inoculants (embryos) during cooling process. At early time, a model of such kind had been given by Oldfield [136] for eutectic growth of gray cast iron: $n = \mathrm{A}\cdot\Delta T^{\mathrm{B}}$. This equation is consistent with reality in condition with small undercooling, however, it is not adapted to large undercooling condition. Rappaz et al. [137] proposed a heterogeneous nucleation model based on Gaussian distribution, i.e. for an undercooling of ΔT, the nucleation rate can be calculated by:

$$N_{\phi} = \frac{\mathrm{d}\left(\Delta T\right)}{\mathrm{d}t}\frac{n_{\max}}{\sqrt{2\pi}\Delta T_{\delta}}\exp\left[-\frac{\left(\Delta T - \Delta T_N\right)^2}{2\left(\Delta T_{\delta}\right)^2}\right] \tag{2.4}$$

where ΔT_N is average nucleation undercooling; ΔT_{δ} is a standard deviation; $n_{\max}$ is the maximal inoculants number density in the parent melt. At first nucleation rate increases with increase of undercooling, but after turning point at $\Delta T = \Delta T_N$, it falls down with further increase of undercooling. This nucleation model has been verified for most technical alloys, and been applied to volume average solidification simulations [121,138]. It is appropriate to note that the values of ΔT_N and ΔT_{δ} must be chosen according to specific solidification experiment, besides, this model was derived for solidification process with stationary melt, thus its applicability in a case with convection remains to be verified.

In order to refine grain structure and improve cast quality, one practical way is to increase grain number density. Various methods have been invented and applied in industry, including: (1) implementation of external force, such as electromagnetic stirring or mechanical stirring to promote dendrite fragmentation; (2) addition of appropriate nucleating agent.

For method (1), the relation between fragment number and melt flow has to be embedded into nucleation transport equation, which was preliminarily done in the work of Zheng et al. [125]. In that work, the fragmentation was assumed induced by remelting of columnar dendrites and the nucleation source from columnar phase could be modeled by Eq. (2.5). The authors also proved that fragment model played a critical role in the origin of equiaxed grains in a simulation for benchmark experiment [23]. However, further simulation-experiment comparison is still needed to provide convincing evidence for this concept.

$$N_{\text{frag}} = \frac{6\gamma\left(\vec{u}_c - \vec{u}_l\right)\nabla c_l \rho_e}{\pi \rho_e \left(d^0_{\text{frag}}\right)^3} \tag{2.5}$$

where γ is an adjustable coefficient that should be determined by some available experimental information; the term $\vec{u}_c - \vec{u}_l$ is the relative velocity between liquid and columnar dendrites; ∇c_l is the concentration gradient in liquid phase; $d^0_{\text{frag}} = \lambda_2 f_{\text{c}}$ is the initial diameter of fragments.

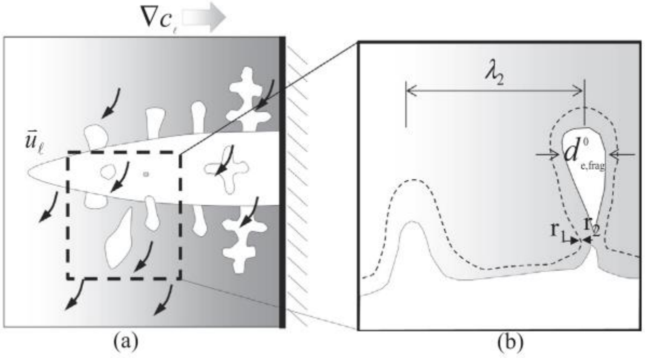

Fig. 2.1 Schematic description of remelting-induced fragmentation: (a) transport of solute-enriched interdendritic melt by the flow, (b) formation of a fragment by remelting of the side arm [23]

For method (2), the motion of inoculants have to be solved independently of the motion of equiaxed grain [139]. Besides, the distribution of population of inoculant particles with particle diameter and corresponding activation undercooling ΔT_c have to be modeled. When nucleation happens, a number of inoculant particles are transferred to grains and the nucleation rate can be determined as [139]:

$$N_\phi = \frac{\mathrm{d}\left(\Delta T\right)}{\mathrm{d}t} \frac{4\Gamma N_0}{\Delta T_c^2 d_0} \exp\left(\frac{4\Gamma}{d_0 \Delta T_c}\right) \tag{2.6}$$

where N_0 is a characteristic inoculant population density; d_0 is the characteristic length of inoculant particle; Γ is Gibbs-Thompson coefficient. The distribution of particle is determined by experimental measurements.

2.4 Kinetic model for phase transition

During solidification of metal alloy, the Lewis number (ratio between thermal and mass diffusivities) is in the order of magnitude 3 [22], thus a consideration of complete 'thermal mixing' at the scale of one grain is widely accepted. The growth of dendrite is dominantly controlled by solute diffusion, either inside or at the boundary of the grain envelope. Grain growth model which defines mass M_i transferred to the phase *i* due to phase transition is crucial for solidification simulation. All conservative equations given above, except the one for grain number density, contain a term related to M_i, which is defined by growth model. Volume average model, unlike CA or PF models, cannot directly simulate the phase interface morphology and interface movement. Instead, an average approach is used to evaluate growth rate as demonstrated in this section. As presented in Table 2.1, mass source in phase *i* due to phase transition can be generally written as: $M_i = S_i^{\mathrm{int}} v_i^* \rho_i$, where S_i^{int} and v_i^* are interface area concentration and interface movement velocity, respectively. Calculations of the two variables can be performed in different ways depending on assumption for grain shape and kinetic condition, as schematically presented in Fig. 2.2. For simplicity, equiaxed grains (*e*-phase) are often assumed with globular shape (Fig. 2.2 (a)) while the columnar grains (*c*-phase) can be regarded as a bunch of cylinders (Fig. 2.2 (b)). In practice, most alloys grow up with dendritic morphology, in which condition interdendritic liquid contacts with curved solid-liquid interface and can be regarded as transition zone between solid and extradendritic liquid for solute and momentum transport. It is customary to introduce an imaginary surface (Fig. 2.2 (c-d)) that encloses solid and interdendritic liquid phases and that is named hereafter grain envelope to distinguish inter- and extradendritic liquid phases.

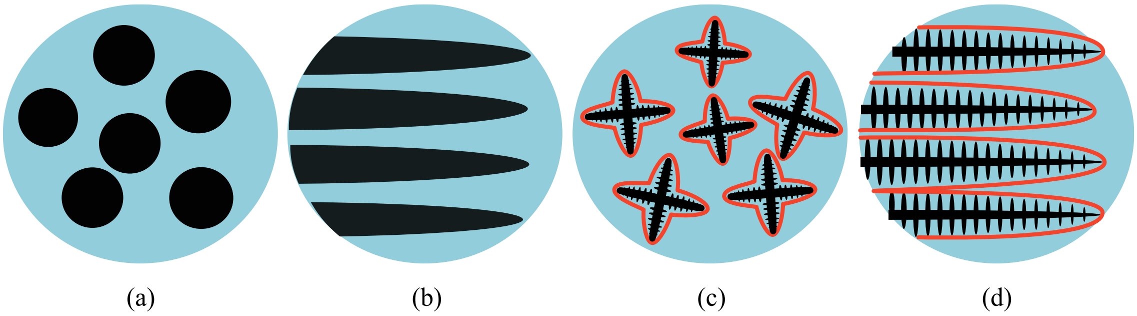
(a) (b) (c) (d)

Fig. 2.2 Schematic morphologies of grain: (a) globular equiaxed grain, (b) cylindrical columnar grain, (c) dendritic equiaxed grain, and (d) dendritic columnar grain. Red lines represent envelope surface

2.4.1 Interface area concentration

(1) Globular/cylindrical grain

Surface area of a single globe is defined by its diameter: $A_e = \pi d_e^2$. Considering a number (n) of equiaxed grains with globular shape per unit volume, the total surface area of all grains per unit volume (or surface area concentration) is S_e: $S_e = A_e / V_0 = (36\pi n)^{1/3} \cdot f_e^{2/3}$, where f_e is equiaxed grain fraction. Similarly, surface area concentration for columnar grains is S_c given as $S_c = 2\sqrt{\pi} \cdot f_c^{1/2} / \lambda_1$, where f_c is columnar grain fraction and λ_1 is primary arm spacing.

(2) Dendritic grain

Considering the different behaviors of inter- and extradendritic liquid phases, a concept of "envelope" (Fig. 2.3) introduced by Rappaz and Thevoz [111] is used and the envelope is defined as an imaginary boundary of grain phase which unifies solid phase (*s*-phase) and interdendritic liquid phase (*d*-phase). Finally, three phases are defined: the solid dendrite, or *s*-phase; the liquid between the solid dendrite arms, so-called interdendritic liquid, or *d*-phase; and the liquid outside of the dendrite, so-called extradendritic liquid, or *l*-phase.

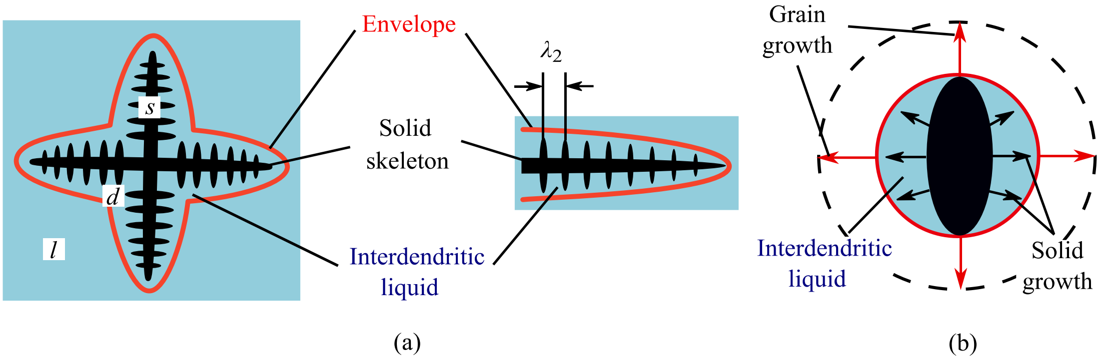

Fig. 2.3 Schematic figure for dendritic structure and grain growth process which consists of expansion of envelope (a) and growth of solid phase at the expense of interdendritic liquid (b)

The liquid concentration at the solid-liquid interface c_l^* is generally supposed to be equal to the thermodynamic equilibrium concentration which is related to local temperature through a phase diagram. Phase transition happens between solid and interdendritic liquid through solid-liquid interface, and also between inter- and extradendritic liquid through grain envelope. Accounting for this configuration, previous assumption for the shape of globular grains (calculation of S_e and S_c) can now be used to account for the shape of grain envelope.

Furthermore, in order to evaluate the rate of solid growth, the surface area of solid skeleton should be considered. Noted that the solid growth process actually is phase transition between *s*-phase and *d*-phase, which happens inside the grain envelope (Fig. 2.3). Therefore, the surface of solid skeleton can also be regarded as *s*-*d* interface inner grains. In most work, such interface inner grains is calculated by secondary arm spacing λ_2: $S_{sd}^e = 2 f_e f_d^e / \lambda_2$, $S_{sd}^c = 2 f_c f_d^c / \lambda_2$ [107]. The value of λ_2 is related to the local solidification time t_f [140] considering the coarsening of secondary arm: $\lambda_2 = M \cdot t_f^{1/3}$, where M is an adjustable coefficient whose value depends on specific alloy and cooling condition. One can find other optional secondary arm spacing models in the references [141–143].

2.4.2 Interface movement velocity

It is accepted that the velociy of motion of solid-liquid interface is defined by constitutional undercooling and the latter is related to the rate of solute transport near the interface, which can be affected by convective flow. Yet, most average algorithms take into account the grain growth model obtained for diffusive growth. It should be noted that while at microscale the growth of solid phase is defined by the motion of solid-liquid interface, in volume average models grain growth may be considered in a more complex way. In globular/cylindrical growth model, solid-liquid interface movement is driven by supersaturation in liquid phase and governed by diffusion rate at interface. In dendritic grain growth, solidification is composed of two parts: (1) solid growth of the interdendritic melt, which is governed by diffusion rate at *s-d* interface; (2) expansion of the grain envelope, which is often assumed proportional to the growth velocity of tips of primary arms of equiaxed/columnar grains. Consequently, the motion of the two types of interfaces has to be taken into account simultaneously. The columnar grain growth is often assumed as directional solidification process thus KGT model built by Kurz, Giovanola and Trivedi [144] is suitable. For equiaxed grain growth LGK model proposed by Lipton, Kurz and Glicksman [145] is more preferable. Below, the three growth models are briefly introduced.

(1) Diffusion governed growth

The solid growth rate is determined by growth velocity v_{ls} at *l-s* interface or v_{ds} at *d-s* interface. Taking example of v_{ls}, the driving force for growth is the difference in solute concentration between c_l(c_d for v_{ds}) and thermodynamic equilibrium concentration c_l^*. The solute diffusion rate is highly dependent on length scale l_{ls} according to Eq. (2.7) [146]:

$$v_{ls} = \frac{2D_l}{l_{ls}} \frac{c_l^* - c_l}{c_l^* - c_s^*} \tag{2.7}$$

The diffusion length is estimated as $R(1 - R/R_f)$ for globular grain assuming a steady state diffusion field, where R and R_f are current and final grain radius, respectively. For three-phase model, the movement velocity v_{ds} of *d-s* interface inside grain envelope can be estimated in a similar way, thus the corresponding diffusion length l_d is often related to the secondary arm spacing λ_2 and solid phase fraction f_s. The diffusion length l_d is calculated as $l_d = f_d\lambda_2/(2f_e)$ [63]. However, it is usually assumed that the interdendritic liquid is solutally well mixed because the liquid mass diffusivity is typically several orders of magnitude larger than that of the solid [25,63,111].

(2) LGK model

The undercooling ahead of the dendrite tip is composed of three parts [145]:

$\Delta T=\Delta T_c+\Delta T_t+\Delta T_R$. The constitutional undercooling ΔT_c, for a binary alloy with liquidus slope m, can be expressed as $\Delta T_c=m(c_l-c_l^*)$. Temperature undercooling ΔT_t means the temperature difference between interface temperature T^* and the one away from interface T_l^∞; ΔT_R is curvature undercooling. According to Gibbs-Thompson relation, a dendrite tip with radius of R will displace the liquidus temperature with amount of: $\Delta T_R=2\Gamma/R$, where Γ is Gibbs-Thompson constant, i.e. the ratio of surface energy to the melting entropy. The undercooling at dendrite tip finally is derived as Eq. (2.8) [147], and tip radius with the stability criterion is obtained as Eq. (2.9).

$$\Delta T=m\left(c_l-\frac{c_l}{1-(1-k_0)\mathrm{Iv}(P_c)}\right)+\frac{L}{c_p}\mathrm{Iv}(P_t)+\frac{2\Gamma}{R} \tag{2.8}$$

$$R=\frac{\Gamma/\sigma^*}{\frac{P_tL}{c_p}-\frac{P_cmc_l(1-k_0)}{1-(1-k_0)\mathrm{Iv}(P_c)}} \tag{2.9}$$

where L is latent heat, c_p is specific heat, $P_t=Rv_{tip}/2\alpha$ and $P_c=Rv_{tip}/2D_l$ are thermal and solutal Péclet number, respectively, α is thermal diffusivity, D_l is solute diffusion coefficient, and $\sigma^*=1/(4\pi^2)$ is stability constant.

(3) KGT model

On the basis of LGK model, Kurz et al. put up with KGT model [144] for tip growth velocity during directional solidification by neglecting the temperature undercooling. Unknown undercooling and tip radius can be solved from Eqs. (2.10) and (2.11).

$$\Delta T=m\left(c_l-\frac{c_l}{1-(1-k_0)\mathrm{Iv}(P_c)}\right)+\frac{2\Gamma}{R} \tag{2.10}$$

$$v_{tip}R^2=\frac{2}{\sigma^*}\frac{\Gamma D_l}{c_l(k_0-1)} \tag{2.11}$$

The Eqs. (2.8) through (2.11) provide implicit relation between thermal and/or solutal undercooling and tip growth velocity which enters into Ivantsov function depending on thermal or solutal Péclet number, respectively: Iv(P_t) or Iv(P_c). With use of various approximation for inverse Ivantsov function one can get an explicit equation for tip velocity and use it in the model.

2.4.3 Shape factor

In order to consider the non-sphere shape of dendritic grain, two factors were introduced [121,123,148]: (1) Growth shape factor ϕ_e^{env}, ϕ_c^{env}, representing the ratio between growth rate of equilibrium sphere to the tip growth velocity. (2) Sphericity ϕ_e^{sph}, ϕ_c^{sph}, representing the ratio of surface area of equilibrium sphere to the actual surface area. For perfectly spherical equiaxed grain or cylindrical columnar grain, all shape factors are equal to 1. Shape factors for equiaxed and columnar grains based on different shape assumptions are summarized in Table 2.2.

Table 2.2 Summary of shape factors based on different assumptions [123]

Equiaxed grain		Columnar grain	
Sphere $\phi_e^{env} = \phi_e^{sph} = 1$	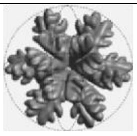	cylinder $\phi_c^{env} = \phi_c^{sph} = 1$	
Octahedron $\phi_e^{env} = 1/\sqrt[3]{\pi}$ $\phi_e^{sph} = \sqrt[3]{\pi}/\sqrt{3}$		Square $\phi_c^{env} = \sqrt{2}/\sqrt{\pi}$ $\phi_c^{sph} = \sqrt{\pi}/2$	
OSP6+ $\phi_e^{env} = \sqrt[3]{11/32\pi}$ $\phi_e^{sph} = \sqrt[3]{484\pi}/(12+\sqrt{3})$		OSW4++ $\phi_c^{env} = 1/\sqrt{\pi}$ $\phi_c^{sph} = \sqrt{\pi/10}$	

+ 6 orthogonal square pyramids (OSP6) with pyramid angle 18.43º;

++ 4 orthogonal square wedges (OSW4) with wedge angle 60º.

2.5 Solute exchange rate by diffusion

It is readily comprehensible that solute redistribution between solidified phase and liquid, with its further transport by diffusion and convection in the latter, is an important phenomenon for predicting macrosegregation. Yet, it deserves notice that the grain growth rate, floatation/sedimentation velocity and even packing phenomenon can also be affected by solute exchange rate with indirect way, especially under convective flow [22]. As it was explained in chapter 1, solute is segregated when liquid is transformed to solid that leads to appearance of solutal boundary layer along the solid-liquid interface. Then rejected solute is transported by diffusion and convection away from the solid. Consequently, processes to be taken into account in simulation are: (1) rejection of solute to the liquid, (2) capture of solute by moving solid-liquid interface, (3) transport of rejected solute by diffusion and, eventually, convection. Rather often diffusion in the solid phase is neglected although some simulations show importance of so-called “back diffusion” [149]. As presented in Table 2.1, these processes are taken into account with two terms J_{ij}^{v} and J_{ij}^{d}. The former is related to solute exchange rate due to solid-liquid transition while the latter treats diffusion flux. Yet, because of complex shape of solid grain, estimation of thickness of diffusion layer around it is not evident.

In most three-phase models, interdendritic liquid is considered well mixed and its average concentration c_d equals to c_l^* [24,63,117,118]. Alternatively, for example in a model of Wu et al. [23], the average value of c_d is calculated according to the diffusion rate at both *s-d* and *l-d* interfaces, as shown schematically in the right part of Fig. 2.4. Such approach maintains a small gap between c_d and c_l^*, avoiding the fluctuation of solute concentration during abrupt change of temperature, thus enhancing the stability of the model under convective flow.

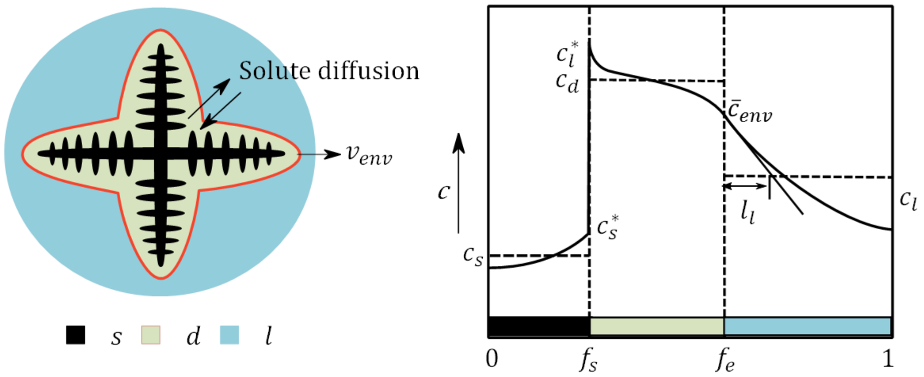

Fig. 2.4 Schematic of grain structure and solute distribution in three-phase model: calculation of solute diffusion flux toward extradendritic liquid requires estimation of diffusion length l_l outside of the grain

The transition from the liquid to the solid phase can be regarded as a combination of the growth of the dendrite, associated with the elongation of the primary dendrite arms at the expense of the extradendritic liquid, and secondary arms' lateral growth during which the interdendritic liquid solidifies. There is a general agreement that dendrite growth is governed by LGK model [145], i.e. its envelope growth velocity v_{env} depends on the constitutional undercooling ahead of the dendrite tip or ahead of a so-called grain envelope. This undercooling corresponds to the local difference between c_l^* and c_l. According to the scheme presented in Fig. 2.4, this difference sharply depends on the solute diffusion length in *l*-phase denoted by l_l. A theoretical solution for l_l exists for diffusive growth of a single grain under steady condition [150] that gives:

$$l_l = \frac{D_l}{v_{\text{env}}} \tag{2.12}$$

where D_l is the solute diffusion coefficient in *l*-phase, and v_{env} is the envelope growth velocity, i.e. velocity of the *l-d* interface related to the grain growth.

This formulation was used by Wu et al. [23] in the equiaxed solidification problem with grain transport and fluid flow despite that it did not take into account the intensification of the diffusive flux by convection. It can be supposed that convection leads to smaller diffusion length, i.e. the transport of the solute from the *d*-phase to the *l*-phase will be intensified thus promoting the enrichment in the *l*-phase. In the two-phase model of Ni et al. [114], the effect of convective flow was accounted for via Sherwood number which should be, however, carefully chosen from experimental data [151]. For two-phase model, there is no distinction between *d*- and *l*-phases, which are commonly referred as a liquid phase, or *f*-phase ($f = l + d$). In this case the diffusion length in *f*-phase is denoted by l_f. In three-phase model of Wang et al. [115], a relative velocity between the liquid and the solid phases was introduced in the expression for the diffusion length. Yet, for weak fluid flow and some range of liquid fraction, both proposed expressions lead to a value of l_l larger the one given by Eq. (2.12). As indicated by Wang et al. [5], generally for non-steady conditions the value of l_l should be smaller than the value given by Eq. (2.12) to keep a continuous enrichment process in the *l*-phase. Appolaire et al.[152] used the boundary layer around an equivalent sphere accounting for the convection as l_l and then limited its maximum value by the length given in Eq. (2.12).

Table 2.3 Diffusion length ahead of the dendrite tip in equiaxed solidification models

Reference	Phases type of grain	Diffusion length l_l or l_f
Rappaz and Thévoz [150]	*l*, *d*, *s* dendritic	$l_l = D_l / v_{tip}$ (no flow)
Ni and Beckermann [114]	*f*, *s* globular	$l_f = \frac{d_s}{2}\left(\frac{1}{1-\left(1-f_f\right)^{1/3}} + \frac{Sc^{1/3}Re^a}{3f_f}\right)^{-1}$
Wang and Beckermann [115]	*l*, *d*, *s* dendritic	$l_l = \frac{d_e}{2+0.865\left(\frac{C_\varepsilon}{f_l}\right)^{1/3}\left(\frac{f_l\lvert\vec{u}_l-\vec{u}_e\rvert}{D_l}\right)^{1/3}}$ with $C_\varepsilon = C_\varepsilon\left(f_l\right)$
Appolaire and Combeau [152]	*l*, *d*, *s* dendritic (single grain in infinite medium)	$l_l = \min\left(d_e / Sh, D_l / v_{tip}\right)$ where $Sh = 2 + 0.6Sc^{1/3}Re^{1/2}$
Wu and Ludwig [148]	*l*, *d*, *s* dendritic	$l_l = \begin{cases} d_e / 2 & \text{globular growth} \\ D_l / v_{\text{env}} & \text{dendritic growth} \end{cases}$

2.6 Motion of liquid and dendrites: “hydrodynamic” phases and drag force

The expression of the momentum exchange or drag force between phases *i* and *j*, denoted as $\overrightarrow{U}_{ij}^{D}$, depends on the choice of phases that represent macroscopic motion in the system. In this way, phases whose velocities may differ may be referred as “hydrodynamic” phases. The phase *j* related to the dendritic grain can be presented only as the solid dendrite in the liquid (Fig. 2.5(a)), or as a union of the solid dendrite and the interdendritic liquid (grain) in the extradendritic liquid (Fig. 2.5(b)). In the latter case, however, a difference in macroscopic velocities between the solid phase, inter- and extradendritic liquid can be taken into account $\vec{u}_d \neq \vec{u}_l$ (Fig. 2.5(c)).

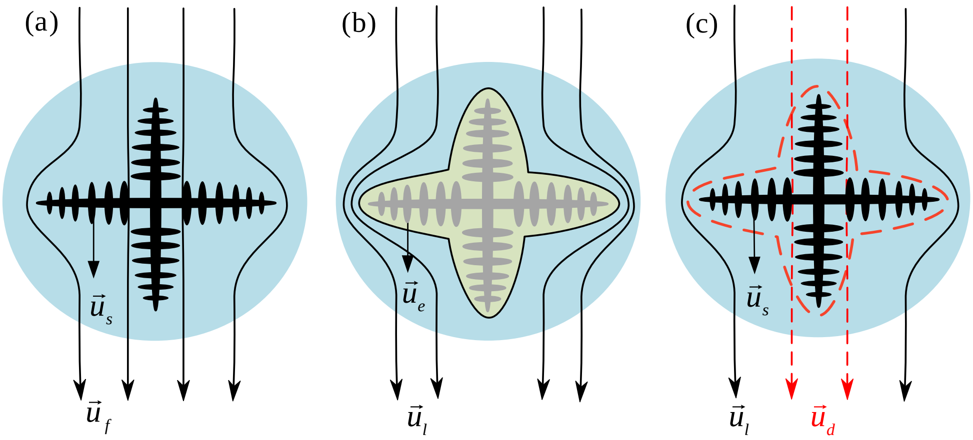

Fig. 2.5 Schematic figure for different unions of phases: (a) solid dendrite (*s*-phase) and liquid phase (*f*-phase), (b) equiaxed grain phase (*e*-phase) and extradendritic liquid phase (*l*-phase), and (c) the solid dendrite (*s*-phase), inter- and extradendritic liquid phases (*d*- and *l*-phases)

Consequently, three-phase model can deal either with three hydrodynamic phases, i.e. velocities of solid, interdendritic liquid and extradendritic liquid could be considered different and require solution of momentum equations for three phases. Yet, in existing three-phase models usually only two hydrodynamic phases are considered since interdendritic liquid is united either with solid phase that gives “grain phase”: $e = (d \cup s)$ or with extradendritic liquid that gives “fluid phase”: $f = (d \cup l)$.

It is customary to treat the momentum exchange while the liquid phase *i* passing through a medium phase *j* using a generalized exchange coefficient K_{ij} and the difference of the phases’ velocities. Below, we review various models for K_{le} which defines exchange coefficient between equiaxed grain and liquid: $\overrightarrow{U}_{le}^{D} = -\overrightarrow{U}_{le}^{D} = K_{le}(\vec{u}_l - \vec{u}_e)$.

Traditionally, there are two approaches to model the interfacial drag between grains and liquid. In the first approach, each equiaxed grain can be treated as a floating particle in bulk liquid, then the total drag force is the sum of the forces acting on all the particles, as seen in Fig. 2.6. In the second approach, the group of grains is regarded as a packed unity, which means that grain boundaries are bonded with neighbors, as seen in Fig. 2.7.

2.6.1 Free floating grains

When grain size and the grain phase fraction is small, the grain movement is dominated by Stokes' law [116]. For a single grain moving in liquid with an equivalent diameter of d_e, it is drawn by liquid with a drag force:

$$\vec{F} = 3\pi\mu_l d_e\left(\vec{u}_l - \vec{u}_e\right) \tag{2.13}$$

Thus the total drag force for all grains in a unit volume can be written as:

$$\vec{U}_{le}^{D} = 3\pi\mu_l d_e n\left(\vec{u}_l - \vec{u}_e\right) = \frac{18 f_e \mu_l}{d_e^2}\left(\vec{u}_l - \vec{u}_e\right) \tag{2.14}$$

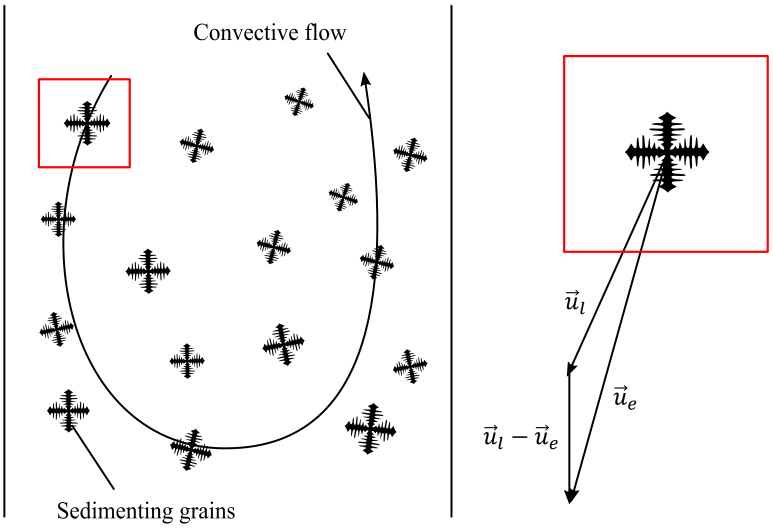

Fig. 2.6 Illustration of interaction of freely moving equiaxed grain with flowing liquid

In practice, in order to consider departures from the idealized single grain settling as described by Stokes' law, a settling ratio C_ε is introduced to account for all factors including the porosity and non-sphericity of the dendrite envelope [116]. Thus a submerged object model is produced as in Eqs. (2.15) and (2.16).

$$\vec{U}_{le}^{D} = K_{le}\left(\vec{u}_l - \vec{u}_e\right) \tag{2.15}$$

$$K_{le} = \frac{18 f_e \mu_l C_\varepsilon}{d_e^2} f_l \tag{2.16}$$

2.6.2 Equiaxed grains network

For high grain fractions, the grain phase behaves like a packed bed regime, a porous medium approach is often adopted, with the permeability K representing a key parameter. According to Darcy's law for flow in packed bed, the drag force must be equal to the pressure gradient that gives:

$$\vec{U}_{le}^{D} = K_{le}\left(\vec{u}_l - \vec{u}_e\right) \tag{2.17}$$

$$K_{le} = \frac{\Delta p}{\Delta x} = \frac{\mu_l}{K} \tag{2.18}$$

The most common semi-empirical model, traditionally used for the permeability of the mushy zone in a columnar dendrite growth, is Kozeny-Carman relation [153] (Table 2.4) which was first proposed by Kozeny and later modified by Carman. The relation was formulated for the pressure drop in a laminar flow passing through a stationary packed column. The latter was treated as a bundle of tangled tubes of various cross-sections. Thus the permeability K can be expressed as:

$$K = \frac{\phi^2 d_e^2 f_l^3}{150 f_e^2} \tag{2.19}$$

where ϕ is the sphericity of the particles in the packed bed. Notice that when using this model, Reynolds number less than approximately 1.0 must be ensured. This relation was used in the model with two phases and globular equiaxed grain developed by Wu et al. [120] and further adopted by the same authors for the drag force between l-phase and e-phase $\overrightarrow{U}_{le}^{D} = -\overrightarrow{U}_{le}^{D}$ in a three-phase equiaxed solidification model [148].

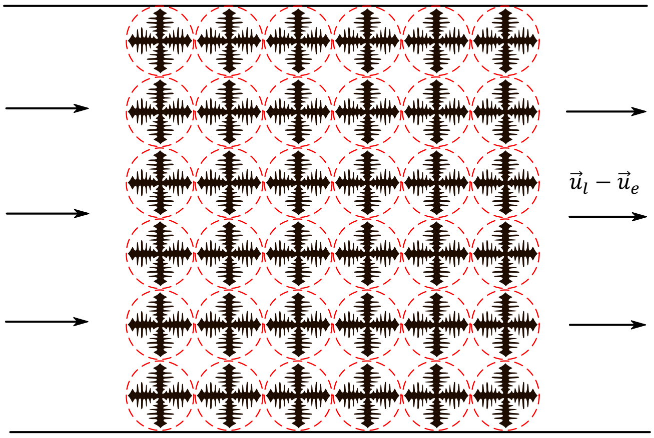

Fig. 2.7 Illustration to equiaxed grain network with liquid passing through it

2.6.3 Unified model

It has been shown that K_{le} can be expressed either via a configuration factor $F_K(f_e, d_e)$ and permeability K of the solidifying phase, or via another configuration factor $F_{CD}(f_e, d_e)$ along with a notion of a drag coefficient C_D, issued from the consideration of a particle moving through the liquid:

$$K_{le} = F_K\left(f_e, d_e\right)\frac{\mu_l}{K} = F_{CD}\left(f_e, d_e\right)C_D\rho_l\left|\vec{u}_l - \vec{u}_e\right| \tag{2.20}$$

In Eq. (2.20) both functions $F_K(f_e, d_e)$ and $F_{CD}(f_e, d_e)$ depend on the fraction of e-phase , and on the characteristic size and sphericity of the particles of that phase. Note that the drag coefficient C_D can take into account the permeability of the e-phase, thus the two configurations indicated above can be equivalent.

Happel [154] unified the two regime through a relationship between pressure and velocity in multiparticle system based on a simple modification of the Navier-Stokes equations of motion and two concentric spheres model. In another equiaxed solidification model with solid and liquid phases (Fig. 2.5(a)), Ni et al. [114] proposed an expression for the drag coefficient C_D which accounted for a modification of the character of the flow during the solidification process. For the low solid fraction ($f_s < 0.5$) the grains were supposed to move rather freely in the liquid, i.e. the interfacial momentum balance between the solid and liquid could be presented using Stokes' law for an individual object moving through the liquid. For $f_s > 0.5$, the solid phase became similar to packed bed, thus the momentum balance can be presented with Kozeny-Carman expression. A similar approach was adopted by Leriche et al. [24] in a three-phase model. For slurry region, they applied the model of Ni et al. [114] but replaced the solid phase fraction with a grain phase fraction; for packed region, a permeability related to secondary arm spacing is applied. In the work of Appolaire et al. [152], the model proposed for the momentum exchange coefficient in a three phase system was verified with the experiment of the sedimentation of the equiaxed grains. Different approximations for these functions and coefficients (see Table 2.4) can be found in literature.

In Wang et al.'s model [115] , the l- and d-phases were united as f-phase: $f_f = f_d + f_l$, yet, the difference between velocities $\vec{u}_d$ and $\vec{u}_l$ was preserved (Fig. 2.5(c)). An expression for the momentum exchange coefficient K_{fs} (Table 2.4) between f- and s-phases was obtained for all solid fractions ranging from 0 to 1 through a general correlation:

$$K_{fs} = \{[\left(1 - f_l\right)K_{ds}]^{\alpha} + \left(K_{le}\right)^{\alpha}\}^{\frac{1}{\alpha}} \tag{2.21}$$

where α is an index to be determined, coefficient K_{ds} is evaluated from secondary arm spacing, coefficient K_{le} was taken from Happel's approach [154] who considered the viscous flow relative to the bed of spherical particles. In this way, the momentum exchange coefficient between liquid and solid can be expressed as:

$$K_{fs} = f_l^2 \frac{\mu_f}{R^2} \frac{\beta_d^2}{\left[(1-f_l)^{\alpha} + (\beta_d / \beta_l)^{2\alpha} \right]^{\frac{1}{\alpha}}} \tag{2.22}$$

where parameters β_d and β_l are referred to [115,116], where the calculation for β_l takes into account the shape factor $C_p(\Phi_e)$ for dendritic grain to have a freedom for estimation of surface area concentration.

Table 2.4 Coefficients and expressions in the equation for the momentum exchange

Reference	Phases type of grain	Coefficients for Eq. (2.20)
Wu et Ludwig [148]	$l, e{=}(d \cup s)$ dendritic	$K_{le} = F_k(f_l, d_e)\frac{\mu_l}{K} = \begin{cases} \frac{180\mu_l f_e^2}{f_l d_e^2} & f_e < f_{sc} \\ \frac{\mu_l f_l^2}{K} & f_e > f_{sc} \end{cases}$
Ni et Beckermann [114]	f, s globular	$K_{fs} = F_{CD}(f_s, d_s) C_D \rho_l \lvert \vec{u}_f - \vec{u}_s \rvert$ $F_{CD} = \frac{3}{4}\frac{f_s}{d_s},\ C_D = \frac{48C_{ke}(1-f_f)}{Re} + C_{ie}$ $Re = \frac{\rho f_f d_s}{\mu_f} \lvert \vec{u}_f - \vec{u}_s \rvert$ $C_{ke} = 0.5, C_{ie} = 7/3$ for $f_f \le 0.5$ $C_{ke}(f_f, Re),\ \ C_{ie}(f_f, Re)$ for $f_f > 0.5$
Apollaire et Combeau [152]	l, d, s dendritic (single crystal in infinite medium)	$F_{CD} = \frac{\rho_f \pi d_e^2}{8},\ C_D = \frac{C_D^{'}}{1.2376\log(\Phi / 0.1556)}$ où $C_D^{'}(Re)$, $(d_e / \sqrt{K})$, Φ is sphericity
Leriche et Combeau [24]	$f{=}(l \cup d), s$ dendritic	Slurry region: $F_{CD} = \frac{3\rho}{4}\frac{f_e}{d_e},\ C_D = \frac{48C_{ke}(1-f_l)}{Re} + C_{ie}$ $C_{ke} = 0.5,\ C_{ie} = 7/3$ for $f_e > 0.5$ $C_{ke}(f_l, Re),\ \ C_{ie}(f_l, Re)$ for $f_e \le 0.5$ Packed region: $K = \frac{\lambda_2^2}{20\pi^2}\frac{f_f^3}{(1-f_f)^2}$

2.7 Packing of equiaxed grains

Packing of equiaxed grains is a unique phenomenon that happens when the equiaxed grains are getting attached to walls of the crucible or impinge other grains that were already attached to boundaries and remain “linked” to the latter.[1] Before getting packed, the grains move freely in melt while after being packed, they are fixed and forms rigid structure similar to columnar grains.

---

[1] In reality equiaxed grains are not attached to the walls, but to small (columnar) grains which initially stay at the wall.

In numerical models this transition is treated with a packing fraction limit, which can be associated either with grain fraction f_p^e or with solid fraction f_p^s, depending on the hydrodynamic phases used in the model (Fig. 2.8). It is of high importance at which fraction grains are getting packed since it determines the intensity of the convective transport between the packed grains and the latter, at large extent, defines final segregation pattern [83]. Besides, once the equiaxed grains get packed, in principal they will be displaced if the solidification shell deforms, thus cause interdendritic liquid flow [155]. In three-phase model the packing is applied to grains while solid fraction inside can be rather small, i.e. the region of interdendritic liquid can be large that assumes further enrichment in the inter- and extradendritic liquid with growth of grains. In two-phase model the packing is applied to the solid phase that means that to have similar situation with large amount of liquid between blocked solid the packing has to be performed earlier. A widely applied value for f_p^e is 0.637 [24,148,156], which approaches the close-packed density given by Scott et al. [157]. However, this value may not be correct for f_p^s in a two-phase model. Olmedilla et al. [158] found that for nonconvex grain shape, value of f_p^s was around 0.38. Krane et al. [83] found that in two-phase solidification model, lower value of f_p^s predicted lighter segregation; results with $f_p^s = 0.1$ were more accord with experimental results.

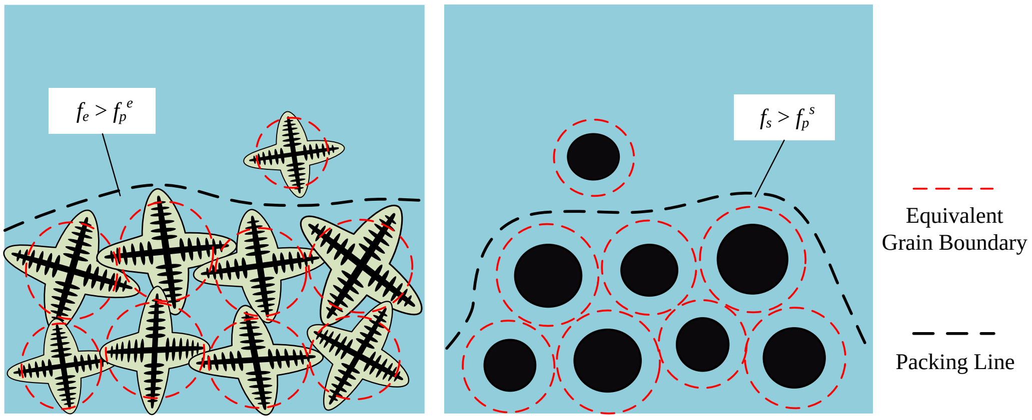

(a) (b)

Fig. 2.8 Schematic figure for grain packing for three-phase model (a) and two-phase model (b)

It is assumed that for a freely moving equiaxed grain whose volume fraction increases to packing fraction limit, its velocity should drop to zero, which numerically can be realized in various ways. Wu et al. [23,121] adopted an effective viscosity μ_e for the phase contains equiaxed grains. When f_e approaches f_p^e, the μ_e increased rapidly to infinity. Založnik et al

[84] neglected the viscous term in equiaxed solidification model, however, the velocity of the phase was forced to be zero once the condition $f_s > f_p^s$ was fulfilled. Plotkowski et al. [159] proposed a smoothing procedure by introducing a transition function:

$$\alpha_t = 1 - 0.5(1 - \tanh\left[100\left(f_p^s - f_s\right)\right] \tag{2.23}$$

According to Eq. 2.23, α_t decreases from 1 to 0 when solid fraction approaches packing limit value. In this way the grain packing phenomenon happened during an interval of solid fraction (Eq. 2.24), rather than a sudden transition at a specific fraction. The same authors [160] also proposed a velocity based packing scheme to account for the effect of the local velocity field on grain packing process.

$$\vec{u}_s = \alpha_t\left(\vec{u}_f + f_s\left(\left(\rho_s - \rho_f\right)\vec{g} - \nabla P\right) / K_{ls}\right) \tag{2.24}$$

2.8 Conclusion

The history and theory of volume average model have been introduced. It can be concluded that volume average method has prominent advantage in describing multiscale phenomena than other existing methods. Volume average solidification model can be easily expanded to realize new functions. Some important issues in volume average modeling have been comprehensively reviewed including nucleation rates, phase transition rates, solute transfer rates, momentum exchange coefficient, and grain packing method. Each of them can have significant effect on modeling results. It is noticed that most of these issues are tightly related to equiaxed solidification modeling. The various choices for solution of these issues give large uncertainty for calculation. Investigation on the role of each issue is critical step before developing an appropriate numerical model. Next chapter will be dedicated to this topic.

Chapter 3 Modeling for equiaxed solidification and addressing key issues

Equiaxed grain structure has better homogeneity than columnar one, therefore, a larger equiaxed grain region is preferred during casting production. Under the action of electromagnetic stirring, the proportion of equiaxed grains in the solidification structure increases significantly, and behavior of equiaxed grains obviously affects the distribution of solute concentration. Although various volume average models have been developed and applied in industry, the reliability of results issued from simulation of equiaxed solidification remains questionable. Compared with columnar one, equiaxed solidification invloves more sophisticated mechanisms and its modeling requires more parameters while numerical predictions of macrosegregation are quite sensitive to selection of parameters. Therefore, a specific investigation on each parameter for equiaxed solidification modeling is necessary. In chapter 2 macroscopic models based on volume averaging procedure were outlined with analysis of key problems arising in application of the model that include:

- Description of nucleation process;
- Calculation of diffusion length;
- Description of momentum exchange between phases;
- Treatment of grains' packing.

In this chapter with addressing key issues mentioned in chapter 2 we make a three-phase solidification model adapted to a case with presence of electromagnetic force. In section 3.1, the system of equations in model is derived. Microscopic scale phenomena are incorporated into macroscopic mass, momentum, energy and solute transport equations. In section 3.2, a thorough and detailed discussion is made regarding the choice of calculation of momentum exchange coefficient. A new packing method is developed aimed to adapt treatment of the phenomenon to moderate convective flow. In section 3.3 we discuss the effect of diffusion length in the extradendritic liquid with convective flow on simulation results. Demonstration is made for a unique grain and further for solidification of an ingot in benchmark configuration. Finally, the whole model is revised and a two time step solution algorithm is provided.

3.1 Coupling of microscale processes and macroscale transport

Among various possibilities for description of solidification accounting for kinetics of dendrite growth (see section 2.4) we choose a presentation based on utilization of the concept of envelope as an imaginary surface which encloses a solid dendrite skeleton (*s*-phase) with some amount of liquid between its arms, so-called interdendritic liquid (*d*-phase). The phase within the envelope, which unifies solid and interdendritic liquid, is considered as an equiaxed grain (*e*-phase) and the liquid outside of the envelope is considered to be extradendritic liquid (*l*-phase). According to volume average method, each of these phases is represented with its volume fraction, i.e. with f_s for solid and f_d,f_l for inter- and extradendritic liquid, respectively. Fraction for grain phase is given as $f_e = f_s + f_d$ and summation rule $f_e + f_l = 1$ fulfills. It is supposed that interdendritic liquid moves together with solid skeleton, i.e. these phases share the same velocity field $\vec{u}_e$ which is different from the velocity $\vec{u}_l$ related to the extradendritic liquid. Consequently, at macroscale equations for momentum conservation are required only for grain and for extradendritic liquid and in case of laminar flow they are given with Navier-Stokes equations. Conditions for grain packed region and unpacked region should be distinguished. If both phases can freely move, the momentum conservation equations are given by Eq. (3.1) and Eq. (3.2) for liquid and grain phases, respectively. If the grain phase get packed, the equation of motion for the grain phase reduces to $\vec{u}_e \equiv 0$ (instead of Eq. (3.2)) while motion of liquid is still described by Eq. (3.1). The algorithm which defines if grain phase should be considered as freely moving or packed is described in section 3.2.2.

$$\begin{aligned}\frac{\partial\left(f_l\rho_l\vec{u}_l\right)}{\partial t}+\nabla\left(f_l\rho_l\vec{u}_l\vec{u}_l\right)=-f_l\nabla P+\nabla\left[\mu_l f_l\left(\nabla\vec{u}_l+\left(\nabla\vec{u}_l\right)^T\right)\right]\\+\vec{F}_{Bl}+\vec{F}_{El}+K_{le}\left(\vec{u}_e-\vec{u}_l\right)\end{aligned}\tag{3.1}$$

$$\begin{aligned}\frac{\partial\left(f_e\rho_e\vec{u}_e\right)}{\partial t}+\nabla\left(f_e\rho_e\vec{u}_e\vec{u}_e\right)=-f_e\nabla P+\nabla\left[\mu_e f_e\left(\nabla\vec{u}_e+\left(\nabla\vec{u}_e\right)^T\right)\right]\\+\vec{F}_{Be}+\vec{F}_{Ee}+K_{le}\left(\vec{u}_l-\vec{u}_e\right)\end{aligned}\tag{3.2}$$

In Eq. (3.1) $\vec{F}_{Bl}$ represents bouyancy force which is treated with Boussinesque approximation for extradendritic liquid accounting for thermal and solutal expansion:

$$\vec{F}_{Bl}=f_l\rho_l\vec{g}\left[\beta_T\left(T_{ref}^b-T_l\right)+\beta_c\left(c_l^{ref}-c_l\right)\right]\tag{3.3}$$

Similar term for grain phase takes Boussinesque approximation for interdendritic liquid and contains additional term for solid phase:

$$\vec{F}_{Be}=f_d\rho_l\vec{g}\left[\beta_T\left(T_{ref}^b-T_l\right)+\beta_c\left(c_l^{ref}-c_d\right)\right]+f_s\left(\rho_s^b-\rho_{ref}\right)\vec{g}\tag{3.4}$$

Then, volume forces $\vec{F}_{El}$ and $\vec{F}_{Ee}$ correspond to electromagnetic force whose calcualtions depend on actual physical problem. This term should be set to zero if no electromagnetic force is applied. Choice for the model of calculation of momentum exchange coefficient K_{le} is presented in section 3.2.1.

We accepted two different options for calculation of dynamic viscosity for grain phase μ_e. In one case characterised with rather weak flow (confer section 3.3.3) we opted for the simple choice $\mu_e = \mu_l$. However, for the case with electromagnetic stirring (confer chapter 4) relation proposed in [114] was chosen:

$$\mu_e = \frac{\mu_l}{f_e}\left[\left(1 - f_e / f_p^e\right)^{-2.5 f_p^e} - \left(1 - f_e\right)\right] \tag{3.5}$$

Solutions of Navier-Stokes equations (3.1) and (3.2) require knowledge of phase fraction which are derived from solution of equations given below. Yet, let us consider first the energy conservation equations that are also written for two phases, i.e. extradendritic liquid and grain phases:

$$\frac{\partial\left(f_l \rho_l h_l\right)}{\partial t} + \nabla\left(f_l \rho_l \vec{u}_l h_l\right) = \nabla\left(\kappa_l f_l \nabla T_l\right) + H^*\left(T_e - T_l\right) + M_{ds} L f_l - M_{le} h^* \tag{3.6}$$

$$\frac{\partial\left(f_e \rho_e h_e\right)}{\partial t} + \nabla\left(f_e \rho_e \vec{u}_e h_e\right) = \nabla\left(\kappa_e f_e \nabla T_e\right) + H^*\left(T_l - T_e\right) + M_{ds} L f_e + M_{le} h^* \tag{3.7}$$

with

$$h_l = \int_{T_{ref}^h}^{T_l} c_p^l dT + H_{ref}, \quad h_e = \int_{T_{ref}^h}^{T_e} c_p^e dT + H_{ref}$$

In Eqs. (3.6) and (3.7), the term $H^*(T_e - T_l)$ taken with different sign is related to energy exchange between phases. It is supposed to be inifitely fast that is modeled with a large value for exchange coefficient H^*. However, tested simulations showed that too large value of H^* will overwhelm the contribution of other terms in the energy conservation and causes the divergence of the numerical simulation [120]. Terms $M_{ds}Lf_l$ and $M_{ds}Lf_e$ represent heat release during transformation of liquid phase into solid (or heat absorption during transformation of solid to liquid) and are related to amount of transited mass M_{ds} whose calcualtion require consideration of processes at microscale as discussed below. Finally, the last term which is similar to both equations, $M_{le}h^*$, is related to phase transition between extradendritic liquid and grain, $M_{le}h^*$ takes value of h_l or h_e depending on whether solidification or melting occurs. Calculation of M_{le} is discussed below.

System of transport equations contains also those for intrinsic averaged concentration c_i ($i = s, l, e$):

$$\frac{\partial\left(f_l \rho_l c_l\right)}{\partial t} + \nabla \cdot \left(f_l \rho_l \vec{u}_l c_l\right) = -J_{le}^d - J_{le}^v - J_\Phi \tag{3.8}$$

$$\frac{\partial\left(f_e\rho_e c_e\right)}{\partial t}+\nabla\cdot\left(f_e\rho_e\vec{u}_e c_e\right)=J_{le}^{d}+J_{le}^{v}+J_{\Phi} \tag{3.9}$$

$$\frac{\partial\left(f_s\rho_s c_s\right)}{\partial t}+\nabla\cdot\left(f_s\rho_s\vec{u}_e c_s\right)=J_{ds}+J_{\Phi} \tag{3.10}$$

Note that transport of concentration in the solid phase occurs with velocity associated with grain fraction. Solute exchange between phases given by terms J_{le}^{d}, J_{le}^{v}, and J_{ds} is related to molecular diffusion as well as to amount of solute entrained with phases transformation and requires consideration of processes at microscale as well as terms M_{ds} and M_{le} mentioned above. J_{Φ} is particular flux related to nucleation process during which some amount of grain and solid fraction appears in the liquid.

The system of macroscopic equations is complemented with mass conservation equations:

$$\frac{\partial\left(f_l\rho_l\right)}{\partial t}+\nabla\cdot\left(f_l\rho_l\vec{u}_l\right)=-M_{le}-M_{\phi} \tag{3.11}$$

$$\frac{\partial\left(f_e\rho_e\right)}{\partial t}+\nabla\cdot\left(f_e\rho_e\vec{u}_e\right)=M_{le}+M_{\phi} \tag{3.12}$$

$$\frac{\partial\left(f_s\rho_s\right)}{\partial t}+\nabla\cdot\left(f_s\rho_s\vec{u}_e\right)=M_{ds}+M_{\phi} \tag{3.13}$$

The grain number density n is transported with velocity of grain phase and corresponding conservation equation is:

$$\frac{\partial n}{\partial t}+\nabla\cdot\left(n\vec{u}_e\right)=N_{\phi} \tag{3.14}$$

where source term N_{ϕ}, namely the nucleation rate, is defined in Eq. (3.26).

To obtain expressions for terms related to mass transport between phases and to solute exchange between them, consideration of a unique grain is convenient. The scheme for an equiaxed grain (Fig. 3.1) shows the distribution of intrinsic concentrations c_l, c_d, and c_s that are associated with extra- and interdendritic liquid and solid phases. In addition to them, averaged concentrations c_l^* and c_s^* are associated with solid-liquid interface for adjacent liquid and solid, respectively (shown in the scheme with solid red and grey lines, respectively). These concentrations are supposed to correspond to liquidus and solidus concentration defined by thermodynamic temperature of the grain and mutually related through the solute partition coefficient k: $c_l^*=(T_l-T_0)/m$ and $c_s^*=kc_l^*$.

It should be stressed that envelope is defined by tips of primary and secondary arms of dendrite but does not coinside with real solid-liquid interface. Because of this another average concentration associated with envelope is introduced in the model and is denoted as $\overline{c}_{env}$. The envelope concentration cannot be obtained from the phase diagram but is determined by the interfacial solute balance, as proposed by Wu et al. [121]:

$$\rho_l \frac{D_l}{l_l}\left(\bar{c}_{env} - c_l\right) + \rho_d \frac{D_d}{l_d}\left(\bar{c}_{env} - c_d\right) = 0 \tag{3.15}$$

Assuming the inter- and extradendritic liquid phases have equal solute diffusion coefficient $D_l = D_d$ and density $\rho_l = \rho_d$, the envelope concentration can be defined based on concentration in the inter- and extradendritic liquid and diffusion lengths in corresponding phases:

$$\bar{c}_{env} = \frac{l_d c_l + l_l c_d}{l_d + l_l} \tag{3.16}$$

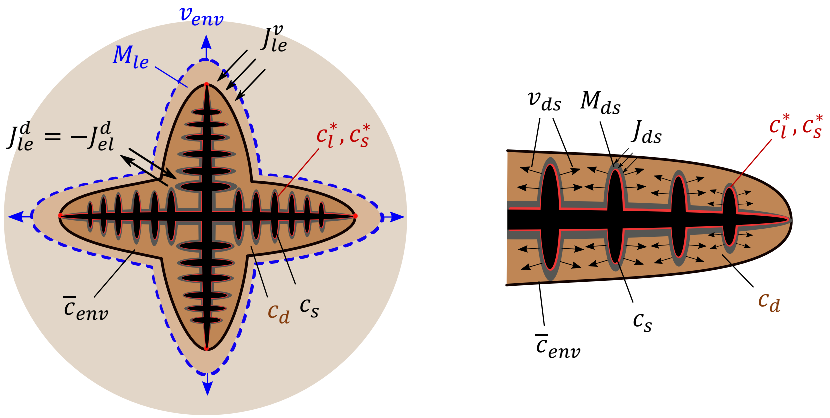

Fig. 3.1 Schematic of solute transport due to growth of envelope and solidification of interdendritic liquid

Similar to approaches adopted elsewhere [40,121], solidification process is seen to be consist of two processes: expansion of the envelope which represents grain growth, i.e. elongation of its primary (and secondary) arms and “thickening” (or expansion) of the solid skeleton with transition of liquid to solid. Relation between concentration c_l^* and concentration in the extradendritic liquid c_l, which corresponds to the solutal undercooling ahead of dendrtie tips defines speed of grain growth V_g according to LGK model [145]:

$$V_g = \frac{D_l m_l \left(\kappa - 1\right) c_l^*}{\pi^2 \Gamma} \left[\frac{c_l^* - c_l}{c_l^* \left(1 - k\right)}\right]^2 \tag{3.17}$$

Yet, this velocity corresponds to tips of dendrite arms. Since in the model grain growth is presented with expansion of the envelope, effect of the shape of the latter is introduced with a shape factor ϕ_M and so-called envelope growth velocity is presented as:

$$v_{env} = \phi_M V_g \tag{3.18}$$

Amounts of mass due to envelope expansion is defined by surface area concentration of envelope and in case of solidification is calculated with velocity of envelope displacement:

$$M_{le} = \rho_l S_e^M v_{env} \tag{3.19}$$

Then, amount of solute transited to the interdendritic liquid from extradendritic liquid due to envelope enlargement is defined through concentration at the envelope introduced above:

$$J_{le}^v = M_{le}\bar{c}_{env} \tag{3.20}$$

Along with "kinematic" transport of solute, molecular diffusion flux also exists between inter- and extradendritic liquid and is defined rather straightforward:

$$J_{le}^d = -\frac{\rho_l S_e^J D_l\left(\bar{c}_{env} - c_l\right)}{l_l} \tag{3.21}$$

Yet, estimation of value of characteristic diffusion length l_l can be done in different manner as it was indicated above. Below in section 3.3 discussion related to definition of l_l is continued and its crucial effect is demonstrated in modeling of a well-known experiment in configuration proposed by Hebditch and Hunt [27].

Expansion of solid skeleton can be treated as solidification of interdendritic liquid. Due to large interface area concentration and narrow space in interdendritic region, the value of c_d can be very close to *s-d* interface solute concentration (liquidus concentration) c_l^*. It should be noted that the interdendritic liquid has a different solute concentration c_d from extradendritic one c_l. In diffusion governed models [111,161], complete solute mixing in interdendritic liquid is often assumed which gives $c_d = c_l^*$ to simplify the system of equations. However, it should be noted that such assumption severely neglected geometrical structure of dendrites. Indeed, the solute transfer and phase transition in interdendritic liquid should be calculated explicitly according to the diffusion-governed growth kinetics at solid-liquid interface [107,148]. Different from the tip growth model for grain envelope, the undercooling in interdendritic liquid is rather small. In this condition, it is more appropriate to calculate the interface movement velocity through interfacial solute balance (Eq. (3.22)) at *s-d* interface instead of LGK model.

$$\left(c_l^* - c_s^*\right) v_{ds} S_s = \frac{D_l S_s\left(c_l^* - c_d\right)}{l_d} + \frac{D_s S_s\left(c_s^* - c_s\right)}{l_s} \tag{3.22}$$

where S_s is *s-d* interface area concentration; l_s is diffusion length in solid skeleton; D_s is solute diffusion coefficient in solid phase. By nelecting solute diffusion in the solid, the third term in Eq. (3.22) vanish, so the *s-d* interface movement velocity is given as:

$$v_{ds} = \frac{D_l\left(c_l^* - c_d\right)}{l_d\left(c_l^* - c_s^*\right)} \tag{3.23}$$

Similarly, M_{ds} and J_{ds} represent the amounts of mass and solute transported from interdendritic liquid to solid due to the motion of the interface between the two phases and in case of solidification are calculated as:

$$M_{ds} = \rho_s \frac{2 f_d}{\lambda_2} v_{ds} \tag{3.24}$$

and

$$J_{ds} = c_s^* M_{ds} \tag{3.25}$$

To conclude consideration of case of solidifcation we have to consider terms related to nucleation phase. It is supposed in the model that grains appear in the bulk volume due to nucleation which happens instantaneously with a nucleation rate N_Φ once the local constitutional undercooling is higher than a predefined one ΔT_{nucl}.

$$N_\phi = \begin{cases} f_l\left(n_{\max} - n\right)/\,\mathrm{d}t & \text{if } \Delta T > \Delta T_{\text{nucl}} \text{ and } n < n_{\max} \\ 0 & \text{else} \end{cases} \tag{3.26}$$

It is assumed that nucleation can still happen in the cell where some amount of grains already exist if the grain number density is less than maximal value. Rather small value of ΔT_{nucl} of order of several degrees implies heterogeneous nucleation. Nucleation makes the number density of the grains n non zero (or increase it), and a small fraction of the solid phase appears due to mass transition from liquid to solid M_Φ accompanied by the corresponding solute flux J_Φ, definition of both these values is rather straightforward:

$$M_\Phi = N_\phi \rho_l \pi d_0^3 / 6 \tag{3.27}$$

$$J_\Phi = M_\phi c_s^* \tag{3.28}$$

where d_0 represents initial grain diameter that was usually assumed as 10^{-6} m [85,120]. Further the grains can be dragged by the flow or their motion can be affected directly by gravity and electromagnetic force. It should be stressed that electromagnetic force acting on the liquid can cause strong flow due to which equiaxed grains can be transported to liquid overheated compared to themselves. That means that remelting process should be taken into account.Wu et al. [120] put up with a solidification/melting model considering solid transport and grain nucleation/destruction, however, the model does not consider the behavior of interdendritic liquid. In Wu's model, the remelting rate was driven by a difference between c_l^* and c_l and is regulated with an adjustable coefficient g_α. This idea is applied to our three-phase model: $M_{le} = \rho_l S_e g_\alpha (c_l^* - c_l)$, $M_{ds} = f_s M_{le} / f_e$.

3.2 Momentum exchange model

In present three-phase model, only two momentum equations are considered (extradendritic liquid phase and equiaxed grain phase), which means that solid phase and interdendritic liquid phase are treated as a unity and will move together all the time. The velocities for the two “hydrodynamic” phases are calculated independently based on their own momentum conservation equations and buoyancy force. It has been stated in chapter 2 that a momentum exchange coefficient K_{le} is used to relate drag force and relative velocity: $\overrightarrow{U}_{le}^{D} = -\overrightarrow{U}_{le}^{D} = K_{le}(\vec{u}_l - \vec{u}_e)$, and the existed models were reviewed. In this section we choose representative formulas for K_{le} and discuss the characteristic of each formula through comparison. Further, the grain packing method is improved for convective condition.

3.2.1 Calculation of momentum exchange coefficient

As listed in Table 2.4 and discussed in section 2.6, the most commonly used model, traditionally used for the permeability of the mushy zone in a columnar dendrite growth, is Kozeny-Carman relation [153]. In equiaxed model Kozeny-Carman relation was also used [115] along with Happel model [154]. Ni and Beckermann [114] also constructed a model using piecewise function. The three formulas are reviewed below with Stokes’ law for comparison. Detailed definition of each parameter can be seen in section 2.6.

（1）Stokes’ law: $$K_{le} = \frac{18 f_e \mu_l}{d_e^2} \tag{3.29}$$

（2）Kozeny-Carman model: $$K_{le} = \frac{150\mu_l}{\phi^2 d_e^2} \frac{?f_e^2}{f_l^3} \tag{3.30}$$

（3）Ni-Beckermann model: $$K_{le} = \frac{3 f_e \rho C_D}{4 d_e} \left| \vec{u}_l - \vec{u}_e \right| \tag{3.31}$$

（4）Happel model: $$K_{le} = 18 f_l^2 f_e \frac{\mu_l}{d_e^2} \frac{2 + 4/3 f_e^{5/3}}{2 - 3 f_e^{1/3} + 3 f_e^{5/3} - 2 f_e^2} \tag{3.32}$$

In the equations above, ϕ is the sphericity of equaixed grain, d_e is the grain diameter whose calculation needs grain number density *n*, the drag coefficient C_D in Ni-Beckermann model is expressed as:

$$C_D = 48 C_{ke} \left(1 - f_f\right) / Re + C_{ie} \tag{3.33}$$

where

$$C_{ke} = \begin{cases} \dfrac{25}{6} & f_l \le 0.5 \\ \dfrac{1}{2}\left(\dfrac{f_l^3}{1 - f_l}\right) 1 + \dfrac{4.7\left(1 - f_l\right)}{1 - 1.83\left(1 - f_l\right)} & f_l > 0.5 \end{cases} \tag{3.34}$$

$$C_{ie} = \begin{cases} \dfrac{7}{3} & f_l \le 0.5 \\ \dfrac{24\left(10^E - 1\right)}{Re\left[1 - 0.9\left(f_l - 0.25\right)^{\frac{1}{3}}\left(1 - f_l\right)^{\frac{2}{3}}\right]^3} & f_l > 0.5 \end{cases} \tag{3.35}$$

and

$$E = 0.261\mathrm{Re}^{0.369} - 0.105Re^{0.431} - \frac{0.124}{1 + \left(\log_{10} Re\right)^2} \tag{3.36}$$

$$Re = \frac{\rho f_l d_g}{\mu_l}\left|\vec{u}_l - \vec{u}_e\right| \tag{3.37}$$

A direct comparison of the dimensionless momentum exchange coefficients $K_{le}d_e^2/\mu_l$ as a function of solid fraction was performed using $\mu_l = 0.001$ kg m^{-1}s^{-1} and $n = 2.4\times10^8$ m^{-3} for Eq.(3.29)-(3.32). Results, presented in Fig. 3.2, demonstrate the increase of exchange coefficient with grain fraction in each case and the difference beween them could be thought to be minor. Yet, a more straightforward comparison can be made with the sediment velocity u_{sed} of grains falling in a stationary liquid.

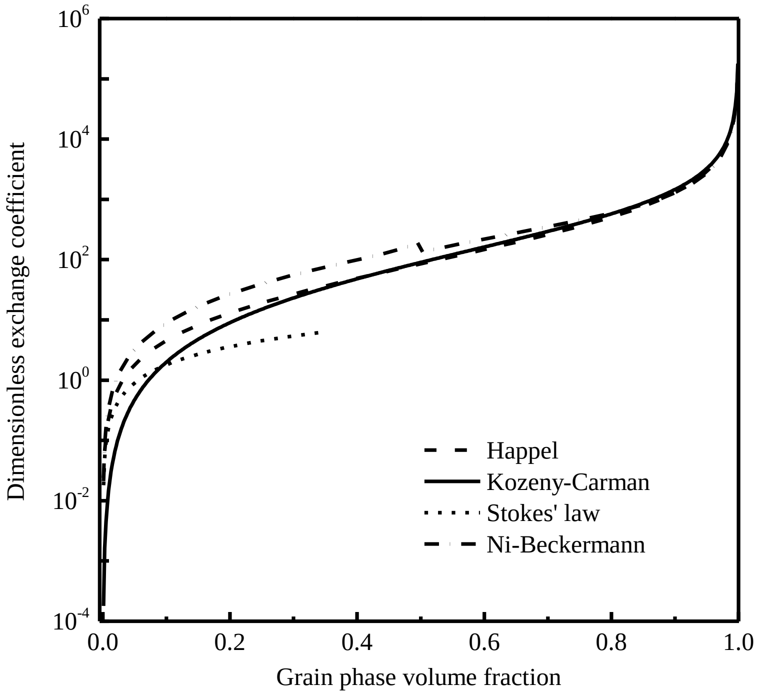

Fig. 3.2 Comparison of dimensionless momentum exchange coefficient between *l*- and *e*- phases

If the density of grain phase is larger than liquid phase, the grain tends to sediment, i.e. move downward to the bottom. The difference in velocity between the liquid and grain phases cannot be enlarged persistently because of the existence of drag force, which will increase with the increase of relative velocity between the two phases (Fig. 3.3). In a case of stationary liquid, velocity of grain $\vec{u}_e$ will increase from zero until the balance between drag force and gravity is realized:

$$\vec{U}_{le}^{D} = K_{le}\left(\vec{u}_e - \vec{0}\right)V_0 = f_e\left(\rho_s - \rho_l\right)V_0\vec{g} \tag{3.38}$$

where V_0 is the unit volume.

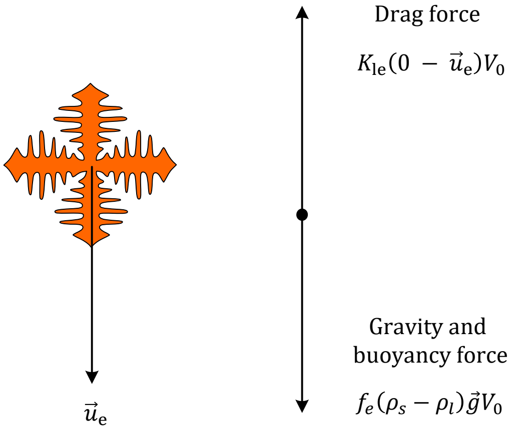

Fig. 3.3 Scheme representing forces acting on an equiaxed grain in stationary liquid

Thus a sedimentation velocity of grain can be explicitly defined as:

$$u_{sed} = f_e\left(\rho_s - \rho_l\right)g / K_{le} \tag{3.39}$$

We estimated this sedimentation velocity for different grain fractions using the density difference $\Delta\rho = 140$ kg m^{-3}, gravity constant $g = 9.81$ m s^{-2}.

Fig. 3.4 presents the results obtained with the three models, while the velocity calculated with the classical Stokes' drag force is also included for comparison. For a large grain fraction region, i.e. $f_e > 0.75$, the Happel model, Ni-Beckermann model, and Kozeny-Carman model predict similar sedimentation velocity, which approaches zero as the amount of liquid decreases. However, for grain fraction approaching zero, the sedimentation velocity calculated with the Happel model and Ni-Beckermann model also moves to zero, similar to the case with the Stokes' law, while use of the Kozeny-Carman equation gives a velocity value moving to infinity. Although discrepancy of Kozeny-Carman equation only occurs when grain fraction is small, it shows disadvantage in description for movement of nuclei and tiny grains. Happel model and Ni-Beckermann model provide good approximation both for the free-particle regime, also including very small nuclei, and the packed bed regime. However, the two models show large difference for range of grain fraction between 0 and 0.75. In this study, Happel model is preferred considering its continuity and explicit physical base. It should be noted that the model used by Wang et al. [115] (Table 2.4) is reduced to the Happel model if the partition of the inter- and extradendritic liquid phases is not considered.

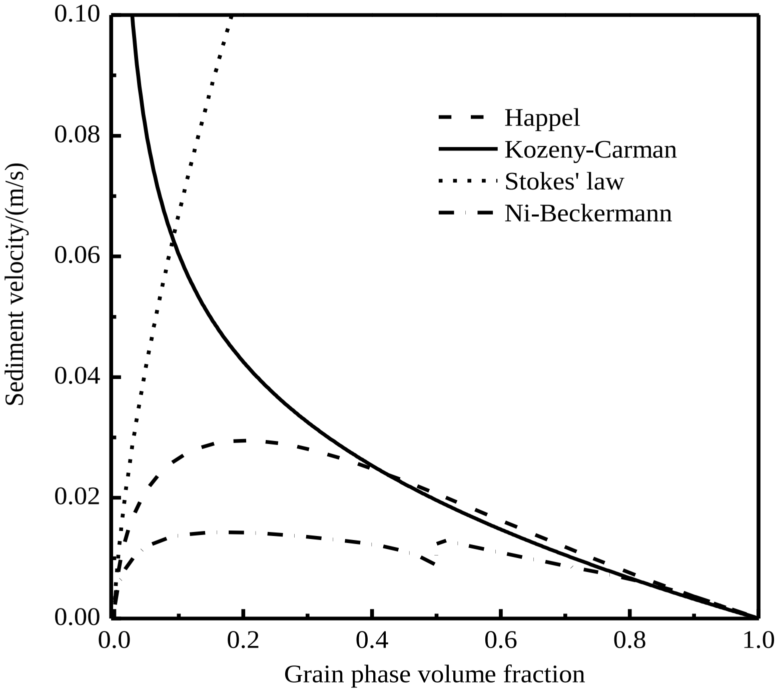

Fig. 3.4 Comparison of sedimentation velocity calculated according to the Eq. 3.39 with different models for momentum exchange coefficient given by Eqs.(3.29-3.32)

In above Kozeny-Carman model, the permeability is calculated according to grain diameter. In practice, when grains get packed, the dendrite arms will attach to each other, thus the structure of inter-grain space gets more complex and characteristic length should be estimated according to grain number density and dendrite arm spacing [85]. Therefore, in most model [84,121,156], different formulas for K_{le} were applied for packed and unpacked region. In present model, for free floating region, i.e. $f_e < f_p^e$, the momentum exchange coefficient between the liquid and grain phases is calculated with the Happel's model [154], which fits well with Stokes' law when $f_e \to 0$. It is supposed that viscosity assigned to grain phase increases gradually with grain growth as was evoked in [113,120], yet, at small grain fraction $\mu_e = \mu_l$. When $f_e \geq f_p^e$, the grain phase is packed, i.e. it becomes immovable while the permeability of the grain fraction is changed and it can be evaluated by Kozeny-Carman equation. However, similar to ref. [84,121,156], a constant characteristic length number d_k is chosen. The flow partition effect between the inter- and extradendritic liquid is neglected. Fig. 3.5 provides values of dimensionless coefficient for full range of grain fraction with different characteristic length d_k.

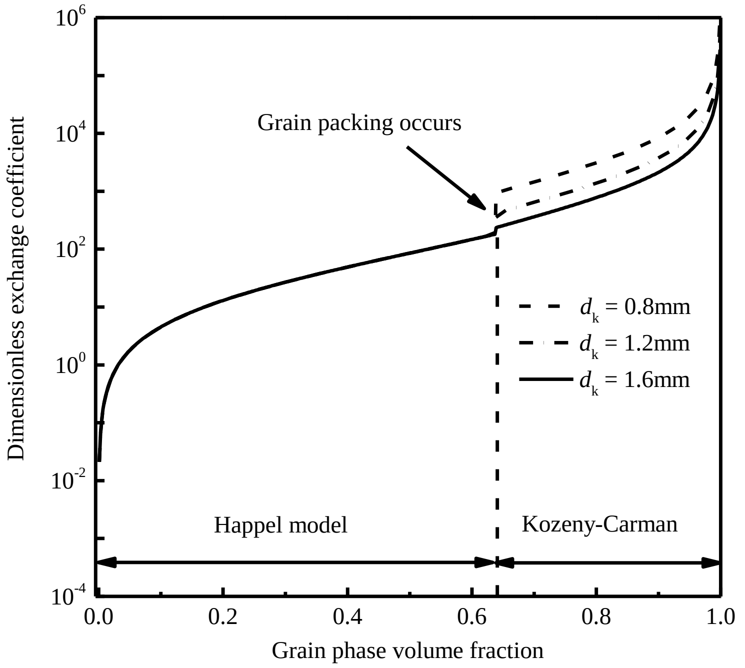

Fig. 3.5 Dimensionless momentum exchange coefficient with different characteristic length

3.2.2 Grain packing criterion

The shape of the dendritic grain is simplified by an “equivalent sphere” when accounting for the momentum interaction between grain and surrounding liquid. This “equivalent sphere” has the same volume as the “natural” contour around the primary and secondary dendrite tips of the grain. In this configuration, it is accepted that the equiaxed grains get packed when its fraction surpasses packing limit value $f_p^e = 0.637$ [24,148,156], which is an approximation of the closest packing fraction of randomly arranged monodisperse spheres. It should be understood that solid fraction at this moment of packing can be small. For two-phase model the packing is applied to the solid phase, hence smaller limit fraction should be applied and accepted to be in the range $f_p^s = 0.1 \sim 0.5$ [83,160,162].

A widely used packing condition is that f_e is higher than f_p^e. This represents mechanical interaction between grains and implies that solidification is initiated at the boundary and continues more or less uniformly. In order to adapt this idea to the case of a rather strong convective flow due to electromagnetic stirring, a new grain packing method has been developed and applied in simulation. It is supposed that to be packed grains should have an immovable neighbor upon which they can attach. A grain packing status marker i_p is adopted to identify whether or not the grains in a calculation cell should be packed. During initialization, a zero value is assigned to i_p in each calculation cell. If the cell of interest is adjacent to the wall or has at least one packed neighboring cell, its i_p value is changed to 1. For the cell marked with $i_p = 1$, once $f_e \geq f_p^e$ is satisfied, the grains get packed and the marker i_p is set to 2, which means that the grain phase motion must be stopped. This procedure is repeated at each time integration step. The critical value of fraction for the grain packing is set to be 0.637 for benchmark simulation (chapter 3 and 4) as ref. [148] and to be 0.4 for ingot solidification (chapter 5) as ref. [40].

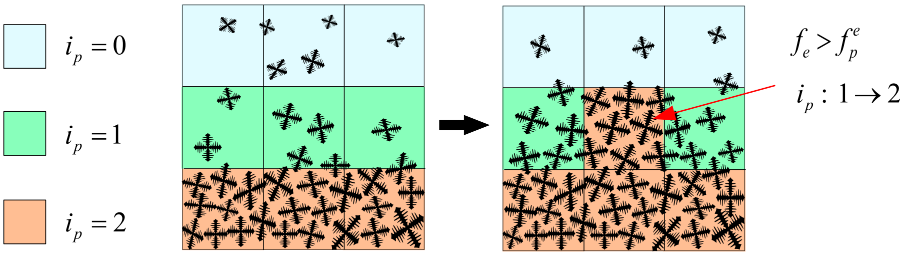

Fig. 3.6 Schematic diagram of the grain packing method

3.3 Effect of diffusion length model on solidification

Determination of diffusion length, especially the diffusion length around the envelope in the extradendritic liquid l_l, drastically affects numerical results as it links phase transition with the enrichment of the extradendritic liquid. According to the equation for the solute flux in (Eq. 3.21) and illustration in Fig. 3.7, if l_l decreases, the solute flux through the envelope intensifies, and the concentration difference between the inter- and extradendritic liquids decreases if the average concentration is conserved within the volume corresponding to the final grain size. Consequently, a smaller solutal undercooling ahead of the dendrite tip leads to a smaller dendrite growth rate. This means that the solid fraction within grain phase f_s^e increases and could promote the sedimentation or floatation of equiaxed grains. Different methods, proposed for calculation of l_l, are discussed above in the introduction, and provided in Table 2.3. All of them emphasize several factors, namely dendrite tip velocity, current and final diameter of the grain (or envelope), and relative velocity between the grain and the liquid phases. Below, we make comparison between several formulas for diffusion length through zero-dimension calculation and numerical simulation for benchmark solidification.

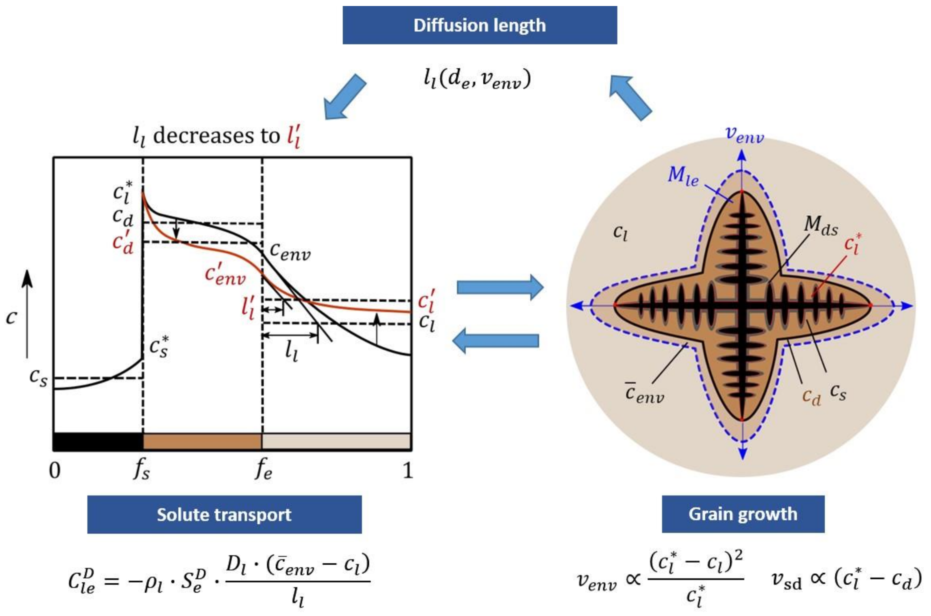

Fig. 3.7 Schematic of relationship between diffusion length, solute transport and grain growth in three-phase equiaxed solidification model

3.3.1 Zero dimension solidification case

Four formulas to be compared are presented in Eqs. (3.40) through (3.43), which are cited from references or constructed based on our knowledge. According to these equations, four calculation cases are defined.

$$l_l = \frac{D_l}{v_{env}} \tag{3.40}$$

$$l_l = \min\left[\frac{d_e}{2}, \frac{D_l}{v_{env}}\right] \tag{3.41}$$

$$l_l = \min\left[\frac{d_e}{2}\left(\frac{1}{1-(1-f_l)^{\frac{1}{3}}}\right)^{-1}, \frac{D_l}{v_{env}}\right] \tag{3.42}$$

$$l_l = \min\left[\frac{d_e}{2}\left(\frac{1}{1-(1-f_l)^{\frac{1}{3}}} + \frac{Sc^{\frac{1}{3}} Re^{a}}{3 f_l}\right)^{-1}, \frac{D_l}{v_{env}}\right] \tag{3.43}$$

In case 1, a diffusion length is determined by envelope growth velocity (Eq. (3.40)) that coresponds to the steady state growth

In case 2, based on Eq. (3.41), the model assumes that, at the initial growth stage, the thickness of the diffusion boundary layer around the envelope is comparable with the grain’s radius.

In case 3 (Eq. (3.42)), the solute interaction between growing grains at the latter stage is taken into account, and thus diffusion length can decrease at the later solidification stage. It should be noted that these phenomena were already taken into account in the models proposed by Martorano et al. [163] and Ciobanas et al.[117] However, their models did not deal with convection.

In case 4, given by Eq. (3.43), in addition to previously described effects, the term $Sc^{1/3}Re^{a}/(3f_l)$ takes into account convection around the equiaxed grain enveloppe. where $Sc = \mu_l/(\rho D_l)$ is the Schmidt number, $Re = |\vec{u}_l - \vec{u}_e|(\rho f_l d_e)/\mu_l$ is a local Reynolds number calculated with the envelope diameter d_e, and $a = (2Re^{0.28} + 4.65)/(3Re^{0.28} + 4.65)$.

In order to quantitatively illustrate the contribution of each individual physical phenomenon (accounted for in the Eq. (3.43)) and the influence of the diffusion length model on phase evolution, a numerical study was conducted for a zero-dimension solidifying system in which temperature is assumed to be uniform in the calculation domain and governed by the following equation [150]:

$$c_p\dot{T} = L\frac{\mathrm{d}f_s}{\mathrm{d}t} - c_p m\frac{\mathrm{d}c_l^*}{\mathrm{d}t} \tag{3.44}$$

In this case c_p is specific heat capacity of the alloy, L is latent heat, m is the slope of liquidus in the phase diagram, and $\dot{T} = 1$ K s^{-1} is the imposed cooling rate. Calculations are carried out for the Sn-5wt%Pb alloy, the same as that investigated in section 3.3.2, the properties of which are given in Table 3.1. The total concentration of the solute in the calculation is conserved. In order to use Eq. (3.43), some additional parameters are required. Grain number density is given a value of 10^9 m^{-3} to determine final grain size. Velocity difference $|\vec{u}_l - \vec{u}_e|$ is imposed to be 0.1 mm s^{-1}, assuming a weak liquid flow around the grains. Results of simulations are presented in Fig. 3.8.

At the early stage ($t < 0.6$ s) of grain growth, grain size is small while the value of D_l/v_{env} is high. Hence, in the expression of Eqs. (3.41) through (3.43), the first term in the bracket prevails, and case 1 differs from the other three cases: see the insert in Fig. 3.8(a). Meanwhile, the effect of convection and solute interaction is negligible. A second growth stage can be identified during a time period from 0.6 s to 2.9 s, when v_{env} increases rapidly, and the second expression in Eqs. (3.41) through (3.43) becomes smaller. Consequently, the value of the diffusion length for all four cases is calculated with the same expression, and evolution of phase fractions (Fig. 3.8(b)) and temperature (Fig. 3.8(c)) in all four cases is almost equivalent.

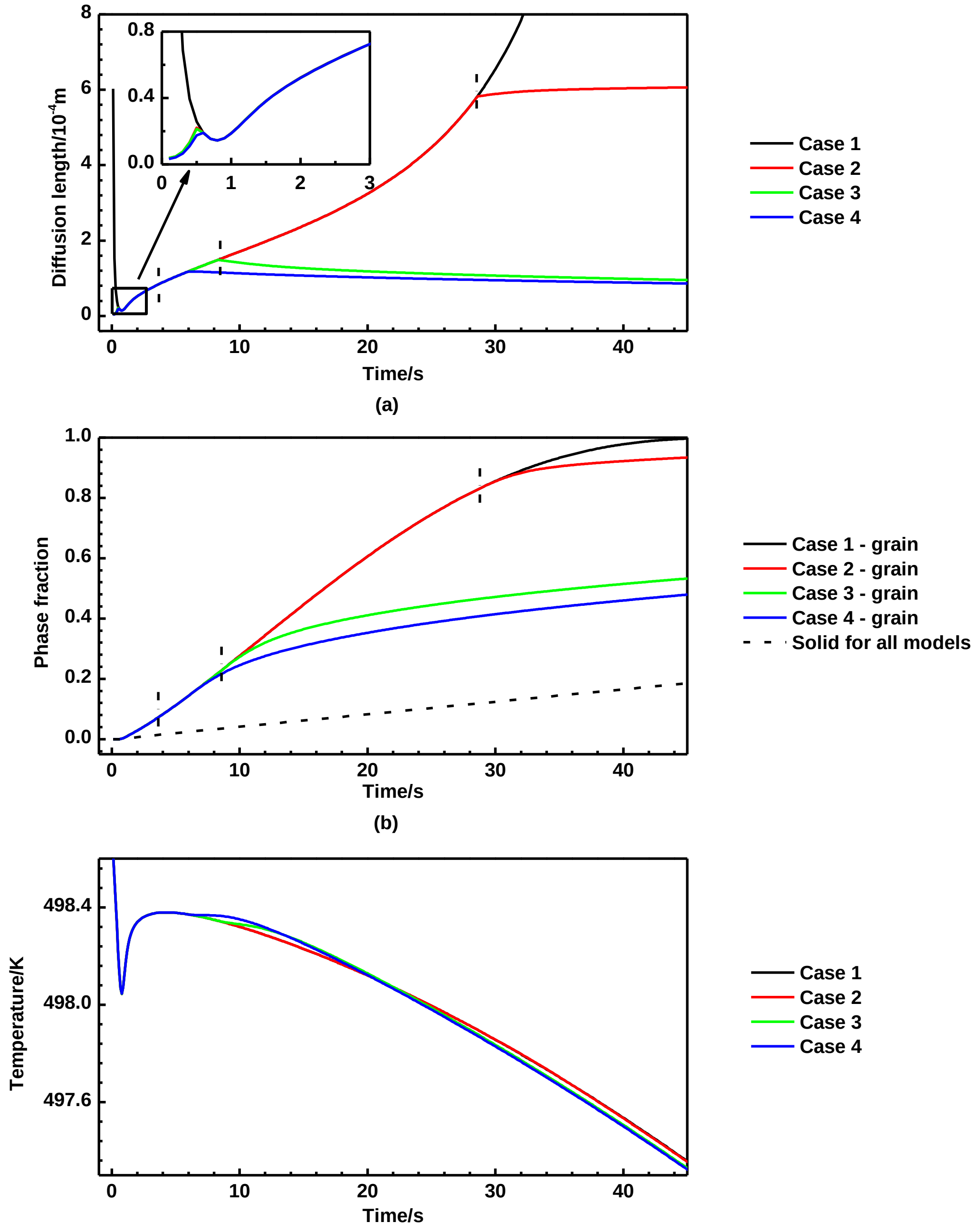

(a)

(b)

(c)

Fig. 3.8 Solidification in a zero dimension uniformly solidifying system obtained with different models (Eqs. (3.40) through (3.43)) for diffusion length: (a) variation of diffusion length in time, (b) evolution of the solid and grain fractions, and (c) temperature evolution

After 2.9 s, the four cases show obvious differences. For case 1 and case 2, diffusion length increases in a similar way until approximately 29 s since v_{env} decreases. In case 3 and case 4, solutal interaction and convective effect become important. Therefore, although in both Eqs. (3.42) and (3.43), the first term in the brackets is chosen, the diffusion length calculated with Eq. (3.43) is smaller due to convection, that also affects the evolution of the grain fraction (Fig.

3.8(b)). It is interesting to note that the diffusion length evolution observed by Torabi Rad et al. [164] experienced similar 3 stages as in cases 2 through 4, although that simulation was made for another alloy system and under a different cooling condition. A remarkable difference in envelope growth is observed between case 1 and case 4 after 45 s of solidification. In the former, the envelopes of neighboring grains impinge ($f_e \approx 1$), and further solidification occurs in the interdendritic liquid, yet the grain fraction in case 4 is only 0.48. Such a difference can greatly influence the solidification process and macrosegregation pattern.

3.3.2 Hebditch-Hunt benchmark simulation

Actually very few benchmark problems related to solidification at macroscale are available as it was indicated in chapter 1 of the thesis. Experiment performed by Hebditch and Hunt several decades ago [27] is considered as benchmark because of analysis of concentration distribution at different stages of solidification along with presentation of solidified macrostructure. This experiment has been modeled repeatedly and nowadays its configuration along with specified boundary conditions serve as a reference for some numerical studies. In particular, it was used in equiaxed simulations [85] although in real experiment solidification with columnar structure was observed. In present work first validation of the equiaxed model under development is also performed with Hebditch-Hunt solidification case, meantime, the effect of diffusion length is investigated.

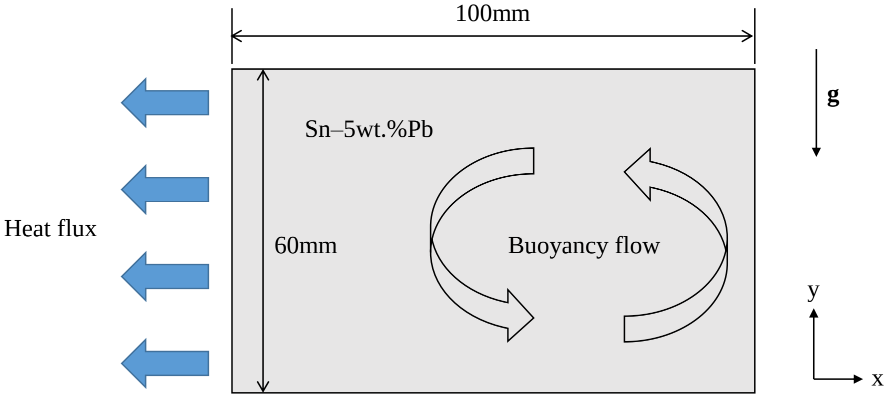

Fig. 3.9 Illustration for the solidification problem under consideration: cooling is imposed over a lateral side and initiates thermal buoyancy flow

Two dimensions of solidification zone (height and width of the crucible) were comparable while thickness of the crucible was taken small. Cooling was performed at one lateral side of the crucible (Fig. 3.9) while other faces were kept adiabatic. In such configuration thermal buoyancy convection develops and can be amplified or damped during solidification by natural convection due to enrichment of the melt by rejected solute component. In our modeling we considered the same configuration. For convenience of comparison, initial and boundary conditions were kept same as reference [85]. Material properties are given in Table 3.1.

Initial conditions: $c_0 = 5$ wt% Pb, $T_0 = 499.15$ K.

Boundary conditions (heat flux):

$$q_{ext} = \begin{cases} H\left(T - T_{ext}\right) & \text{for left wall} \\ 0 & \text{for other walls} \end{cases} \tag{3.45}$$

where $H = 300$ W m^{-2}s^{-1} and $T_{ext} = 298.15$ K.

Table 3.1 Phase diagram data and material properties

	Symbol	**Units**	**Value**	**Refs.**
Phase diagram				
Melting temperature of pure Sn	T_{Sn}	K	505.15	
Eutectic temperature	T_{eut}	K	456.15	
Partition coefficient	k	1	0.0656	[85]
Liquidus slope	m	K	-128.6	[85]
Material properties				
Reference mass density	ρ_{ref}	kg m^{-3}	7000	[85]
Density of solid for buoyancy force	$\rho_{\mathrm{s}}^{\mathrm{b}}$	kg m^{-3}	7143	[85]
Reference temperature for density	T_{ref}	K	499.15	
Liquid solutal expansion coefficient	β_c	(wt%)$^{-1}$	5.3×10^{-3}	[85]
Liquid thermal expansion coefficient	β_T	K^{-1}	6.0×10^{-5}	[85]
Reference solute concentration for density	c_{ref}	wt%	5.0	
Specific heat	$c_{\mathrm{p}}^{\mathrm{l}},\ c_{\mathrm{p}}^{\mathrm{e}}$	J kg^{-1}K^{-1}	260	[85]
Thermal conductivity	$\kappa_{\mathrm{e}},\ \kappa_{\mathrm{l}}$	W m^{-1}K^{-1}	55	[85]
Latent heat	L	J kg^{-1}	61000	[85]
Diffusion coefficient for liquid	D_{l}	m^{2}s^{-1}	1×10^{-8}	[85]
Dynamic viscosity	$\mu_{\mathrm{l}},\ \mu_{\mathrm{e}}$	kg m^{-1}s^{-1}	0.001	[85]
Volume heat transfer coefficient	H^*	W m^{-3}K^{-1}	1×10^9	[120]
Gibbs –Thomson coefficient	Γ	m K	2×10^{-7}	[92]
Maximum grain number density	$n_{\max}$	m^{-3}	1×10^9	[85]
Initial grain diameter	d_0	m	1×10^{-6}	
Secondary arm spacing	λ_2	m	9×10^{-5}	
Shape factor for dendrite growth	ϕ_{M}	1	0.683	[148]
Sphericity	ϕ_{J}	1	0.283	[148]
Packing limit fraction	$f_{\mathrm{p}}^{\mathrm{e}}$	1	0.637	[148]

Hereafter, case A corresponds to the results obtained with diffusion length given by Eq. 3.40. Similarly, case B refers to simulation performed with diffusion length given by Eq. 3.43, where convective effect is accounted for. Other numerical parameters for cases A and B are identical. At the beginning of solidification process, the liquid next to the cooling side flows downwards due to thermal and solutal buoyancy effects. Nucleation happens once the local undercooling is higher than the nucleation undercooling. Until 5 s, the nucleation and growth of grains happen mostly near the cooling face, as seen in Fig. 3.10 (a.1-2, b.1-2). According to the material properties (see Table 3.1), the solute-poor nuclei and grains have higher density than liquid. Therefore, being subject to the drag force and gravity, they are further transported by the fluid flow, sediment, and accumulate at the bottom of cavity, forming a weak negative segregation layer. Meanwhile, a liquid layer enriched with Pb is situated a few millimeters above (Fig. 3.10(c.1-2)). As solidification proceeds, these segregation phenomena become more pronounced.

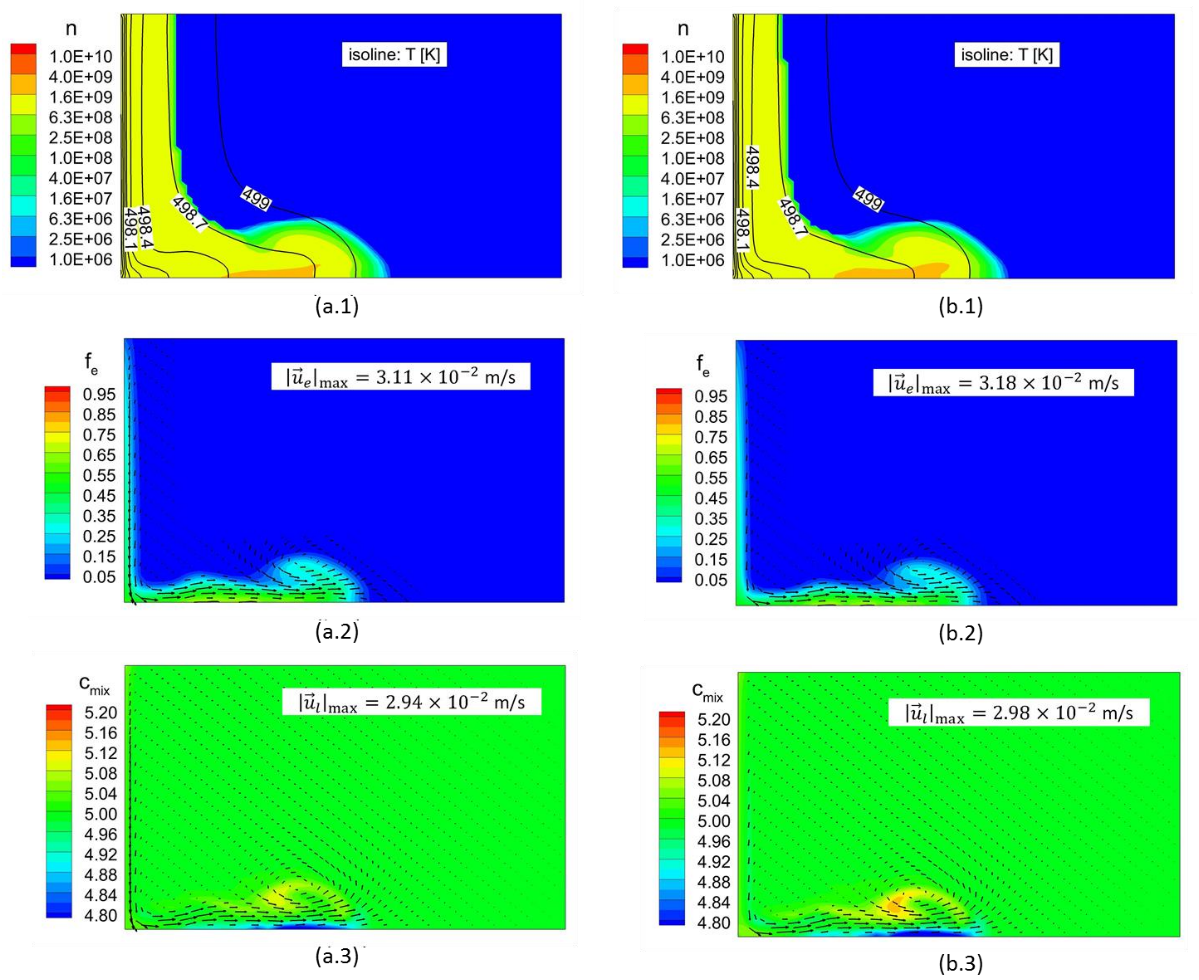

(a.1) (b.1)

(a.2) (b.2)

(a.3) (b.3)

Fig. 3.10 Various fields at solidification time of 5 s for case A (left) and B(right): (a.1, b.1) temperature and grain number density, (a.2, b.2) grain phase fraction and velocity, and (a.3,b.3) averaged solute concentration (in wt% Pb) and liquid phase velocity

As described in section 3.2.2, when grain phase faction f_e increases above the packing fraction limit f_p^e, a packed region appears. For example at 10 s, a thin layer of packed grains already forms at the bottom (Fig. 3.11 (a.2, b.2)). When grains arrive at the right wall, they rise, flow backwards and disperse into the bulk of liquid. The packed grain layer gradually heaps up from the bottom of cavity to the top. It can be seen that the segregation in case B is slightly larger than case A through comparison between Fig. 3.11 (a.3) and Fig. 3.11 (b.3).

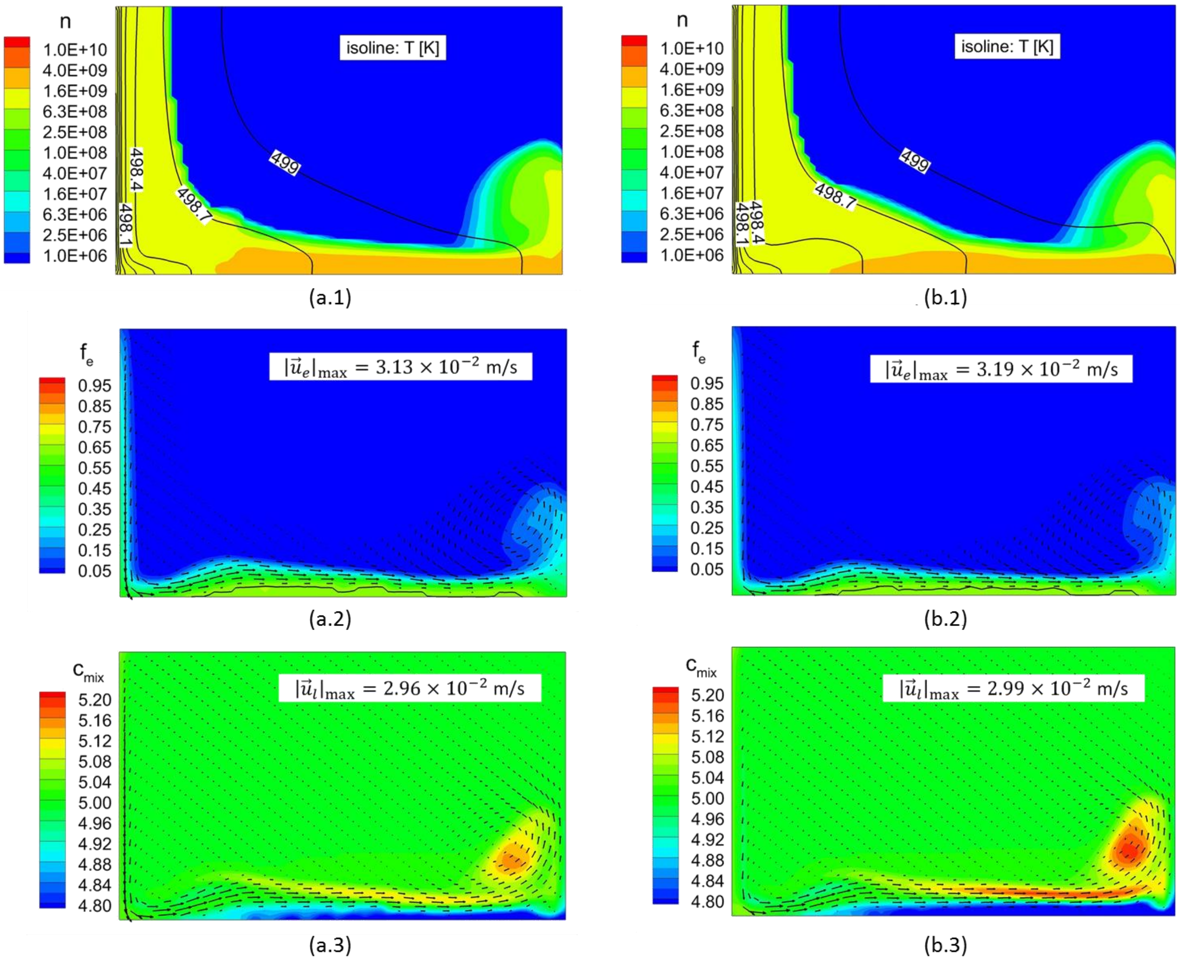

(a.1) (b.1)

(a.2) (b.2)

(a.3) (b.3)

Fig. 3.11 Various fields at solidification time of 10 s for case A (left) and B (right): (a.1, b.1) temperature and grain number density, (a.2, b.2) grain phase fraction and velocity, and (a.3,b.3) averaged solute concentration (in wt% Pb) and liquid phase velocity

This result is reverse to the zero-dimension solidification case that was considered in section 3.3.1 because the rejected solute is not conserved within a grain but is redistributed in the bulk liquid. Compared with case A, solute transport between inter- and extradendritic liquid in case B is stronger since it accounts for the grain size and intensification due to convection. This leads to a smaller dendrite tip growth velocity and grain growth rate. Consequently, packed grain layer grows more quickly in case A than in case B (Fig. 3.11(a.2, b.2)). Another difference between cases deserves notice is the velocities of phases. For both liquid and grain phases, the velocities in case B shows larger maximal value than that in case A, which indicates that the overall buoyancy force in case B is stronger. The reason for such result is that in case B solid growth is more rapid and liquid is more enriched with Pb.

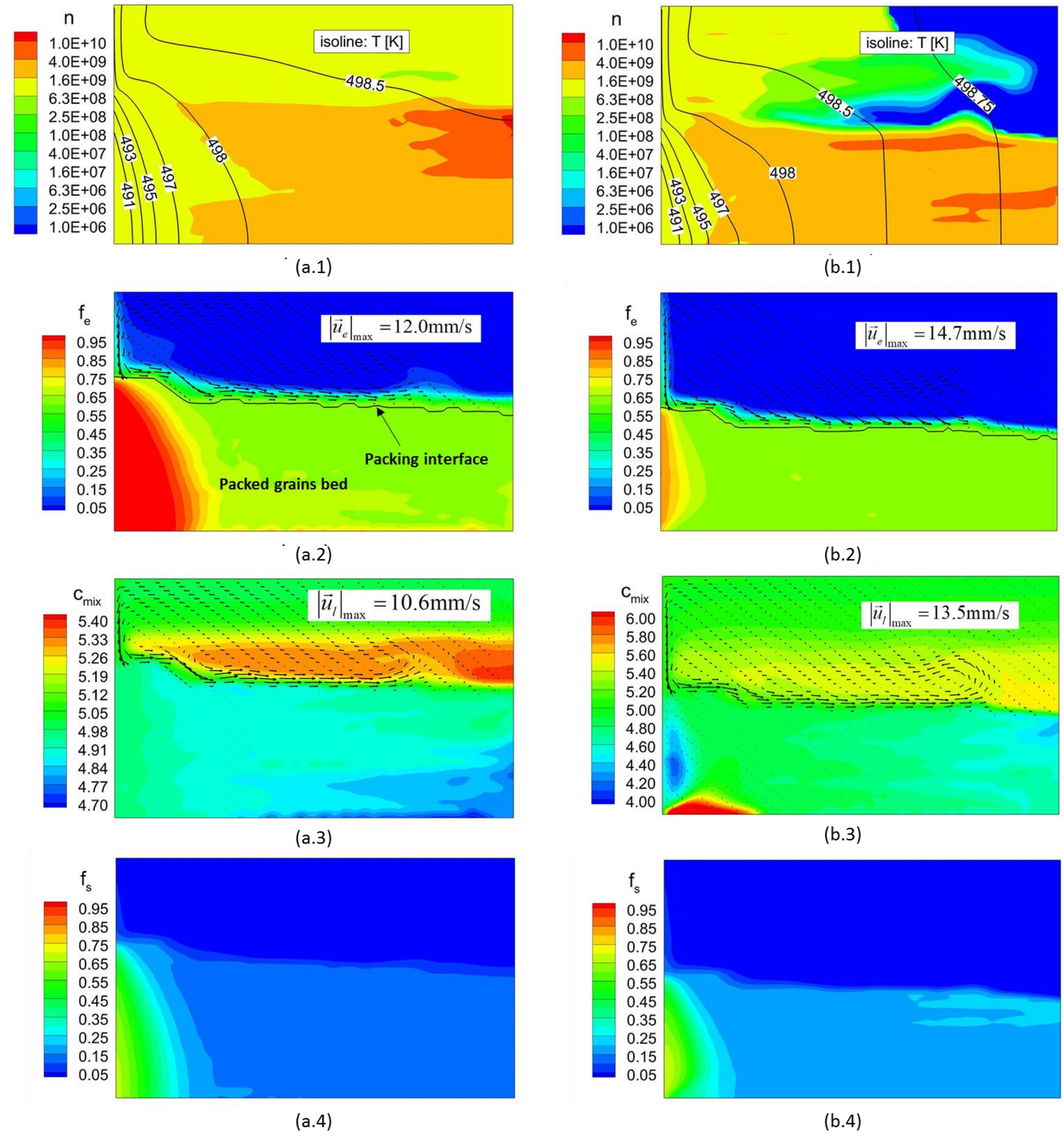

(a.1) (b.1)

(a.2) (b.2)

(a.3) (b.3)

(a.4) (b.4)

Fig. 3.12 Various fields at solidification time of 75 s for case A (left) and B(right): (a.1, b.1) temperature and grain number density, (a.2, b.2) grain phase fraction and velocity, (a.3,b.3) averaged solute concentration (in wt% Pb) and liquid phase velocity, and (a.4,b.4) solid fraction

The packed grain layer gradually piles up from the bottom of the cavity to the top. Some grains reach the packing limit fraction before arriving at the right wall, forming a gentle slope towards the east, as seen in Fig. 3.12 where the results at 75 s for both cases are presented. The upward liquid flow through the packed bed depletes its solute concentration and enriches the liquid layer above the bed for both cases (Fig. 3.12 (a.3, b.3)). Particularly for case B, the downward liquid flow in the packed porous zone brings the solute down, forming a small enriched pool at the bottom of the cavity (Fig. 3.12 (b.3)). At 75 s, differences in grain growth and macrosegregation between two cases become more pronounced. A less intense enrichment of the extradendritic liquid and a higher grain growth velocity in case A lead to a faster increase in the height of the packed bed despite a slower grain sedimentation velocity in this case (compare Fig. 3.12(a.2) and (b.2)).

At 250 seconds of solidification, almost the entire cavity is occupied by packed grains. (Fig. 3.13 (a.2, b.2)). For case A, a slightly enriched layer of the extradendritic liquid remains on the top of packed grain region (Fig. 3.13 (a.3)), because the buoyancy term related to solute concentration is small and the permeability of the packed grain region rapidly decreases. Although there is still interdendritic liquid inside the grain phase, the current model assumes that it has the velocity of the grain phase, yet, the latter is already packed, i.e. immovable. For case B, the extradendritic liquid still circulates between packed grains, however, liquid flow in this area is weak due to the large flow resistance in the packed region, as shown in Fig. 3.13(b.3), and maximal liquid flow velocity in the packed region is only 6.5×10^{-4} m s^{-1}. However, this weak liquid flow can influence solute distribution if sufficient time is provided. Due to buoyancy force and residual fluid flow, the enriched liquid descends and is replaced by the liquid from upstream. Continued enrichment at the bottom leads to strong positive segregation over the entire bottom. The overall result is that a region with semicircular shape forms near the cooling face, corresponding to a negative segregated region at the same place, while positive segregation forms in the bottom righthand region (Fig. 3.13 (b.3)).

Comparison of packed grain bed evolution is presented in Fig. 3.14. The packed bed grows fast at the beginning before slowing down due to the solidification process. A less intense enrichment of the extradendritic liquid and a higher grain growth velocity in case A lead to a faster increase in the height of the packed bed despite in this case the sedimentation velocity of grain is slower (Fig. 3.12). In Fig. 3.14, a height of the packed bed estimated from the results obtained by Založnik et al. [85] with a two-phase model is also presented for comparison. The conclusion can be drawn that present three-phase models with the packing limit value of 0.637 predict faster growth of the packed bed than the two-phase model with the packing limit value of 0.3 for the solid fraction.

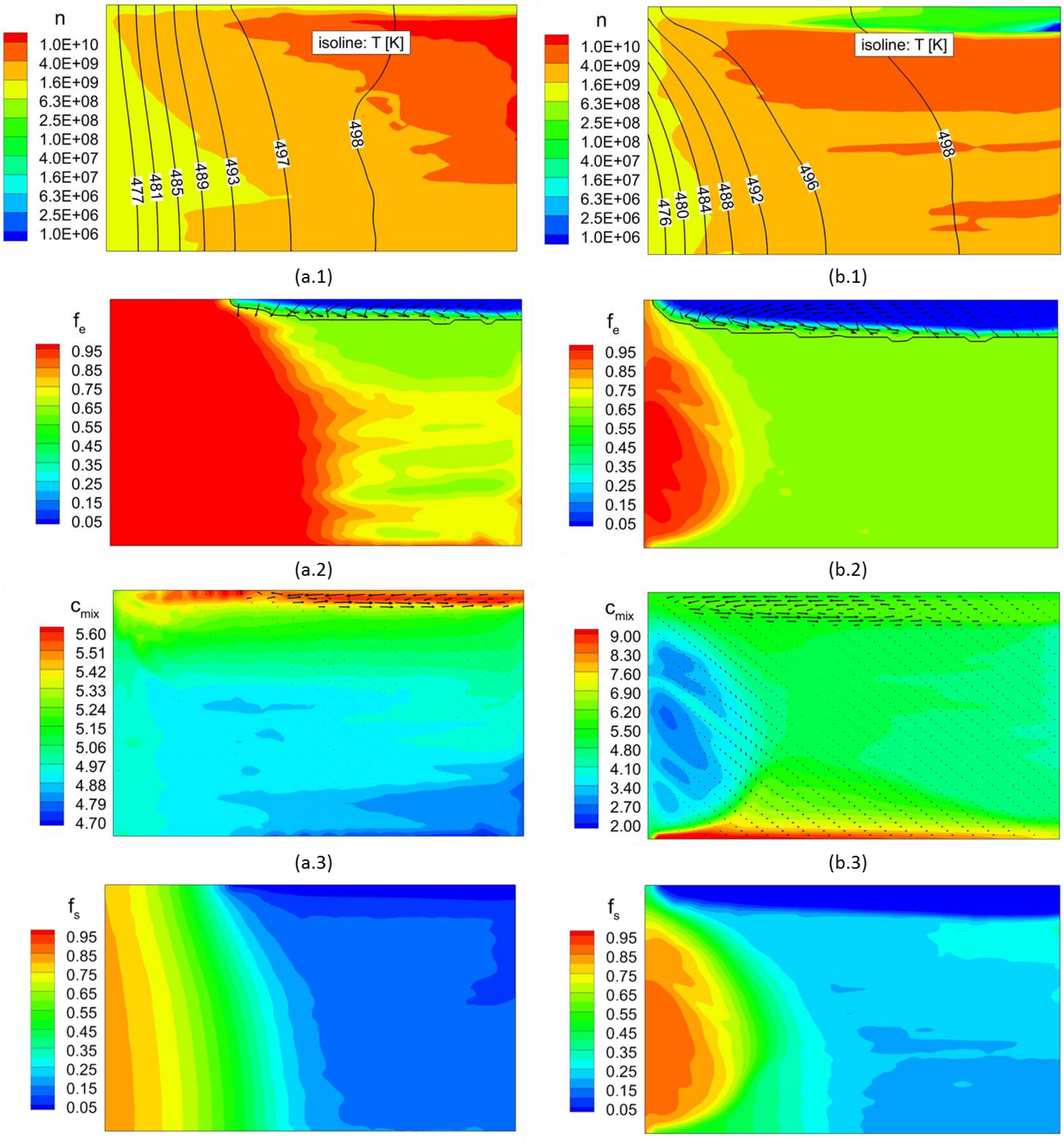

(a.1) (b.1)

(a.2) (b.2)

(a.3) (b.3)

(a.4) (b.4)

Fig. 3.13 Various fields at solidification time of 250 s for case A (left) and B(right): (a.1, b.1) temperature and grain number density, (a.2, b.2) grain phase fraction and velocity, (a.3,b.3) averaged solute concentration (in wt% Pb) and liquid phase velocity, and (a.4,b.4) solid fraction

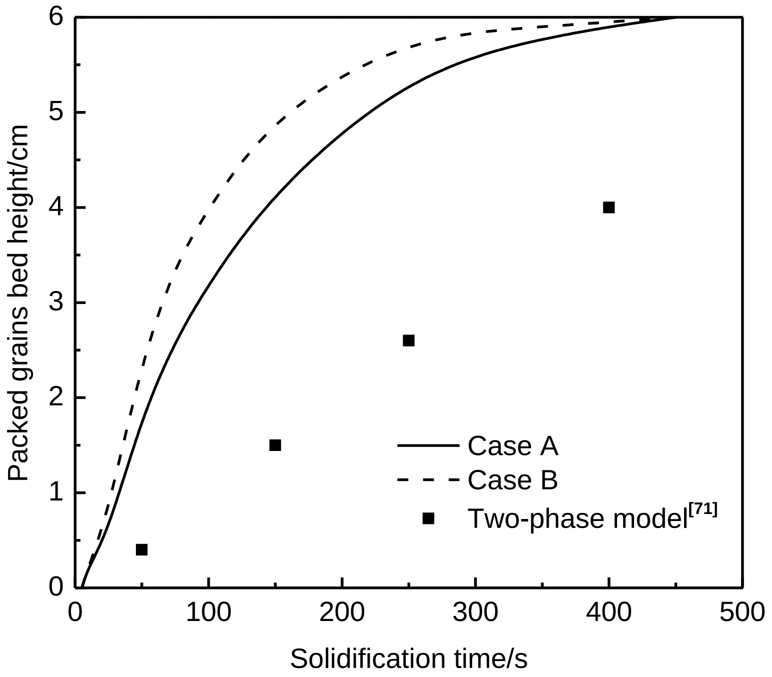

Fig. 3.14 Comparison of packed grain bed evolution

After 250 s, for case A, solute distribution barely changes, as can be seen in Fig. 3.15. Although solidification proceeds in a horizontal direction from the cooling side to the adiabatic side, slightly enriched liquid is then captured at the top by the packed grains whose fraction is not far from 1. Finally, an upward pointing concentration gradient forms in the sample (Fig. 3.15). For the same solidification case, a segregation pattern similar to that in case A was also obtained with a two-phase equiaxed model [85].

For case B, some segregation channels are initiated from the cooling side, similar to the result from another equiaxed solidification model [159,165] and the columnar solidification model [70,91,166]. These channels are determined by thermosolutal buoyancy and the local fluctuations in permeability of the packed zone. Cells with higher solute content will have a lower liquidus temperature, and therefore, a lower solid fraction for a given temperature. Therefore, envelope growth can be accelerated at one location, or suppressed at another location depending on the flow field and solute concentration distribution. Fluctuation of envelope growth will influence the permeability term in the momentum equation, and then further affect the flow field. This mechanism generates a positive feedback loop, allowing channels to continue to grow. In Fig. 3.16, average solute concentration distribution is overlaid with the vectors for velocity in the extradendritic liquid and isolines of the solid fraction for $f_s = 0.5$ and $f_s = 0.9$. Areas with lower composition correspond to the protrusions of the solid into the bulk fluid flow during the earlier solidification stage. Liquid flow is most intense near the isoline

$f_s = 0.5$ from the lefthand side, i.e. in the zone $f_s > 0.5$. It is observed that a new channel appears on the existing channel from t = 400 s to t = 550 s (Fig. 3.16). After that, channel formation stops but macrosegregation continue to evolve.

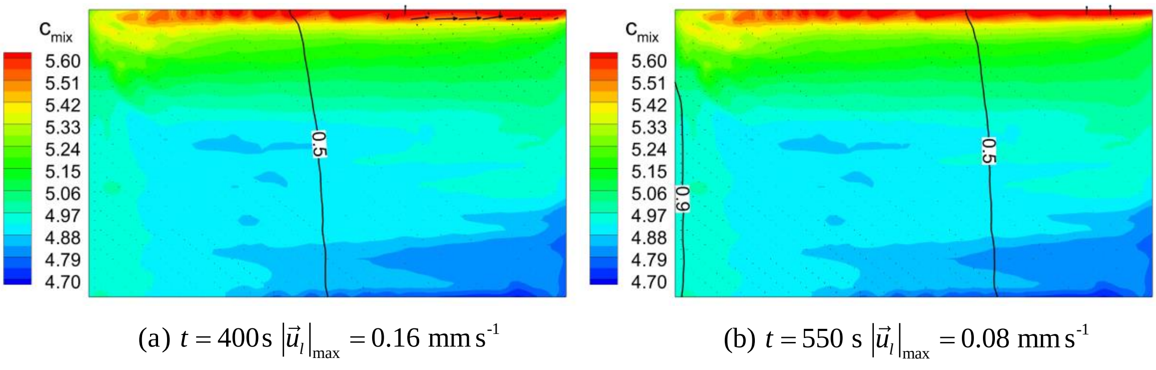

(a) $t = 400\text{s}\ |\vec{u}_l|_{\max} = 0.16\ \text{mm s}^{-1}$ (b) $t = 550\ \text{s}\ |\vec{u}_l|_{\max} = 0.08\ \text{mm s}^{-1}$

Fig. 3.15 Evolution of macrosegregation with most grains being packed in case A: solute distribution is shown with isolines of solid fraction and vectors for flow velocity in *l*-phase at times (a) 400 s, (b) 550 s

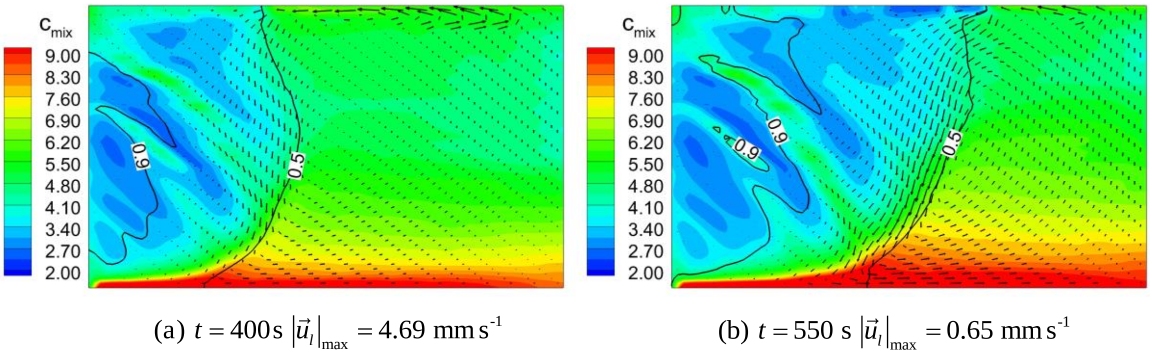

(a) $t = 400\text{s}\ |\vec{u}_l|_{\max} = 4.69\ \text{mm s}^{-1}$ (b) $t = 550\ \text{s}\ |\vec{u}_l|_{\max} = 0.65\ \text{mm s}^{-1}$

Fig. 3.16 Evolution of macrosegregation with most grains being packed in case B: solute distribution is shown with isolines of solid fraction and vectors for flow velocity in *l*-phase at times (a) 400 s, (b) 550 s

Final macrosegregation map (1000 s) is presented in Fig. 3.17. The formation of channels is observed in case B but not in case A. Similar to a columnar solidification [70,91,166], the channels are initiated near the cooling side and directed downwards following the fluid flow, which circumflexes the grains already packed at the lefthand wall, making the channels convex upward. For case A, the *l*-phase is quickly exhausted, meaning that the extradendritic liquid flow becomes too weak to affect solute distribution and to form channels. Previous comparison between two cases shows that solid growth in case A is slower than in case B due to the smaller diffusion rate of the solute from the solidifying dendrite to the extradendritic liquid. Finally, in case B, positive enrichment forms at the bottom righthand part of the cavity, as shown in the macrosegregation map (Fig. 3.17(b)), while in case A, a discontinuous positive segregation chain is presented at the top (Fig. 3.17(a)). The segregation degree in case A is much smaller, from 4.8% to 5.8%, than that in case B, from 1.9% to 13.4%.

It should be noted that the segregation pattern in case B is close to the original experimental result (except channels) [27] although mainly columnar grain structure was found in the experiment (Fig. 3.17(d)). This can be explained by the fact that in the present simulation, the dendrite equiaxed structure grows quickly before being packed into a bed that occupies the entire cavity. During further solidification, the packed grains cannot move anymore, and thus behave like a columnar dendrite structure.

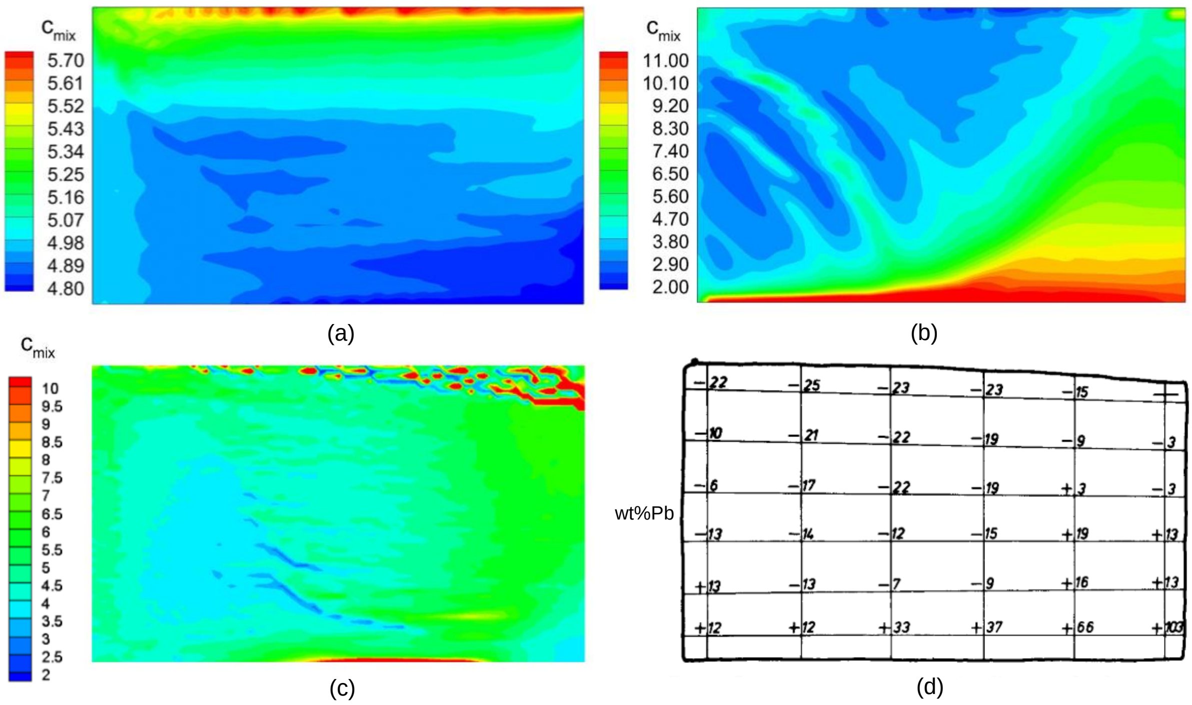

Fig. 3.17 Segregation map for case A (a), for case B (b), from two-phase model [85] (c), and from experimental measurement (d) [27]

3.4 Review of proposed solidification model

3.4.1 Governing equations

System of governing equations (Table 3.2) along with closure relations in Table 3.3 represent processes whose description is given above. It is appropriate to remind that these equations are macroscopic and obtained from microscopic ones after averaging of the latter over a representative volume. Yet, notation traditionally used for intrinsic values averaged over a volume is omitted as it was indicated above.

Table 3.2 Conservation equations

Name	Conservation equation
Mass	$\frac{\partial\left(f_l\rho_l\right)}{\partial t}+\nabla\left(f_l\rho_l\vec{u}_l\right)=M_{el}-M_{\Phi}$ $\frac{\partial\left(f_e\rho_e\right)}{\partial t}+\nabla\left(f_e\rho_e\vec{u}_e\right)=M_{le}+M_{\Phi}$ $\frac{\partial\left(f_e f_s^e\right)}{\partial t}+\nabla\left(f_e f_s^e\vec{u}_e\right)=M_{ds}+M_{\Phi}$
Momentum	$\frac{\partial\left(f_l\rho_l\vec{u}_l\right)}{\partial t}+\nabla\left(f_l\rho_l\vec{u}_l\vec{u}_l\right)=-f_l\nabla P+\nabla\left[\mu_l f_l\left(\nabla\vec{u}_l+\left(\nabla\vec{u}_l\right)^T\right)\right]$ $+\vec{F}_{Bl}+\vec{F}_{El}+K_{le}\left(\vec{u}_e-\vec{u}_l\right)$ $\frac{\partial\left(f_e\rho_e\vec{u}_e\right)}{\partial t}+\nabla\left(f_e\rho_e\vec{u}_e\vec{u}_e\right)=-f_e\nabla P+\nabla\left[\mu_e f_e\left(\nabla\vec{u}_e+\left(\nabla\vec{u}_e\right)^T\right)\right]$ $+\vec{F}_{Be}+\vec{F}_{Ee}+K_{le}\left(\vec{u}_l-\vec{u}_e\right)$ $\mu_e=\mu_l/\left(3.5f_e\right)\left[\left(1-f_e/f_p^e\right)^{-2.5f_p^e}-\left(1-f_e\right)\right]$
Energy	$\frac{\partial\left(f_l\rho_l h_l\right)}{\partial t}+\nabla\left(f_l\rho_l\vec{u}_l h_l\right)=\nabla\left(\kappa_l f_l\nabla T_l\right)+M_{ds}Lf_l-M_{le}h^*+H^*\left(T_e-T_l\right)$ $\frac{\partial\left(f_e\rho_e h_e\right)}{\partial t}+\nabla\left(f_e\rho_e\vec{u}_e h_e\right)=\nabla\left(\kappa_e f_e\nabla T_e\right)+M_{ds}Lf_e+M_{le}h^*+H^*\left(T_l-T_e\right)$ $h_l=\int_{T_{ref}^h}^{T_l}c_p^l dT_l+H_{ref},\quad h_e=\int_{T_{ref}^h}^{T_e}c_p^e dT_e+H_{ref}$
Solute	$\frac{\partial\left(f_l\rho_l c_l\right)}{\partial t}+\nabla\left(f_l\rho_l\vec{u}_l c_l\right)=-J_{le}^d-J_{le}^v-J_{\Phi}$ $\frac{\partial\left(f_e\rho_e c_e\right)}{\partial t}+\nabla\left(f_e\rho_e\vec{u}_e c_e\right)=J_{le}^d+J_{le}^v+J_{\Phi}$ $\frac{\partial\left(f_s\rho_s c_s\right)}{\partial t}+\nabla\left(f_s\rho_s\vec{u}_e c_s\right)=J_{ds}+J_{\Phi}$
Grain number density	$\frac{\partial}{\partial \mathrm{t}}n+\nabla\left(\vec{u}_e n\right)=N_{\Phi}$

Table 3.3 Sources terms and auxiliary equations

Source and interaction terms in Navier-Stokes equations	
$\vec{F}_{Bl} = f_l \rho_l \vec{g}\left[\beta_T\left(T_{ref}^b - T_l\right) + \beta_c\left(c_l^{ref} - c_l\right)\right]$	
$\vec{F}_{Be} = f_d \rho_l \vec{g}\left[\beta_T\left(T_{ref}^b - T_l\right) + \beta_c\left(c_l^{ref} - c_d\right)\right] + f_s\left(\rho_s^b - \rho_{ref}\right)\vec{g}$	
$K_{le} = \begin{cases} 18 f_l^2 f_e \dfrac{\mu_l}{d_e^2} \dfrac{2 + 4/3 f_e^{5/3}}{2 - 3 f_e^{1/3} + 3 f_e^{5/3} - 2 f_e^2} & f_e < f_p^e \\ 150 \mu_l f_e^2 / \left(d_k^2 f_l^3\right) & f_e \geq f_p^e \end{cases}$	
Source in energy equations	
$h^* = \begin{cases} h_l & \text{Solidifying} \\ h_e & \text{Remelting} \end{cases}$	
Nucleation rate	
$N_\phi = \begin{cases} f_l\left(n_{max} - n\right)/dt & \text{if}\,\Delta T > \Delta T_{nucl}\,\text{and}\,n < n_{max} \\ 0 & \text{else} \end{cases}$	
Mass exchange between the phases	
$M_\Phi = d\left(N_\phi \rho_l \pi d_0^3 / 6\right)/dt$	$M_{ds} = \begin{cases} \rho_s 2 f_d v_{ds} / \lambda_2 & \text{Solidifying} \\ f_s M_{le} / f_e & \text{Remelting} \end{cases}$
$M_{le} = \begin{cases} \rho_l S_e v_{env} & \text{Solidifying} \\ \rho_l S_e g_\alpha\left(c_l^* - c_l\right) & \text{Remelting} \end{cases}$	
Solute exchange between the phases	
$J_{le}^d = -\rho_l S_e D_l\left(\bar{c}_{env} - c_l\right)/l_l/\phi_J$	$J_\Phi = M_\phi c_s^*$
$J_{le}^v = M_{le}\bar{c}_{env}$	$J_{ds} = c_s^* M_{ds}$
Auxilary expressions	
$f_e c_e = f_d c_d + f_s c_s$	$\bar{c}_{env} = \left(l_d c_l + l_l c_d\right)/\left(l_d + l_l\right)$
$S_e = (36\pi n)^{1/3} f_e^{2/3}$	$\rho_e = \dfrac{f_d \rho_l + f_s \rho_s}{f_d + f_s}$
$\kappa_e = \dfrac{f_d \kappa_l + f_s \kappa_s}{f_d + f_s}$	$c_p^e = \dfrac{f_d \rho_l c_p^l + f_s \rho_s c_p^s}{f_d \rho_l + f_s \rho_s}$
$v_{env} = \phi_M \dfrac{D_l m_l\left(\kappa - 1\right)c_l^*}{\pi^2 \Gamma}\left[\dfrac{c_l^* - c_l}{c_l^*\left(1 - k\right)}\right]^2$	$v_{ds} = \dfrac{D_l\left(c_l^* - c_d\right)}{l_d\left(c_l^* - c_s^*\right)}$
$l_l = \min\left\{\dfrac{D_l}{v_{env}}, \dfrac{d_e}{2 + 2 Sc^{1/3} Re^a / \left(3 f_l\right)}\right\}$	$a = \dfrac{2Re^{0.28} + 4.65}{3\left(Re^{0.28} + 4.65\right)}$
$Sc = \mu_l / \left(\rho_l D_l\right)$ $Re = \left\lvert\vec{u}_l - \vec{u}_e\right\rvert\left(\rho_l f_l d_e\right)/\mu_l$	$l_d = f_d \lambda_2 / \left(2 f_e\right)$

3.4.2 Two time step solution algorithm

To reduce simulation time, the processes occurring at macroscopic and microscopic scales are modeled with different time step sizes, as shown in Fig. 3.18.

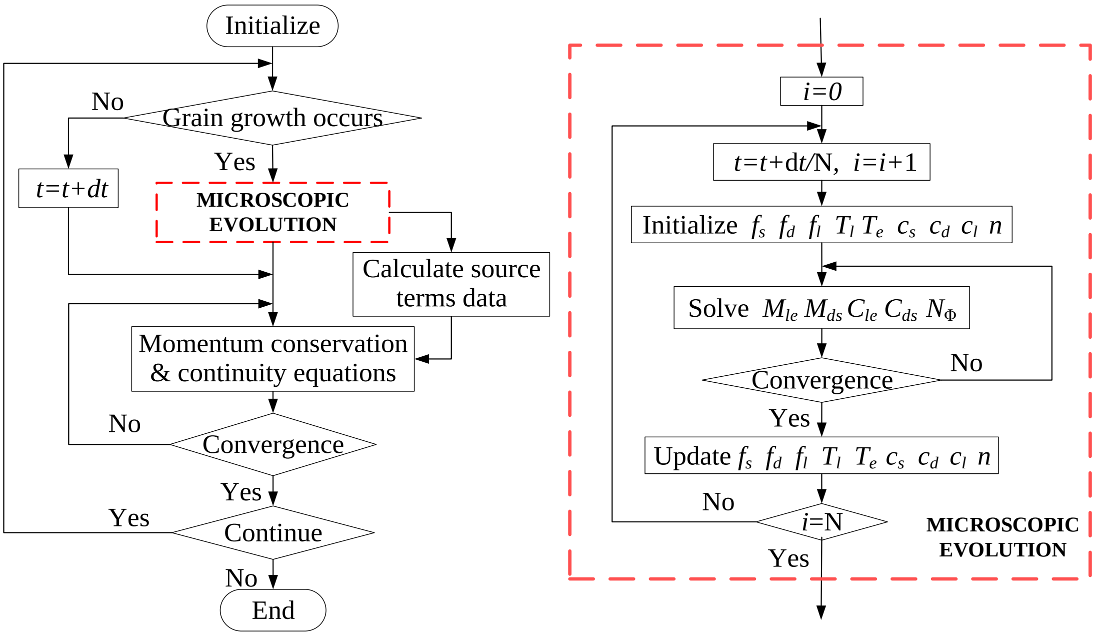

Fig. 3.18 Two time step solution algorithm

For each intensive medium property Ψ, representing phase fraction, solute concentration, temperature or grain number density, a balance equation can generally be written as:

$$\frac{\mathrm{d}(\rho\Psi)}{\mathrm{d}t}+\nabla(\rho\vec{u}\Psi)=\nabla(\lambda_{\Psi}\nabla\Psi)+S_{\Psi} \tag{3.46}$$

where the convection term $\nabla(\rho\vec{u}\Psi)$ and the diffusion term $\nabla(\lambda_{\Psi}\nabla\Psi)$ represent macroscale transport phenomena. The source term S_{Ψ} is mainly induced by microscale evolution, including the nucleation and exchange of mass, energy and solute between phases. A two time step method is based on an assumption that microscopic exchange only has a slight influence on macroscopic transportation. A larger time step size Δt, used for calculation of macroscopic transportation, is divided into N sub-steps $\Delta\tau=\Delta t/N$ used for time integration of the microscopic exchange rate. Microscopic exchange is calculated locally by omitting the macroscale transport terms giving:

$$\frac{d(\rho\Psi)}{d\tau}=S_{\Psi} \tag{3.47}$$

Each variable is initialized as Ψ_0, which is the transport solution from the last time step. The value at sub-step i is calculated with the first-order time integration scheme using data from the previous sub-step i-1:

$$\rho\Psi_i = \rho\Psi_{i-1} + S_{\Psi,i-1}\Delta\tau \tag{3.48}$$

In each sub-step, at first an amount of nuclei $(N_{\Phi}\Delta\tau)/N$ is added, then the rate of phase transition is determined, after that, the solute concentration and enthalpy content are calculated for each phase. Finally, the values of $\sum_{i=1}^{N} S_{\Psi,\mathrm{i}} = \rho(\Psi_N\text{-}\Psi_0)/\Delta t$ are recorded and then used as source terms for solving macroscopic transport equations, including multiphase flow field and transport of energy and solute concentration. The macroscopic calculation, including multiphase flow field and transport of energy, solute and grain number density, are solved by ANSYS FLUENT ® software in which the modeling of the solidification at the microscale is implemented with user-defined functions.

3.5 Conclusion

A modernized three-phase solidification model was proposed and applied for simulation of equiaxed dendritic solidification accounting for grain transport under the buoyancy flow. In the model, an additional criterion proposed for the treatment of the grain packing phenomenon allows us to take into account properly those grains whose fraction exceeds a theoretical packing limit but which were transported in the middle of the bulk liquid and, consequently, should not be blocked. Furthermore, a new equation was proposed for calculation of diffusion length that combines the factors affecting diffusion length in the extradendritic liquid, including a convective flow around the grains.

The drastic effect of diffusion length was demonstrated with two simulations of the solidification of a binary alloy Sn-5wt%Pb in the configuration of Hebditch-Hunt benchmark: case B used a proposed equation, while case A used a diffusion length purely dependent on envelope growth velocity. The numerical results showed that the case including the proposed equation for diffusion length predicted a slower growth of the packed grain bed at the bottom of the cavity, formation of channels near the cooling side, and a final segregation pattern with an enriched layer at the bottom. The overall final segregation pattern in case B was similar to the results obtained with the columnar model used earlier as well as to the experimental one.

Chapter 4 Modeling of benchmark experiment with natural convection and electromagnetic stirring

Three-phase numerical model described with equations summarized in chapter 3 (Table 3.2 and 3.3) is based on multiple assumptions and before their utilization for purposes of predictions it is necessary to perform validation of the model. This can be done by application of the model to benchmark, i.e. to a problem in which boundary conditions are rather well known as well as some results related to solidification, for example, final segregation map. In this chapter, we present application of developed model to experimental benchmark with electromagnetic stirring in which mostly equiaxed structure was obtained. Yet, modeling of solidification in benchmark experiment is preceded by description of definition of electromagnetic force acting in the liquid. The latter was created with a flat coil (similar to a linear motor) which was placed beneath the cavity and alimented with a three-phase AC current with a frequency *f*. Knowledge of distribution of electromagnetic force which drives flow of the melt is vital for simulation of convection. That is why special efforts are taken to estimate it as discussed in section 4.2. Discussion of problems related to modeling of turbulent flow in solidification problem is given in section 4.3 and results of simulation of benchmark problem are presented in section 4.4, where the effect of amplitude of electromagnetic force on simulation results is discussed.

4.1 Set-up of AFRODITE experiment

Solidification benchmark experiment set-up, referred hereafter as AFRODITE, was developed by SIMAP-EPM (Grenoble, France) laboratory in the frame of ESA-MAP[2] CETSOL and ameliorated due to ANR[3] SMACS and ESA-MAP MICAST [167]. The experiment was designed to understand the formation of macrosegregation during solidification and to provide usable quantitative data for validation of numerical models. Benchmark set-up whose scheme is shown in Fig. 4.1 has the following main features:

(1) A rectangular cavity with dimensions: length 100 mm × height 60 mm × width 10 mm.

---

[2] ESA-MAP : Microgravity application program (MAP) coordinated by European Spatial Agency (ESA)

[3] ANR : Agence National de Recherche, system of national french projects

(2) Stainless steel crucible with welded 50 thermocouples that are soldered into the cavity's wall. They almost touch the melt and their measurements allow one to follow the evolution of temperature field during solidification process.

(3) Two independent lateral heat exchangers are put in contact with lateral left and right sides of the cavity to control boundary conditions at the lateral walls. Each exchanger consists a resistive heater, a water cooling system, 9 thermocouples and a feed-back control.

(4) A Kirchhoff box to reduce convective and radiative heat losses from other side walls of cavity (< 0.18 Watt) (not shown in the scheme).

(5) A linear motor is placed at bottom of cavity to generate a travelling magnetic field. It is applied before solidification to homogenize temperature and solute concentration, and also can be used during solidification to study the effect of stirring.

(6) The experiment is conducted inside a vacuum chamber to minimize the influence of natural convection around the sample (chamber is not shown in the scheme).

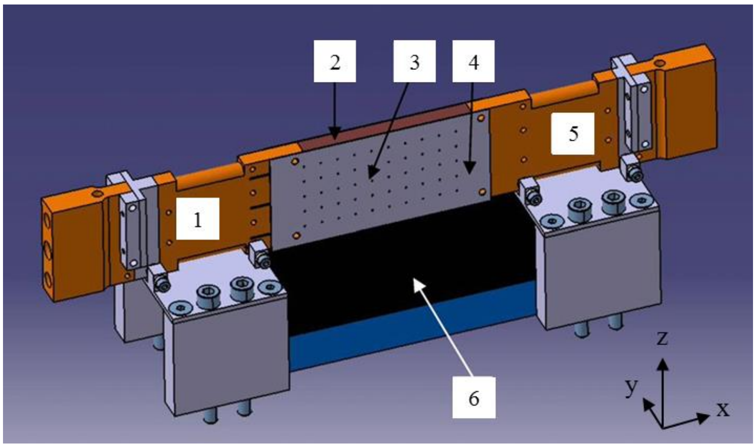

Fig. 4.1 Sketch of AFRODITE set-up: 1. Left heat exchanger; 2. Sn-10wt%Pb sample; 3. Thermocouples position matrix; 4. The stainless steel crucible; 5. Right heat exchanger; 6. Linear motor [87]

At the beginning of the experiment, a solid sample was placed in the cavity where it was melted, then overheated and kept at a uniform temperature for some time during which an electromagnetic stirring was applied to homogenize the liquid. After that an initial temperature distribution was imposed in the cavity via regulation of temperatures on the left and right heat exchangers. Most experiments (with and without EMS) were performed with a difference of 40 degrees between the left and right heat exchangers, yet, as explained below, temperature difference across the solidifying volume might be smaller. Finally, solidification was performed with cooling of the lateral sides of the cavity. Temperature variation at the heat exchangers of the cavity during experiment is schematically shown in Fig. 4.2. To introduce the electromagnetic force, a travelling magnetic field was created with a flat coil placed horizontally below the cavity. Direction of the Lorentz force depends on the polarity of the electric potential applied to the coil. In such configuration, the Lorentz force acts in the liquid mostly along the bottom and decreases exponentially in the vertical direction, an analytical expression for it is given below in section 4.2.

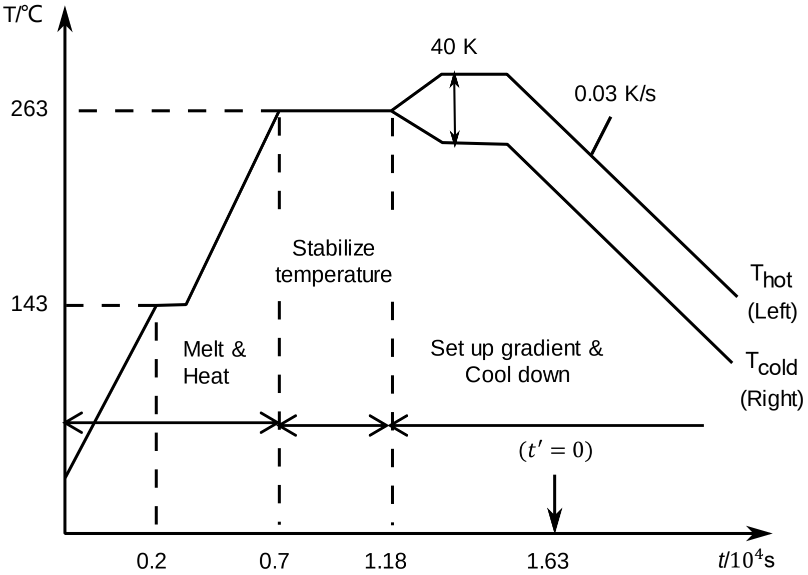

Fig. 4.2 Temperature variation at the heat exchangers of the cavity during experiment. Time scale is shown for one of reported experiments, obtained in private communication

The first experiment with this set-up was performed with a pure tin [88], then effect of different initial concentrations in solidification of a Sn-Pb alloy was studied [168]. Samples of Sn-Pb alloy solidified under natural convection demonstrated mainly columnar structure with a small amount of equiaxed grains formed in a zone which solidified the latest. Several pronounced channels enriched with the solute always appeared in the samples near the colder side. These experiments served for development and validation of numerical models [23,91,92]. Recently, Hachani et al. reported a series of experiments with the AFRODITE set-up aimed to investigate the effect of various modes of EMS on the solidification of a Sn-Pb alloy [90]. In that work, four solidification conditions were compared: (1) Natural convection; (2) Electromagnetic force applied in the same direction of natural convection; (3) Electromagnetic force applied in the opposite direction of natural convection; (4) Electromagnetic force whose direction was alternated periodically.

In particular, it was found that for the case with the Lorentz force acting in a direction opposite to the flow caused by the gravity, the structure of the samples consisted mainly of the equiaxed grains whose size varied slightly over the sample, as presented in Fig. 4.3. The objective of current work is to simulate this case through the three-phase volume average equiaxed solidification model described in chapter 3, and compare numerical results with experimental ones.

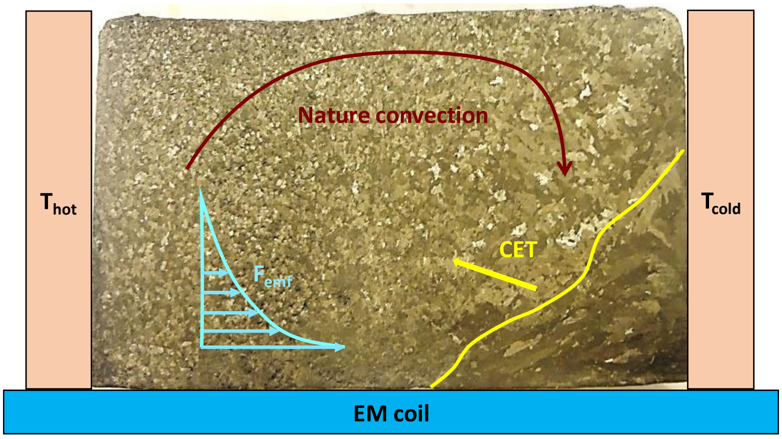

Fig. 4.3 Experimental results of Sn-10wt%Pb alloy in the AFRODITE system with electromagnetic force opposing natural convection [90]. Natural convection in liquid initially is caused by temperature distribution and enhanced due to rejection of heavier solute (Pb) near the cold boundary

4.2 Preliminary modeling of electromagnetic force

In experiment, a flat coil (similar to a linear motor) was placed beneath the cavity to create stirring of the liquid (Fig. 4.4). Analytical solution to corresponding two-dimensional electromagnetic problem was presented by Wang et al. [169] and provided expression for the effective force acting along the x-axis with amplitude decaying with the distance to the coil:

$$F_x = C_E \pi f \sigma k_E A_E^2 \exp\left(-2k_E z\right) \tag{4.1}$$

where C_E is an adjustable parameter accounting for the finite size of the coil, A_E corresponds to the amplitude of the potential vector at the inner surface of the bottom side of the cavity, $k_E = \pi/\tau = 2\pi/l$ is a wave number defined by coil pole pitch τ and related wavelength $l = 2\tau$. If the narrowness of cavity is taken into account, i.e. $j_y(y = \pm a) = 0$ should be satisfied, then, according to Wang et al. [169] the k_E have to be replaced by k_E^* [169]:

$$F_x = C_E \pi f \sigma k_E^* A_E^2 \exp\left(-2k_E^* z\right) \tag{4.2}$$

$$k_E^* = \sqrt{k_E^2 + \left(\frac{\pi}{2a}\right)^2} \tag{4.3}$$

where a is half width of liquid domain in y direction.

In Eqs. (4.2) and (4.3), k_E and k_E^* are defined by geometry of the coil and by the thickness of the cavity. For the case under consideration, the two values are $k_E = 65.45\ \mathrm{m}^{-1}$ and $k_E^* = 320.65\ \mathrm{m}^{-1}$, respectively. The amplitude of potential vector A_E can be evaluated through measurement for electromagnetic intensity. For the case with electric current of $I = 8.2$ A and magnetic field frequency of $f = 50$ Hz, the measured magnetic field amplitude along the x-axis and very near the stirrer surface ($z = 0$) is around 45 mT, that gives estimation for $A_E \approx 0.0068$ T m.

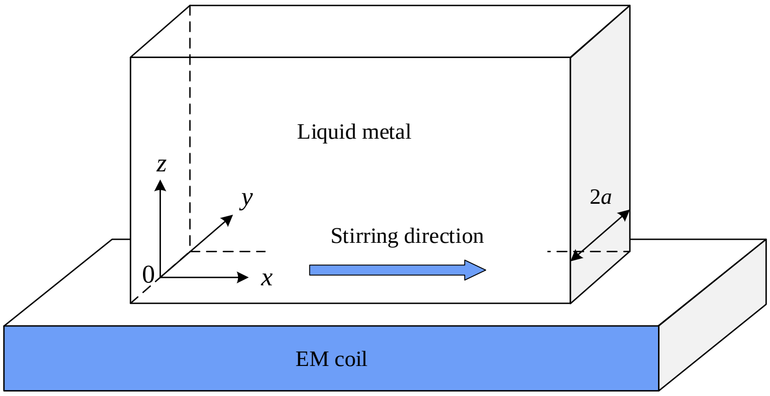

Fig. 4.4 Sketch of the liquid metal domain and linear motor and coordinate system

Yet, reduction coefficient C_E in Eq. (4.2) still has to be determined. The idea is to conduct a series of simulation using different values of C_E and to compare results with measurements of velocity thus getting the estimation for C_E. In particular, the comparison is made between the velocity profiles obtained with Doppler measurements during stirring of Ga-Sn-In alloy and results of corresponding numerical simulations. Such measurements of velocity profile were performed by Hachani et al. [167]. In the experiment, liquid alloy is stirred by linear electromagnetic stirrer in a thin parallelepiped cavity with same dimensions as AFRODITE cavity. The alloy is composed of 67 wt% Ga-20.5 wt% Sn-12.5 wt% In and remains liquid during experiment. The schematic of equipment and defined coordinate system are indicated in Fig. 4.5. In the experiment, ultrasonic Doppler velocimetry (UDV) method was used to measure velocities along several lines, but results were reported only for two profiles [167]. One of the probe transducers was placed at position of (0 mm, 0 mm, 7 mm) to detect distribution of horizontal component velocity along x-direction. Another transducer was placed at position of (4 mm, 0 mm, 60 mm) to detect vertical component velocity along z-direction.

In the following, we present simulation of flow field of Ga-Sn-In alloy in the cavity with electromagnetic stirring made for comparisons with experimental data. The considered case has current intensity of 8.2 A and frequency of 50 Hz, measured profile of corresponding velocities were presented in [167] and are reproduced below in Fig. 4.7 with red dots. Alloy's physical properties are given in Table 4.1 while electromagnetic force is described with expression (4.1) or (4.2-4.3) depending on definition of wave number.

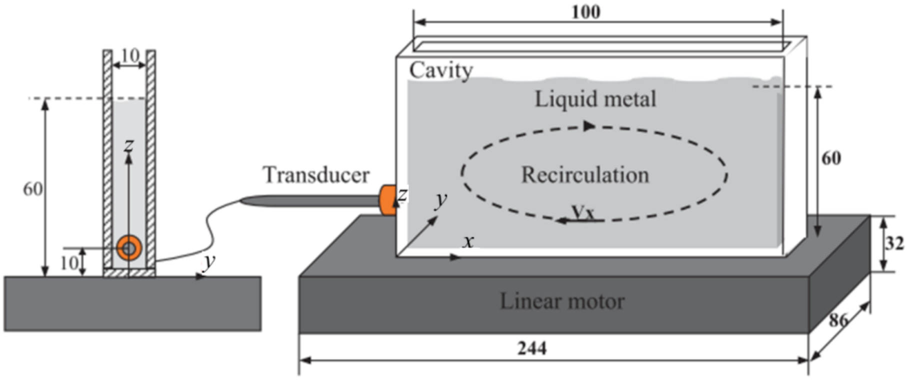

Fig. 4.5 Sketch of equipment for velocity measurement for Ga-Sn-In alloy pool, unit of lengths: mm [167]

Coefficient C_E defines intensity of the force and, consequently, intensity of convection. On the other hand, such simulations allow one to estimate whether effect of narrowness of cavity was properly taken into account in expression (4.8) for wave number k_E^*. For this, two values for wave number (Eq. (4.1) or Eq. (4.2)) were taken in calculations for the force that gave different shapes for calculated velocity profiles. For convenience of comparison, we accepted a general expression (Eq. (4.4)):

$$F_x = A_{emf} \exp\left(-2k_{emf} z\right) \tag{4.4}$$

Representative four combinations of A_{emf} and k_{emf} to be applied in simulations are listed in Table. 4.2. In that table, the range of value for C_E has been pre-selected to match calculation and measurements for magnitude of velocity. It should be noted that Eq. (4.4) neglects variation of the electromagnetic force along x direction which can have effect on the flow, especially near the walls of the cavity.

Table 4.1 Physical properties of Ga-Sn-In alloy

	Symbol	Unit	Value
Melting point	T_m	K	283.65
Mass density	ρ	kg·m^{-3}	6400
Electrical conductivity	σ	Ohm^{-1}·m^{-1}	3.4×10^4
Dynamic viscosity	$\mu_l\ \mu_e$	Pa·s	0.0022

Table 4.2 Parameters used in simulations of flow field of Ga-Sn-In alloy under electromagnetic stirring

Case number	C_E	Consider narrowness	A_{emf}, N m^{-3}	k_{emf}, m^{-1}
1	0.01	Yes	784.7	320.65
2	0.01	No	160.2	65.45
3	0.02	Yes	1569.4	320.65
4	0.02	No	320.4	65.45

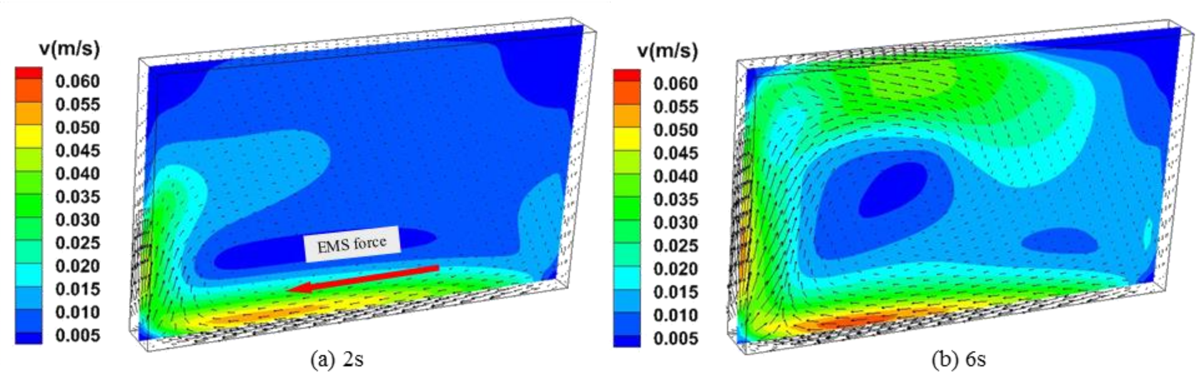

(a) 2s (b) 6s

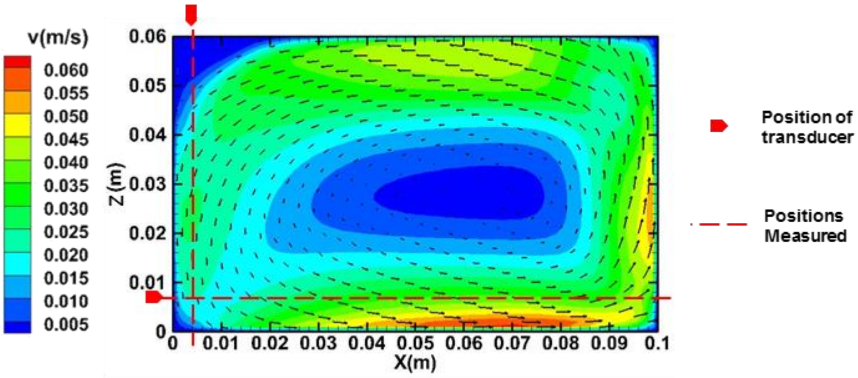

(c) 60s

Fig. 4.6 Flow field in “AFRODITE” cavity at different stirring time for A_{emf} = 320 N m^{-3}, k_{emf} = 65.45 m^{-1}. Velocity magnitude contour is shown for the mid-plane of the cavity

Since alloy remains liquid and does not require heating, no buoyancy force exists in the liquid. Fig. 4.6 shows example of the evolution of flow field inside the cavity. Note that in measurement the electromagnetic force was acting in negative direction along *x*-axis. In the beginning, the melt near bottom starts to move rightwards. With the continuous action of the electromagnetic force, the melt flow velocity continuously increases, forming a counterclockwise vortex. Then two small vortexes in opposite directions appear at the left upper and right upper corners. According to simulation results, it takes around 60 second to form a stable flow field. It can be seen that the melt flow rate in the lower part is faster because the electromagnetic force is at the bottom. Numerical results are compared with those obtained by

UDV in Fig. 4.7. It should be noted that analysis of results obtained with UDV technique reveals their potential inaccuracy. First, a blind zone about 1 cm exists ahead of each transducer and because of chosen position of the latter most of velocity variation actually happens in this zone both for vertical and horizontal direction. Furthermore, in both measured profiles value of velocity near the cavity wall differs from zero. Also, it should be noted that measurements taken in vertical direction have to be considered with serious precautions. Indeed, UDV requires no-gap between the transducer and the wall surrounding the media in which velocity is measured. Yet, in the experimental set-up the upper boundary of the cavity is actually open, therefore, a good contact between transducer and media cannot be provided. Furthermore, free surface can displace vertically because of dynamic pressure due to electromagnetic force, yet, this also perturbs measurements. On the other hand, taking into account the existence of free surface in numerical simulations is not straightforward because Ga-Sn-In alloy is prone to oxidation. That means that boundary conditions on free surface could not be easily defined because oxidation presumes variation of viscosity and surface tension. Therefore, one could hardly expect similarity between measured and calculated velocity profiles along the vertical line. Of course, boundary conditions imposed at the upper surface may affect flow in the whole cavity. Finally, according to illustration of flow (Fig. 4.6) and indication of line of measurements it is seen that both lines are located very close to the boundary layer, which means that slight mistake in their location leads to drastic change of velocity value.

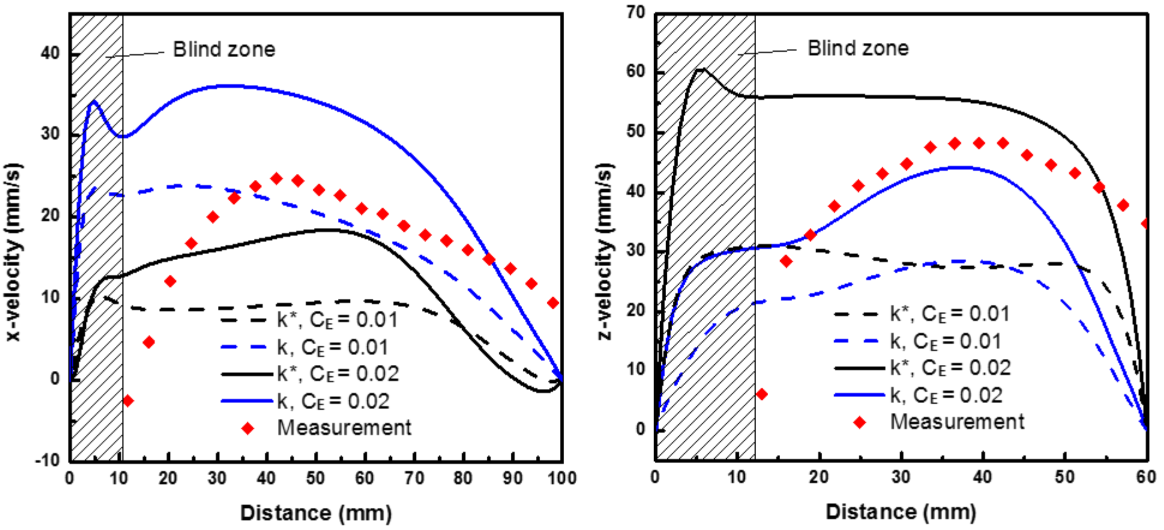

(a) (b)

Fig. 4.7 Comparison of velocity profiles between calculation (black and blue lines) and measurement (red dots) made with UV transducer placed horizontally at (x = 0 mm, y = 7 mm) (a) and vertically at (x = 4 mm, y = 60 mm) (b). Calculations made with k_{emf} = 65.45 m^{-1} and k_{emf} = 320.65 m^{-1}

With all these remarks taken into account we found that the value $k_{emf} = 65\ \mathrm{m}^{-1}$ and the value of C_E between 0.01 and 0.02 provide good agreement between simulations and measurements. According to Eq. (4.2), the value $A_{emf} = C_E\, \pi f \sigma k_{emf} A_E^2$ for the calculation for Pb-Sn alloy solidification below can be estimated between 94.2 N m^{-3} and 188.5 N m^{-3} giving that $k_{emf} = 65\ \mathrm{m}^{-1}$ and electrical conductivity $\sigma = 2.0\times10^{6}\ \mathrm{Ohm}^{-1}\mathrm{m}^{-1}$ as in Table 4.5.

4.3 Accounting for flow instabilities via realizable $k_\varepsilon - \varepsilon$ model

In chapter 3 we presented a three-phase model for solidification in equiaxed regime which couples macroscale transport phenomena and microscale processes related to the phase transition. However, that model was developed accounting for laminar character of the flow of phases. In the case under consideration, co-existence of opposed forces in solidifying region induces weak rapid oscillations of velocity and temperature fields. In this condition, to attain convergence of hydrodynamic equations at the early stage of solidification, use of turbulent hydrodynamic model is necessary and it has to be coupled with solidification model. Yet, standard approach for turbulent theory, based on Reynolds averaging of Navier-Stokes equations assumes time-averaging procedure of instantaneous velocity field thus providing transport equations for mean flow as well for mean values of temperature and concentration, and for enhancement of diffusive transport due to velocity fluctuations. On the other hand, it should be reminded that governing equations for solidification are obtained with volume averaging procedure. Consecutive application of these two averaging procedures – on a representative volume and on time – to initial system of instantaneous microscopic equations is not evident because transport phenomena at microscale cannot be treated without accounting for velocity fluctuation during short period of time, i.e. two averaging procedures actually could not be performed independently. In a more rigorous way, both procedures could be replaced with a unique ensemble statistical averaging [117,118,170], nevertheless, final equations would also contain terms related to combinations of microscale and short-time phenomena, for which closure relations are required [170].

In this section, we discuss the possibility to couple a realizable $k_\varepsilon - \varepsilon$ turbulent model to developed solidification model. The $k_\varepsilon - \varepsilon$ model is built on a general assumption that velocity, pressure, temperature, etc. in the turbulent flow can be presented as a sum of its time mean value and fluctuating component: $\xi = \langle\xi\rangle_t + \xi'$. Then, Boussinesque approximation relates Reynolds stress tensor composed of product of the fluctuating components of the velocity averaged in time $\langle u_i' u_j' \rangle_t$ to the gradient of mean velocity and turbulent kinetic energy k_ε via eddy viscosity (turbulent viscosity) μ_t, which is supposed to be isotropic. This leads to appearance of turbulent viscosity in momentum equations and so-called $k_\varepsilon - \varepsilon$ model proposes equations for the turbulent energy k_ε and its dissipation ε along with some empirical relations aimed to close the system of equations. Intensification of conductive heat transport due to the interaction of turbulent vortices is introduced in the equation of energy transport via turbulent thermal conductivity and diffuse transport of species should also be intensified due to turbulent diffusivity. A specific difficulty related to multiphase flow is that turbulence can be treated for a mixture of phases, either be assigned to one of phases or could be treated separately for each phase. In the present thesis the first option is selected and equations which replace Navier-Stokes equations (3.1), (3.2), (3.6) and (3.7) in the set of governing equations as well as equations for k_ε and ε are given below.

$$\begin{aligned}\frac{\partial\left(f_i\rho_i\vec{u}_i\right)}{\partial t}+\nabla\left(f_i\rho_i\vec{u}_i\vec{u}_i\right)=&-f_i\nabla P+\nabla\left[\left(\mu_i+\mu_{t,i}\right)f_i\left(\nabla\vec{u}_i+\left(\nabla\vec{u}_i\right)^T\right)\right]\\&+\vec{F}_{Bi}+\vec{F}_{Ei}+K_{ij}\left(\vec{u}_j-\vec{u}_i\right)\end{aligned} \tag{4.5}$$

$$\frac{\partial\left(f_i\rho_i h_i\right)}{\partial t}+\nabla\left(f_i\rho_i\vec{u}_i h_i\right)=\nabla\left(\left(\kappa_i+\kappa_{t,i}\right)f_i\nabla T_i\right)-M_{ij}h^*+H^*\left(T_j-T_i\right) \tag{4.6}$$

$$\frac{\partial\left(\rho_m k_\varepsilon\right)}{\partial t}+\nabla\left(\rho_m\vec{u}_m k_\varepsilon\right)=\nabla\cdot\left[\left(\mu_m+\frac{\mu_{t,m}}{\sigma_k}\right)\nabla k_\varepsilon\right]+G_{k,m}-\rho_m\varepsilon \tag{4.7}$$

$$\begin{aligned}\frac{\partial\left(\rho_m\varepsilon\right)}{\partial t}+\nabla\left(\rho_m\vec{u}_m\varepsilon\right)=\nabla\cdot\left[\left(\mu_m+\frac{\mu_{t,m}}{\sigma_\varepsilon}\right)\nabla\varepsilon\right]+\rho_m C_1 S\varepsilon\\-\rho_m C_2\frac{\varepsilon^2}{k_\varepsilon+\sqrt{\mu_{t,m}\varepsilon/\rho_m}}\end{aligned} \tag{4.8}$$

$$\mu_{t,m}=\rho_m C_\mu k_\varepsilon^2/\varepsilon \tag{4.9}$$

$$\rho_m=f_l\rho_l+f_e\rho_e,\quad \mu_m=f_l\mu_l+f_e\mu_e,\quad \vec{u}_m=\left(f_l\rho_l\vec{u}_l+f_e\rho_e\vec{u}_e\right)/\rho_m \tag{4.10}$$

$$\mu_{t,i}=\mu_{t,m}\rho_i/\rho_m,\qquad k_{t,i}=c_{p,i}\mu_{t,i}/Pr_t \tag{4.11}$$

In the Eqs. (4.5) through (4.11) index $i = l$, e denotes a phase to which transport equation is related and index m is used for mixture of l- and e-phases, whose properties are defined by Eqs. (4.10) and (4.11). Closure relations and values for constants used in Eqs. (4.5)-(4.11) are given in Table 4.3.

Yet, the question arises about those zones where grain phase velocity is nearly zero or the grains are already packed. Generally it is supposed that turbulence should be dumped within the semi-solid region (mushy zone) as well as within grain packed region. In models dealing with solidification this is realized via modification of a coefficient C_μ in calculation of turbulent viscosity accounting for the value of a turbulent Reynolds number as was proposed in a low-Reynolds number model [171].

$$C_\mu = 0.09\exp\left[-\frac{A_1}{\left(1+0.02Re_t\right)^{A_2}}\right],\quad Re_t = \frac{\rho_l k_\varepsilon}{\mu_l \varepsilon} \tag{4.12}$$

Similar expression was used in the later works [172–174], however, the values of constants A_1, A_2 in [172] were taken slightly differently. It should be noted that the expression (Eq. 4.12) for C_μ as well as the values for the constants are taken from the experimental studies of liquid flow near the walls. To adapt this to two-phase model, in the work of [173] this expression was multiplied by a square root of liquid fraction whereas in [174] molecular viscosity of the liquid was taken dependent on solid fraction. Additionally, extra destruction term (similar to Darcy term in momentum equation) was introduced into the equation of turbulent energy k_ε in [172], a destruction term was used in equation for energy dissipation in [173] and [174]. Moreover, an additional damping term for the floating mushy zone was introduced in [174] to overcome constraints related to the use of a unique velocity field for the two phases.

Table 4.3 Empirical constants and functions in realizable $k_\varepsilon - \varepsilon$ model

Parameters	Parameters
$G_{\mathrm{k,m}} = 2\mu_{\mathrm{t}} S^2$	$S = \sqrt{S_{\mathrm{ij}} S_{\mathrm{ij}}}$
$S_{\mathrm{ij}} = 1/2\left(\partial u_{\mathrm{j}}/\partial x_{\mathrm{i}} + \partial u_{\mathrm{i}}/\partial x_{\mathrm{j}}\right)$	$C_1 = \max\left[0.43, \eta/\left(\eta+5\right)\right]$
$\eta = \sqrt{2} S k_\varepsilon/\varepsilon$	$C_\mu = 1/\left(4.04 + A_{\mathrm{s}} k_\varepsilon U^*\right)/\varepsilon)$
$A_{\mathrm{s}} = \sqrt{6}\cos\varphi$	$\varphi = \cos^{-1}\left(\sqrt{6}W\right)/3$
$U^* = \sqrt{S_{\mathrm{ij}} S_{\mathrm{ij}} + \tilde{\Omega}_{\mathrm{ij}} \tilde{\Omega}_{\mathrm{ij}}}$	$\Omega_{\mathrm{ij}} = 1/2\left(\partial u_{\mathrm{j}}/\partial x_{\mathrm{i}} - \partial u_{\mathrm{i}}/\partial x_{\mathrm{j}}\right)$
$W = S_{\mathrm{ij}} S_{\mathrm{jk}} S_{\mathrm{ki}}/S^3$	$Pr_{\mathrm{t}} = 0.85$
$C_2 = 1.9$	$A_0 = 4.4$
$\sigma_{\mathrm{k}} = 1.0$	$\sigma_\varepsilon = 1.2$

In realizable $k_\varepsilon - \varepsilon$ model proposed in ANSYS FLUENT ® the coefficient C_μ used for calculation of the turbulent viscosity is not constant either (contrary to standard $k_\varepsilon - \varepsilon$ or RNG models), yet coefficients were tuned to treat properly free jet spreading. Modeling of destruction and production terms in the equation for ε was also optimized for solutions of problems related to jets. It could be supposed that in the realizable $k_\varepsilon - \varepsilon$ model damping of the turbulence in the floating mushy zone as well as in packed bed region is not so efficient as in low-Reynolds models in [172–174]. Yet, as it was demonstrated below, for the problem under study turbulent viscosity is not so high even at the beginning of solidification and the appearance of packed grains should diminish the intensity of the flow. Therefore, the effects related to enhancement of heat and solute diffusive transport will disappear in the grain packed region and will decrease in the floating mushy zone. That is why in further calculations we used a system of equations that describes turbulent flow with $k_\varepsilon - \varepsilon$ approximation, i.e. Eqs. (4.5) through (4.11) (and closure relations in Table 4.3). However, equations for phase and solute transport including equations for diffusion fluxes and relations for diffusion length in Tables 3.2 and 3.3 remained unchanged.

4.4 Boundary conditions, initial state and properties of alloy

It should be underlined that in the experiment temperature distribution prior to the solidification as well as cooling rate during solidification are programmed and controlled via temperature measurements at the heat exchangers. As discussed elsewhere [92,167], a contact resistance may exist between the wall and the bulk and be dependent on the wettability of the walls by melt, on motion of liquid and on distribution of liquid fraction in the volume because of the shrinkage during solidification (Fig. 4.8(a)). That means that the actual temperature difference across the bulk should be smaller compared to that imposed on the heat exchangers and vary with transition from liquid to solid state. Furthermore, the lateral cooling rate in the experiment can deviate from programmed one if intense solidification accompanied by a large amount of heat release occurs or if the water cooling is not sufficient. To take these effects into account, temperature at the inner side of the lateral walls is recalculated using temperature measurement made by the thermocouples placed on the heat exchangers and those on the frontal side of the cavity near their lateral sides.

According to the sketch in Fig.4.8(a), if convective heat transfer is neglected near the lateral wall, the heat flux should conserve along the horizontal axis x. Using a finite difference discretization, this condition for the left side of the cavity can be written as [167]:

$$\kappa_H \left(1.5T_{FL3} - 2T_{FL4} + 0.5T_{FL8}\right) / \Delta x_{H,T} = \kappa_s \left(T_{LB} - T_{L21}\right) / \left(x_{L21} - x_{FL3}\right) \tag{4.13}$$

where $\kappa_H = 401$ W m^{-1}K^{-1} and $\kappa_S = 55$ W m^{-1}K^{-1} are the thermal conductivities of the heat exchanger (made of copper) and the sample, respectively; $\Delta x_{H,T} = 1.5$ cm is the distance between the thermocouples at the heat exchanger; T_{LB} is the temperature at the inner side of the left boundary. Other variables represent temperature values at the thermocouples given with their numbers and position in Fig. 4.8(a).

Consequently, the value of T_{LB} (T_{RB} for the right side) can be found using values of temperature measured by neighboring thermocouples. The programmed boundary temperature curves for both lateral sides are presented in Fig. 4.8(b). Yet, there exist small oscillations in the programmed temperature data that may be related to the “noise” of thermocouples that seems unreasonable to be taken into accounted. It could be appropriate to “smooth” the calculated variations T_{LB} and T_{RB} in time t with analytical expressions as Eq. (4.14) by polynomial regression.

$$T'_{\mathrm{LB}}\left(T'_{\mathrm{RB}}\right)=a_1t^4+a_2t^3+a_3t^2+a_4t+a_5 \tag{4.14}$$

where t is time; $a_1 \sim a_5$ are fitting parameters, as gathered in Table 4.4. Thus calculated temperature can be used as uniform Dirichlet boundary condition at the inner surface of the lateral sides of the cavity.

Table 4.4 Fitting parameters for temperature curve

	a_1	a_2	a_3	a_4	a_5
T'_{LB}	-7.051342×10^{-12}	1.066523×10^{-8}	1.0992×10^{-5}	-0.0362674	237.9
T'_{RB}	8.13619×10^{-12}	-3.303026×10^{-8}	4.33585×10^{-5}	-0.041834	225.0

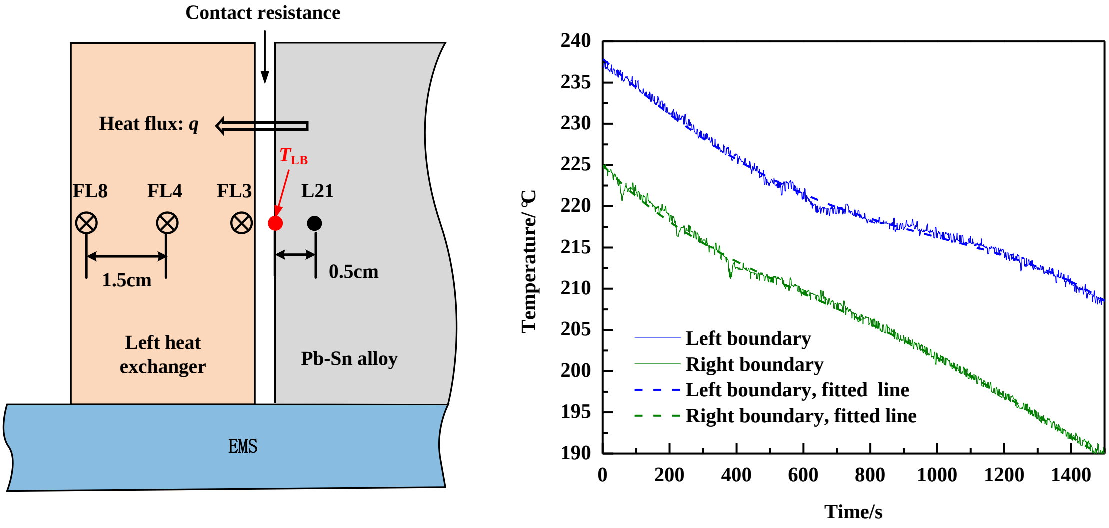

(a) (b)

Fig. 4.8 Sketch of the AFRODITE set-up with indication of position of some thermocouples and the contact resistance between the heat exchanger and solidifying volume (a), evolution of programmed temperature at heat exchangers during the whole experiment (b)

Initial state in simulations corresponds to the uniform distribution of the nominal concentration 10 wt% of Pb in the pure liquid and uniform temperature gradient inside the cavity corresponding to the temperature of 511.05 K (237.9 ˚C) and 498.15 K (225.0 ˚C) applied at the left and the right lateral sides, respectively. This corresponds approximately to 16300 s (Fig. 4.2) of the physical time in the solidification experiment. In calculation, the solid density is assumed constant, i.e. $\rho_s^b = 7199\ \mathrm{kg\ m^{-3}}$, corresponding to $c_s = k_p c_0$ and $T = T_{ref}^b$, and calculated according to Stankus's expression [175]. Similarly, reference liquid density is given as $\rho_{ref} = 7246\ \mathrm{kg\ m^{-3}}$, corresponding to $c_l = c_0$ and $T = T_{ref}^b$. The liquid density is strongly dependent on the solute (Pb) mass fraction and temperature. In the work, Boussinesq approach is used with expansion coefficients (β_T and β_c) from ref. [85]. During solidification, with decrease of temperature and increase of solute concentration in liquid, the liquid density tends to increase, therefore, the liquid is always heavier than solid in whole process. Properties of the alloy and values for some other physical parameters are given in Table 4.5.

Table 4.5 Phase diagram, material properties and calculation parameters

	Symbol	Units	Value	Ref.
Phase diagram for Sn-Pb				
Melting temperature of pure Sn	T_{Sn}	K	505	
Eutectic temperature	T_{eut}	K	456	
Liquidus slope	m	$\mathrm{K(wt\%)^{-1}}$	-1.286	[85]
Partition coefficient	k		0.0656	[85]
Nominal concentration of Pb	c_0	wt%	10	
Physical properties				
Reference density(liquid)	ρ_{ref}	$\mathrm{kg\ m^{-3}}$	7246	[175]
Density	$\rho_e,\ \rho_l,\ \rho_s$	$\mathrm{kg\ m^{-3}}$	7246	[175]
Reference temperature	T_{ref}^b	K	510.15	
Thermal expansion coefficient	β_T	$\mathrm{K^{-1}}$	6.0×10^{-5}	[85]
Solutal expansion coefficient	β_c	$\mathrm{(wt\%)^{-1}}$	5.3×10^{-3}	[85]
Density of solid phase in buoyancy term	ρ_s^b	$\mathrm{kg\ m^{-3}}$	7199	[175]
Thermal conductivity	$\kappa_e,\ \kappa_l,\ \kappa_s$	$\mathrm{W\ m^{-1}K^{-1}}$	55.0	[85]
Latent heat	L	$\mathrm{J\ kg^{-1}}$	61000	[85]
Specific heat	$c_p^l,\ c_p^s$	$\mathrm{J\ kg^{-1}\ K^{-1}}$	260	[85]
Diffusion coefficient for liquid	D_l	$\mathrm{m^2\ s^{-1}}$	10^{-8}	[85]
Dynamic viscosity for liquid	μ_l	Pa s	0.001	[85]
Characteristic length	d_k	m	2×10^{-4}	[85]
Electrical conductivity	σ	$\mathrm{Ohm^{-1}\ m^{-1}}$	2.0×10^{6}	[176]
Gibbs –Thomson coefficient	Γ	m K	2×10^{-7}	[92]
Inductor parameters				
Wave vector	k_{emf}	$\mathrm{m^{-1}}$	65	[167]
AC current frequency	f	Hz	50	[169]
Amplitude of electromagnetic force	A_{emf}	$\mathrm{N\ m^{-3}}$	180	

4.5 Calcualtion Results

In this section, three-dimensional simulations are performed with the grid comprising 100 × 60 × 15 mesh cells and different values of the adjustable coefficient A_{emf} in the expression for the electromagnetic force (Eq. 4.4). Detailed discussion of the solidification process given in section 4.5.1-4.5.4 is made for A_{emf} = 180 N m^{-3} but final results in section 4.5.5 are presented also for A_{emf} = 110 N m^{-3} and A_{emf} = 150 N m^{-3} . In calculations the electromagnetic force is activated from the beginning and cooling is taken into account via boundary conditions (Eq.(4.20)) recalculated from experimental data and applied at the lateral sides of the cavity. Before presenting the calculated multi-fields results that have complex interaction with each other, a short overview for the solidification process is in necessary.

Once the calculation starts, the flow field is driven by both buoyancy force and electromagnetic force. It takes about 60 second to get the forced convection developed, then the flow field keeps stable until around 240 s. During this stage, temperature distribution defined by forced flow in the most part of the cavity remains quasi-stationary and temperature in cavity decreases mostly uniformly with a cooling rate of 0.03 K s^{-1} as was programmed in the experiment [167]. Nearly at 240 s, temperature at the colder side becomes equal to liquidus temperature of alloy at nominal concentration that initiate nucleation and grain growth there. After that, solidification proceeds according to the cooling condition of both lateral sides until the end.

Simulation starts with a cavity filled with liquid melt, at this stage only equations related to the extradendritic liquid are used, no phase transition or interaction between phase is involved. In Fig. 4.9 temperature distribution with a superposed velocity field and distribution of turbulent characteristics k_ε and $\mu_{t,m}$ are presented for median section of the cavity. In the cavity the main flow direction is anticlockwise dominated by EMS force. It means that the thermal buoyancy force is quite weak compared to EMS fore. Only in the upper left corner, the natural convection prevails the EMS force and forms a small clockwise flow vortex. The maximum value of liquid velocity, which is ~4.91 cm s^{-1}, appears near the bottom of the cavity.

Turbulence kinetic energy in the volume is nearly 5.5×10^{-5} m^{4}s^{-2} that gives velocity oscillation of order of $u' \approx \sqrt{2/3k_\varepsilon} \approx 6\times10^{-3}$ m s^{-1} and the mean flow velocity of about 4.5×10^{-2} m s^{-1}. One can estimate the intensity of the turbulence to be about 13%, i.e. medium intensity. This could be expected since the value of the Reynolds number $Re \approx 6000$ based on a hydraulic diameter for a lateral side wall $D \approx 1.7 \times 10^{-2}$ m also indicates moderate turbulence. It should be noted that at this stage calculated turbulent viscosity does not exceed 5.5 × 10^{-2} Pa·s and is localized near the hotter wall while in the most of the cavity it is less than 1.0 × 10^{-2} Pa·s. Provided that the densities of all phases are equal, the ratio of turbulent and molecular viscosity varies from $\mu_{t,i}/\mu_i \approx 55$ to 10, which is rather low compared to other works where solidification under EMS was studied. Indeed, in [172] this ratio was equal to 208 at the beginning of solidification and decreased to 20 in the zone of pure liquid when more than a half of the cavity was solidified. In continuous ingot solidification [173] the maximal value of turbulent viscosity was 1.1 Pa·s, i.e. nearly 200 times higher than molecular one. In calculations accompanied presentation of a turbulent model by Poole and El-Kaddah [174], the ratio $\mu_{t,i}/\mu_i$ in pure liquid was about 60 almost everywhere in the cavity and then decreased during solidification to 30 within the mushy zone keeping its initial value in the liquid and when its value did not exceed 15 the flow was declared laminar.

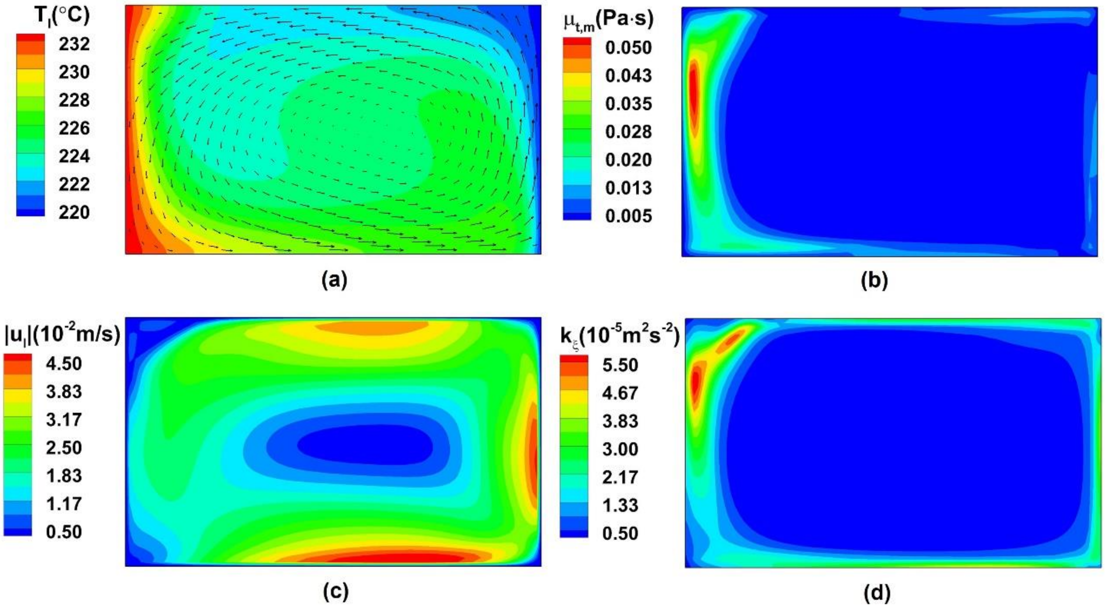

(a) (b)

(c) (d)

Fig. 4.9 Temperature distribution and liquid flow vectors (a), turbulent viscosity distribution (b), magnitude of liquid phase velocity (c), and turbulent kinetic energy distribution (d) prior solidification (t = 150 s) for A_{emf} = 180 N m^{-3}

Regarding intensification of heat exchange, the estimated maximal value of turbulent thermal conductivity according to (22) is $\kappa_{t,i} \approx 12$ W m^{-1}K^{-1}, i.e. of order of 20% of thermal conductivity of material. Similar estimation for diffusion coefficient of solute gives $D_{l,t} = \mu_{t,l}/(\rho_l Pr_t) \approx 7\times10^{-6}$ m^{2}s^{-1} that indicates significant increase of diffusive transport. However, in stirred pure liquid as well as between moving grains convective solute transport should still prevail over diffusive one.

Fig. 4.10 shows cooling curves measured during experiment at several points L21, L22, L25, L29 and L30 inside the cavity. Similar curves but obtained in numerical simulations are presented in Fig. 4.11. It can be seen that the temperature at the point L22 happens to be lower than the ones at the point L29 (closer to the colder wall) and at the point L25 (at the cavity center), which is different from the measurements. This "inversion" in temperature distribution is due to a vortex caused by EMS which brings cold liquid close to the hotter wall. Since non-monotone temperature distribution was not observed in measurements, it can be assumed that the electromagnetic force was probably overesimated in calculations. It should be noted however that the experimental cooling curves indeed demonstrate that temperature values on the thermocouples L25, L29 and L30 were rather close. Interestingly, various stages of solidification process can be identified in cooling curves obtained in simulation (Fig. 4.11).

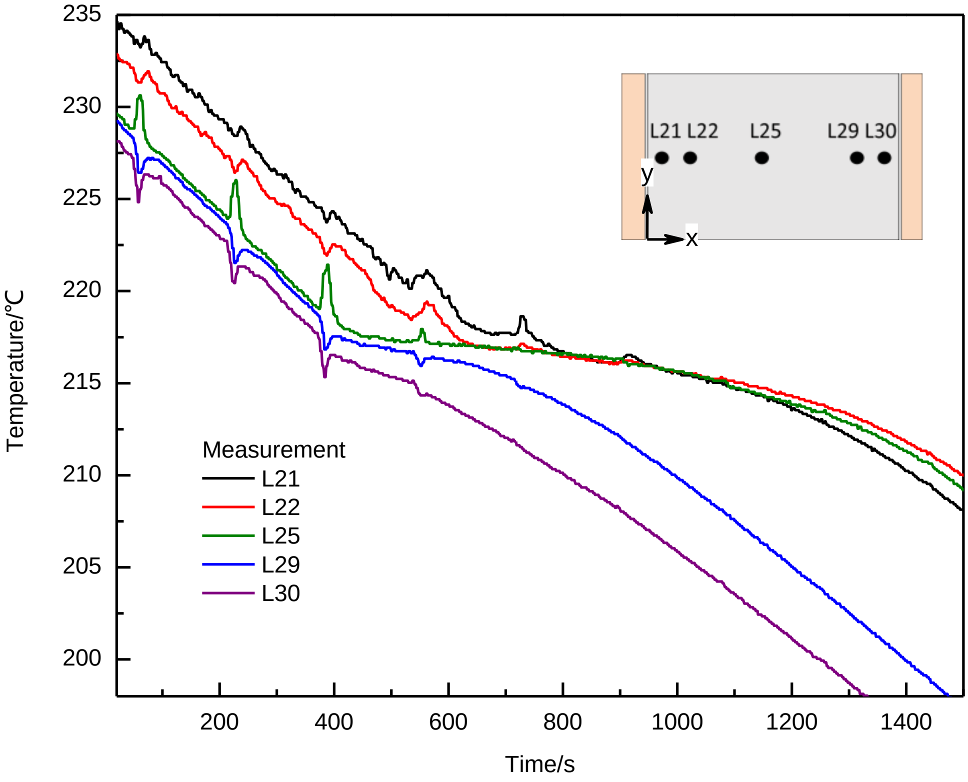

Fig. 4.10 Cooling curves obtained through measurements at positions corresponding to location of thermocouples L21, L22, L25, L29 and L30 (y = 30 mm for all and x = 5 mm, x = 15 mm, x = 45 mm, x = 85 mm, and x = 95 mm, respectively)

At about 360 s, cooling rate slows down for all points and all curves start to display fluctuation till 550 s. Analysis of distribution of temperature, grain fraction and flow field at t = 375 s, 385 s and 395 s in Fig. 4.13 explains the nature of oscillations which is related to instantaneous damping of the forced convection and intensification of natural one because of enrichment of rejected Pb in the liquid. Further, temperature decreases more slowly for points which are close to hotter side (L21, L22) than for those close to colder side (L29, L30). The cooling curve of the point in the center (L25) gets closer to the cooling curve at the hotter side. In Ref. [177], the cooling curves and temperature fields evolution obtained in simulation have been compared with experimental measurements. Two set of results show similar tendency. Relative instantaneous local error between calculated and experimentally measured temperature which can be introduced as $\max\{|T_{\text{calc}} - T_{\text{mean}}|/(T_{\text{LEFT}} - T_{\text{RIGHT}})\}$, displays maximal value of about 13% in the center of the cavity at early stage of solidification.

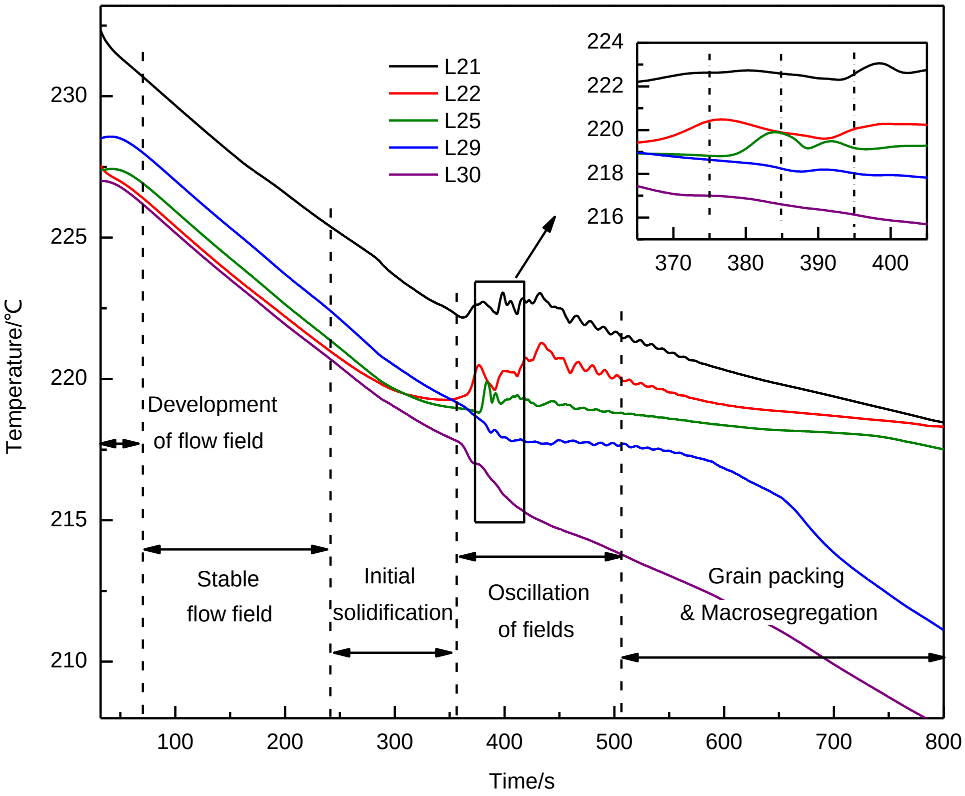

Fig. 4.11 Calculated cooling curves obtained in simulations at positions corresponding to location of thermocouples L21, L22, L25, L29, and L30 (y = 30 mm for all and x = 5 mm, x = 15 mm, x = 45 mm, x = 85 mm, and x = 95 mm, respectively) and indication for different solidification stages

Below, the phenomena occurring at different solidification stages will be described in detail. In each solidification time, multiphase flow and distribution of temperature, grain number density, concentration and phase fraction will be presented. Concentration of Pb in mixture used in presentation of the results is calculated as:

$$c_{mix} = \frac{\rho_l f_l c_l + \rho_e f_e c_e}{\rho_l f_l + \rho_e f_e} \tag{4.15}$$

4.5.1 Initial nucleation and solidification

Once local temperature gets below liquidus temperature, nucleation and grain growth start. In simulated case solidification initiated at the top of the colder wall. Even if little later nucleation occurs over the whole surface of this lateral wall, equiaxed grains are brought mainly upwards to this corner due to convection driven by the electromagnetic force as well as due to their floatation (Fig. 4.12(b)). At the early stage of solidification, most of these grains are captured and further dragged by forced convection toward the center of the cavity, where they are remelted in the high temperature region. Therefore, till *t* = 300 s, equiaxed grains exist mainly at the upper right corner of cavity as seen in Fig. 4.12(c), where a very weak negative segregation appears (Fig. 4.12(d)). However, the flow field does not have visible change compared to the result at *t* = 150 s, because the buoyancy force at this stage is still too weak.

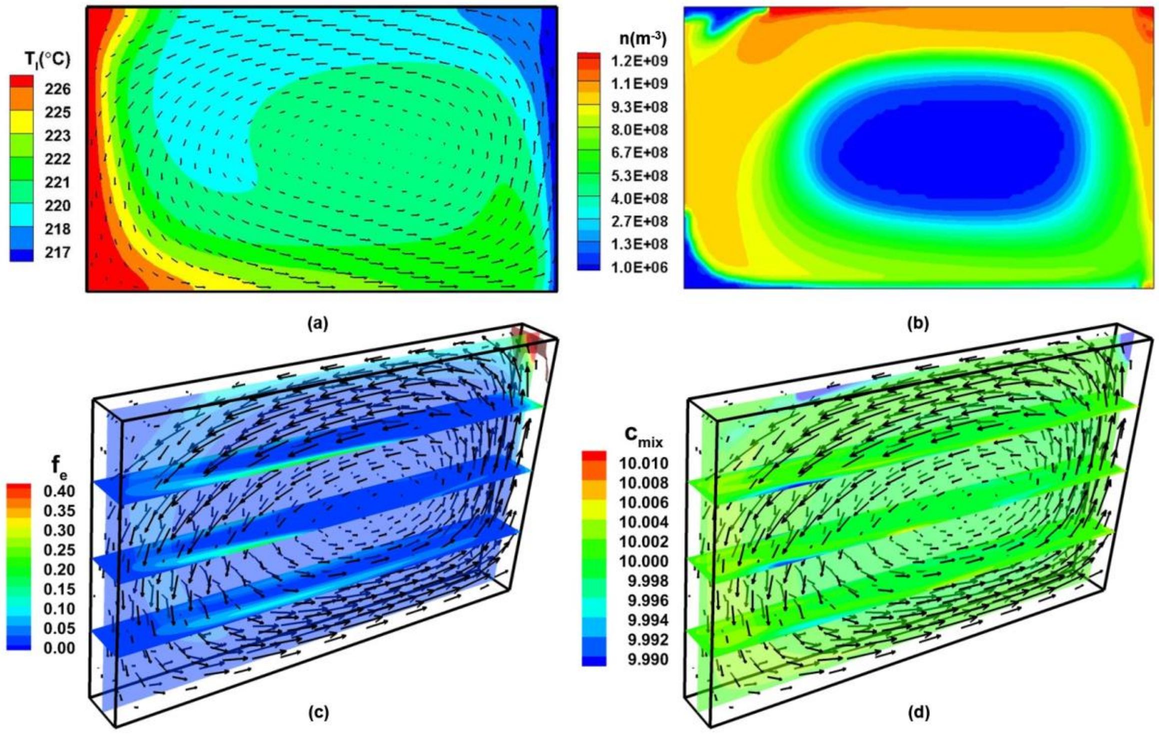

Fig. 4.12 Temperature distribution and liquid flow vectors (a), grain number density (b), grain fraction and grain velocity (c), and distribution of the concentration of Pb in the mixture and velocity in the liquid (d) at *t* = 300 s. Maximal velocities are (a) 49.04 mm s^{-1}, (c) 50.39 mm s^{-1}, and (d) 50.37 mm s^{-1}.

4.5.2 Oscillation of flow field in early stage, grain packing

As solidification progresses, because the enrichment of Pb makes the liquid phase at colder side denser, the thermo-solutal buoyancy force is strengthened and counteracts the effect of electromagnetic force. Gradually, the clockwise vortex expands from the upper left corner to the whole upper region of cavity. However, during this process, oscillations are observed in cooling curves as shown in Fig. 4.11. The oscillations continue for about 100 s, then the amplitude of oscillation becomes weaker with the time, indicating that the multiphase flow field tends to stabilize. Let us have a closer look at the moment when oscillations of the cooling curves were observed. The Fig. 4.13 shows the distribution of temperature, of the solid fraction overlaid with grain velocity, and of the intrinsic concentration in the extradendritic liquid c_l overlaid with velocity of the liquid $\vec{u}_l$ for three moments of time with interval of 10 second.

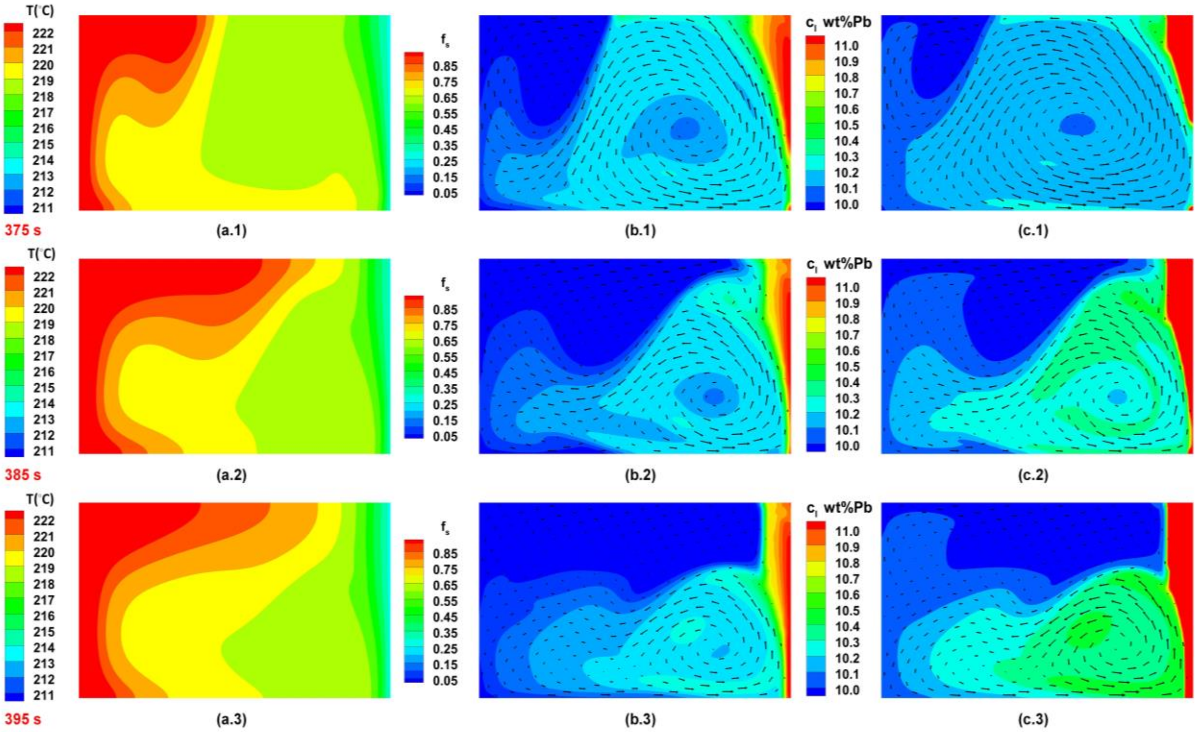

Fig. 4.13 Distribution of temperature (a.1, a.2, a.3), of the solid fraction with superposed field of grain phase velocity (b.1, b.2, b.3) and intrinsic concentration in extradendrtitic liquid overlaid with the velocity field in the liquid (c.1, c.2, c.3) for three moments of time indicated in the insert of the Fig. 4.8. Maximal velocity is 35 mm s^{-1} in all figures.

At this stage of solidification, the vortex caused by thermo-solutal convection occupies the upper-left part of the volume. The vortex enlarges and the speed of flow in this vortex increases due to rejection of the heavier solute (Pb) when grain nucleates and solidifies. This instantly damps the forced convection at the top and hotter fluid moves along the top of cavity toward the colder wall and this affects also temperature distribution in the cavity center. Yet, growing grains are moving downwards and to the left due to the interaction of the natural and forced convection in the liquid. That makes the source of the rejected Pb to move as well, consequently, the vortex of natural flow changes its position and starts to occupy mainly the upper part of the volume while the vortex of forced convection becomes stretched till the hotter wall in the bottom that brings the colder fluid to the cavity center and also alters again the motion of the growing grains and the source of the rejected Pb. This process of vortices' rearrangement repeats and causes oscillations in the cooling curves.

4.5.3 Grain movement and formation of segregation

When the volume faction of equiaxed grains attains packing limit $f_p^e = 0.637$, the grains next to the wall get packed and become immovable. Grains are brought upwards and survive at some distance from the colder wall, and grow up with the decrease of temperature in the volume. During the period from t = 350 s to 540 s the layer of packed grains extends downwards from the grain floating in the cavity, then leftwards. In Fig. 4.14(c), the interface between unpacked region and packed region is presented with a iso-surface $f_e = f_p^e$. Liquid flow in packed region becomes weak due to rapid increase of flow resistance in the mushy zone.

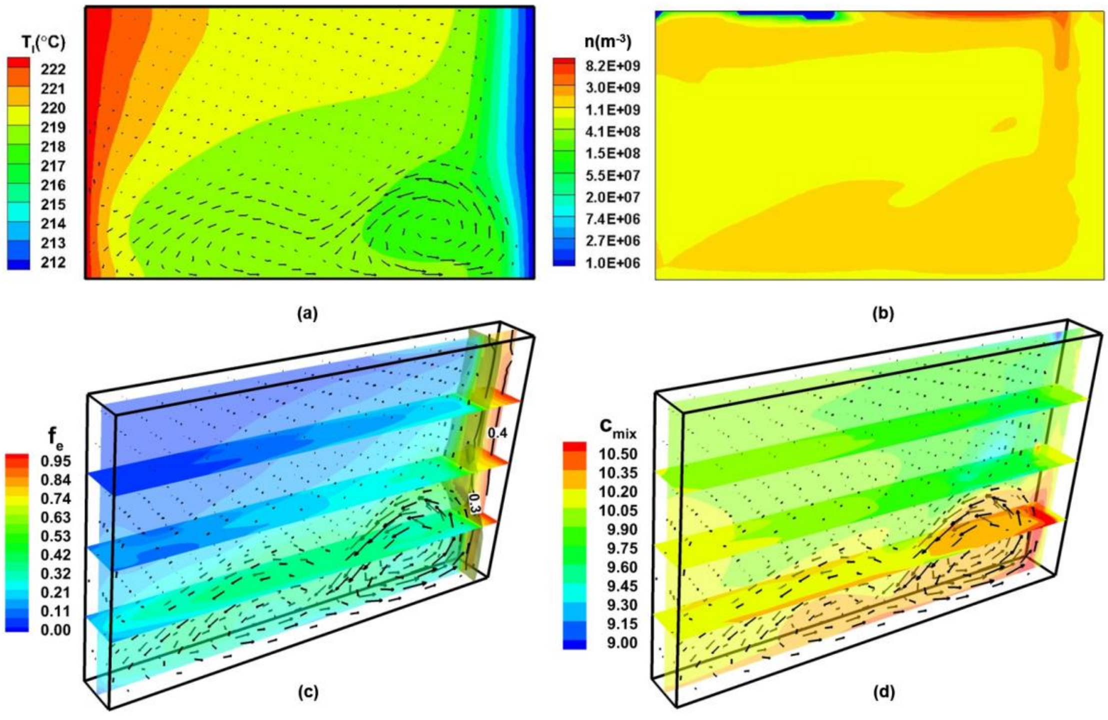

Fig. 4.14 Temperature distribution and liquid flow vectors (a), grain number density (b), grain fraction and grain velocity (c), and distribution of the concentration of Pb in the mixture and velocity in the liquid (d) at t = 540 s. Maximal velocities are (a) 31.07 mm s^{-1}, (c) 32.44 mm s^{-1}, and (d) 32.51 mm s^{-1}

At t = 540 s, the shape of the isotherms is clearly defined by two vortices existing in the liquid (Fig. 4.14(a)). The center and lower parts of cavity have almost uniform temperature whose value is close to the liquidus temperature of the alloy at its nominal concentration, T_L=219 °C. In fact, as it can be seen in Fig. 4.14(c), equiaxed grains exist in this region. Temperature value is maintained near the liquidus temperature due to the release of latent heat during grain growth in the region closer to the colder wall and also due to the heat absorption during grains' remelting in the region closer to the hotter wall. Because of this the temperature gradient at the right lateral wall is larger than at the left one.

Although most equixed grain phase is located at lower region of cavity, it is found that the grain number density has maximal value at the top. The grain layer at top forms mainly by the floatation of grains in cavity. During the time grains move up, their sizes get smaller because they are partly remelted in high temperature environment. These smaller grains are brought by downward flow at colder side to the bottom and increase the grain number density there. A region near upper left corner shows almost empty of grain, that means nuclei and grains were completely remelted by the rightwards melt flow there.

During solidification the heavy solute Pb rejected into the liquid phase makes the buoyancy effect more pronounced that alters forced convection. At t = 540 s, the vortex generated by electromagnetic force in the liquid is located only in a lower part of the cavity and has maximal velocity of about 32 mm s^{-1} (Fig. 4.14(c and d)). In fact, at this stage flow can be considered almost laminar. Yet, the intensity of the forced flow is sufficient to take the equiaxed grains away from the lower part of the colder wall, retarding their packing in this region. A layer enriched with Pb starts to form at the bottom of the cavity due to sedimentation of heavier liquid through the mushy zone (Fig. 4.14(d)). The concentration of Pb has a maximal instantaneous value at the highest point of the vortex of forced convection. Concentration in the center of the cavity is affected by the presence of grains which contain smaller amount of Pb and the zone slightly impoverished in Pb starts to form.

At t = 900 s, the isotherms gradually become vertical and less distorted (Fig. 4.15(a)). Due to the packing of equiaxed grains, the liquid flow becomes weaker thus the heat is transferred mainly by conduction. Although, temperature difference between the left and the right lateral walls exists, temperature is mostly uniform in the cavity, because its variation is concentrated near the colder (right) side. Around t = 900 s, the cooling rate at left lateral side gets slower, therefore, grains have more time to float up before getting packed, that is why the upper left corner and bottom of packed zone show large grain number density (Fig. 4.15(b)). A half of the cavity is filled with the packed grains which makes a ”rigid network” (Fig. 4.15(c)). Flow of the liquid between packed grains is weak but it contributes to final macrosegregation. Liquid enriched with Pb continuously flows downwards, depleting the upper part of the volume while enriching the lower part. Vortex driven by electromagnetic force still exists below the packed region, yet it is displaced to the warmer lateral wall and tends to shrink to the bottom. Another vortex is formed above the latter and occupies only small region near the hotter wall (Fig. 15(d)).

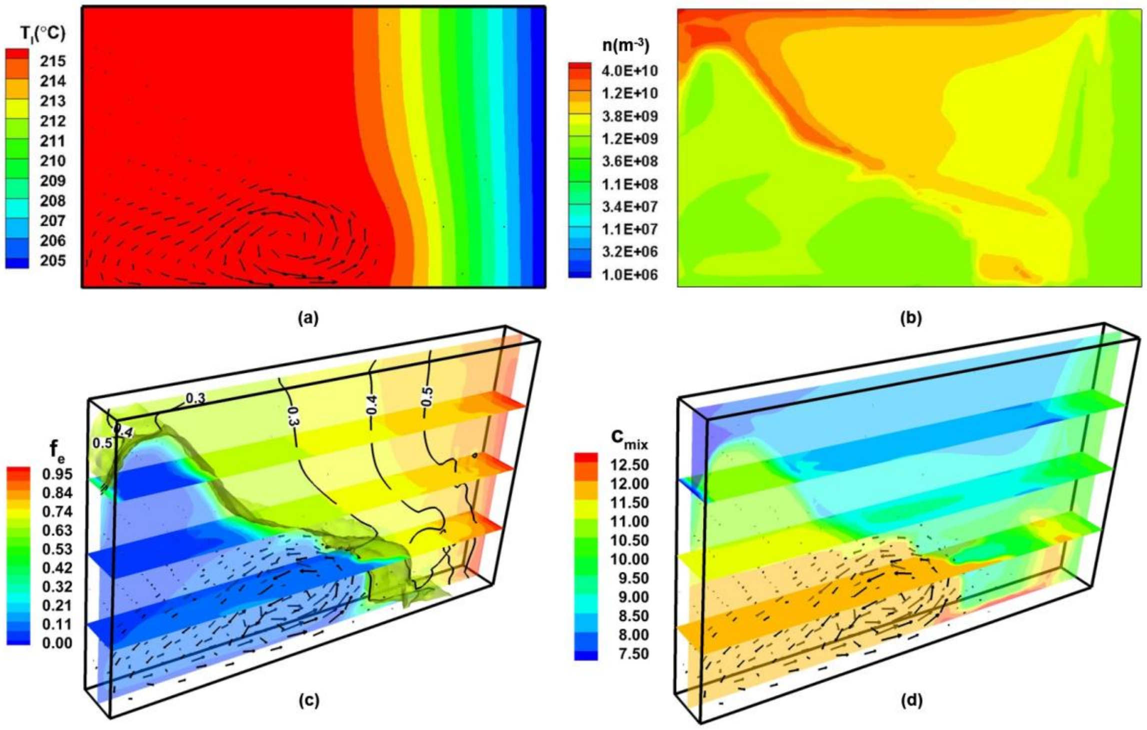

Fig. 4.15 Temperature distribution and liquid flow vectors (a), grain number density (b), grain fraction and grain velocity (c), and distribution of the concentration of Pb in the mixture and velocity in the liquid (d) at *t* = 900 s. Maximal velocities are (a) 28.91 mm s^{-1}, (c) 29.09 mm s^{-1}, and (d) 29.09 mm s^{-1}

At *t* = 1440 s, the temperature gradient at the colder wall decreases as presented in Fig. 4.16(a). It means that the latent heat release is stopped, i.e. liquid fraction becomes small in this zone. Yet the temperature gradient near the left lateral wall is small, indicating slow temperature decrease there. As seen in Fig. 4.16 (c and d), weak liquid flow still exists at the bottom layer with maximum velocity of only 0.1 mm s^{-1}. This part of liquid is highly enriched and requires lower temperature for solidification. Yet, since the flow is very weak and is constrained by surrounding solid, the character of the solute distribution formed by this moment can hardly be affected. Due to the high concentration of Pb in liquid near the bottom of cavity, the solidification there becomes quite slow. Grains is subjected to stronger buoyancy force and continuously float up to the boundary of the packed zone, forming a layer with larger grain number density there.

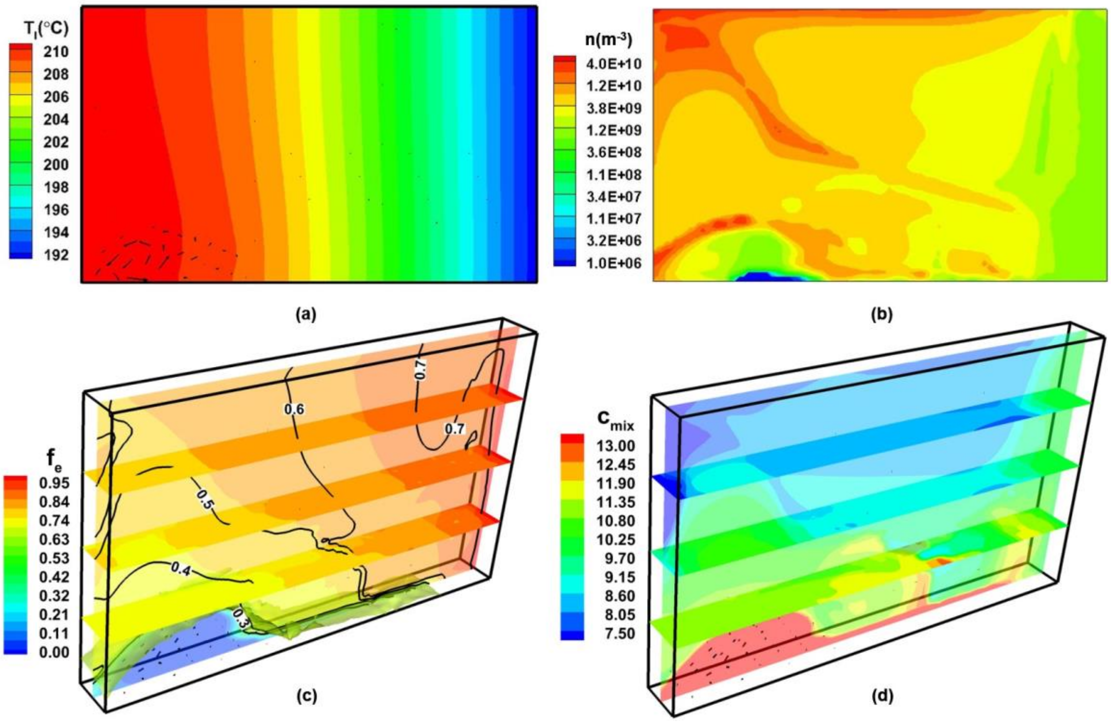

Fig. 4.16 Temperature distribution and liquid flow vectors (a), grain number density (b), grain fraction and grain velocity (c), and distribution of the concentration of Pb in the mixture and velocity in the liquid (d) at *t* = 1440 s. Maximal velocities are (a) 6.68 mm s^{-1}, (c) 7.63 mm s^{-1}, and (d) 6.68 mm s^{-1}

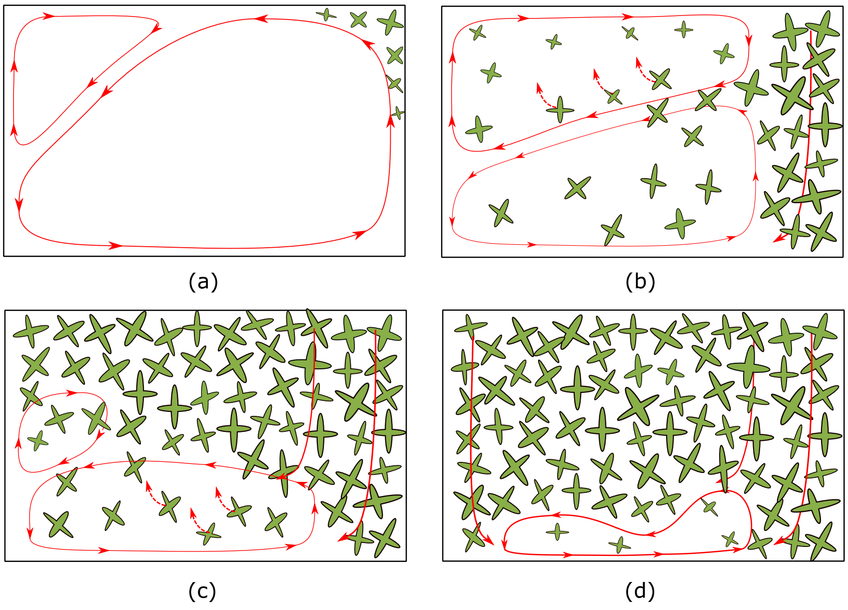

Fig. 4.17 Schematic figure of grain movement and flow mode at different solidification time: (a) 300 s - forced convection prevails in the cavity, small vortex of thermal buoyancy flow survives near the hotter wall at the top, (b) 540 s – forced convection is damped because of grains packed over the right boundary, less intense thermal and solutal natural convection occupy upper half of the cavity, (c) 900 s – packed grains occupy most of the cavity, only small vortices of natural and forced convection remain, enriched liquid descends through packed gains, and (d)1440 s – mainly descend of residual liquid remains

Overall, evolutions of grain growth and movement as well as liquid flow field during solidification are illustrated in Fig. 4.17. The nucleation and grain growth start from upper right corner where grains' packing also begins a little later. Grains which avoided packing are transported to the entire cavity, while packed zone extends over the whole colder side, then extends leftwards. Since free moving grains continuously float up due to their lower density, the packed layer grows from top to bottom. Descend of heavier enriched liquid during the whole solidification process causes enrichment with Pb near the bottom of cavity.

4.5.4 Density of grain number and macrosegregation map

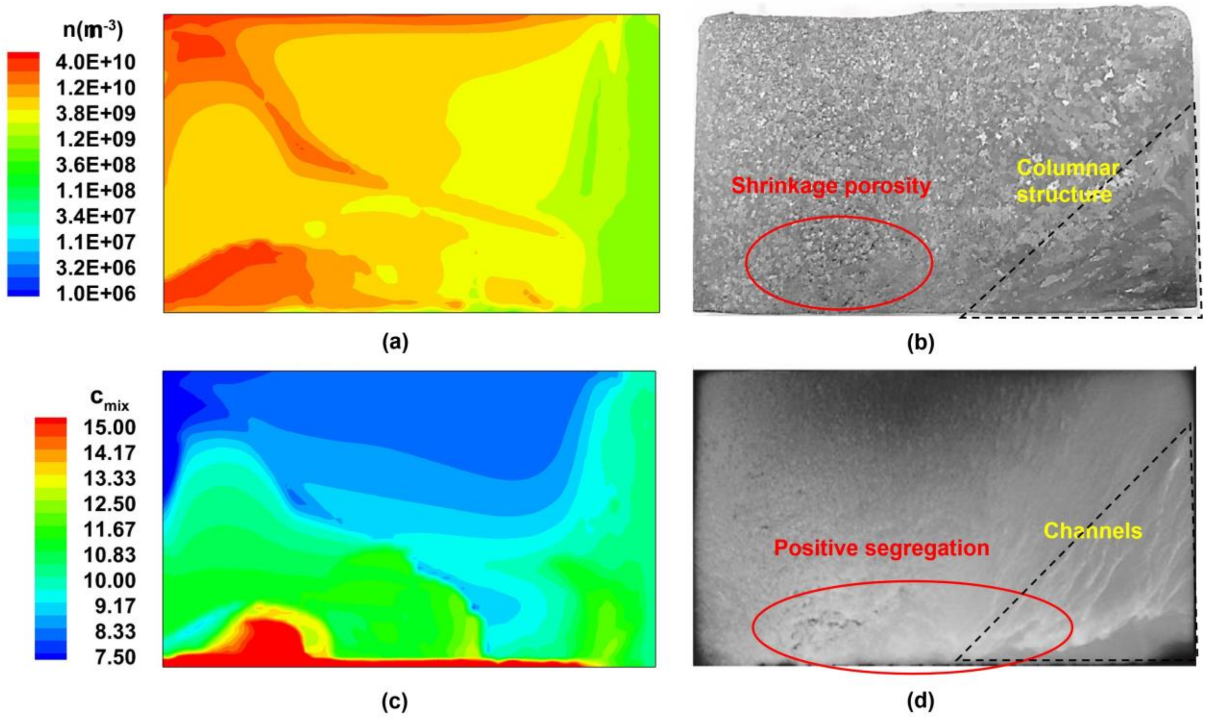

Fig. 4.18 Comparison between calculated and experimental results: (a) distribution of grain number density; (b) macrosegregation map; (c) solidification structure; (d) X-ray photo. Figures (b) and (d) are reprinted from publication [90]

It was mentioned in section 1.1.4 that EMS induced forced flow may "produce" dendritic fragments in melt, which further serve as nuclei of equiaxed grains. Some nucleation models aiming to quantitatively account the number of fragments under convection are under development and were briefly reviewed in section 2.3. Yet, in present work a simple nucleation model (Eq. (3.26)) was applied. Nucleation happens if the local constitutional undercooling is higher than a predefined one ΔT_{nucl} and the local grain number density is less than maximal value $n_{\max}$. Calculated distribution of grain number density displays almost monotone increase from the right (colder) wall to the left (warmer) wall along with a layer of high grain number density at the top (Fig. 4.18(a)). This corresponds to experimental result with quite fine equiaxed grains at the top of cavity, coarse grain structure near the colder side and finer one near the warmer (Fig. 4.18(c)). Such distribution can be explained by EMS driving flow which takes away grains from colder side toward the center while these grains tend to float up because they have smaller density than liquid phase. Also, at the bottom of cavity where the last stage of solidification occurs, simulation shows quite large grain number density. In experiment, this region is occupied by porosities because of shrinkage that also indicates that it was solidified at the end of the process.

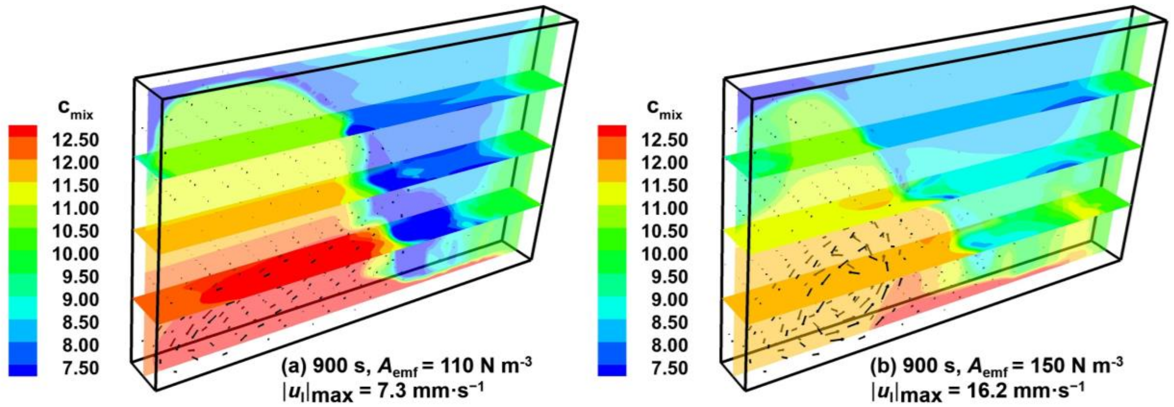

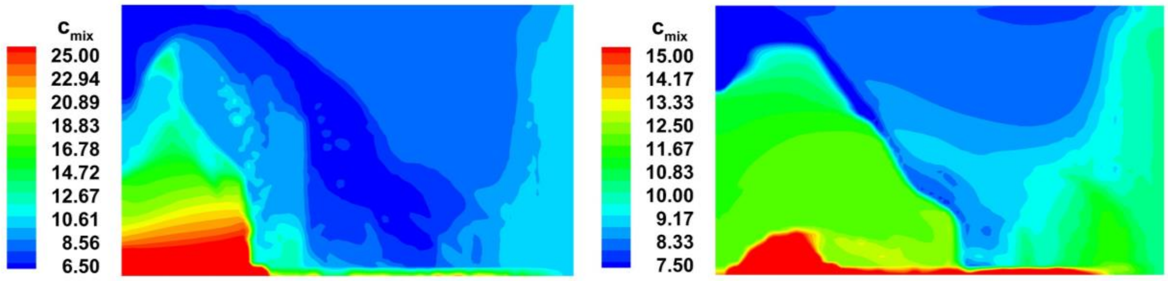

(c) 2000 s, A_{emf} = 110 N m^{-3} (d) 2000 s, A_{emf} = 150 N m^{-3}

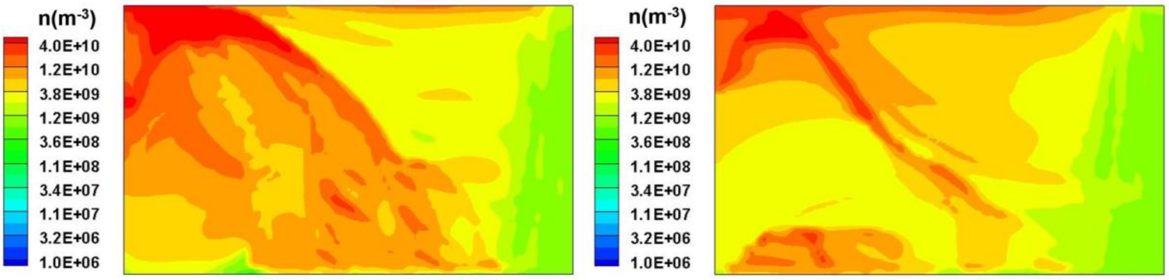

(e) 2000 s, A_{emf} = 110 N m^{-3} (f) 2000 s, A_{emf} = 150 N m^{-3}

Fig. 4.19 Effect of amplitude of electromagnetic force on final macrosegregation map and grain number density distribution

Final macrosegregation map displays variation of Pb concentration in the range from 7.5wt% to 15wt% with positive segregation at the center of the cavity bottom and region of negative segregation located at the top (Fig. 4.18(b)). Segregation at the bottom is formed due to the descend of enriched liquid during the whole solidification process. Interestingly this convective transport of solute becomes extremely significant through the growing packed grains. Segregation map obtained numerically agrees qualitatively with X-radiography of as-solidified sample benchmark (Fig. 4.18(d)). Some segregation channels at right lower corner are not reproduced in calculations that is probably related to the growth of columnar grains, which is not taken into account in current simulation. Indeed, since columnar grains are supposed to be attached to the boundary, they would resist fluid flow and would make it less intense. Hence, intensity of EMS driving flow could be overestimated in the present solidification model which considers only equiaxed grains. Quantitative comparison can be performed between calculated segregation map and results of ICP (Inductively Coupled Plasma) analysis of as-solidified sample presented in Fig. 11(c) of ref. [90]. Because of accumulation of Pb during solidification, a zone near the bottom remains liquid sate for a long time.

In order to understand the role of EMS, we performed calculations with different intensities of the electromagntic force. Grain number density and final macrosegregation patterns calculated with two other values of the adjustable coefficient A_{emf}= 150N m^{-3} and A_{emf} = 110N m^{-3} are shown in Fig. 4.19. Obvious differences can be observed between the three cases and the effect of intensity of electromagntic force on macrosegregation can be seen in two aspects:

(1) with EMS force decreases, the macrosegregation get stronger, because more enriched liquid descends with less resistance from EMS force;

(2) weaker EMS makes positive segregation region more displaced to the warmer wall. The reason is that EMS driving flow brings more grains from solidification frontier and replaces them with enriched liquid.

4.6 Conclusion

In present work a three-phase volume average equiaxed solidification model which accounts for the grains transport is applied for modeling of the AFRODITE experiment on solidification of Sn-10 wt% Pb alloy under the forced convective flow driven by EMS. Main observations and results can be summarized as follows. Electromagnetic force created in the liquid during the process drives fluid flow in the direction opposite to the action of thermo-solutal buoyancy force. The flow is slightly turbulent before solidification starts. With rejection of heavier solute due to solidification, the forced flow is damped and natural convection starts to occupy larger volume in the cavity. Interaction between the two vortices causes temperature oscillations and defines the shape of a zone with negative segregation at the top of the cavity. When equiaxed grains get packed, downward flow of highy enriched liquid through the rigid structure leads to accumulation of Pb at the bottom. The shape of the zone with a positive segregation is defined by the action of the electromagnetic force. Macrosegregation map obtained in simulation is similar to the pattern observed with X-Ray radiography of the solidified sample except a small zone where columnar growth happened.

Although the model provided results close to experimental one, multiple questions arises concerning numerical parameters and closure relations. One of them, related to the closure relation for growth parameters of dendrite grains as well as drag coefficients in case of turbulent flow was already mentioned above. To these questions joins also turbulence damping inside the mushy zone. Another question concerns macroscale electromagnetic force. Generally, electrical conductivity of solid can be several times higher than of liquid. During solidification this factor is not important in the beginning of the process because the solid fraction is small, therefore, variation of induced magnetic field and electric current inside the solidifying volume due to presence of the solid grains is negligible, the same is true for the results of the Lorentz force. Yet, induced fields should be altered if grains with rather high solid fraction accumulates in macro-groups. It could be supposed that in this case the local variation of the electromagnetic force acting on grains is not important because at high fractions the grains are packed while their solid fraction can be still small. Yet, local variation in conductivity can affect force distribution everywhere in the volume, i.e. including the pure melt. Furthermore, it is generally supposed that electromagnetic stirring promotes fragmentation of dendrites and these fragments serve as nucleation sites or already present equiaxed grains. This can be introduced into the model using various assumption [23,178]. In the present work this phenomena was not taken into account to decrease number of uncertain parameters, yet, it deserves further study.

Chapter 5 Use of equiaxed solidification model to simulate macrosegregation of industrial ingot

Manufacturing of large-size ingot is a fundamental process in industrial production of heavy machinery. Numerical simulation is a main tool for revealing mechanisms that lead to appearance of these defects with aim of optimizing the process. Most solidificaion models assume that the solid phase is fixed and segregation is originated only from transport of solute through long distance liquid flow and remelting of solid [133]. However, it should be noted that nucleation, growth and movement of equiaxed grains are important factors affecting macrosegregation. The author of the present thesis sincerely believes that the development of equiaxed models [40,86,109,179] was strongly motivated by their use in modeling of ingot solidification. Futhermore, three-phase columnar and equiaxed models [24,128,131,180], as well as models with an even greater number of phases [181] began to be exploited. Although these models allow some insight into the origin of various zones that form in the ingot [93], it must be accepted that these simulations are very sensitive to the choice made for closure relations and numerical parameters . On the other hand, application of pure equiaxed models with regard to large ingots was studied only for a very limited combination of parameters. In chapter 3, we presented a three-phase equiaxed solidification model that accounted for the growth of equiaxed grains, their motion, and formation of macrosegregation. In chapter 4, this model was validated through numerical simulation for benchmark solidification of a Sn-10 wt% Pb alloy in the AFRODITE set-up.

In this chapter, based on the three-phase equiaxed solidification model, solidification of a 2.45 ton ingot is simulated and the effect of some process factors is investigated. In section 5.1, problem description is introduced and parameters used in modeling process are given. In section 5.2, results of numerical simulation are analyzed and compared with experimental results. The role of moving equiaxed grains in formation of macrosegregation is analyzed. In section 5.3, effect of cooling intensity on the macrosegregation results is studied.

Electromagnetic stirring (EMS) has been applied in a number of solidification processes, including direct chill (DC) casting [182], Bridgman furnaces [183], and most commonly in continuous casting processes. It has been proved that EMS can relieve segregation in both microscale and macroscale. In section 5.4, the effect of EMS on solidification of ingot is preliminarily investigated through numerical simulations.

5.1 Configuration of ingot and calculation parameters

Numerical simulation is used to predict macrosegregation in a 2.45 ton steel ingot that corresponds to a cast experiment made some time ago [93]. Hereafter we suppose that the composition of the ingot is presented as a binary alloy Fe–0.45 wt% C. The ingot was cast in a chill mold which had height of 1.448 m. The ingot had pyramid shape with square in a basis whose side size varied from 0.432 m at the bottom to 0.483 m at the top of chill, as schematically illustrated in Fig. 5.1(a). The computational domain and mesh are presented in Fig. 5.1(b).

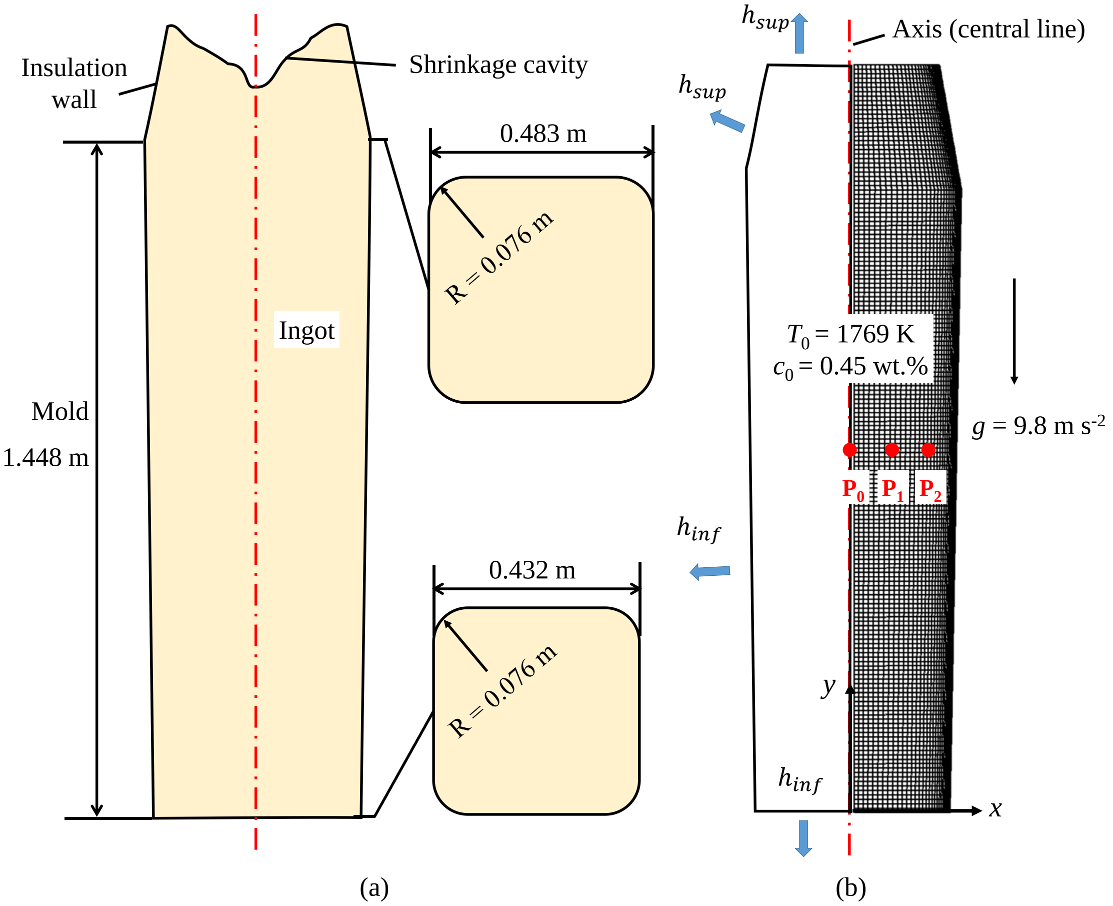

Fig. 5.1 Schematic of 2.45 ton ingot with indication of sizes [93] (a) and corresponding calculation domain (b). The initial conditions for the simulations are T_0 = 1769 K, c_0 = 0.45 wt%, and zero velocities in the liquid. The two coefficients for convective heat exchange, are h_{sup} and h_{inf}, with the upper and lower parts of the ingot surface defining the intensity of convective heat removal from the ingot as $h_{sup}(T - 373\text{ K})$ and $h_{inf}(T - 373\text{ K})$ for these parts, respectively. The indicated points P_0, P_1, and P_2 serve for the analysis of the calculation results

For the current simulation, only the ingot is taken into consideration without surrounding multi-layer mold, and a 2D axisymmetric geometry is used to approximate three-dimensional shape of the ingot. Most of the mesh cells have general size of 1 cm × 1 cm but cells near the cooling boundary were refined to 0.2 cm × 1 cm for more precise calculation of thermal gradient, dynamic boundary layer and related transport processes. At the beginning of simulation, the hot metal in mold is supposed to be still and of uniform temperature of 1769 K, i.e. overheated by ~0.1 K with respect to its nominal liquidus temperature. Cooling conditions are applied directly to ingot's surface and are written via convective heat exchange accounting for heat transfer through different construction elements. Similar to the ref. [131], external temperature is set to 373 K and two different convective heat transfer coefficients are applied: $h_{sup} = 30\ \mathrm{W\ m^{-2}K^{-1}}$ in upper zone and $h_{inf} = 300\ \mathrm{W\ m^{-2}K^{-1}}$ in lower zone. The boundary and initial conditions are indicated in Fig. 5.1(b).

It was found in experiment that a layer of columnar grains appeared near the ingot surface and the thickness of this layer depends upon the initial temperature of the melt, nature of mold, size of ingot and composition of steel. Yet, in current simulation, only equiaxed solidification structure is taken into consideration. In present equiaxed solidification model, multiphase flow, energy transport, grain growth and solute transport are coupled within volume average method. As it was presented above in chapter 3 and 4, three phases are defined: solid phase (*s*-phase), interdendritic liquid phase (*d*-phase), and extradendritic liquid phase (*l*-phase). When accounting for multiphase flow, only two moving phases are distinguished: extradendritic liquid corresponding to *l*-phase and equiaxed grain phase (*e*-phase) that is actually composed of united *s*-phase and *d*-phase. The growth rate of equiaxed grain is calculated by LGK model [145] (given in chapter 3 with Eq. (3.17)) while solid phase growth is defined by solute transport rate (Eq. (3.23) and (3.24)). Yet, the equation for nucleation rate was updated similar to ref. [40] and is presented in the form of Eq. (5.1). The latter means that, grain number density of $n_{max} = 2 \times 10^9\ \mathrm{m^{-3}}$ is generated per unit of time in those cells of the mesh where the local undercooling is greater than nucleation undercooling for the first time, or where the local grain density is less than $1\ \mathrm{m^{-3}}$ and local temperature is below nucleation temperature.

$$N_\phi(t) = \begin{cases} n_{max}/\mathrm{dt} & \text{if } \Delta T > \Delta T_{nucl} \text{ and } \displaystyle\int_0^t N_\phi \,\mathrm{d}t = 0 \\ n_{max}/\mathrm{dt} & \text{if } \Delta T > \Delta T_{nucl} \text{ and } n < 1 \\ 0 & \text{else} \end{cases} \tag{5.1}$$

Multiphase flow is solved with Eulerian model existing in ANSYS FLUENT ® with modification of some terms as was explained above in chapter 3. Similar to ref. [40], equiaxed grains are assumed to be blocked at a grain fraction of 0.4. The equations for physical fields conservations and micro-scale exchange rates and solution procedures have been detailed in chapter 3 and can be found in Table 3.2 or 3.3. Thermodynamic and physical properties of the Fe-C alloy are listed in Table 5.1. The two time step solution algorithm (detailed in section 3.4.2) is applied with time step size d*t* of 0.01 s and the number of sub-steps *N* of 20.

5.2 Simulation results

For a clear vision for the ingot solidification process, in this section, at first we present the temperature field, nucleation and grain growth, then investigate the macrosegregation formation mechanism, after that a comparison between calculation and experiment measurement is made.

Table 5.1 Thermodynamic and physical properties

Property	Symbols	Units	Quantity	Ref.
Melting point of pure iron	T_f	K	1805.15	[40]
Liquidus slope	m	$K(wt\%)^{-1}$	-80.45	[40]
Equilibrium partition coefficient	k	1	0.314	[40]
Reference density	ρ_{ref}	$kg\ m^{-3}$	7200	[184]
Solid–liquid density difference	$\Delta\rho$	$kg\ m^{-3}$	200	
Specific heat	c_p^l, c_p^e	$J\ kg^{-1}K^{-1}$	725	[185]
Thermal conductivity	κ_l, κ_e	$W\ m^{-1}K^{-1}$	34	[40]
Latent heat	L	$J\ kg^{-1}$	2.72×10^{5}	[185]
Viscosity	μ_l, μ_e	$kg\ m^{-1}s^{-1}$	4.2×10^{-3}	[40]
Thermal expansion coefficient	β_T	K^{-1}	1.07×10^{-4}	[40]
Solutal expansion coefficient	β_c	$(wt\%)^{-1}$	1.4×10^{-2}	[40]
Maximal grain number density	n_{max}	m^{-3}	2.0×10^{9}	[131]
Grain packing limit fraction	f_p^e	1	0.4	[40]
Secondary arm spacing	λ_2	m	5.0×10^{-4}	[40]
Shape factor for tip growth	ϕ_M	1	0.18	[151]
Sphericity	ϕ_J	1	0.53	[151]
Diffusion coefficient (liquid)	D_l	m^2s^{-1}	2.0×10^{-8}	[40]
Gibbs-Thomson coefficient	Γ	m K	1.9×10^{-7}	[186]

5.2.1 Nucleation and grain growth

According to the variation in the convective heat exchange coefficient along the ingot surface, the coldest zone formed at the bottom corner (Fig. 5.2(a)) and the very first grains nucleated there when local temperature dropped below the liquidus temperature. Then nucleation extended over the bottom, sidewall, and top of the ingot, as presented in Fig. 5.3(a-b), via the distribution of the grain number density. Although redistribution of the grain number density due to grain sedimentation was observed near the top boundary (Fig. 5.3(a)), after a while these grains were dispersed into bulk liquid (Fig. 5.3(b-c)). The liquid near the chilled boundary and the nucleated grains moved downward, the former as a result of buoyancy due to the temperature difference, the latter due to drag force from the liquid and the imposed density difference between solid and liquid. Indeed, although the solid fraction was very small at 20 s and 50 s, after cooling started, the grains moved faster than liquid, as presented in Fig. 5.4(a-b). Due to strong cooling, the temperature near the ingot surface decreased rapidly and melt undercooling remained high, meaning that the grains descending along the wall grew quickly. Once grain volume fraction reached the packing limit value, the grains became attached to the wall or to the already packed layer and became immovable.

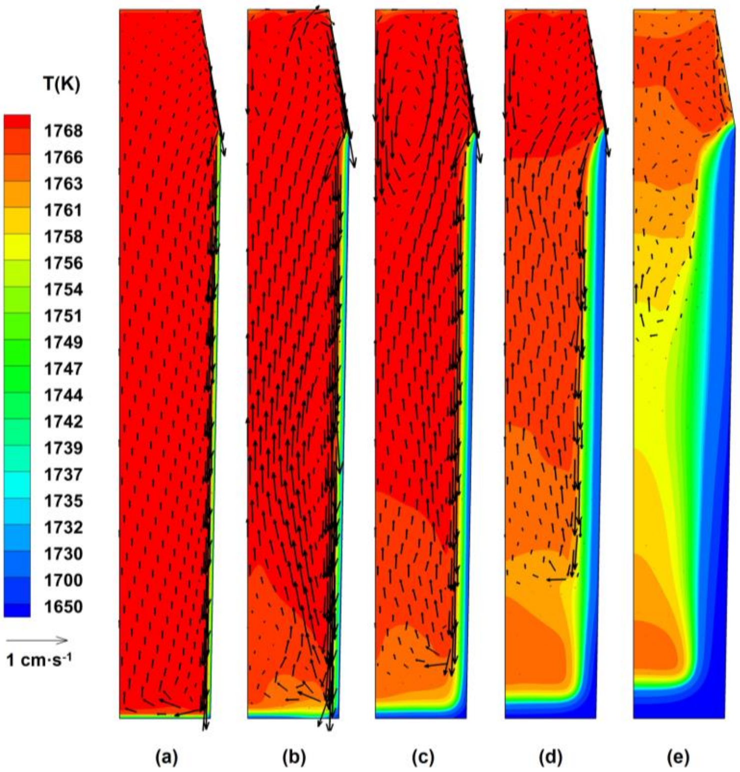

Fig. 5.2 Temperature distribution and velocity vectors of liquid phase at different solidification times: (a) 20 s, (b) 50 s, (c) 100 s, (d) 200 s, and (e) 400 s

At *t* = 20 s, a thin packed layer was mainly located near the bottom and lower sidewall, as seen in Fig. 5.4(a). Some grains descended to the bottom of the volume before being “captured” and may have accumulated there. However, the melt flow changed direction at the bottom of the ingot, moved toward the central axis, and rose to the middle region of the ingot.

Consequently, some grains were dragged upward by the flow (Fig. 5.3(b)), but with lower velocity (Fig. 5.4(b)). It can be noted that the grain number density in the layer packed over the sidewall was slightly below the maximal value $n_{\max} = 2 \times 10^9$ m^{-3}, whereas at the ingot bottom and central axis this value could locally be as high as 6×10^9 m^{-3}.As the packing layer at the sidewall thickened, the temperature gradient and thermal buoyancy force at the solidification frontier decreased. The downward velocity of the liquid slowly decreased with time while the gravity force acting on the free-floating grains increased as they grew.

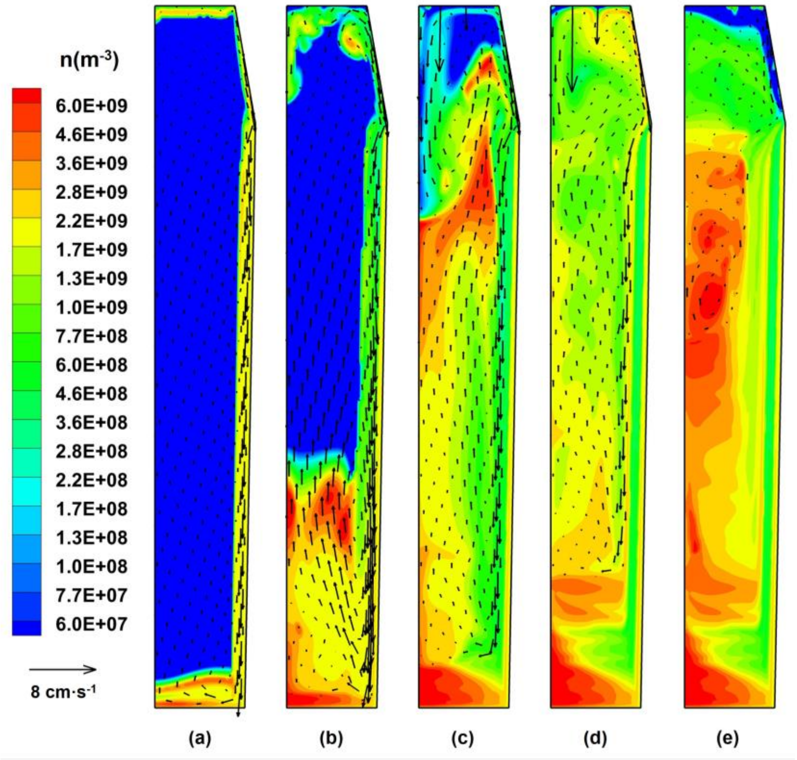

Fig. 5.3 Grain number density distribution and velocity vectors of grain phase at different solidification times: (a) 20 s, (b) 50 s, (c) 100 s, (d) 200 s, and (e) 400 s

At t = 100 s, the equiaxed grains ahead of the packed layer continuously descended to the bottom region, whereas the incoming flow from the upper region had virtually no nuclei or grains. Because of the descend of cold melt/grains near side wall, the temperature decrease rate near bottom is faster than the one near side wall. However, vertical temperature gradient is smaller than horizontal one (Fig. 5.2(c)). In fact, the grain number density was low in these cells but remained above the 1 m^{-3} that prevents new nucleation there. Consequently, the grain number density in the region within 1 cm to 4 cm from the lateral surface was less than the mean value (Fig. 5.3(c)). The lack of equiaxed grains in this region can explain why, in real ingots, the corresponding location is occupied by a columnar structure. At t = 100 s, a large grain number density was also observed in the upper region of the ingot, whereas the grain phase was mainly concentrated in the lower region (Fig. 5.4(c)), indicating that a large number of small grains were dragged by the central upward flow. On the contrary, some larger equiaxed grains sedimented to the bottom since the buoyancy term related to their heavier mass prevailed over the upward drag force from the melt and piled up at the ingot center. This could be observed by grain number density at the ingot bottom, which was in the range of $3\times10^9 \sim 6\times10^9$ m^{-3} (Fig. 5.3(c)), and by the grain fraction distribution (Fig. 5.4(c)).

As discussed below, solutal convection started to affect liquid phase flow after 100 s and supported the ascending melt flow near the central axis. At the same time, solid growth increased the mass of equiaxed grains, meaning that the grains in the upper region tended to fall down and continuously pile up toward the top of the ingot (Fig. 5.3(d) and Fig. 5.4(d)). At t = 400 s, equiaxed grains had filled most of the volume in the chill mold. At a later stage, solidification slowed down as the heat transfer rate in the hot top region was much lower. Finally, at about t = 1000 s, the whole ingot was fully filled by packed grain, but solidification continued for a long time until the temperature dropped below the eutectic temperature of 1461.37 K [103]. However, we stopped the calculation at this stage because the grain distribution and macrosegregation would then barely change due to the very weak flow of residual liquid in the packed zone.

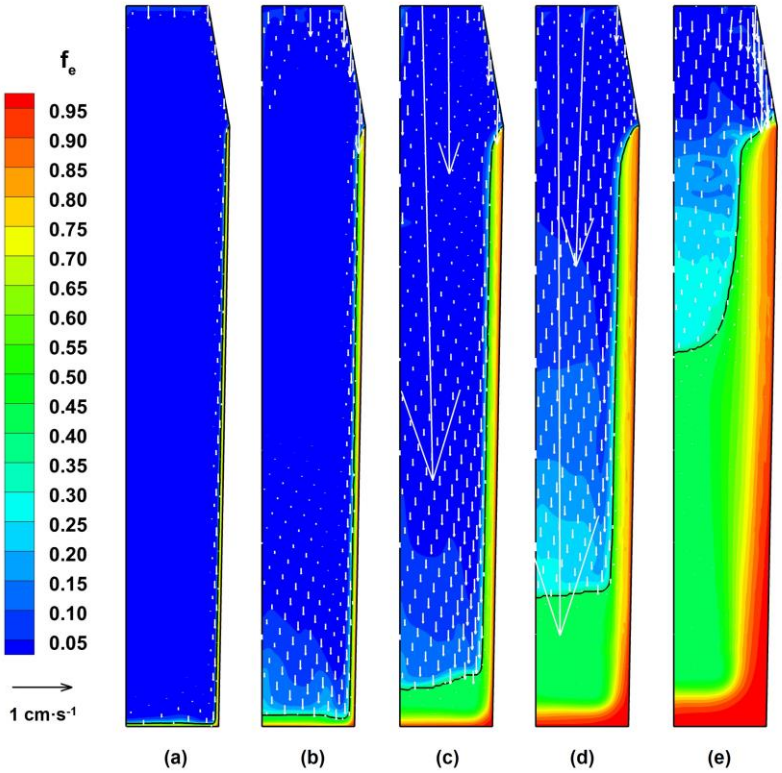

Fig. 5.4 Grain phase fraction distribution relative velocity vectors between grain phase and liquid phase at different solidification times: (a) 20 s, (b) 50 s, (c) 100 s, (d) 200 s, and (e) 400 s

5.2.2 Macrosegregation formation

The segregation in the ingot is described by segregation index (Seg. Index, or SI), which can be formulated by Eq. 5.2:

$$\mathrm{SI} = \frac{c_{mix} - c_0}{c_0} \tag{5.2}$$

where the solute concentration for the solid and liquid mixture c_{mix} is calculated as the sum of the averaged concentration in the grain phase and extradendritic liquid weighted with corresponding volume fractions: $c_{mix} = f_e c_e + f_l c_l$.

To understand the evolution of the segregation pattern presented in Fig. 5.5, it should be borne in mind that solute is rejected at the interface between the solid phase and the interdendritic liquid and is transported to the extradendritic liquid according to the evolution of the fraction corresponding to the interdendritic liquid and by diffusion. In the model, the effect of convective flow on boundary layer thickness around the envelope surface is taken into account. Further distribution of the solute in the bulk is defined by the flow of extradenritic liquid, which is affected by thermal and solutal buoyancy force, as well as by grain motion.

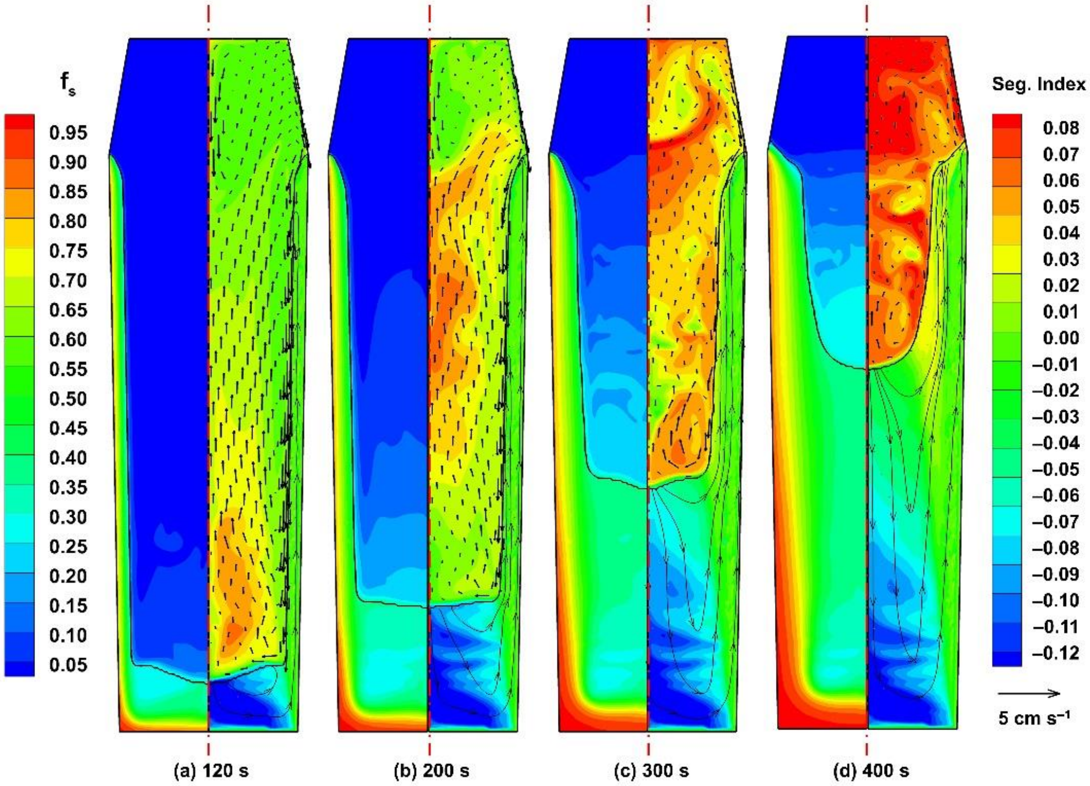

Fig. 5.5 Solid phase fraction distribution (left half) and distribution of the solute concentration in the mixture overlapped by streamlines of fluid flow in packed region and by velocity vectors of liquid phase in unpacked region (right half) at different solidification times: (a) 120 s, (b) 200 s, (c) 300 s, and (d) 400 s. The black line indicates the interface between the packed and unpacked regions

At the initial cooling stage, when both extradendritic liquid and grains descended along the wall, equiaxed grains grew but the solid fraction remained small. Consequently, little solute was rejected at this stage. The growth of the solid phase became noticeable inside the packed layer, mainly at the bottom, leading to the emergence of a "plume" near the central axis at 120 s, with an ascending flow as the extradendritic liquid enriched with carbon became lighter (Fig. 5.5(a)). The upward flow inside the packed layer over the sidewall could probably be attributed to the pressure effect rather than to solutal buoyancy. However, to confirm this statement, additional parametric studies would be required. This flow was very weak since it occurred between grains whose fraction was within the range of 0.6 ~ 0.9, and provided strong resistance to the flow. The instantaneous segregation pattern presented at t = 200 s was defined by the redistribution of solute, which was continuously rejected by the solid phase growing in a lower ingot region, due to the upward flow of extrandendritic liquid. The latter was supported by solutal buoyancy but was counteracted by a drag force from descending grains (Fig. 5.5(b)). Since the local value of solutal gravity was dependent on the solute distribution in the liquid and varied with time, it may have been balanced by the downward drag force or even conceded to the latter. This led to oscillation of the vertical component of velocity in the liquid in the central part of the ingot, resulting in negative segregation in the form of a "Christmas tree." Similarly, at a later stage (300 s and 400 s, Fig. 5.5(c-d), respectively), the clockwise vortex just above the packed layer was the result of upward solutal convection and the downward motion of grains. Incipient formation of vertical channels could be observed at t = 300 s (Fig. 5.5(c)) at the edge of the packed layer, where the solid fraction increased (~0.3), whereas the extradendritic liquid flow still had a velocity in the order of several millimeters per second.

As mentioned above, we believed that the final segregation pattern could be evaluated at t = 1000 s (Fig. 5.6(c)), since by that time the ingot was filled with packed grains with a fraction of more than 0.4 for most of the volume. Consequently, residual flow between the grains was negligibly small (~10^{-12} m s^{-1}) and practically did not affect distribution of the solute at the later solidification stage. As proof, it can be noted that the segregation pattern at the bottom part of the ingot did not change between t = 400 s (Fig. 5.5(d, right) and t = 1000 s (Fig. 5.6(c, left), (note that the color scale is slightly different between the indicated figures), but changes occurred in the upper part of the ingot where grains were not yet packed at t = 400 s.

Note that in Fig. 5.6(c), results obtained with two different grids with cell sizes of 5 mm × 5 mm and 10 mm × 10 mm are presented. Similar to previously reported studies, mesh size did not severely affect macrosegregation distribution. Rather, the difference related to mesoscale in terms of the number and location of the segregation channels at the upper part of the ingot and in the bottom zone of negative segregation. Thus, simulation with both grids showed vertical segregation channels (Fig. 5.6(c)), the formation of which started at $t = 300$ s. However, with coarser mesh these channels were less pronounced and had a different configuration. It should be stressed that qualitatively similar vertical segregation lines were also observed in experiments near the columnar-equiaxed transition line (Fig. 5.6(b)).

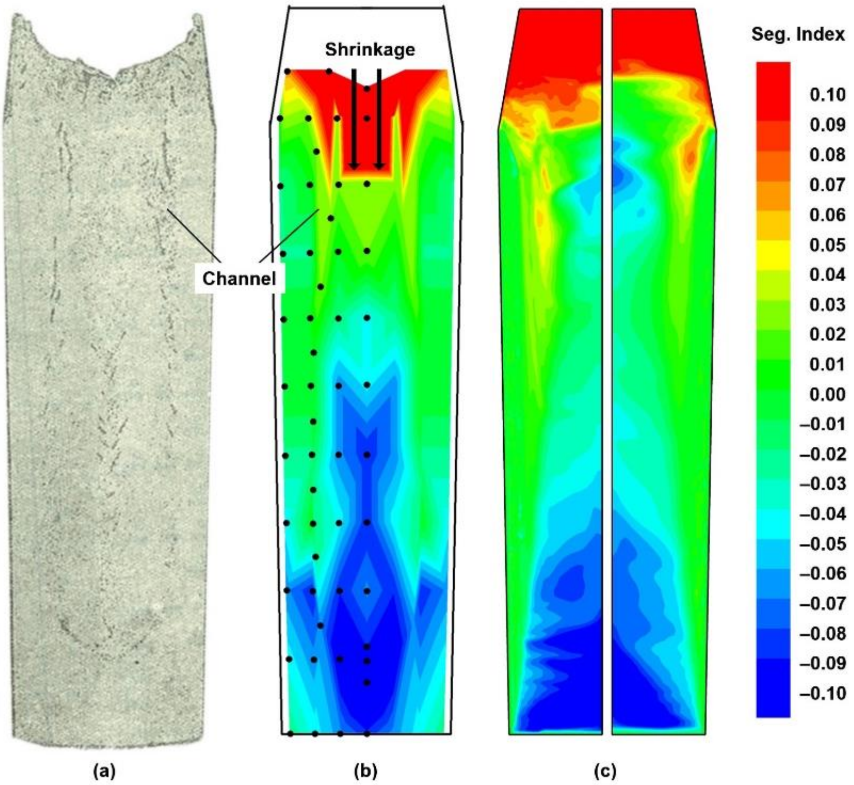

Fig. 5.6 Comparison of macrosegregation map between experiment and calculation: (a) Sulphur print [93], (b) measured carbon segregation index [93], (c) calculated carbon segregation index at $t = 1000$ s. Left: fine mesh. Right: coarse mesh

The shape of the negative segregation zone obtained in the simulation was different than the reported one. In our opinion, this can be attributed mainly to the uncertainty of the boundary conditions that governed tem-perature distribution in the bottom corner of the ingot. Furthermore, the lack of measurements close to the ingot bottom did not really permit comparisons in the bottom vicinity. The discrepancy in height of the negative segregation zone between the experiments and the calculations probably indicates that interaction between ascending solutal flow and grain sedimentation was not extremely well reproduced. Yet again, this can be attributed to boundary conditions, since variation in cooling intensity clearly affected the height of that zone (Section 5.3). However, another option is the effect of shrinkage during solidification, which was not taken into account in the mod-el and which could affect the flow of both phases when the solid fraction starts to de-velop. Moreover, an air gap may appear between the casting and the mold due to shrinkage, thereby increasing thermal resistance at the cooled wall and altering boundary conditions. Finally, it is clearly shrinkage that affected segregation at the last solidification stage in the experiment and that defined solute distribution in the upper part of the ingot. Consequently, comparison was not really possible for this zone. We discuss the role of columnar dendrites in our conclusion.

A comparison of the segregation index along the central line between the calculation and the measurement (Fig. 5.7) shows that the calculation accurately reproduced a general trend detectable in the measurements, i.e., negative segregation in the lower region and positive segregation in the upper region. Macrosegregation distribution along the central line predicted by the present model was compared with that carried out for the same-sized ingot with a three-phase mixed columnar-equiaxed model [131], in which equiaxed dendrites were considered globular. Similar to results reported elsewhere for 3.3 ton ingots [103,110], negative segregation at the centerline obtained with globular equiaxed grains was strongly overestimated [131], whereas results with the proposed description matched more accurately with the experiment.

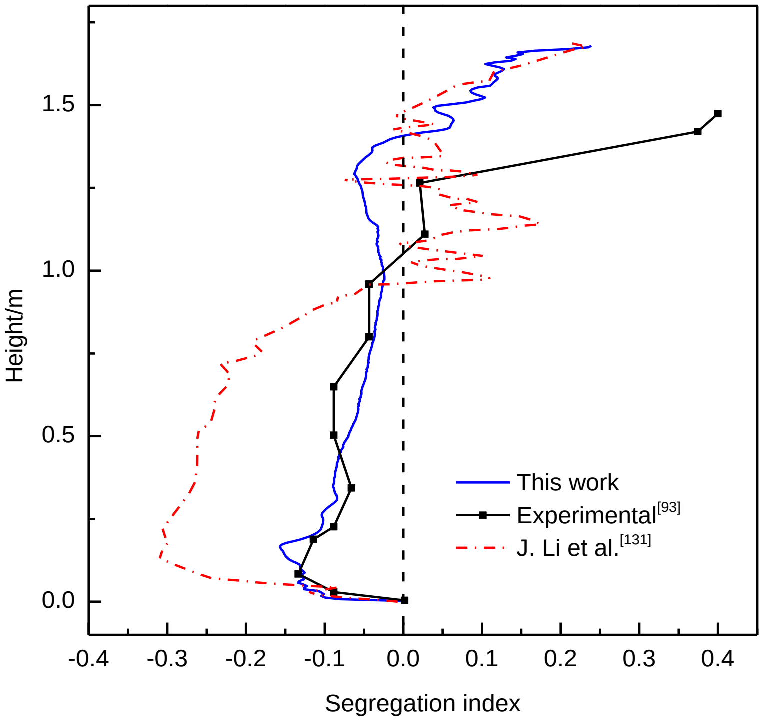

Fig. 5.7 Comparison for distribution of segregation index along central line of ingot between calculation, experimental measurement [93], and Li et al.'s work [131].

5.3 Effect of cooling intensity of mold

It has long been understood that an increase in ingot size favors macrosegregation formation. It has been demonstrated numerically that a special cooling procedure [187] or an increase in cooling rate [188] could alleviate macrosegregation. However, the effect of the cooling rate was studied with a fixed solid phase. In this section, we present a study aimed at verifying the effect of surface cooling intensity on final carbon macrosegregation with an equiaxed model. Initial conditions and ambient temperature remained the same as in the previous section, but the heat transfer coefficient h_{inf} was set to 100 W $m^{-2}K^{-1}$, 300 W $m^{-2}K^{-1}$, 600 W $m^{-2}K^{-1}$, and 1000 W $m^{-2}K^{-1}$, respectively. Although it is virtually impossible for the latter value of the heat transfer coefficient to be reached in industrial conditions, because this value was considered earlier [188] it is kept here as an illustration of a limiting case.

5.3.1 Macrosegregation

For all heat transfer coefficient values, the final distribution of the carbon concentration (Fig. 5.8) presented positive segregation at the upper region of the ingot, which remained hot for a long time and was the last to solidify, and a negative cone near the ingot bottom. However, as the value of h_{inf} increased, the volume of ingots with very low segregation, $-0.02 \leq \mathrm{SI} \leq 0.03$, also increased, whereas the height of the negative segregation cone at the bottom decreased. The positive segregation channels, discussed in section 4.2, were also observed for higher values of the heat transfer coefficient (Fig. 5.8(c-d)). However, their locations were transferred deeper into the ingot core, i.e., they moved closer to the axis of symmetry and farther from the top of the ingot. In Fig. 5.9, variation of segregation index along the central line is presented for four calculation cases. The results indicate that macrosegregation is decreased by enhancing the cooling intensity.

5.3.2 Flow field

Flow fields of l-phase obtained at t = 100 s in calculations with different values of convective heat exchange coefficient are compared in Fig. 5.10. When the cooling intensity increased, the grain growth near side wall was faster and thus the grain packed layer there was thicker. The packed layer resisted the global flow field, therefore, at this time, the downward velocity decreased with increase of h_{inf}.

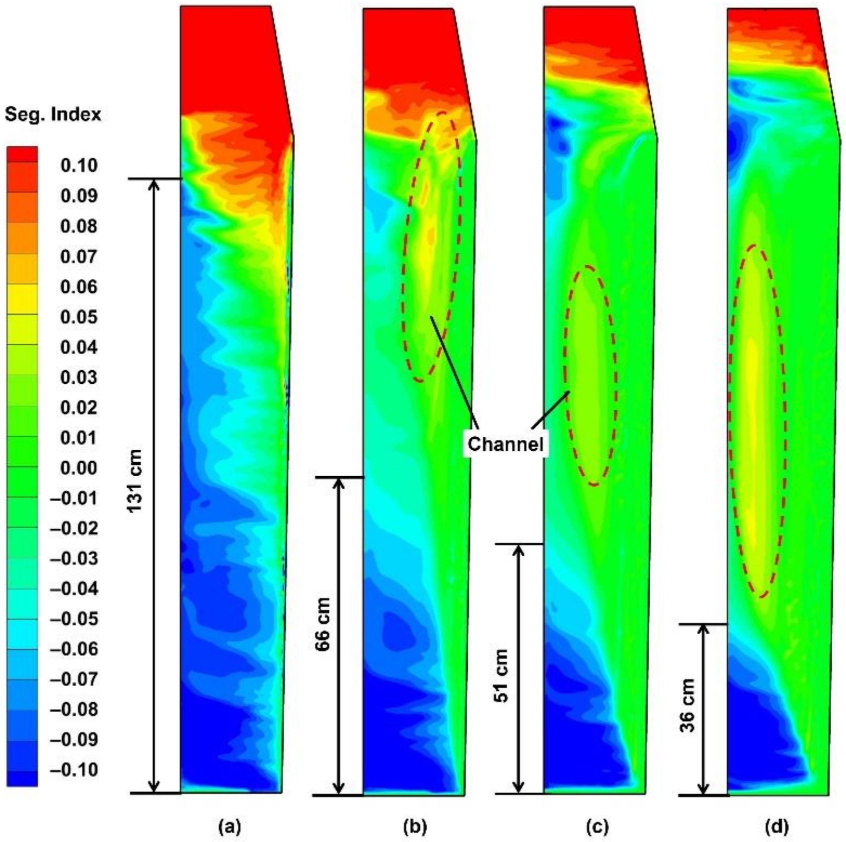

Fig. 5.8 The final carbon segregation index profiles under different cooling intensities: (a) 100 W m^{-2} K^{-1}, (b) 300 W m^{-2} K^{-1}, (c) 600 W m^{-2} K^{-1}, and (d)1000 W m^{-2} K^{-1}

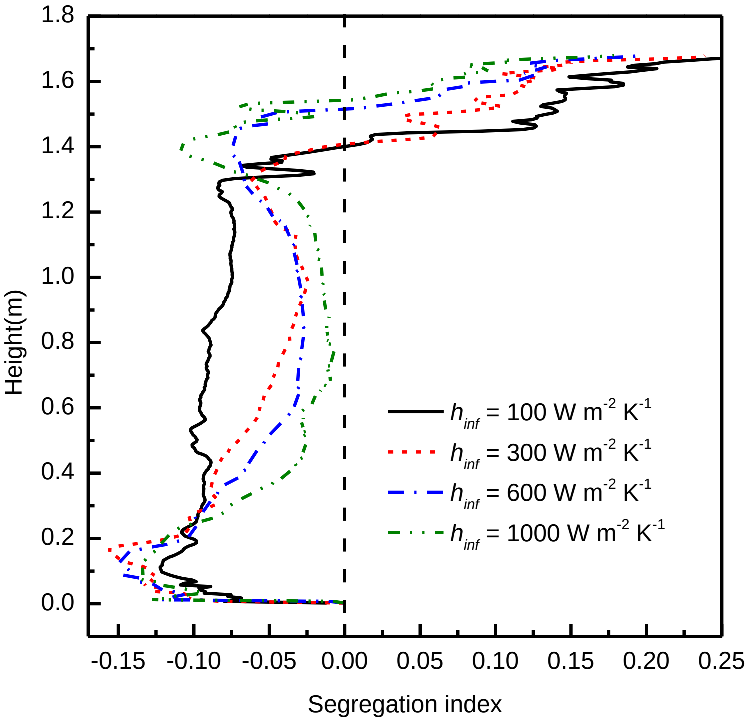

Fig. 5.9 The diagram of final carbon segregation index under different cooling intensities

To explain the effect of the cooling rate at different solidification stages, it is appropriate to analyze fluid flow at characteristic points P_0 (0, 0.8), P_1 (0.1, 0.8), and P_2 (0.2, 0.8), the positions of which are indicated in Fig. 5.1(b). In Fig. 5.9, a comparison of the evolution of the vertical component of liquid velocity over time at these points is presented for considered heat transfer coefficient values. Generally, the overall flow loop descended along the solidification front, which was parallel to the sidewall, and ascended in the ingot core, meaning that the vertical velocity had mainly a positive value at P_0 (Fig. 5.9(a)) and mainly a negative value at P_2 (Fig. 5.9(c)). When the grain phase was packed, liquid flow velocity approached zero due to large flow resistance from the fixed grain network. It is easy to observe that, at each point, the velocity obtained in the calculation with larger cooling coefficients reverted to zero at earlier stages.

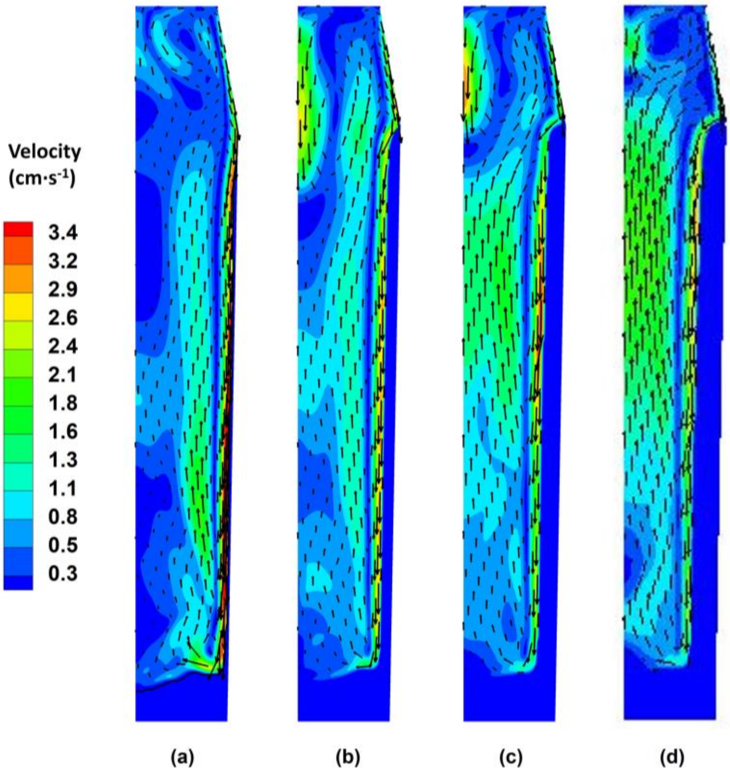

Fig. 5.10 Liquid flow fields and contour of magnitude of velocity at t = 100 s under different cooling intensities: (a) 100 W m^{-2} K^{-1}, (b) 300 W m^{-2} K^{-1}, (c) 600 W m^{-2} K^{-1}, and (d)1000 W m^{-2} K^{-1}

The downward flow of liquid along the cooled sidewall intensified as the heat transfer coefficient increased. However it should be borne in mind that higher cooling rates promote earlier and faster growth of the solid phase, and this has a twofold effect. On the one hand, sedimentation of grains starts earlier everywhere in the volume and should be more intense. On the other hand, solute rejection at the solid–liquid interface also increases and contributes more intensively to the ascending flow. As already discussed above, the variation in the vertical component of velocity of extradendritic liquid near the axis and in the central part of the ingot is a result of competition between solutal upward convection and the downward drag effect from sedimenting grains.

Fig. 5.11(a) shows that with stronger surface cooling, the upward flow rate at the central line monotonically increased with a maximal value of 2.27 cm s^{-1} for h_{inf} = 100 W $m^{-2}K^{-1}$ versus 2.75 cm s^{-1} at t = 72 s for h_{inf} = 1000 W $m^{-2}K^{-1}$. That means that solutal buoyancy was stronger with a larger h_{inf} and that more grains, the solid fraction of which was still small, were transported by the central flow to the upper region under stronger cooling conditions. A decrease in velocity signified an increase in solid fraction at point P_0, whereas, since the axial velocity remained positive, the downward drag force from the grains was not enough to reverse the liquid motion at the early stage of the process. Grains with a solid fraction descended, but "released" rejected solute that again helped intensify the upward solute convection. This process was repeated twice for h_{inf} = 1000 W $m^{-2}K^{-1}$ with large variations in amplitude of axial velocity, and was stopped by the packed layer, which reached this height at ~200 s (Fig. 5.12(d)). For smaller heat transfer coefficients, competition between growth of the solid fraction followed by descending grains and solutal convection gave rise to multiple flow oscillations that were finally also stopped due to grain packing. These oscillations gave an irregular form to the central zone of negative segregation.

The results obtained at point P_2, 0.2 m from the central line and about 0.03 m from the ingot surface, are presented in Fig. 5.11(c). Here, the downward velocity value initially increased due to development of the flow field under the action of thermal buoyancy, before quickly reverting to zero when the packing layer reached that point. For the lowest value of the heat transfer coefficient, the process was different and was accompanied by flow oscillations that indicated flow instabilities similar to those described above. The effect of these instabilities on solute distribution in the ingot was also visible in Figure 8a as a variation in the segregation index near the ingot boundary. Finally, the flow behavior at point P_1, located 0.1 m from the central line (Fig. 5.11(b)), presented a combination of effects described for point P_0 at the axis, which were followed by a change in flow direction to a descending one due to the sedimentation of the grains, the solid fraction of which was sufficiently developed to counteract solutal convection. Yet with the lowest value of h_{inf}, velocity oscillations persisted until the packed layer was reached.

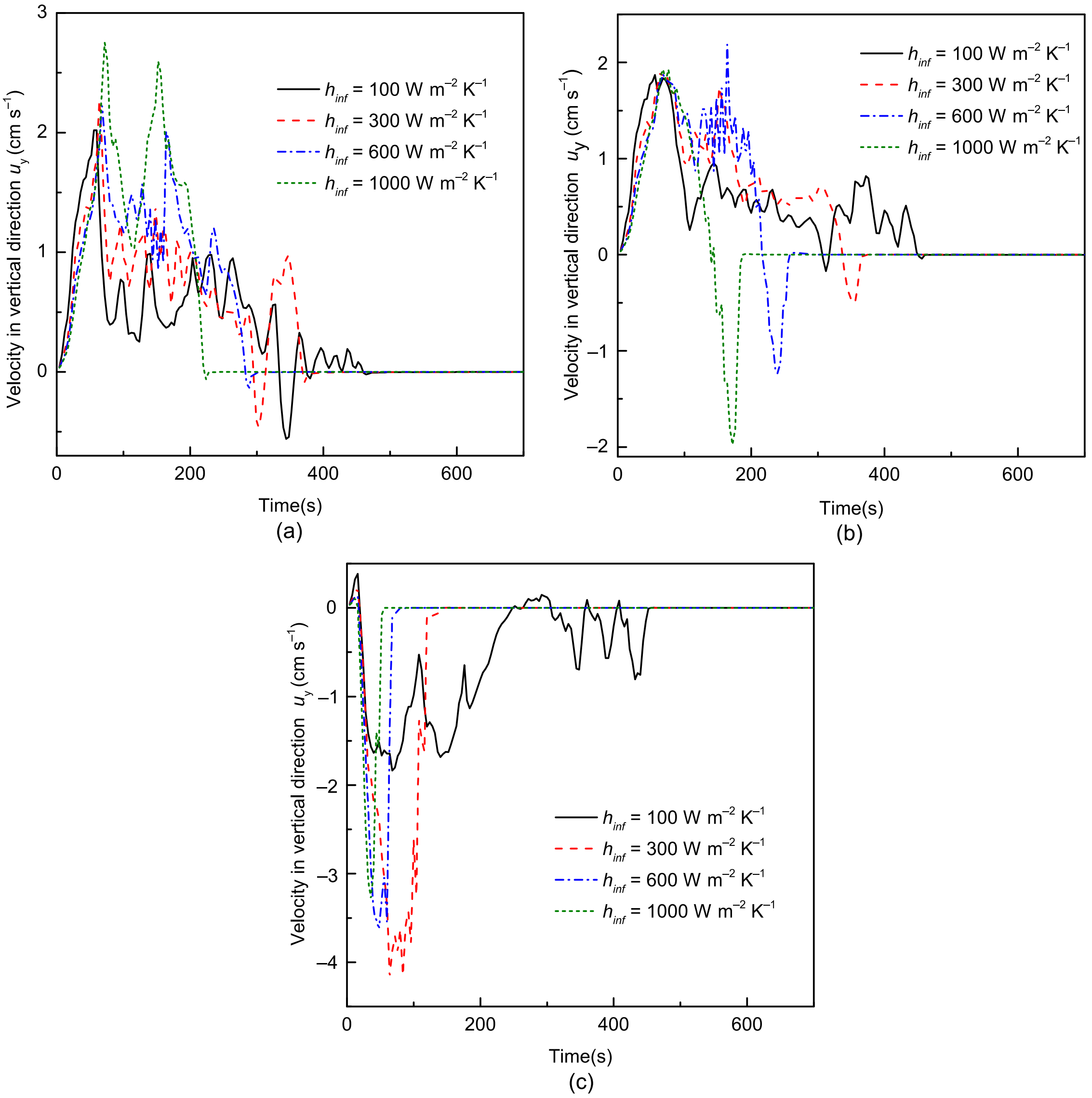

Fig. 5.11 Variation of vertical component of liquid velocity at points P_0 (a), P_1 (b) and P_2 (c) during solidification for different values of heat transfer coefficients

5.3.3 Evolution of packed bed

The evolution of the location of the zone edge (the packing line) for different cases is shown in Fig. 5.12. The comparison was performed for periods of time, ranging from the beginning of cooling until the moment when the equiaxed grains piled up to the top of the mold. This took about 960 s, where $h_{inf} = 100$ W m^{-2}K^{-1}, 540 s where $h_{inf} = 300$ W m^{-2}K^{-1}, 360 s where $h_{inf} = 600$ W m^{-2}K^{-1}, and 300 s where $h_{inf} = 1000$ W m^{-2}K^{-1} for grains piling up the mold. After this, it took 500 more seconds for the equiaxed grains to fill the hot top region for each case. It should be noted that ingot solidification was still far from completion since the grains were packed at $f_e = 0.4$, whereas the solid fraction varied from 0.25 to 0.3.

The grain packed layer grew from two ways: piling up from bottom or sticking to side wall. Whether equiaxed grains get packed near the side wall depended on competition between sedimentation velocity and envelope growth rate. If the envelope grew quickly, then the grains would get packed before arriving at bottom. For h_{inf} = 100 W m^{-2}K^{-1}, due to small cooling rate and envelop growth rate, most of equiaxed grain sank to the bottom along the cooled side. In this way, solid grains coming from the outer solidified region mainly accumulated at the bottom, resulting in a packed bed built up from the bottom side. The shape of packing line under h_{inf} = 100 W m^{-2}K^{-1} was relatively flatter comparing to other cases. When the surface cooling was intensified, more grains get packed at the side wall (Fig. 5.12(b) and Fig. 5.12(d)). The packing lines showed slopes towards the central line. For Fig. 5.12(b), it is seen that the slope of packing line increased from t = 60 s to t = 240 s, then decreased from t = 240 s to t = 480 s because of the decrease of cooling rate. The slope of packing line in Fig. 5.12(c) and Fig. 5.12(d) evolved in a similar way as Fig. 5.12(b). The maximal slope of packing line increased with the intensification of surface cooling condition.

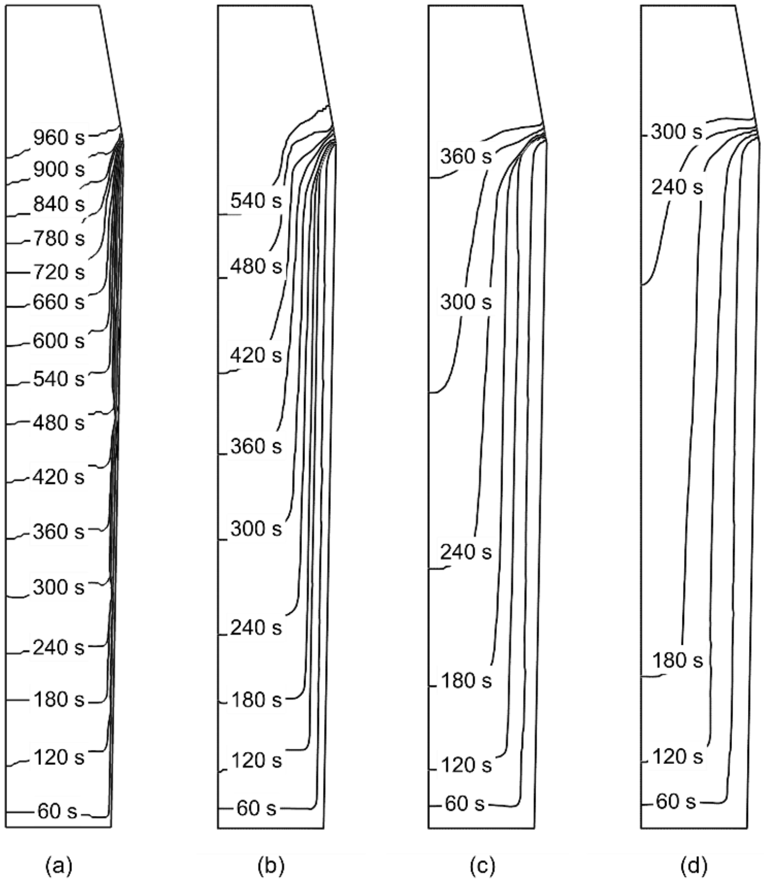

Fig. 5.12 Packing line evolution at different heat transfer coefficients under different cooling intensities: (a) 100 W m^{-2} K^{-1}, (b) 300 W m^{-2} K^{-1}, (c) 600 W m^{-2} K^{-1}, and (d)1000 W m^{-2} K^{-1}.

5.3.4 Grain number density

Fig. 5.13 presents the final grain number density distribution under different cooling intensities. It is seen that the distribution of grain number density became less homogeneous when h_{inf} increased from 100 W m^{-2} K^{-1} to 600 W m^{-2} K^{-1}.

The maximum grain number densities in Fig. 5.13(a-d) were 4.02×10^9 m^{-3}, 6.91×10^9 m^{-3}, 7.67×10^9 m^{-3}, and 6.79×10^9 m^{-3}, respectively. In Fig. 5.13(b, c, d), maximum value appeared in the joint region between hot top and mold. The formation of this fine grain region was the result of central upward flow and grain sedimentation in the hot top region. A thin layer poor of grain could be observed in each case. This layer was next to side wall for the case under h_{inf} = 100 W m^{-2}K^{-1}, and moves inwards when the surface cooling was intensified.

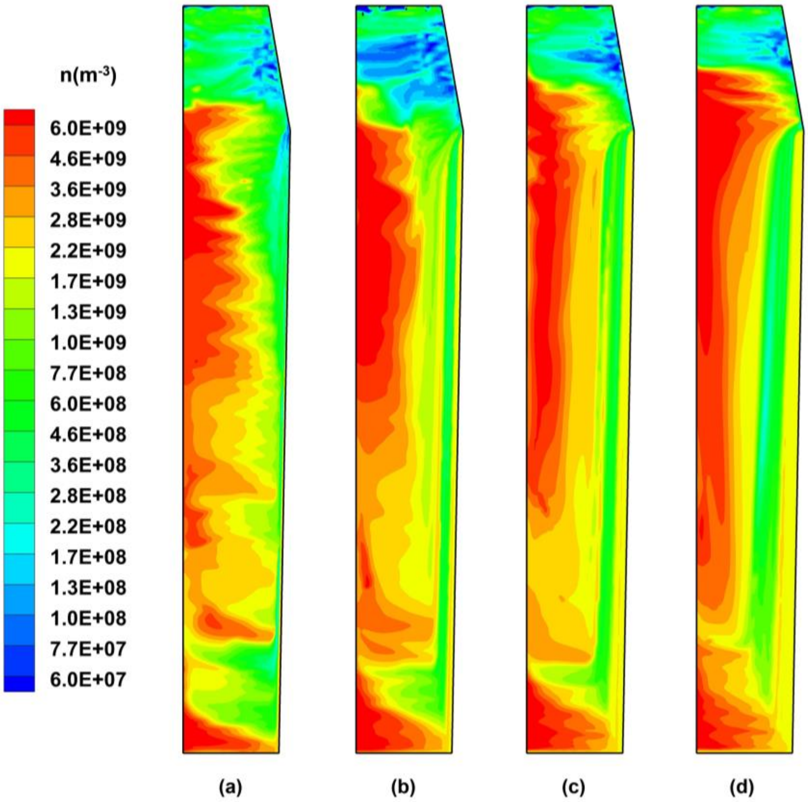

Fig. 5.13 Grain number density distribution under different cooling intensities: (a) 100 W m^{-2} K^{-1}, (b) 300 W m^{-2} K^{-1}, (c) 600 W m^{-2} K^{-1}, and (d)1000 W m^{-2} K^{-1}

5.4 Effect of electromagnetic force on solidification of ingot

5.4.1 Distribution of magnetic field and electromagnetic force

In casting, Rotating Magnetic Field (RMF) and Travelling Magnetic Field (TMF) can be employed to generate electromagentic stirring (EMS) in the liquid. Rather often, axial symmetry of the ingot assumes use of RMF in which the Lorentz force is acting in the azimutal direction creating primary circumferential flow while the axial flow is a secondary one. However, in the present work we consider use of TMF, i.e. a stirrer placed near the ingot wall (Fig.5.14) is a linear motor similar to that considered in chapter 4 about the AFRODITE benchmark. In this case the Lorentz force is acting along the side wall of the ingot and creates meridional flow.

Without going into details of solution of Maxwell equations, let us suppose that, similarly to the case presented in chapter 4, the electromagnetic force acting in the liquid is given with Eq.(5.3). For the following equations, the y'-axis points towards the metallic medium with $y' = 0$ positioned at its surface:

$$F_{Ex'} = \frac{\delta(x') C_E \pi f \sigma B_0^2}{k_E} \exp(-2k_E y') \tag{5.3}$$

where σ is electric conductivity; f_0 frequency of current; $k_E = \pi/\tau$ is the wave number and $\tau = 0.125$ m is the pole pitch; B_0 is the amplitude of magnetic induction intensity at y'=0. $\delta(x')$ represents the distribution interval of electromagnetic field:

$$\delta(x') = \begin{cases} 1 & \text{if } x'_{min} < x' < x'_{max} \\ 0 & \text{else} \end{cases} \tag{5.4}$$

where x'_{min} and x'_{max} define the x' coordinate range of stirrer as indicated in Fig. 5.14, beyond which range the electromagnetic foece is assumed inexistent.

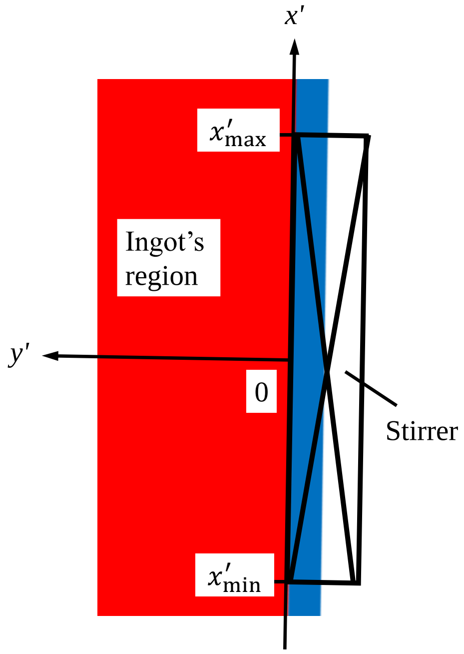

Fig. 5.14 Coordinate system for calculation of electromagnetic field in ingot

Table 5.2 Parameters and material properties relating to electromagnetic field calculation

Parameters	Symble	Unit	Value
Electric conductivity	σ	A V^{-1} m^{-1}	7.14×10^5
magnetic permeability	μ	V s A^{-1} m^{-1}	1.2566×10^{-6}
Ample of magnetic intensity	B_0	mT	30/20/10
Frequency	f_0	Hz	10
Pole pitch	τ	m	0.125

The distributions of time averaged electromagnetic force $\langle F_{Ex'}\rangle$ along *y'* direction obtained based on the data in Table 5.2 with different amplitude of B_0 are presented in Fig. 5.15. The electromagnetic force showed maximum value at the place nearest to the EMS surface, and it decreased exponentially from the surface to the inner region of ingot. The maximal electromagnetic force showed 357 N m^{-3} when B_0 = 20 mT.

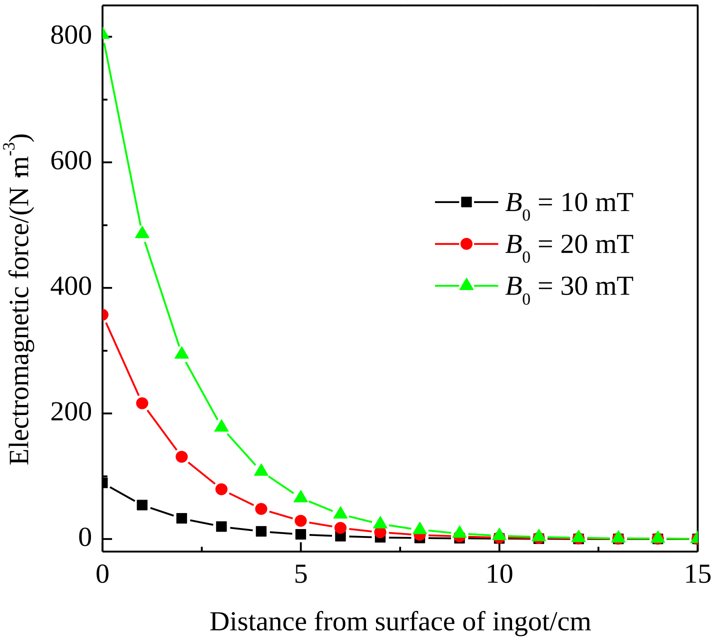

Fig. 5.15 Calculated distribution of time averaged electromagnetic force

5.4.2 Effect of stirring direction and stirring intensity

In order to investigate the effect of electromagnetic stirring, three simulation cases are conducted, i.e., with no EMS, with downward EMS and with upward EMS. The calculated results showed that the macrosegregation was relieved with the application of electromagnetic stirring, meantime, the downward EMS was more favourable than upward one, as seen in Fig. 5.16.

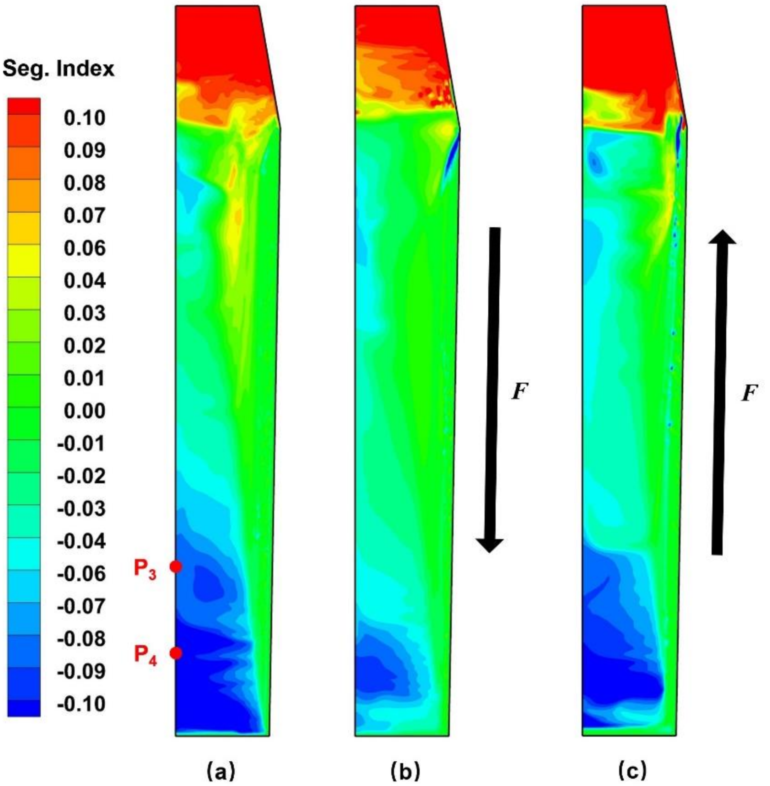

Fig. 5.16 Comparison of macrosegregation map with and without electromagnetic stirring. (a) No EMS; (b) downward EMS with $B_0 = 20$ mT; (c) upward EMS with $B_0 = 20$ mT

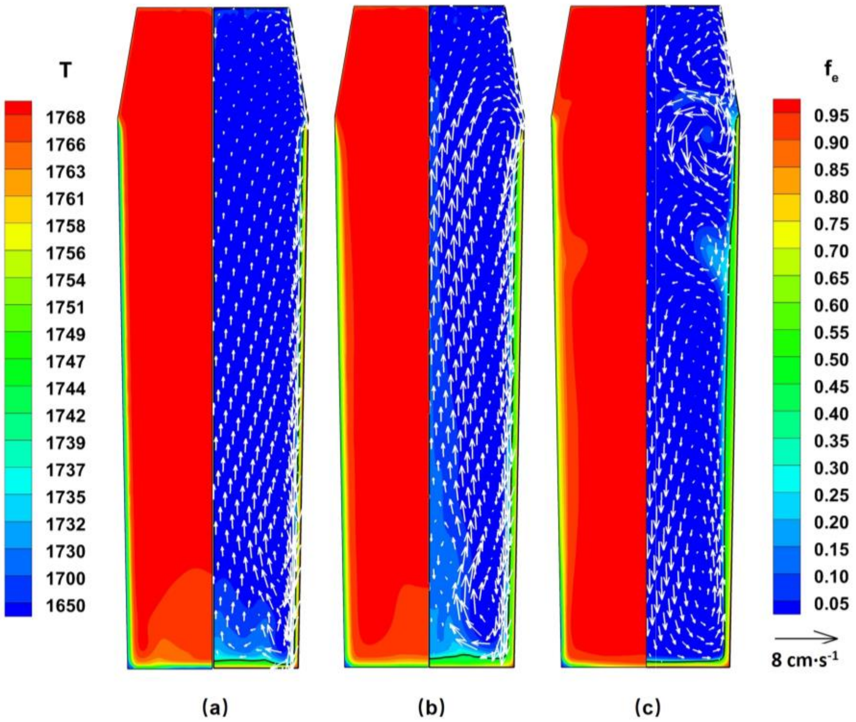

Fig. 5.17 Flow field and distributions of temperature and grain phase fractions at $t = 50$ s. (a) No EMS; (b) downward EMS with $B_0 = 20$ mT; (c) upward EMS with $B_0 = 20$ mT

The distributions of temperature and grain phase fraction in ingot at solidification time t = 50 s with and without EMS are compared in Fig. 5.16. With absence of EMS, i.e. B_0 = 0 T, the cold melt near the surface flowed downwards under the action of thermal buoyancy force, reducing the temperature of the lower region. Equiaxed grains moved to the bottom and formed a thin packed layer there. When a downward electromagnetic stirring (B_0 = 20 mT) was applied, the flow region was obviously enlarged, meantime, more equiaxed grains arrived to the bottom region and some of them moved upwards along central line (Fig. 5.16(b)). The maximum flow velocity increased from 2.93 cm s^{-1} to 4.06 cm s^{-1}. When an upward electromagnetic stirring was applied, the electromagnetic force acted in opposite direction of thermal buoyancy force. At time t = 50 s, thermal bouyancy force was small and the melt flow was dominated by electromagnetic force. The melt near cooling surface carrying the equiaxed grains flowed upwards, then turned downward when approaching the hot top region, therefore, the sedimentation of equiaxed grains was delayed, and that is why the packed layer in Fig. 5.17(c) was thinner than the other two cases.

The distributions of temperature and grain phase fraction in ingot at solidification time of t = 100 s with and without EMS are compared in Fig. 5.18. When electromagnetic stirring was applied, the overall temperature in the ingot was lower and the equiaxed grain packed layer got thicker. The equiaxed grain in packed layer was fixed and resisted the liquid flow, therefore, the flow intensity became weaker than the moment of t = 50 s and the effect of electromagnetic force was limited. Under the action of downward forced convection, more equiaxed grains were transported to the bottom, then to the central line and moved upwards (Fig. 5.18(b)). However, the upward electromagnetic stirring did not effectively strengthen the melt flow (Fig. 5.18(c)), because the buoyancy force still counteracted it.

The change of temperature and equiaxed grain fraction at points (P_3 and P_4) is shown in Fig. 5.19. The locations of P_3 (0, 0.2) and P_4 (0, 0.4) are indicated in Fig. 5.16. The obtained curves showed obvious fluctuation for the cases with EMS before the grain packing happened (Fig. 5.18(a)), which could be ascribed to the change of melt flow under electromagnetic force. In the period of time shortly before the occurance of grain packing, the melt flow velocity slowed down, which was beneficial for the settling of equiaxed grains, thus the increase rate of grain phase fraction suddenly increased. Compared with the point P_3, the point P_4 was nearer to the bottom of the ingot, thus the temperature there had a faster decrease rate. Both upward and downward electromagnetic stirring helped to homogenize the temperature distribution at the initial stage of solidification. Under the downward EMS, the effect of stirring lasted for a longer time, with which the grain growth rate was larger than the other two cases.

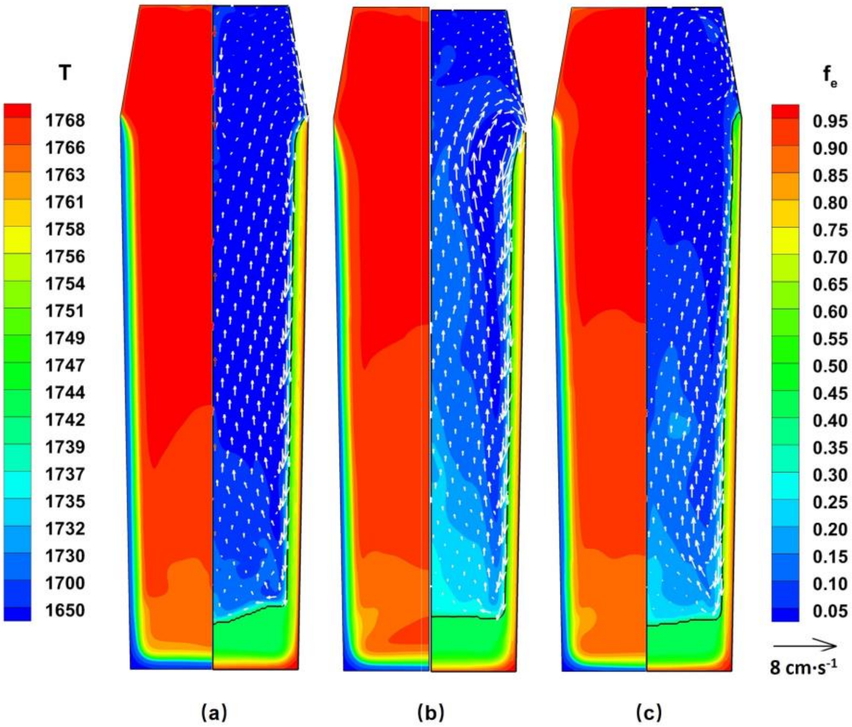

Fig. 5.18 Flow field and distributions of temperature and grain phase fractions at t = 100 s. (a) No EMS; (b) downward EMS with B_0 = 20 mT; (c) upward EMS with B_0 = 20 mT

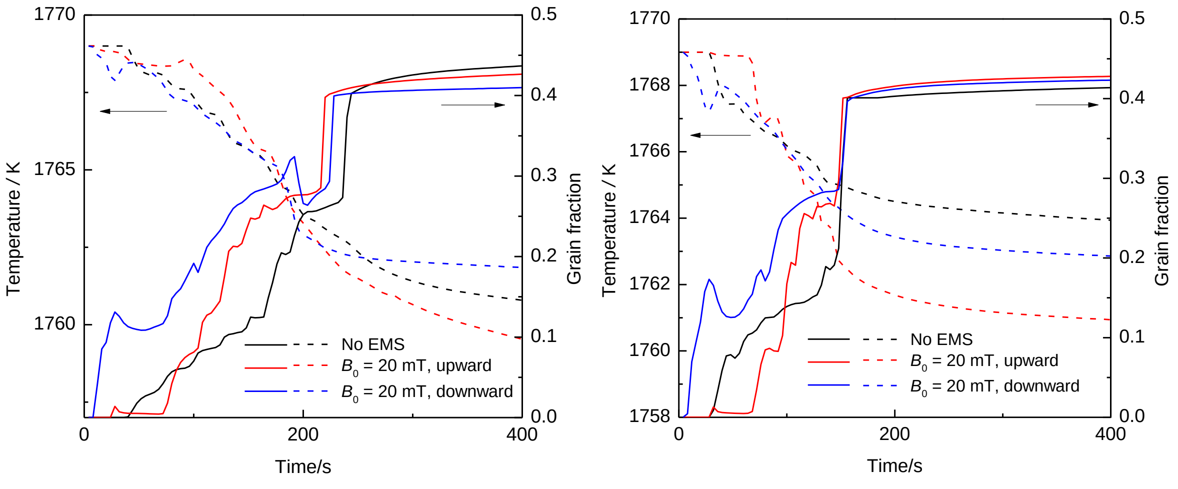

(a) (b)

Fig. 5.19 Evolution of temperature and grain phase fraction at points P_3 (a) and P_4 (b)

Fig. 5.20 shows the simulation results of macrosegregation of ingot under downward electromagnetic stirring with different stirring intensities. The results showed that when B_0 increased to 20 mT, the macrosegregation of ingot was significantly improved, because the electromagnetic stirring accelerated the solidification process of ingot, reducing the time for solute transportation. However, an obvious negative segregation band appeared near the junction of mold and hot top, which appeared because the strong flow continuously flowed through the grain packed layer and took away the enriched melt there. According to the parameters chosen in this study, higher magnetic induction intensity B_0 brought better improvement effect for macrosegregation, but the negative segregation band was also more significant. Therefore, the intensity of electromagnetic stirring should be controlled within a reasonable range.

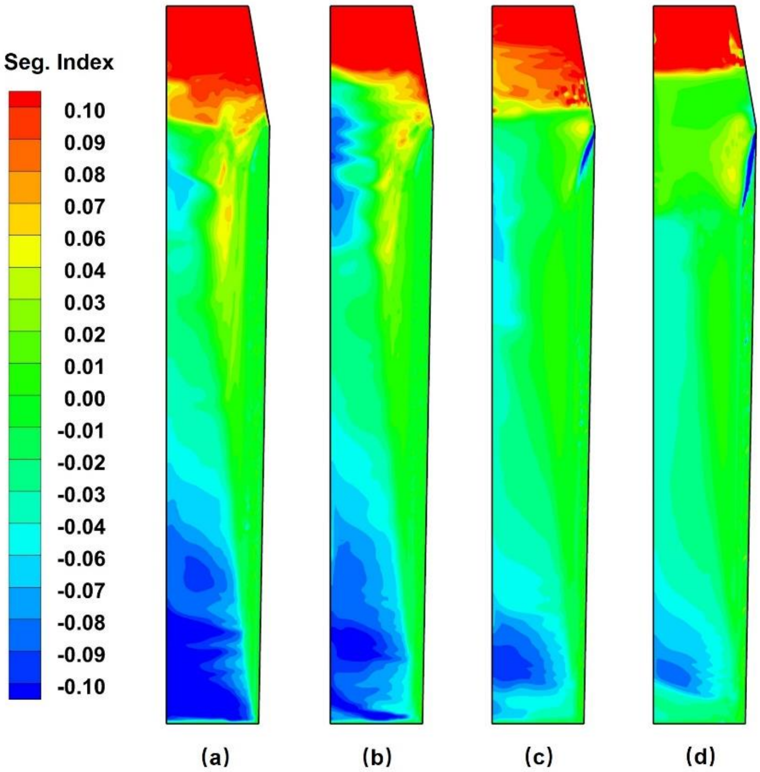

Fig. 5.20 Final macrosegregation maps: (a) $B_0 = 0$ T, (b) $B_0 = 0.01$ T, (c) $B_0 = 0.02$ T, and (d) $B_0 = 0.03$ T

5.4.3 Effect of position of electromagnetic stirrer

Previous studies have shown that downward EMS is beneficial to the improvement of macrosegregation in ingots. Below we investigate the effect of the position of EMS on its efficiency. Four cases are defined with EMS acting on different zones: (1) whole height of mold; (2) upper half area of mold; (3) lower half area of mold; (4) upper quarter area of mold. The calculated macrosegregation maps of above cases are presented in Fig. 5.21. The result showed that the improvement of macrosegregation was the best when the EMS acts on the whole mold height (Fig. 5.21(a)). Comparison between Fig. 5.21(b) and Fig. 5.21(c) indicated that the stirring had better efficiency if EMS was installed at an upper region of ingot. Fig. 4.21(d) showed that a well improvement of macrosegregation could be achieved even if the the EMS was only implemented at upper quarter region of mold.

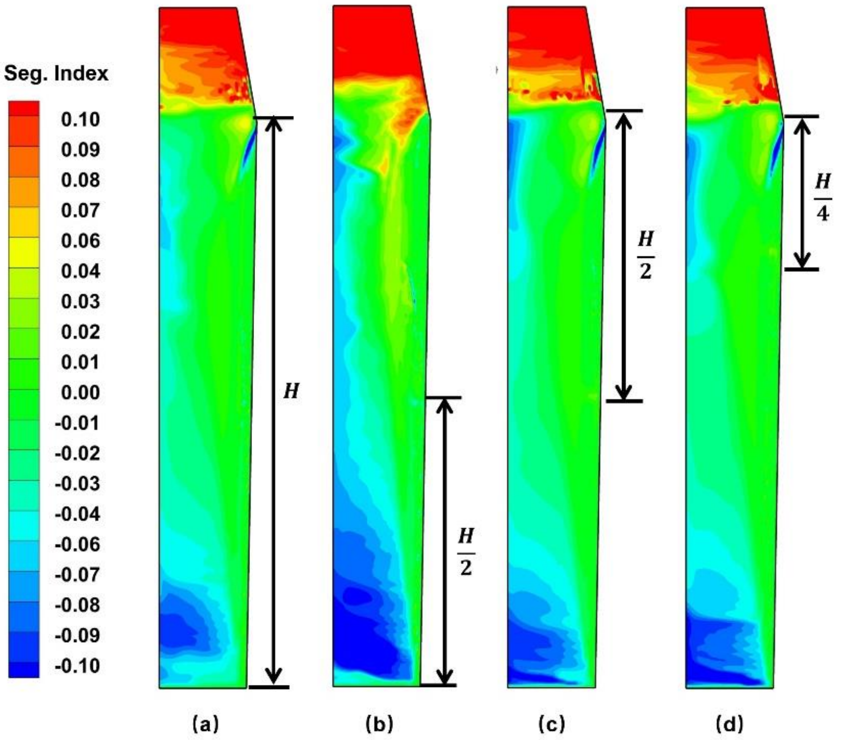

Fig. 5.21 Comparison of macrosegregation maps. (a) EMS installed for whole mold, (b) EMS installed at lower half region, (c) EMS installed at upper half region, and (d) EMS installed at upper quarter region

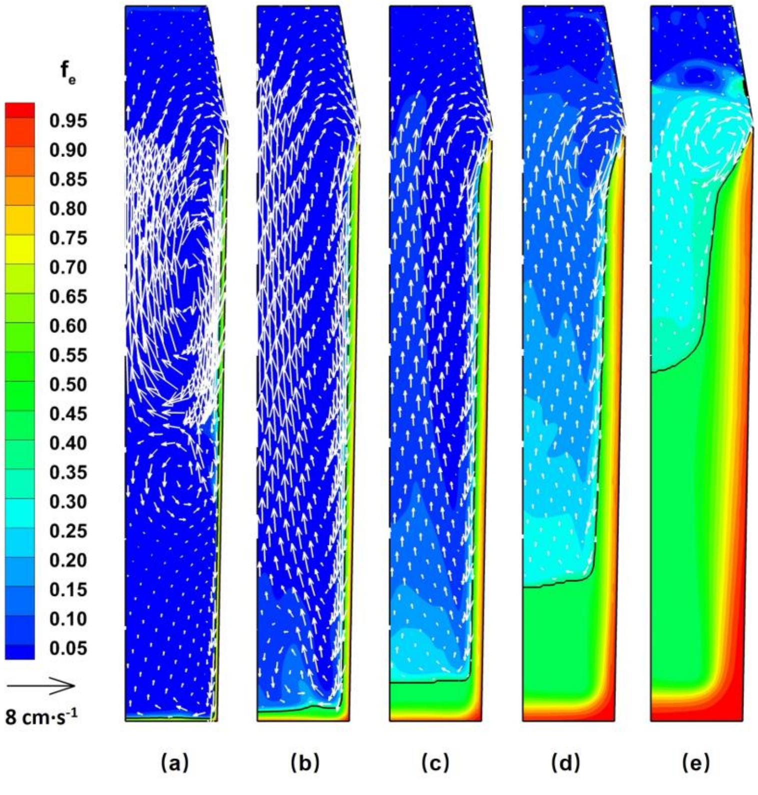

Fig. 5.22 Flow field and distribution of grain phase fraction at different solidification time for the case with EMS installed at upper region: (a) 20 s, (b) 60 s, (c) 120 s, (d) 200 s, and (e) 300 s

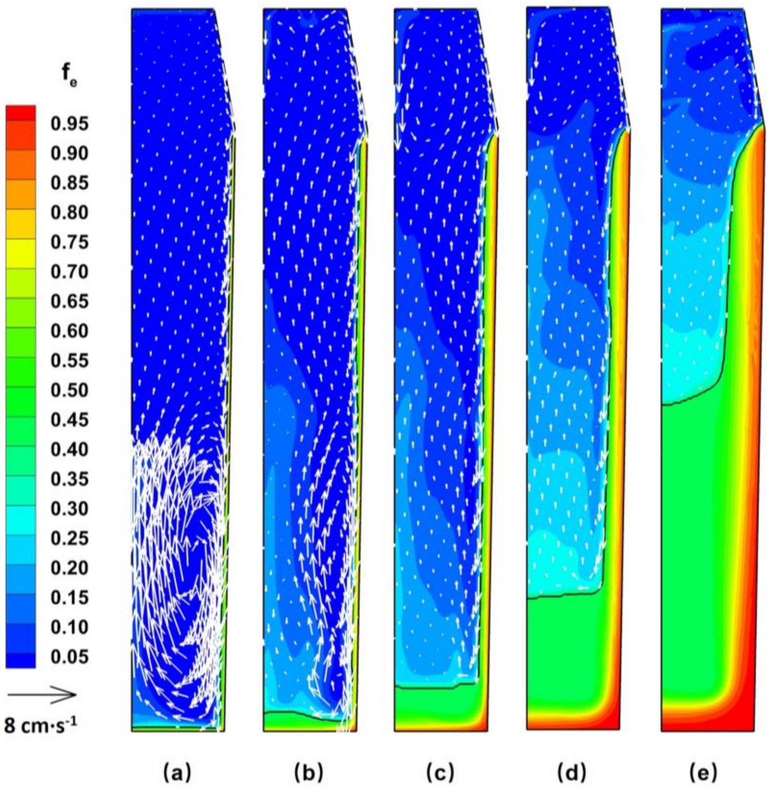

Fig. 5.23 Flow field and distribution of grain phase fraction at different solidification time for the case with EMS installed at lower region: (a) 20 s, (b) 60 s, (c) 120 s, (d) 200 s, and (e) 300 s

When the EMS was installed at upper place, initially, the electromagnetic force created a local clockwise vortex at the upper region of ingot (5.22(a)), then this vortex expanded to lower region (5.22(b)), causing a global circulation of melt flow in the ingot (5.22(c)). When the equiaxed grain fraction at lower region increased, the effect of EMS therein was weakened. When the EMS was placed at the lower place, at early time, the electromagnetic force locally intensified a clockwise melt flow (5.23(a)). However, with the growth of grain packed layer, the effect of electromagnetic force became weak quickly, and the melt flow rate in the ingot slowed down. One can conclude that the effect of EMS was weakened by grain packer layer and this layer prefered to grow from lower region until top, therefore, when the EMS was placed at upper position, the effect of stirring could last for longer time, which was benefical for enhancing convection and accelerating solidification process.

5.5 Conclusion

A three-phase equiaxed solidification model was applied to study the formation of macrosegregation in a 2.45 ton industrial steel ingot. A comparison of the calculated macrosegregation with the reported measurements showed their qualitative agreement despite uncertainties in boundary conditions and a rather sizeable simplification of physical phenomena in the model. Numerical results revealed flow instabilities related to competition between solutal and thermal buoyancy effects in the liquid, added to which was the gravity force acting on grains depending on the solid fraction. These instabilities led to an irregular form of the central zone with negative segregation perturbed by horizontal channels and the emergence of long vertical channels, also observed in experiments. However, V-type channels along the axis were not reproduced.

To illustrate the influence of cooling intensity on ingot solidification, four different surface heat transfer coefficients were applied. The results showed that under stronger surface cooling condition, flow was stabilized by faster development of the packed layer, solidification process was accelerated, and the time for solute exchange between moving grains and liquid was limited, finally, a better solute homogeneity of ingot was achieved. Yet, in real industrial processes, improvement of cooling conditions is difficult because of the formation of an air gap between the solidifying ingot and the mold due to shrinkage. Therefore, more investigation is needed to improve the cooling conditions of chill molds.

One of the most important simplifications in the model was the absence of the shrinkage effect, which might alter the multiphase flow during the process once the solid phase starts to appear, and which was clearly responsible for the segregation pattern in the upper part of the ingot. The role of columnar growth, which was not taken into account in the model, is, however, less clear. Indeed, in simulation, a layer of packed grains along the cooled walls and bottom appeared quite quickly once the process began and somehow corresponded to columnar dendrites observed in various reported experiments.

The effect of EMS on solidification process and macrosegregtaion formation of ingot was investigated through a series of simulations. Results showed that EMS strengthened the melt flow near the wall, inhibited the packing of equiaxed grains near the side wall, promoted the accumulation of equiaxed grains at the bottom of the ingot, reduced the solute exchange between equiaxed grains and the surrounding liquid, and thus relieved the macrosegregation of ingot. The downward EMS had a more obvious effect in improving solute homogeneity. When the applied magnetic induction intensity increased, the degree of macrosegregation in the central area of ingot was significantly reduced, yet the enhanced stirring intensity led to negative segregation band in outer area of the ingot.When the EMS was placed at upper part of the ingot, the effective stirring time was longer, which was more favourable for relieving macrosegregation of ingot.

Chapter 6 Conclusions and recommendations for future work

Computational methods have nowadays become an efficient tool to understand phenomena during solidification and to predict macrosegregation in casts and ingots. The crucial role of proper description for the nucleation, growth and movement of equiaxed grains in solidification modeling has been draw attention on via both experimental and numerical researches. Present work focus on the numerical modeling for equiaxed solidification under convective flow with use of volume average method. After comprehensive literature review of existing volume average models and different solutions proposed for some crucial issues, a new version of three-phase solidification model was introduced. This model was tested in simulations of two laboratory benchmark solidification processes prior its application to study of solidification process and macrosegregtaion formation in industrial ingot. The main conclusions are summarized below.

(1) In the new version of the solidificaion model of in equiaxed regime the following aspects were revised regarding the presence of covective flow:

a. Happel approximation for the momentum exchange coefficient between the two hydrodynamic phases provides a good approximation both for free moving particles and the packed bed regimes. Therefore, the Happel approximation can be recommended for use in equiaxed solidification modeling.

b. An additional criterion proposed for the treatment of the grain packing phenomenon allowed us to take into account properly those grains whose fraction exceeds a theoretical packing limit but which were transported in the middle of the bulk liquid and, consequently, should not be blocked.

c. An equation for diffusion length in the extradendritic liquid was proposed combining the factors including grain size and a convective flow around the grain.

(2) At the stage of validation of the model with laboratory scale solidification benchmarks:

a. The drastic effect of the adopted model for diffusion length in the extradendritic liquid was demonstrated with solidification of a binary alloy Sn-5 wt% Pb in the configuration of Hebditch-Hunt benchmark. Results obtained with a model for diffusion length proposed in our work were compared with results obtained with a traditionally used model. The numerical results showed that the case including the proposed equation for diffusion length predicted a slower growth of the packed grain bed at the bottom of the cavity, formation of channels near the cooling side, and a final segregation pattern with an enriched layer at the bottom.

b. Developed equiaxed solidification model was applied for modeling of the AFRODITE experiment on solidification of Sn-10 wt% Pb alloy with presence of both natural flow and EMS driven flow. It was demonstrated that with rejection of heavier solute due to solidification, the forced flow was damped and natural convection started to occupy larger volume in the cavity. It was observed from simulation results that the interaction between the natural flow and EMS driven flow caused oscillations of temperature and flow fields during a certain stage of solidification. When equiaxed grains get packed, downward flow of highly enriched liquid through the rigid structure led to accumulation of Pb at the bottom. The calculation results qualitatively agreed with experimental measurements including the final macrosegregation map and temperature field evolution. Further numerical studies demonstrated that the intensity of the electromagnetic force affected the shape of the zone of positive sergregation.

(3) Application of the model to simulation of an industry steel ingot

a. The developed model was applied to study the formation of macrosegregation in a 2.45 ton industry steel ingot. The predicted macrosegregation distribution agreed qualitatively with the experimental data. Equiaxed sedimentation was a very important mechanism responsible for the formation of global segregation in such ingots. Equiaxed grain grew up near the cold wall but some of them sedimented to the bottom, forming a cone with negative segregation. Melt enriched with carbon was expelled to upper region and finally caused a positive segregated top region. The liquid flow in the packed zone was extremely weak thus cannot affect final segregation distribution.

b. To illustrate the influence of cooling intensity on ingot solidification, four different surface heat transfer coefficients were applied. The results showed that under stronger surface cooling condition, flow was stabilized by faster development of the packed layer, solidification process was accelerated, and the time for solute exchange between moving grains and liquid was limited, finally, a better solute homogeneity of ingot is achieved.

c. The effect of EMS on solidification process and macrosegregtaion formation of ingot was investigated through a series of simulations. Results showed that EMS strengthened the melt flow near the wall, inhibited the packing of equiaxed grains near the side wall, promoted the accumulation of equiaxed grains at the bottom of the ingot, reduced the solute exchange between equiaxed grains and the surrounding liquid, and thus relieved the macrosegregation of ingot. The downward EMS had a more obvious effect in improving solute homogeneity. When the applied magnetic induction intensity increased, the degree of macrosegregation in the central area of ingot was significantly reduced, yet the enhanced stirring intensity led to negative segregation band in the outer area of the ingot.When the EMS was placed at the upper part of the ingot, the effective stirring time was longer, which was more favourable for relieving macrosegregation of ingot.

Present thesis tried to improve the equiaxed solidification model to better accounting for convective flow. Yet, it has to be admitted that there remain some problems in modeling awaiting to be properly addressed. Here some future directions are pointed out:

(1) In present model, the interdendritic liquid flow always moves together with the solid phase based on an assumption that the permeability in interdendritic region is obviously smaller than the region out of grain envelop. However, if the ratio of solid fraction to grain fraction is small, the relative movement between solid and interdendritic liquid should be taken into account. Since it is neglected , the segregation intensity predicted with application of the present model is often smaller compared to what is found with measurements performed with a real sample. Yet, it should be noted that the predicted segregation intensity is often overestimated in another configuration of solidification model that assumes interdendritic liquid move together with extradendritic liquid. Wang and Beckermann [116] proposed a correlation equation to account for the partition coefficient in liquid some time ago, and this method need to be interpreted in modernlized solidification model.

(2) The developed equiaxed solidification model has to be extended into mixed columnar-equiaxed model in the future. The criterion for columnar-equiaxed transition has to be defined. To evaluate the influence of the forced flow on columnar-equiaxed transition, the fragmentation of dendrites also needs to be considered into the model in some way. This has been preliminary studied by Wu and co-workers [125], but the calculated results from their model largely depend on the chosen values for fragmentation parameters. Besides, the model assumed that the fragments broken from columnar dendrites are the only source of initial equiaxed grains.

(3) Present equiaxed model was developed based on laminar flow of phases and the turbulence was taken into account via transport equations for mean flow as well for mean values of temperature and concentration, and enhancement of diffusive transport due to velocity fluctuations. Yet, this method is not evident because transport phenomena at microscale cannot be treated separately of velocity fluctuation at short time period. A unique ensemble statistical averaging [117] can be applied in the future to combine microscale and short-time phenomena.

(4) Although present thesis conducted simulation for an AFRODITE benchmark experiment in which the application of EMS greatly promotes the equiaxed growth, yet columnar structure is still observed in a small part of the sample solidified in the experiment. A more advanced benchmark experiment for pure equiaxed solidification is highly needed. It probably can be realized through decreasing temperature gradient, using smoother inner wall of mold, or applying proper stirring mode, etc.

References

[1] Kurz W, Fisher D J. Fundamentals of solidification [M]. Aedermannsdorf: Trans Tech Publications, 1989.

[2] Dantzig J A, Rappaz M. Solidification [M]. Lausanne: EPFL Press, 2016.

[3] Rutter J W, Chalmers B. A prismatic substructure formed during solidification of metals [J]. Canadian Journal of Physics, 1953, 31(1): 15-39.

[4] Tiller W, Jackson K, Rutter J, et al. The redistribution of solute atoms during the solidification of metals [J]. Acta Metallurgica, 1953, 1(4): 428-437.

[5] Losert W, Shi B Q, Cummins H Z. Evolution of dendritic patterns during alloy solidification: Onset of the initial instability [J]. Proceedings of the National Academy of Sciences, 1998, 95(2): 431-438.

[6] Mullins W W, Sekerka R F. Stability of a planar interface during solidification of dilute binary alloy [J]. Journal of Applied Physics, 1964, 35(2): 444-451.

[7] Hunt J D. Steady state columnar and equiaxed growth of dendrites and eutectic [J]. Materials Science and Engineering, 1984, 65(1): 75-83.

[8] Martorano M A, Beckermann C, Gandin C A. A solutal interaction mechanism for the columnar-to-equiaxed transition in alloy solidification [J]. Metallurgical and Materials Transactions A, 2003, 34(8): 1657-1674.

[9] Xu Y, Xu X J, Li Z, et al. Dendrite growth characteristics and segregation control of bearing steel billet with rotational electromagnetic stirring [J]. High Temperature Materials and Processes, 2017, 36(4): 339-346.

[10] Xu Y, Wang T, Wang F, et al. Influence of lower frequency electromagnetic field on dendritic crystal growth in special alloys [J]. Journal of Crystal Growth, 2017, 468: 506-509.

[11] Li X, Wang X, Bao Y P, et al. Effect of electromagnetic stirring on the solidification behavior of high-magnetic-induction grain-oriented silicon steel continuous casting slab [J]. JOM, 2020, 72(10): 3628-3633.

[12] Lesoult G. Macrosegregation in steel strands and ingots: Characterisation, formation and consequences [J]. Materials Science and Engineering: A, 2005, 413/414: 19-29.

[13] Ohno A, Chijin Shokan. The solidification of metals [M]. Tokyo: Chijin Shokan, 1976.

[14] Garabedian H, Strickland-Constable R F. Collision breeding of ice crystals [J]. Journal of Crystal Growth, 1974, 22(3): 188-192.

[15] Vogel A. Turbulent flow and solidification: stir-cast microstructure [J]. Metal Science, 1978, 12(12): 576-578.

[16] Jackson K A, Hunt J D, Uhlmann D R, et al. On the origin of the equiaxed zone in castings [J]. Transactions of the Metallurgical Society of AIME, 1966, 236(2): 139-149.

[17] Campanella T, Charbon C, Rappaz M. Grain refinement induced by electromagnetic stirring: A dendrite fragmentation criterion [J]. Metallurgical and Materials Transactions A, 2004, 35(10): 3201-3210.

[18] Itoh Y, Okajima T, Maede H, et al. Refining of solidification structures of continuously cast type 430 stainless steel slabs by electromagnetic stirring [J]. Transactions of the Iron and Steel Institute of Japan, 1982, 22(3): 223-229.

[19] Gäumann M, Bezencon C, Canalis P, et al. Single-crystal laser deposition of superalloys: processing-microstructure maps [J]. Acta materialia, 2001, 49(6): 1051-1062.

[20] Gäumann M, Trivedi R, Kurz W. Nucleation ahead of the advancing interface in directional solidification [J]. Materials Science and Engineering: A, 1997, 226–228(1): 763-769.

[21] Rappaz M, Gandin C A, Desbiolles J L, et al. Prediction of grain structures in various solidification processes [J]. Metallurgical and Materials Transactions A, 1996, 27(3): 695-705.

[22] Wu M, Ludwig A, Kharicha A. Volume-averaged modeling of multiphase flow phenomena during alloy solidification [J]. Metals, 2019, 9(2): 229.

[23] Zheng Y, Wu M, Karimi-Sibaki E, et al. Use of a mixed columnar-equiaxed solidification model to analyse the formation of as-cast structure and macrosegregation in a Sn-10 wt% Pb benchmark experiment [J]. International Journal of Heat and Mass Transfer, 2018, 122: 939-953.

[24] Leriche N, Combeau H, Gandin C A, et al. Modelling of columnar-to-equiaxed and equiaxed-to- columnar transitions in ingots using a multiphase model [A]//IOP Conference Series: Materials Science and Engineering [C]. IOP Publishing, 2015, 84(1): 1-8.

[25] Leriche N. Étude de la transition colonnaire-equiaxe dans les lingots et en coulée continue

d’acier et influence du mouvement des grains [D]. Nancy: Université de Lorraine, 2015.

[26] Wu M, Könözsy L, Ludwig A, et al. On the formation of macrosegregations in steel ingot castings [J]. Steel Research International, 2008, 79(8): 637-644.

[27] Hebditch D J, Hunt J D. Observations of ingot macrosegregation on model systems [J]. Metallurgical Transactions, 1974, 5(7): 1557-1564.

[28] Ludwig A, Wu M, Kharicha A. On Macrosegregation [J]. Metallurgical and Materials Transactions A, 2015, 46(11): 4854-4867.

[29] Shevchenko N, Boden S, Gerbeth G, et al. Chimney formation in solidifying Ga-25wt pct In alloys under the influence of thermosolutal melt convection [J]. Metallurgical and Materials Transactions A, 2013, 44(8): 3797-3808.

[30] Wang F, Wang E, Jia P, et al. Effect of electromagnetic continuous casting on TiN distribution and internal crack of Incoloy800H alloy billet [J]. Acta Metallurgica Sinica, 2017, 53(1): 97-106.

[31] Wang F, Zhang L, Deng A, et al. Continuous casting of incoloy800H superalloy billet under an alternating electromagnetic field [J]. Metals, 2015, 6(1): 2.

[32] Eckert S, Nikrityuk P A, Willers B, et al. Electromagnetic melt flow control during solidification of metallic alloys [J]. The European Physical Journal Special Topics, 2013, 220(1): 123-137.

[33] Wu H, Wei N, Bao Y, et al. Effect of M-EMS on the solidification structure of a steel billet [J]. International Journal of Minerals, Metallurgy, and Materials, 2011, 18(2): 159.

[34] Wang F, Wang E, Zhang L, et al. Influence of electromagnetic stirring (EMS) on the microstructure and mechanical property of Incoloy825 superalloy [J]. Journal of Manufacturing Processes, 2017, 26: 364-371.

[35] Steinbach S, Ratke L. The effect of rotating magnetic fields on the microstructure of directionally solidified Al-Si-Mg alloys [J]. Materials Science and Engineering: A, 2005, 413-414: 200-204.

[36] Spitzer K H, Reiter G, Schwerdtfeger K. Multi-frequency electromagnetic stirring of liquid metals [J]. ISIJ International, 1996, 36(5): 487-492.

[37] Li W S, Shen H F, Liu B C. Three-dimensional simulation of thermosolutal convection and macrosegregation in steel ingots [J]. Steel Research International, 2010, 81(11): 994-1000.

[38] Flemings M C. Principles of control of soundness and homogeneity of large ingots [J]. Scandinavian Journal of Metallurgy, 1976, 5: 1-15.

[39] Olsson A, West R, Fredriksson H. Macrosegregation in ingots [J]. Scandinavian Journal of Metallurgy, 1986, 15(2): 104-112.

[40] Combeau H, Založnik M, Hans S, et al. Prediction of macrosegregation in steel ingots: Influence of the motion and the morphology of equiaxed grains [J]. Metallurgical and Materials Transactions B, 2009, 40(3): 289-304.

[41] Zheng Y, Wu M, Kharicha A, et al. Simulation of macrosegregation in a large vertical continuous casting of steel [A]//IOP Conference Series: Materials Science and Engineering [C]. IOP Publishing, 2016, 143(1): 012032.

[42] Tveito K O, Pakanati A, M'hamdi M, et al. A simplified three-phase model of equiaxed solidification for the prediction of microstructure and macrosegregation in castings [J]. Metallurgical and Materials Transactions A, 2018, 49(7): 2778-2794.

[43] Ludwig A, Gruber-Pretzler M, Wu M, et al. About the formation of macrosegregations during continuous casting of Sn-bronze [J]. Fluid Dynamics and Materials Processing, 2005, 1(4): 285-300.

[44] Nadella R, Eskin D G, Du Q, et al. Macrosegregation in direct-chill casting of aluminium alloys [J]. Progress in Materials Science, 2008, 53(3): 421-480.

[45] Miyazaki M, Isobe K, Murao T. Formation mechanism and modeling of centerline segregation [J]. Nippon Steel Technical Report, 2013, 104: 48-53.

[46] Kajatani T, Drezet J M, Rappaz M. Numerical simulation of deformation-induced segregation in continuous casting of steel [J]. Metallurgical and Materials Transactions A, 2001, 32(6): 1479-1491.

[47] Thome R, Harste K. Principles of billet soft-reduction and consequences for continuous casting [J]. ISIJ International, 2006, 46(12): 1839-1844.

[48] Mayer F, Wu M, Ludwig A. On the formation of centreline segregation in continuous slab casting of steel due to bulging and/or feeding [J]. Steel Research International, 2010, 81(8): 660-667.

[49] Voller V R, Porte-Agel F. Moore's law and numerical modeling [J]. Journal of Computational Physics, 2002, 179(2): 698-703.

[50] Flemings M C. Solidification processing [M]. New York: McGraw-Hill, 1974.

[51] Chalmers B. Principles of solidification [M]. New York: John Wiley & Sons, 1964.

[52] Spittle J A, Brown S G R. Computer simulation of the effects of alloy variables on the grain structures of castings [J]. Acta Metallurgica, 1989, 37(7): 1803-1810.

[53] Zhu P, Smith R W. Dynamic simulation of crystal growth by Monte Carlo method-I. Model description and kinetics [J]. Acta Metallurgica et Materialia, 1992, 40(4): 683-692.

[54] Beltran-Sanchez L, Stefanescu D M. Growth of solutal dendrites: A cellular automaton model and its quantitative capabilities [J]. Metallurgical and Materials Transactions A, 2003, 34(2): 367-382.

[55] Rappaz M, Gandin C A. Probabilistic modelling of microstructure formation in solidification processes [J]. Acta Metallurgica et Materialia, 1993, 41(2): 345-360.

[56] Wang W, Lee P D, Mclean M. A model of solidification microstructures in nickel-based superalloys: predicting primary dendrite spacing selection [J]. Acta Materialia, 2003, 51(10): 2971-2987.

[57] Steinbach I, Schmitz G J. Direct numerical simulation of solidification structure using the phase field method [A]//Modeling of Casting, Welding, and Advanced Solidification Processes VII [C]. The Minerals, Metals and Materials Society, 1998: 521-532.

[58] Kobayashi R. Modeling and numerical simulations of dendritic crystal growth [J]. Physica D: Nonlinear Phenomena, 1993, 63(3-4): 410-423.

[59] Asta M, Beckermann C, Karma A, et al. Solidification microstructures and solid-state parallels: Recent developments, future directions [J]. Acta Materialia, 2009, 57(4): 941-971.

[60] Voller V. A multi-scale/multi-physics modeling framework for solidification systems [A]//The 5th International Conference on CFD in the Process Industries [C], 2006: 13-15.

[61] Trindade L B, Nadalon J E A, Contini A C, et al. Modeling of solidification in continuous casting round billet with mold electromagnetic stirring (M-EMS) [J]. Steel Research International, 2017, 88(4): 1-8.

[62] Hou Z, Jiang F, Cheng G. Solidification structure and compactness degree of central equiaxed grain zone in continuous casting billet using cellular automaton-finite element method [J]. ISIJ International, 2012, 52(7): 1301-1309.

[63] Wang C Y, Beckermann C. A multiphase solute diffusion model for dendritic alloy solidification [J]. Metallurgical and Materials Transactions A, 1993, 24(12): 2787-2802.

[64] Guan R, Ji C, Zhu M, et al. Numerical simulation of V-shaped segregation in continuous casting blooms based on a microsegregation model [J]. Metallurgical and Materials Transactions B, 2018, 49(5): 2571-2583.

[65] Pakanati A, Tveito K O, M'Hamdi M, et al. Application of an equiaxed grain growth and transport model to study macrosegregation in a DC casting experiment [J]. Metallurgical and Materials Transactions A, 2019, 50(4): 1773-1786.

[66] Viardin A, Založnik M, Souhar Y, et al. Mesoscopic modeling of spacing and grain selection in columnar dendritic solidification: Envelope versus phase-field model [J]. Acta Materialia, 2017, 122: 386-399.

[67] Tourret D, Francois M M, Clarke A J. Multiscale dendritic needle network model of alloy solidification with fluid flow [J]. Computational Materials Science, 2019, 162: 206-227.

[68] Tu W T, Shen H F, Liu B C. Numerical simulations of macrosegregation: A comparison between orthogonal grids and non-orthogonal grids [J]. Advanced Materials Research, 2014, 968: 214-217.

[69] Nguyen T T M, Combeau H, Založnik M, et al. Multi-scale Unite element modelling of solidification structures by a splitting method taking into account the transport of equiaxed grains [A]//IOP Conference Series: Materials Science and Engineering [C]. IOP Publishing, 2015, 84: 012007.

[70] Ahmad N, Rappaz J, Desbiolles J L, et al. Numerical simulation of macrosegregation: a comparison between finite volume method and finite element method predictions and a confrontation with experiments [J]. Metallurgical and Materials Transactions A, 1998, 29(2): 617-630.

[71] Beckermann C, Viskanta R. Double-diffusive convection during dendritic solidification of a binary mixture [J]. Physico Chemical Hydrodynamics, 1988, 10: 195-213.

[72] Könözsy L, Eck S, Kharicha M S, et al. Experimental and numerical investigations of NH_4Cl solidification in a mould: Part 2: Numerical results [J]. International Journal of Cast Metals Research, 2009, 22(1-4): 172-174.

[73] Kharicha M S, Eck S, Könözsy L, et al. Experimental and numerical investigations of NH_4Cl solidification in a mould: Part 1: Experimental results [J]. International Journal of

Cast Metals Research, 2009, 22(1-4): 168-171.

[74] Ghenai C, Mudunuri A, Lin C X, et al. Double-diffusive convection during solidification of a metal analog system (NH_4Cl-H_2O) in a differentially heated cavity [J]. Experimental Thermal and Fluid Science, 2003, 28(1): 23-35.

[75] Wu M, Stefan-Kharicha M, Kharicha A, et al. Numerical investigation of an in-situ observed flow regimes during solidification of an NH_4Cl-70 wt%H_2O solution [A]//IOP Conference Series: Materials Science and Engineering [C]. IOP Publishing, 2020, 861(1): 012041.

[76] Wu M, Stefan-kharicha M, Kharicha A, et al. A numerical study on solidification of NH_4Cl–70wt%H_2O solution in a water-cooled mould with a large sample thickness [J]. International Journal of Heat and Mass Transfer, 2021, 164: 120566.

[77] Shahani H, Amberg G, Fredriksson H. On the formation of macrosegregations in unidirectionally solidified Sn-Pb and Pb-Sn alloys [J]. Metallurgical Transactions A, 1992, 23(8): 2301-2311.

[78] Prescott P J, Incropera F P, Gaskell D R. Convective transport phenomena and macrosegregation during solidification of a binary metal alloy: II—Experiments and comparisons with numerical predictions [J]. Journal of Heat Transfer, 1994, 116(3): 742-749.

[79] Krane M J M, Incropera F P. Experimental validation of continuum mixture model for binary alloy solidification [J]. Journal of Heat Transfer, 1997, 119(4): 783-791.

[80] Krane M J M, Incropera F P, Gaskell D R. Solidification of a ternary metal alloy: A comparison of experimental measurements and model predictions in a Pb-Sb-Sn system [J]. Metallurgical and Materials Transactions A, 1998, 29(3): 843-853.

[81] Bellet M, Combeau H, Fautrelle Y, et al. Call for contributions to a numerical benchmark problem for 2D columnar solidification of binary alloys [J]. International Journal of Thermal Sciences, 2009, 48(11): 2013-2016.

[82] Combeau H, Bellet M, Fautrelle Y, et al. Analysis of a numerical benchmark for columnar solidification of binary alloys [A]//IOP Conference Series: Materials Science and Engineering [C]. IOP Publishing, 2012, 33(1): 012086.

[83] Krane M J M. Macrosegregation development during solidification of a multicomponent alloy with free-floating solid particles [J]. Applied Mathematical Modelling, 2004, 28(1):

95-107.

[84] Založnik M, Kumar A, Combeau H. An operator splitting scheme for coupling macroscopic transport and grain growth in a two-phase multiscale solidification model: Part II - Application of the model [J]. Computational Materials Science, 2010, 48(1): 11-21.

[85] Založnik M, Kumar A, Combeau H. An operator splitting scheme for coupling macroscopic transport and grain growth in a two-phase multiscale solidification model: Part II-Application of the model [J]. Computational Materials Science, 2010, 48(1): 11-21.

[86] Nguyen T T M, Gandin C A, Combeau H, et al. Finite element multi-scale modeling of chemical segregation in steel solidification taking into account the transport of equiaxed grains [J]. Metallurgical and Materials Transactions A, 2018, 49(5): 1725-1748.

[87] Wang X D, Petitpas P, Garnier C, et al. A quasi two-dimensional benchmark experiment for the solidification of a tin-lead binary alloy [J]. Comptes Rendus Mécanique, 2007, 335(5): 336-341.

[88] Wang X, Fautrelle Y. An investigation of the influence of natural convection on tin solidification using a quasi two-dimensional experimental benchmark [J]. International Journal of Heat and Mass Transfer, 2009, 52(23-24): 5624-5633.

[89] Hachani L, Zaidat K, Saadi B, et al. Solidification of Sn-Pb alloys: Experiments on the influence of the initial concentration [J]. International Journal of Thermal Sciences, 2015, 91: 34-48.

[90] Hachani L, Zaidat K, Fautrelle Y. Experimental study of the solidification of Sn-10 wt%Pb alloy under different forced convection in benchmark experiment [J]. International Journal of Heat and Mass Transfer, 2015, 85: 438-454.

[91] Boussaa R, Hachani L, Budenkova O, et al. Macrosegregations in Sn-3 wt%Pb alloy solidification: Experimental and 3D numerical simulation investigations [J]. International Journal of Heat and Mass Transfer, 2016, 100: 680-690.

[92] Carozzani T, Gandin C A, Digonnet H, et al. Direct simulation of a solidification benchmark experiment [J]. Metallurgical and Materials Transactions A, 2013, 44(2): 873-887.

[93] Report on the heterogeneity of steel ingots [J]. Journal of Iron Steel Institution, 1926, 113:

39-176.

[94] Flemings M C. Directional solidification and composite structures [A]//Surfaces and Interfaces II. Sagamore Army Materials Research Conference Proceedings [C]. Springer, 1968: 313-352.

[95] Fredriksson H, Hillert M. On the formation of the central equiaxed zone in ingots[J]. Metallurgical Transactions, 1972, 3(2): 569–574.

[96] Fredriksson H, Nilsson S O. On the formation of macrosegregations in ingots [J]. Metallurgical Transactions B, 1978, 9(1): 111-120.

[97] Mehrabian R, Keane M A, Flemings M C. Experiments on macrosegregation and freckle formation [J]. Metallurgical Transactions, 1970, 1(11): 3238-3241.

[98] Fujii T, Poirier D R, Flemings M C. Macrosegregation in a multicomponent low alloy steel [J]. Metallurgical Transactions B, 1979, 10(3): 331-339.

[99] Gu J P, Beckermann C. Simulation of convection and macrosegregation in a large steel ingot [J]. Metallurgical and Materials Transactions A: Physical Metallurgy and Materials Science, 1999, 30(5): 1357-1366.

[100] Pardeshi R, Voller V R, Singh A K, et al. An explicit-implicit time stepping scheme for solidification models [J]. International Journal of Heat and Mass Transfer, 2008, 51(13-14): 3399-3409.

[101] Pickering E J. Macrosegregation in steel ingots: The applicability of modelling and characterisation techniques [J]. ISIJ International, 2013, 53(6): 935-949.

[102] Vannier I, Combeau H, Lesoult G. Numerical model for prediction of the final segregation pattern of bearing steel ingots [J]. Materials Science and Engineering: A, 1993, 173(1-2): 317-321.

[103] Založnik M, Combeau H. Thermosolutal flow in steel ingots and the formation of mesosegregates [J]. International Journal of Thermal Sciences, 2010, 49(9): 1500-1509.

[104] Li W, Shen H, Zhang X, et al. Modeling of species transport and macrosegregation in heavy steel ingots [J]. Metallurgical and Materials Transactions B, 2014, 45(2): 464-471.

[105] Chuang Y K, Schwerdtfeger K. Equations for calculating sedimentation segregation in killed steel [J]. Archiv Eisenhuttenwesen, 1975, 46(5): 303-310.

[106] Beckermann C, Wang C Y. Multiphase/-scale modeling of alloy solidification [J]. Annual Review of Heat Transfer, 1995, 6(6): 115-198.

[107] Wu M, Fjeld A, Ludwig A. Modelling mixed columnar-equiaxed solidification with melt convection and grain sedimentation-Part I: Model description [J]. Computational Materials Science, 2010, 50(1): 32-42.

[108] Ge H, Ren F, Li J, et al. Modelling of ingot size effects on macrosegregation in steel castings [J]. Journal of Materials Processing Technology, 2018, 252: 362-369.

[109] Liu D R, Sang B G, Kang X H, et al. Modelling of macrosegregation in large steel ingot with considering solid movement [J]. Acta Physica Sinica, 2009, 58(13): 104-111.

[110] Li W S, Shen H F, Liu B C. Numerical simulation of macrosegregation in steel ingots using a two-phase model [J]. International Journal of Minerals, Metallurgy and Materials, 2012, 19(9): 787-794.

[111] Rappaz M, Thévoz P H. Solute diffusion model for equiaxed dendritic growth [J]. Acta Metallurgica, 1987, 35(7): 1487-1497.

[112] Poirier D R, Nandapurkar P J, Ganesan S. The energy and solute conservation equations for dendritic solidification [J]. Metallurgical Transactions B, 1991, 22(6): 889-900.

[113] Ni J, Beckermann C. A volume-averaged two-phase model for transport phenomena during solidification [J]. Metallurgical Transactions B, 1991, 22(3): 349-361.

[114] Ni J, Beckermann C. Modeling of globulitic alloy solidification with convection [J]. Journal of Materials Processing and Manufacturing Science, 1993, 2: 217-231.

[115] Wang C Y, Beckermann C. Equiaxed dendritic solidification with convection: Part I. Multiscale/multiphase modeling [J]. Metallurgical and Materials Transactions A, 1996, 27(9): 2754-2764.

[116] Wang C Y, Ahuja S, Beckermann C, et al. Multiparticle interfacial drag in equiaxed solidification [J]. Metallurgical and Materials Transactions B, 1995, 26(1): 111-119.

[117] Ciobanas A I, Fautrelle Y. Ensemble averaged multiphase Eulerian model for columnar/equiaxed solidification of a binary alloy: I. The mathematical model [J]. Journal of Physics D, 2007, 40(12): 3733-3762.

[118] Ciobanas A I, Fautrelle Y. Ensemble averaged multi-phase Eulerian model for columnar/equiaxed solidification of a binary alloy: II. Simulation of the columnar-to-equiaxed transition (CET) [J]. Journal of Physics D, 2007, 40(14): 4310-4336.

[119] Nielsen Ø, Mo A, Appolaire B, et al. Measurements and modeling of the microstructural morphology during equiaxed solidification of Al-Cu alloys [J]. Metallurgical and

Materials Transactions A, 2001, 32(8): 2049-2060.

[120] Ludwig A, Wu M. Modeling of globular equiaxed solidification with a two-phase approach [J]. Metallurgical and Materials Transactions A, 2002, 33(12): 3673-3683.

[121] Wu M, Ludwig A. Modeling equiaxed solidification with melt convection and grain sedimentation-I: Model description [J]. Acta Materialia, 2009, 57(19): 5621-5631.

[122] Hao J, Grasser M, Wu M, et al. A 3-phase model for mixed columnar-equiaxed solidification in DC casting of bronze [A]//IOP Conference Series: Materials Science and Engineering [C]. IOP Publishing, 2011, 27(1): 012015.

[123] Wu M, Fjeld A, Ludwig A. Modelling mixed columnar-equiaxed solidification with melt convection and grain sedimentation-Part I: Model description [J]. Computational Materials Science, 2010, 50(1):32-42.

[124] Wu M, Kharicha A, Ludwig A. Using four-phase Eulerian volume averaging approach to model macrosegregation and shrinkage cavity [A]//IOP Conference Series: Materials Science and Engineering [C]. IOP Publishing, 2015, 84(1): 12006.

[125] Zheng Y, Wu M, Kharicha A, et al. Incorporation of fragmentation into a volume average solidification model [J]. Modelling and Simulation in Materials Science and Engineering, 2017, 26(1): 15004.

[126] Feng Y, Založnik M, Thomas B G, et al. Meso-scale simulation of liquid feeding in an equiaxed dendritic mushy zone [J]. Materialia, 2020, 9: 100612.

[127] Feller R J, Beckermann C. Modeling of solidification of metal-matrix participate composites with convection [J]. Metallurgical and Materials Transactions B, 1997, 28(6): 1165-1183.

[128] Cai D, Ren F, Ge H, et al. Modelling of inclusion effects on macrosegregation in solidifying steel ingot with a multi-phase approach [J]. Metallurgical and Materials Transactions A, 2019, 50(3): 1323-1332.

[129] Jiang D, Zhu M. Solidification structure and macrosegregation of billet continuous casting process with dual electromagnetic stirrings in mold and final stage of solidification: A numerical study [J]. Metallurgical and Materials Transactions B, 2016, 47(6): 3446-3458.

[130] Jiang D, Wang W, Luo S, et al. Numerical simulation of slab centerline segregation with mechanical reduction during continuous casting process [J]. International Journal of Heat

and Mass Transfer, 2018, 122: 315-323.

[131] Li J, Wu M, Ludwig A, et al. Simulation of macrosegregation in a 2.45-ton steel ingot using a three-phase mixed columnar-equiaxed model [J]. International Journal of Heat and Mass Transfer, 2014, 72: 668-679.

[132] Wu M, Li J, Ludwig A, et al. Modeling diffusion-governed solidification of ternary alloys-Part 1: Coupling solidification kinetics with thermodynamics [J]. Computational Materials Science, 2013, 79: 830-840.

[133] Mehrabian R, Keane M, Flemings M C. Interdendritic fluid flow and macrosegregation; Influence of gravity [J]. Metallurgical and Materials Transactions, 1970, 1(5): 1209-1220.

[134] Könözsy L, Ishmurzin A, Grasser M, et al. Columnar to equiaxed transition during ingot casting using ternary alloy composition [A]//Materials Science Forum [C], Trans Tech Publications, 2010, 649: 349-354.

[135] Stefanescu D M, Upadhya G, Bandyopadhyay D. Heat transfer-solidification kinetics modeling of solidification of castings [J]. Metallurgical Transactions A, 1990, 21(3): 997-1005.

[136] Oldfield W. A quantitative approach to casting solidification: freezing of cast iron [J]. ASM Transaction, 1966, 59: 945-961.

[137] Thévoz P, Desbiolles J L, Rappaz M. Modeling of equiaxed microstructure formation in casting [J]. Metallurgical Transactions A, 1989, 20(2): 311-322.

[138] Wu M, Ludwig A, Bührig-Polaczek A, et al. Influence of convection and grain movement on globular equiaxed solidification [J]. International Journal of Heat and Mass Transfer, 2003, 46(15): 2819-2832.

[139] Bedel M, Tveito K O, Založnik M, et al. A model study of the impact of the transport of inoculant particles on microstructure formation during solidification [J]. Computational Materials Science, 2015, 102: 95-109.

[140] Won Y M, Kim K, Yeo T, et al. Effect of cooling rate on ZST, LIT and ZDT of carbon steels near melting point [J]. ISIJ International, 1998, 38(10): 1093-1099.

[141] Jacobi H, Schwerdtfeger K. Dendrite morphology of steady state unidirectionally solidified steel [J]. Metallurgical Transactions A, 1976, 7(6): 811-820.

[142] Imagumbai M. Behaviors of manganese-sulfide in aluminum-killed steel solidified Uni-directionally in steady state - dendrite structure and inclusions [J]. ISIJ International,

1994, 34(11): 896-905.

[143] Nuri Y, Ohashi T, Hiromoto T, et al. Solidification microstructure of ingots and continuously cast slabs treated with rare earth metal [J]. Tetsu-to-Hagane, 1980, 66(6): 618-627.

[144] Kurz W, Giovanola B, Trivedi R. Theory of microstructural development during rapid solidification [J]. Acta Metallurgica, 1986, 34(5): 823-830.

[145] Lipton J, Glicksman M E, Kurz W. Dendritic growth into undercooled alloy metals [J]. Materials Science and Engineering, 1984, 65(1): 57-63.

[146] Ludwig A, Wu M. Modeling the columnar-to-equiaxed transition with a three-phase Eulerian approach [J]. Materials Science and Engineering: A, 2005, 413-414: 109-114.

[147] Invanstov G P. Temperature field around spherical, cylindrical, and needle-shaped crystals which grow in supercooled melts[J]. Doklady Akademii Nauk , 1947, 58: 567-569.

[148] Wu M, Ludwig A. Modeling equiaxed solidification with melt convection and grain sedimentation-II. Model verification [J]. Acta Materialia, 2009, 57(19): 5632-5644.

[149] Won Y M, Thomas B G. Simple model of microsegregation during solidification of steels [J]. Metallurgical and Materials Transactions A, 2001, 32(7): 1755-1767.

[150] Rappaz M, Thévoz P H. Solute diffusion model for equiaxed dendritic growth: Analytical solution [J]. Acta Metallurgica, 1987, 35(12): 2929-2933.

[151] Badillo A, Ceynar D, Beckermann C. Growth of equiaxed dendritic crystals settling in an undercooled melt, Part 2: Internal solid fraction [J]. Journal of Crystal Growth, 2007, 309(2): 216-224.

[152] Appolaire B, Combeau H, Lesoult G. Modeling of equiaxed growth in multicomponent alloys accounting for convection and for the globular/dendritic morphological transition [J]. Materials Science and Engineering: A, 2008, 487(1-2): 33-45.

[153] Bird R B, Stewart W E, Lightfoot E N. Transport phenomena [M]. New York: John Wiley and Sons, 1960.

[154] Happel J. Viscous flow in multiparticle systems: Slow motion of fluids relative to beds of spherical particles [J]. AIChE Journal, 1958, 4(2): 197-201.

[155] Guan R, Ji C, Wu C, et al. Numerical modelling of fluid flow and macrosegregation in a continuous casting slab with asymmetrical bulging and mechanical reduction [J].

International Journal of Heat and Mass Transfer, 2019, 141: 503-516.

[156] Jiang D, Zhu M. Center segregation with final electromagnetic stirring in billet continuous casting process [J]. Metallurgical and Materials Transactions B, 2017, 48(1): 444-455.

[157] Scott G D, Kilgour D M. The density of random close packing of spheres [J]. Journal of Physics D, 1969, 2(6): 863.

[158] Olmedilla A, Založnik M, Combeau H. DEM simulation of dendritic grain random packing: Application to metal alloy solidification [A]//EPJ Web of Conferences [C]. EDP Sciences, 2017, 140: 06002.

[159] Plotkowski A, Krane M J M. A continuum grain attachment model for simulations of equiaxed solidification [J]. Computational Materials Science, 2016, 124: 238-248.

[160] Plotkowski A, Krane M J M. The effect of velocity based packing schemes on macrosegregation development in simulations of equiaxed solidification [J]. Applied Mathematical Modelling, 2016, 40(21-22): 9212-9227.

[161] Wang C Y, Beckermann C. A unified solute diffusion model for columnar and equiaxed dendritic alloy solidification [J]. Materials Science and Engineering: A, 1993, 171(1-2): 199-211.

[162] Olmedilla A, Založnik M, Messmer T, et al. Packing dynamics of spherical and nonconvex grains sedimenting at low Stokes number[J]. Physical Review E, 2019, 99(1): 12907.

[163] Martorano M A, Biscuola V B. Columnar front tracking algorithm for prediction of the columnar-to-equiaxed transition in two-dimensional solidification [J]. Modelling and Simulation in Materials Science and Engineering, 2006, 14(7): 1225-1243.

[164] Torabi Rad M, Založnik M, Combeau H, et al. Upscaling mesoscopic simulation results to develop constitutive relations for macroscopic modeling of equiaxed dendritic solidification [J]. Materialia, 2019, 5: 100231.

[165] Plotkowski A, Krane M J M. On the numerical prediction of channel segregation [J]. International Journal of Heat and Mass Transfer, 2016, 100: 11-23.

[166] Kumar A, Dussoubs B, Založnik M, et al. Effect of discretization of permeability term and mesh size on macro- and meso-segregation predictions [J]. Journal of Physics D: Applied Physics, 2009, 42(10): 105503.

[167] Hachani L. Etude de l'influence de la convection naturelle et forcée sur le processus de la solidification: cas d'un alliage métallique binaire [D]. Grenoble: Université de Grenoble, 2014.

[168] Fautrelle Y, Wang X D, Hachani L, et al. Solidification of Sn-Pb alloys: Experiments on the influence of the initial concentration [J]. International Journal of Thermal Sciences, 2015, 91: 34-48.

[169] Wang X, Moreau R, Etay J, et al. A periodically reversed flow driven by a modulated traveling magnetic field: Part II. theoretical model [J]. Metallurgical and Materials Transactions B, 2009, 40(1): 104-113.

[170] Drew D A. Mathematical modeling of two-phase flow [J]. Annual Review of Fluid Mechanics, 1983, 15(1): 261-291.

[171] Jones W P, Launder B E. The prediction of laminarization with a two-equation model of turbulence [J]. International Journal of Heat and Mass Transfer, 1972, 15(2): 301-314.

[172] Prescott P J, Incropera F P. The effect of turbulence on solidification of a binary metal alloy with electromagnetic stirring [J]. Journal of Heat Transfer, 1995, 117(3): 716-724.

[173] Shyy W, Pang Y, Hunter G B, et al. Effect of turbulent heat transfer on continuous ingot solidification [J]. Journal of Engineering Materials and Technology, 1991, 115(1):8-16.

[174] Poole G M, Heyen M, Nastac L, et al. Numerical modeling of macrosegregation in binary alloys solidifying in the presence of electromagnetic stirring [J]. Metallurgical and Materials Transactions B, 2014, 45(5): 1834-1841.

[175] Stankus S V, Khairulin R A. The density of alloys of tin-lead system in the solid and liquid states [J]. High Temperature, 2006, 44(3): 389-395.

[176] Plevachuk Y, Sklyarchuk V, Yakymovych A, et al. Electronic properties and viscosity of liquid Pb-Sn alloys [J]. Journal of Alloys and Compounds, 2005, 394(1-2): 63-68.

[177] Wang T, Hachani L, Fautrelle Y, et al. Numerical modeling of a benchmark experiment on equiaxed solidification of a Sn–Pb alloy with electromagnetic stirring and natural convection [J]. International Journal of Heat and Mass Transfer, 2020, 151: 119414.

[178] Sachi S, Založnik M, Combeau H, et al. Analysis of columnar-to-equiaxed transition experiment in lab scale steel casting by a multiphase model [A]//IOP Conference Series: Materials Science and Engineering [C]. IOP Publishing, 2019, 529(1): 12039.

[179] Kumar A, Založnik M, Combeau H. Prediction of equiaxed grain structure and

macrosegregation in an industrial steel ingot: comparison with experiment [J]. International Journal of Advances in Engineering Sciences and Applied Mathematics, 2010, 2(4): 140-148.

[180] Wu M, Nunner G, Ludwig A, et al. Evaluation of a mixed columnar-equiaxed solidification model with laboratory castings [A]//IOP Conference Series: Materials Science and Engineering [C]. IOP Publishing, 2012, 27(1): 012018.

[181] Wu M, Ludwig A, Kharicha A. A four phase model for the macrosegregation and shrinkage cavity during solidification of steel ingot [J]. Applied Mathematical Modelling, 2017, 41: 102-120.

[182] Zhu Q F, Zhao Z H, Cui J Z, et al. Effect of combined application of electromagnetic fields on horizontal direct chill casting of 7050 aluminium alloy [J]. Materials Science and Technology, 2008, 24(5): 560-566.

[183] Wang X, Ma N, Bliss D F, et al. Combining static and rotating magnetic fields during modified vertical Bridgman crystal growth [J]. Journal of Thermophysics and Heat Transfer, 2007, 21(4): 736-743.

[184] Kubota K, Murakami K, Okamoto T. Fluid flow and macrosegregation in cylindrical ingots [J]. Materials Science and Engineering, 1986, 79(1): 67-77.

[185] Sun H, Zhang J. Study on the macrosegregation behavior for the bloom continuous casting: Model Development and Validation [J]. Metallurgical and Materials Transactions B, 2014, 45(3): 1133-1149.

[186] Dou K, Yang Z, Liu Q, et al. Influence of secondary cooling mode on solidification structure and macro-segregation behavior for high-carbon continuous casting bloom [J]. High Temperature Materials and Processes, 2017, 36(7): 741-753.

[187] Ge H, Ren F, Cai D, et al. Gradual-cooling solidification approach to alleviate macrosegregation in large steel ingots [J]. Journal of Materials Processing Technology, 2018, 262: 232-238.

[188] Meng Q, Wang F, Li C, et al. Numerical simulation of macrosegregation in water-cooled heavy flat ingot during solidification [J]. JOM, 2014, 66(7): 1166-1174.

List of publications with abstracts

[1] **T. Wang**, S. Semenov, E. Wang, Y. Delannoy, Y. Fautrelle, and O. Budenkova, Effect of diffusion length in modeling of equiaxed dendritic solidification under buoyancy flow in a configuration of Hebditch–Hunt experiment [J]. Metallurgical and Materials Transactions B, 2019, 50(6): 3039-3054. (Chapter 2 and Chapter 3)

Abstract: Modeling of equiaxed solidification is vital for understanding the solidification process of metallic alloys. In this work, an extended literature review is given for the models currently used for equiaxed solidification simulations. Based on this analysis, we present a three-phase multiscale equiaxed solidification model in which some approximations regarding solute transport at microscopic scale are put together in a new way and incorporated into macroscopic transport equations. For the latter, a term relating to the momentum exchange between the two phases is revised, and a modification for the grain packing algorithm is proposed. A modernized model for equiaxed dendrite growth is tested using a case of solidification of Sn-5 wt pct Pb alloy in a parallelepiped cavity that mimics the Hebditch–Hunt experiment. The results obtained using two approaches to calculate diffusion length are presented and compared both with each other and with numerical results from elsewhere. It is demonstrated that diffusion length has a crucial effect on the final segregation pattern.

[2] **T. Wang**, L. Hachani, Y. Fautrelle, Y. Delannoy, E. Wang, X. Wang, and O. Budenkova, Numerical modeling of a benchmark experiment on equiaxed solidification of a Sn-Pb alloy with electromagnetic stirring and natural convection [J]. International Journal of Heat and Mass Transfer, 2020, 151: 119414. (Chapter 4)

Abstract: A three-phase volume averaged equiaxed model is applied to simulation of an experiment on solidification of the binary alloy Sn-10 wt% Pb subjected to the electromagnetic stirring. The experiment, whose description was published earlier, was performed in a parallelepiped cavity under controlled cooling conditions and with real-time two-dimensional temperature measurement over a lateral surface of the cavity co-planar with direction of solidification. Applied numerical model treats motion of the liquid and equiaxed grains whose growth kinetics is taken into account and uses a double time step scheme to accelerate solution. Growth of columnar dendrite is not considered. It is shown that electromagnetic force acting in a direction opposite to the natural convection flow creates moderately turbulent flow in pure liquid which is treated with a realizable $k_\varepsilon{-}\varepsilon$ model. It is demonstrated that calculated temperature distribution in the cavity well reproduces temperature maps reconstructed from thermocouples measurements throughout the experiment. Final macrosegregation map and distribution of density grain number are qualitatively similar to those obtained in the experiment. Variation of intensity of electromagnetic stirring in numerical model shows that this affects shape and localization of positive segregation region at the bottom of the cavity.

[3] **T. Wang**, E. Wang, Y. Delannoy, Y. Fautrelle, and O. Budenkova, Numerical simulation of macrosegregation formation in a 2.45 ton steel ingot using a three-phase equiaxed solidification model [J]. Metals, 2021, 11(2): 262. (Chapter 5)

Abstract: In the present work macrosegregation during solidification of a 2.45 ton steel ingot is simulated with a pure equiaxed model, which was tested previously via modeling of a benchmark experiment. While the columnar structure is not taken into account, a packed layer formed over inner walls of the mold at an early stage of solidification reproduces to some extent phenomena generally related to zones of columnar dendrites. Furthermore, it is demonstrated that interaction of free-floating equiaxed grains with ascending convective flow in the bulk liquid results in flow instabilities. This defines the irregular form of the negative segregation zone, the formation of which at the ingot bottom corresponds to experimental observation. Vertical channels reported in experimental measurements are reproduced in simulations. It is confirmed that intensification of ingot cooling may decrease segregation in the ingot.

[4] **T. Wang**, E. Wang, Y. Delannoy, Y. Fautrelle, and O. Budenkova, Three-phase numerical modeling for equiaxed solidification of Sn–10 wt% Pb alloy under forced convection driven by electromagnetic force [C]. IOP: Materials Science and Engineering, 2019, 529: 012030. (Chapter 4)

Abstract: A three-phase equiaxed solidification model where macroscale heat transfer and fluid flow are coupled with microscale nucleation and dendrite growth, is applied to the simulation of the macrosegregation in binary alloy solidification subjected to the electromagnetic stirring. The investigated experimental solidification case is conducted in a cavity which has a good control of the thermal boundary conditions. The proposed model uses a double time step scheme to accelerate the solution. Electromagnetic force is introduced as a source term into momentum equation in analytical form. To account for the friction from the side walls, a 2D½ flow model is applied to a three-dimensional experimental configuration. A comparison between the results of simulation and experimental ones is made.

[5] **T. Wang**, S. Semenov, E. Wang, Y. Delannoy, Y. Fautrelle, and O. Budenkova, Comparison of two-phase and three-phase macroscopic models of equiaxed grain growth in solidification of binary alloy with electromagnetic stirring [C]. IOP: Materials Science and Engineering, 2020, 861: 012026. (Chapter 4)

Abstract: Simulations of equiaxed solidification using two-phase and three-phase models are performed for the experimental benchmark AFRODITE with electromagnetic stirring. A three-phase model presented by authors elsewhere accounts for solid phase, inter- and extradendritic liquid phases. With respect to that model, the two-phase approach can be considered as reduced or simplified, yet, this implies also less number of assumptions regarding closure relations. In simulations, as expected, final segregation obtained with two–phase model is stronger, yet, it is qualitatively similar to the segregation pattern obtained with three-phase model.

[6] **T Wang**, O. Budenkova, Y. Delannoy, Y. Fautrelle, and E. Wang, A 3-phase equiaxed solidification numerical model for binary alloy coupling macroscopic transport and grain growth [C]. Solidification and Gravity VII, Hungary, 2017. (Chapter 3)

Abstract: Modeling equiaxed solidification plays an important role in comprehension of solidification of metallic alloys and serves for prediction of the final solid structure and components' segregation. In the work, a 3-phase model which couples heat, mass, solute and momentum transportation for both grain phase and extradendritic liquid phase is presented for equiaxed solidification. A special attention is given to the calculation of the diffusion length at the interface between interdendritic and extradendritic liquid phases as well as to the momentum exchange coefficient between the liquid and grain phases. It is demonstrated that both the two parameters have critical effect on simulation results. The model is tested using a case of solidification of a binary alloy in a rectangular cavity. The results obtained in simulations are compared with other numerical results.